UNIVERSIDAD DE CHILE
FACULTAD DE CIENCIAS FÍSICAS Y MATEMÁTICAS
DEPARTAMENTO DE ASTRONOMÍA

# DETECTION AND CHARACTERIZATION OF SINGLE AND DOUBLE STELLAR/PLANETARY SYSTEMS

TESIS PARA OPTAR AL GRADO DE
DOCTORA EN CIENCIAS, MENCIÓN ASTRONOMÍA

MARITZA GABRIELA SOTO VÁSQUEZ

PROFESOR GUÍA:
JAMES STEWART JENKINS

MIEMBROS DE LA COMISIÓN:
GUILLEM ANGLADA-ESCUDÉ
RICARDO RODRIGO MUÑOZ VIDAL
PATRICIO MICHEL ROJO RUBKE

Este trabajo ha sido parcialmente financiado por CONICYT-PCHA/Doctorado Nacional/2014-21141037

SANTIAGO DE CHILE
2018

RESUMEN DE LA MEMORIA PARA OPTAR
AL TÍTULO DE DOCTORA EN CIENCIAS, MENCIÓN ASTRONOMÍA
POR: MARITZA GABRIELA SOTO VÁSQUEZ
FECHA: 20 DE JUNIO, 2018
PROF. GUÍA: JAMES STEWART JENKINS

# DETECTION AND CHARACTERIZATION OF SINGLE AND DOUBLE STELLAR/PLANETARY SYSTEMS

El crecimiento exponencial del número de exoplanetas descubiertos en los últimos años ha derivado en un mayor entendimiento de los planetas en la galaxia, de los cuales la Tierra es miembro; pero aún nos queda un gran camino por delante. El propósito de esta tesis es descubrir y confirmar nuevos planetas orbitando estrellas enanas y gigantes, además de desarrollar técnicas para extraer la mayor cantidad de información posible de las estrellas, permitiendo así una mayor compresión de los sistemas planetarios en estudio.

Primero, analizamos datos crudos tomados con FEROS de las estrellas HD 11977, HD 47536, HD 110014, y HD122430, todas con al menos un planeta descubierto. Confirmamos la existencia de los planetas orbitando a HD 11977, HD 47536 y HD 110012, pero con parámetros orbitales distintos a los publicados. Además, no encontramos evidencia que respaldara la existencia del segundo planeta orbitando a HD 47536, ni que hubiese planetas alrededor de HD 122430 y HD 70573. Finalmente, reportamos el descubrimiento de un segundo planeta orbitanto a HD 110014, con una masa mínima de 3.1 $M_{\rm Jup}$y periodo orbital de 130 días.

Luego, usando datos fotométricos de la campaña 11 y 12 de la misión K2, junto con mediciones de velocidad radial tomados con los espectrógrafos HARPS, FEROS, y Coralie, reportamos el descubrimiento de dos planetas Jupiter calientes orbitando a dos estrellas enanas. Encontramos que K2-237 b y K2-238 b tienen masas de $1.36^{+0.10}_{-0.10}$ y $0.86^{+0.13}_{-0.12}$ $M_{\rm Jup}$, radio de $1.63^{+0.07}_{-0.08}$ y $1.30^{+0.15}_{-0.14}$ $R_{\rm Jup}$, y orbitan a sus estrellas con órbitas de 1.28 y 3.2 días, respectivamente. El gran tamaño de K2-237 b nos lleva a concluir que corresponde a un Jupiter caliente altamente inflado, mientras que el radio de K2-238 b es consistente con modelos teóricos. K2-237 b representa un excelente laboratorio para estudios de atmósferas planetarias.

Finalmente, desarrollamos una herramiento que permite el cálculo automático de parámetros estelares para grandes cantidades de estrellas, usando espectros echelle de alta resolución. SPECIES mide anchos equivalentes para un gran número de líneas de fierro y los usa para resolver la ecuación de transferencia radiativa asumiento equilibrio termodinámico local para obtener los párametros atmosféricos. Estos valores son usados para obtener la abundancia de 11 elementos químicos en las atmósferas estelares. La velocidad de rotación y de macroturbulencia son obtenidos usando fórmulas calibradas a la temperatura estelar, y perfiles de línea sintéticos que igualen a los perfiles medidos para cinco líneas de absorción. SPECIES obtiene la masa, radio y edad interpolando en isocronas MIST, usando el método Bayesiano. Luego de una serie de pruebas encontramos que los parámetros que obtiene SPECIES son congruentes con los de la literatura. También derivamos relaciones analíticas que describen las correlaciones entre los parámetros, e implementamos nuevos métodos para trabajar con estas correlaciones en la obtención de las incertezas asociadas a cada medición.

RESUMEN DE LA MEMORIA PARA OPTAR
AL TÍTULO DE DOCTORA EN CIENCIAS, MENCIÓN ASTRONOMÍA
POR: MARITZA GABRIELA SOTO VÁSQUEZ
FECHA: 20 DE JUNIO, 2018
PROF. GUÍA: JAMES STEWART JENKINS

# DETECTION AND CHARACTERIZATION OF SINGLE AND DOUBLE STELLAR/PLANETARY SYSTEMS

The exponential growth of the exoplanet detection frequency in the past years has led to a great improvement in our understanding of the population of planets in the galaxy; of which the Earth is one, yet we are still very much at the beginning of a long road ahead. The aim of this thesis work is to discover and confirm new planetary candidates orbiting dwarf and giant stars, as well as to develop techniques to extract as much information from the host-star as possible, allowing a deeper understanding of the planetary system under study.

We first reanalyzed raw FEROS data for the stars HD 11977, HD 47536, HD 70573, HD 110014 and HD 122430, all of which were claimed to have at least one planetary companion. We confirmed the existence of the planets around HD 11977, HD 47536 and HD 110014, but with different orbital parameters than those previously published. In addition, we found no evidence of the second planet candidate around HD 47536, nor any companions orbiting HD 122430 and HD 70573, and therefore we helped debias de population statistics for giant stars. Finally, we report the discovery of a second planet around HD 110014, with a minimum mass of 3.1 $M_{\text{Jup}}$ and a orbital period of 130 d.

Next, using photometric data from Campaigns 11 and 12 of the K2 mission, along with radial velocity measurements from the HARPS, FEROS, and Coralie spectrographs, we report the discovery of two hot Jupiters orbiting two dwarf stars. We find that K2-237 b and K2-238 b have masses of $1.36^{+0.10}_{-0.10}$ and $0.86^{+0.13}_{-0.12}$ $M_{\text{Jup}}$, radii of $1.63^{+0.07}_{-0.08}$ and $1.30^{+0.15}_{-0.14}$ $R_{\text{Jup}}$, and are orbiting their host stars in 2.18 and 3.2 day orbits, respectively. The large radius of K2-237 b leads us to conclude that this corresponds to a highly inflated hot Jupiter-type planet, while the radius of K2-238 b is consistent with theoretical models. K2-237 b represents an excellent laboratory for planetary atmosphere studies.

Finally, we develop a tool that allows the automated calculation of stellar parameters for a large number of stars, using high-resolution echelle spectra. SPECIES measures the equivalent widths of many iron lines and uses them to solve the radiative transfer equation assuming local thermodynamic equilibrium to obtain the atmospheric parameters. These values are used to derive the abundance of an additional 11 important chemical elements in the stellar photosphere. Rotation and macroturbulent velocity are obtained using temperature calibrators and synthetic line profiles to match the observed spectra of five absorption lines. SPECIES derives the mass, radius, and age, by interpolating in a grid of MIST isochrones, using a Bayesian approach. After thorough testing we found that SPECIES obtains bulk parameters that are in good agreement with those in the literature. We also obtained analytic relations to describe the correlations between different parameters, and we implemented new methods to better handle these correlations, providing a better description of the uncertainties associated with the measurements.

# Agradecimientos

Hay muchas personas que me ayudaron a completar este trabajo de Tesis, y no podré mencionarlos a todos en esta página. Primero, debo agradecer a mi profesor guía. James, creo que fuiste el mejor guía que me pudo haber tocado. Siempre me trataste como una igual, y eso me dio la confianza de hablarte de cualquier tema, de poder ir a tu oficina y preguntarte lo que fuese, sin importar lo básico o simple que fuese esa duda. A pesar de que siempre me empujabas a seguir trabajando, nunca me sentí presionada, y sabía que podía trabajar a mi propio ritmo. Bajo tu guía siento que me fui convirtiendo poco a poco en una investigadora más independiente. Fuiste un muy buen amigo en todo este proceso, desde el primer día, y no habría podido terminar este trabajo sin tu apoyo ni guía. I also want to thank Didier Queloz, for being a great advisor during my time in Cambridge. Even though you always had so much work to do, you still found the time to talk with me, and take interest in my research. I really thank all your support.

Quiero también agradecer a mi familia por todo el apoyo que siempre me dieron. Por nunca dudar de esta carrera que decidí seguir, y por apoyarme desde el primer momento que mostré interés en la astronomía. Por siempre mostrarse orgullosos de mis logros, y emocionarse cada vez que aparecía mi cara en algún lado. También una mención muy importante a todas mis mascotas, que siempre quieren pasar tiempo conmigo, yo también quiero pasar todo mi tiempo con ellos.

Finalmente, quiero agradecer a todas las personas que hicieron mi paso por Calán una experiencia muy divertida. A todas las personas que pasaron por mi oficina: la Paula S, Paula L., Srini, Jose, Elise, Matías S., Coni, y Bica. Ustedes hacían el ir a Calán algo no terrible, porque siempre sabía que me iban a hacer reir, y que siempre podía contarles a ustedes lo que fuese que me pasara. Cada vez que me sentía frustrada o aburrida de todo, ustedes me levantaban el ánimo. La oficina 'Pequeños Placeres' es de verdad la mejor de Calán, donde todo pasa, y la más divertida de estar. Aunque a veces se tornaba difícil trabajar porque todos estábamos hablando, no lo cambiaría por nada. Una mención especial al Matías D, que siempre entendió mi frustración con Calán y la investigación, junto con otras cosas. I must also thank my very dear friends Irina and Lucinda. You two, along with Penny and the cats, made my months in Cambridge some of the best ones I've ever had. We were the best housemates ever, and I'll always remember our Tasty Thursdays, and the Friday's going out. All the gin we had is something I also miss. I know we will remain friends forever, and I hope we meet many more times again in the future. I love you my girls.

# Contents

# List of Tables

# List of Figures

# Introduction

Among the main goals in astronomy throughout history, is to understand the formation of the Solar System, and the search for other worlds like the Earth. The detection of exoplanets was a key-element in path to reach those goals, but due to the very high level of precision necessary for for the detection of planets orbiting other stars, it was not possible up until only two decades ago. In 1995, Michel Mayor and Didier Queloz reported the discovery of the first exoplanet orbiting a Solar-like star (Mayor and Queloz 1995), changing our understanding of planetary formation. This planet, 51 Pegasi b, is unlike anything we'd ever seen in our Solar System. It was a Jupiter-mass planet, orbiting a Sun-like star, but with an orbital period of $\sim 4$ days. It was what is known now as a 'hot Jupiter' planet. It left astronomers wondering about its formation and survival at such a short distance from its star, receiving an amount of radiation higher than any other planet in our Solar System. 51 Pegasi b was just the first one over a thousand exoplanets discovered until now, with characteristics nothing like we knew before, and have forced astronomers to reformulate formation theories, and to improve our understanding of the Solar System and realize its uniqueness.

The aim of this thesis project can be divided into two parts: detection of exoplanets and host star characterization. Exoplanet detection was done following two of the most used methods: transit photometry and stellar radial velocity. These are described in the first section of this chapter, along with a brief summary of the other detection methods. Stellar characterization was done by using high-resolution spectra, which allows us to derive atmospheric parameters and physical dimensions, like mass and radius. Stellar parameters can then be used to characterize the detected systems. The physics that govern stellar atmospheres are described in section 0.2.1, as well as the theory behind the methods used in this thesis project to derive their characteristics.

## 0.1 Detection Methods

Exoplanet detection is not an easy task for astronomers, and it requires high precision telescopes and instruments. In most of the cases, indirect methods focused on the study of the stars are used for the detection of planets. This is due to the large contrasts between the radiation emitted from the star, compared to that of the planet, as well as their large differences in size and mass in most cases. Figure 1 shows the orbital period against mass and radius for all the planets detected up to March 2018[1], separated by detection method. As can bee seen, two methods are responsible for over 90% of detections up to date: stellar radial velocity and transit photometry. Before going into

---

[1] `http://exoplanet.eu`

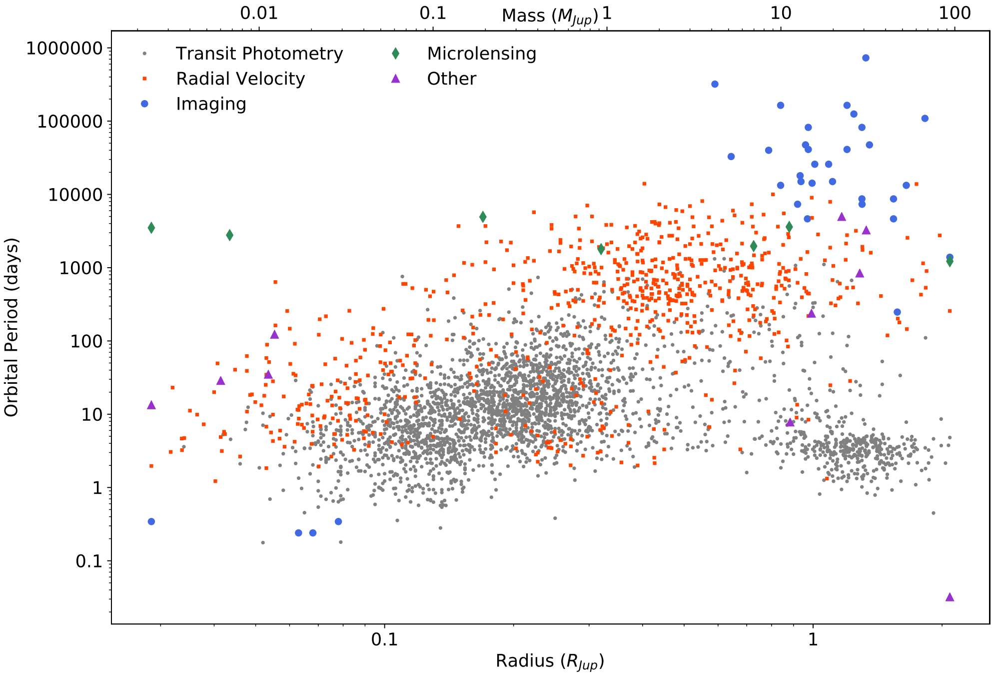

Figure 1: Orbital period versus planetary mass and radius for confirmed planets. Different colors and symbols represent the different detection methods used.

detail about these two methods, I will give a brief summary of the other methods mentioned in Figure 1.

### 0.1.1 Gravitational Microlensing

Gravitational microlensing makes use of a specific outcome from Einstein's Theory of General Relativity for the detection of exoplanets. According to the theory, the presence of a massive body curves the local spacetime and deflects the background light passing closeby. The massive body producing the space curvature will act as a lens. A star in our galaxy can then become a lens to the light coming from a more distant star that is passing behind the lens star. This will produce an apparent increase in the brightness of the lens star, which can last for days.

If the lens star has a planet orbiting it, then, and given the right geometric configuration, this planet can act as an additional lens source, increasing the brightness of the lens star but for a short period of time, much less than that of the whole microlensing event. Figure 2 shows one example of a microlensing event. This method is sensitive to planets orbiting at large distances ($\sim 1 - 10$ AU), but can detect planets with masses down to the Earth's. Unfortunately, a microlensing event is a one-at-a-time event, and follow-up observations are very difficult to perform as the host stars are usually very distant.

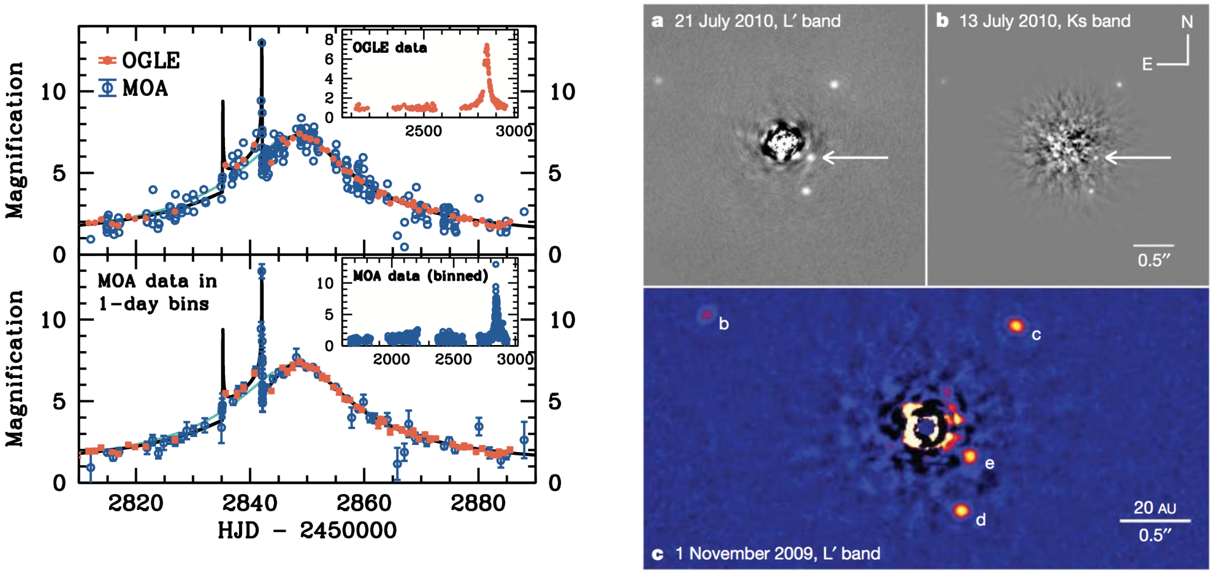

Figure 2: Left panel: OGLE-2003-BLG-235/MOA- 2003-BLG-53Lb, first microlensing planet detected by Bond et al. (2004). Right panel: HR8799, with its four planets detected through direct imaging in the IR by Marois et al. (2010).

### 0.1.2 Direct Imaging

As its name suggests, this method consists of obtaining direct images of planets orbiting other stars. This is very difficult to achieve, as the planets are generally thousands to billions of times fainter than their host stars. That limits the range of exoplanets that can be detected by this method to massive and young planets orbiting at large separations. Even with these difficulties, it has been possible to detect several planets using this method. One example is the system orbiting the star HR8799 (Figure 2). One of its great advantages is that it is possible to study the planets directly, instead of relying on indirect methods (which will be explained in the next sections).

For more details about these two methods, see Fischer et al. (2014).

### 0.1.3 Radial Velocities

The radial velocity (RV) method consists of measuring the radial movement of a star, produced by a planet orbiting it. The motion of two bodies interacting via a gravitational force (two-body problem) can be reduced to that of a single body, moving by an external gravitational force.

Consider two objects, with masses $m_1$ and $m_2$ and positions $\vec{r_1}$ and $\vec{r_2}$, respectively, according to an arbitrary coordinate system (Figure 3, left panel). The relative position vector, $\vec{r}$, will be defined as $\vec{r} = \vec{r_1} - \vec{r_2} = r\hat{r}$, where $r$ is the distance between body 1 and 2, and $\hat{r}$ is the unit vector pointing from body 2 to body 1. Using Newton's third law, it is possible to demonstrate that the force acting on both objects is the same as the one acting on an object of mass $\mu = m_1 m_2/(m_1 + m_2)$ (called the reduced mass), at a distance $r$ from the center.

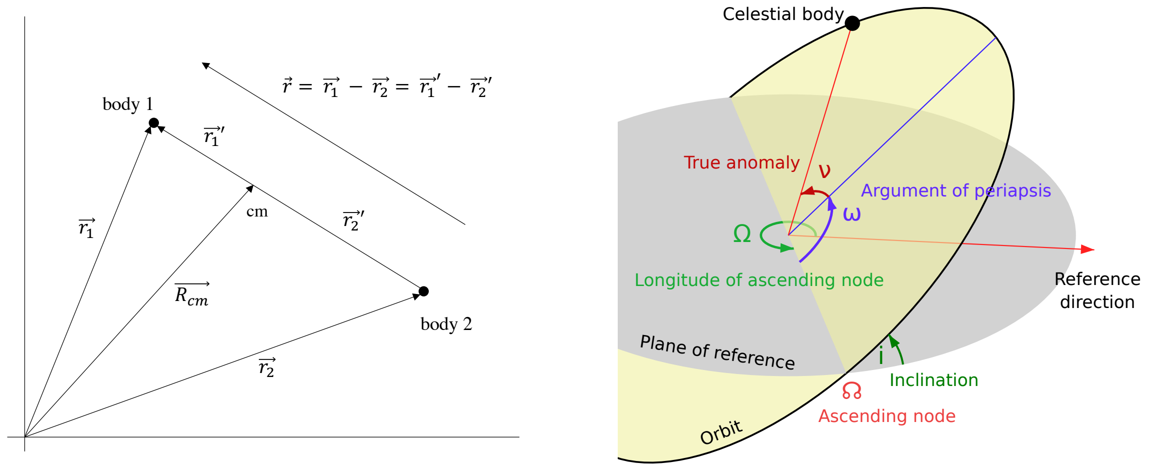

Figure 3: Left panel: Diagram of two bodies interacting via their gravitational force, in an arbitrary coordinates system. Right panel: Orbital elements of a body moving in an elliptical orbit. Image by Lasunncty at the English language Wikipedia, CC BY-SA 3.0, `http://www.gnu.org/copyleft/fdl.html`.

We define now the center of mass of the two bodies system, $\vec{R_{cm}}$, as $\vec{R_{cm}} = (m_1\vec{r_1} + m_2\vec{r_2})/(m_1 + m_2)$. Then, following Figure 3, $\vec{r} = \vec{r_1} - \vec{r_2} = \vec{r_1}' - \vec{r_2}'$, and

$$\vec{r_1}' = \vec{r_1} - \vec{R_{cm}} = \frac{\mu}{m_1}\vec{r} \tag{1}$$

The orbit of the object with mass $m = \mu$, the reduced mass, moving only by the force of gravity, will describe an elliptical orbit, given by

$$r = \frac{a(1 - \mathrm{e}^2)}{1 + \mathrm{e}\cos\nu} \tag{2}$$

where $a$ is the semi-major axis, e is the eccentricity, and $\nu$ is called the true anomaly of an ellipse, defined as the angle between the argument of periapsis and the body (see Figure 3, right panel). The true anomaly as a function of time can be computed using Kepler's equation. Then, using equation 1, we see that

$$r_1' = \frac{m_2}{m_1 + m_2} \cdot \frac{a(1 - \mathrm{e}^2)}{1 + \mathrm{e}\cos\nu}, \tag{3}$$

and a similar relation can be found for $r_2'$. Equation 3 describes the position of body 1 with respect to the center of mass of the system. We now need an expression for the velocity of body 1 (which we will consider as the star) with respect to an arbitrary reference direction. If we consider the right panel of Figure 3, we see that the projection of $r$, in the reference direction, is $r_{1,z}' = r_1' \sin(\nu + \omega) \sin \mathrm{i}$, where $\omega$ is the angle between the ascending node and the argument of periapsis, and i is the inclination of the system with respect to the reference direction. If we derive the above expression, we obtain that the radial velocity of body 1, with respect to the center of mass, is

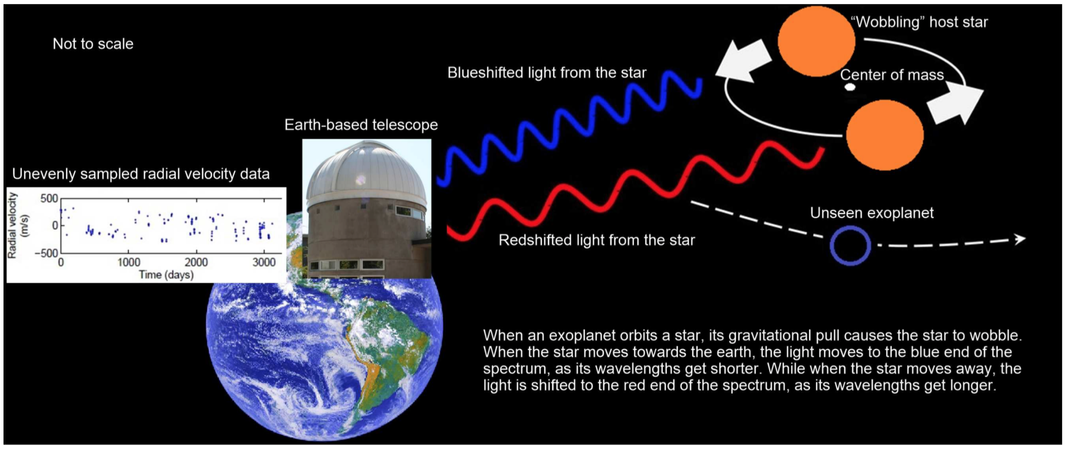

When an exoplanet orbits a star, its gravitational pull causes the star to wobble. When the star moves towards the earth, the light moves to the blue end of the spectrum, as its wavelengths get shorter. While when the star moves away, the light is shifted to the red end of the spectrum, as its wavelengths get longer.

Figure 4: Diagram showing how we can relate the movement of a star to an unseen exoplanet, and how we can measure it from Earth. Figure taken from Salman Khan et al. (2016).

$$v_{1,r} = \sqrt{\frac{G}{(m_1 + m_2)a(1-\mathrm{e}^2)}}m_2 \sin \mathrm{i} \cdot (\cos(\omega + \nu) + \mathrm{e}\cos\omega) \tag{4}$$

The radial velocity semi-amplitude is the term inside the square root, and can be expressed in more practical terms as

$$K_1 = \frac{28.4329 \mathrm{m\,s^{-1}}}{\sqrt{1-\mathrm{e}^2}} \frac{m_2 \sin \mathrm{i}}{M_{\mathrm{Jup}}} \left(\frac{m_1 + m_2}{M_\odot}\right)^{-1/2} \left(\frac{a}{1\mathrm{AU}}\right)^{-1/2} \tag{5}$$

$$K_1 = \frac{28.4329 \mathrm{m\,s^{-1}}}{\sqrt{1-\mathrm{e}^2}} \frac{m_2 \sin \mathrm{i}}{M_{\mathrm{Jup}}} \left(\frac{m_1 + m_2}{M_\odot}\right)^{-2/3} \left(\frac{P}{1\mathrm{yr}}\right)^{-1/3} \tag{6}$$

The semi-amplitude of the radial velocity measured then depends strongly on the mass of the planet (called minimum mass due to the sin i term, which can not be derived only with radial velocity data). It will also depend on the orbital period of the planet, or its semi-major axis. A Jupiter-mass planet, in a one year orbit, will produce a velocity in the host star of $\sim 28$ m $\mathrm{s}^{-1}$. Hot Jupiters, with orbits of less than 10 days and masses comparable to those of Jupiter, will translate into large RV amplitudes ($\sim 60$ m $\mathrm{s}^{-1}$), explaining why the first planets detected (for example, 51 Pegasi b) were of this kind.

### Measuring radial velocities

The measurement of stellar RVs is possible thanks to the Doppler effect. Under the assumption of a flat spacetime, a photon of wavelength $\lambda_0$ emitted by a source moving at velocity $v$ with respect to the observer, will be detected at wavelength $\lambda$, shifted by an amount given by:

$$z \equiv \frac{\lambda - \lambda_0}{\lambda_0} = \frac{1}{\gamma(1 + v/c)} - 1. \tag{7}$$

$z$ is known as the redshift, and $\gamma$ is the relativistic factor $1/(1-(v/c)^2)$, where $c$ is the speed of light. If we know $\lambda_0$ (also called restframe wavelength), and measure $\lambda$ (observed wavelength), then we can derive the speed $v$ at which the emitting object is moving, with respect to a reference frame. Higher order terms have been neglected due to $v \ll c$ in exoplanet studies, but their effect have been reviewed in Lindegren and Dravins (2003).

For a star, we can measure its spectrum, which will be filled with absorption lines produced by elements, ions and molecules (in very cool stars) in its photosphere. If there is no contamination from other sources, then all these lines should be produced by the same source (the star in this case), and the Doppler shift will be measured for all the lines present in the spectra. Figure 4 shows a schematic representation of the RV measurement method.

One important aspect to consider when measuring radial velocities is that the Earth is also a moving system, it rotates and orbits around the Sun. The velocities measured from Earth then have to be corrected for this movement. For that, the International Astronomical Union (IAU) has set the Solar System barycenter as the International Celestial Reference System (ICRS). The correction for the Earth's movement is then called the barycentric correction, and corresponds to the values we would have measured if we were situated at the center of the ICRS. A more detailed description of the barycentric correction, including all the factors considered for its correct measurement, and its application in exoplanet studies, can be found in Wright and Eastman (2014).

### Requirements for high precision measurements

Many aspects come in play when obtaining precise radial velocities from a stellar object, both instrumental and physical sources. First, we need a source capable of providing a high number of isolated absorption lines. Hot stars (with $T_{\text{eff}} > 10000$ K) will have all chemical elements partly ionized, and the transitions observable in the optical and near-IR will be mostly depopulated. These stars usually have high rotation velocities, resulting in broader lines for which it is harder to precisely measure its center. On the other hand, very cool stars ($T_{\text{eff}} \leq 3500$) will have an overpopulation of absorption, resulting in blended lines, in times also overlapping with molecular bands. These stars also emit most of their flux in the IR, where most of the absorption bands produced by water and other molecules found within our atmosphere are located. This interference makes it harder to measure these stars's spectra from Earth with current instrumentation. FGK stars correspond then to the classical targets observed in radial velocity studies. In recent years, M-dwarfs have also been considered as good candidates for RV monitoring. They are less massive than FGK stars, meaning that it is possible to detect less massive planets orbiting them, and the noise of the signals is often not limited by brightness but activity. A new generation of spectrographs in the IR has been developed to target these stars for RV studies (e.g. CARMENES, Quirrenbach et al. 2014).

On the instrumental side, the resolving power, $R = \lambda/\Delta\lambda$, needed to measure velocities to a precision of $\sim 1-7$ m s$^{-1}$ is $R = 50000-100000$. High resolution spectrographs, called echelle spectrographs, reach this level of resolution by having high blaze angles and working at high spectral orders. They also use a cross dispersing element that disperses the light in the perpenticular direction, separating the spectrum into different orders that are placed one over the other in a 2-dimensional CCD. The most precises spectrographs are currently HARPS (Mayor et al. 2003), located in the 3.6m telescope at the La Silla Observatory; and ESPRESSO (Pepe et al. 2010), at the ESO Paranal Observatory.

As was hinted before, the shape of the lines also have an effect on the RV precision. For narrow lines it is easier to correctly measure its central wavelength than broad or blended lines. If we assume the lines have approximately a Gaussian shape, then the RV precision will be

$$\sigma_{\mathrm{RV}} \sim \frac{\sqrt{\mathrm{FWHM}}}{C \cdot \mathrm{SNR}}, \tag{8}$$

where FWHM is the full width at half maximum of the line, $C$ is the depth divided by the continuum (also called contrast), and SNR is the signal-to-noise ratio in the continuum. This translates into lower precision for stars with high rotational velocity, or observed with low resolution spectrographs, or very faint stars (low SNR). In practise, radial velocities are measured by cross-correlating (Tonry and Davis 1979) the spectrum with a binary mask, usually with a set of lines representative of different spectral types. The result, called cross-correlation function (CCF), will then serve as a representation of the average profile of the absorption lines in the spectrum. More details about this method, as well as formulas to estimate $\sigma_{\mathrm{RV}}$ from the CCF, are mentioned in Baranne et al. (1996); Bouchy et al. (2001); Pepe et al. (2002).

Another method used to measure the RVs consists of placing a gas cell in the incoming light beam of the star before it reaches the spectrograph, allowing one to forward model the spectrum point spread function and doppler velocity (Butler et al. 1996a). I refer the reader to Marcy and Butler (1992), Valenti et al. (1995), and Butler et al. (1996a) for more details about this method.

## Detection of periodic radial velocity signals

One of the most classical methods to detect periodic signals in RV data is to use the Lomb-Scargle (LS) periodogram (Lomb 1976; Scargle 1982). This consists of fitting sine curves with a certain test period to the data. In this case, the dataset at time $t_j$ will be given by $X(t_j) = A\cos(\omega t_j) + B\sin(\omega t_j) + C$, then the highest probability period (at frequency $\omega$) of the dataset $X_j$ is the one that returns the strongest power $P$, defined as (Scargle 1982, Equation 10):

$$P(\omega) = \frac{1}{2}\left\{\frac{\left[\sum_j X_j \cos\omega(t_j - \tau)\right]^2}{\sum_j \cos^2\omega(t_j - \tau)} + \frac{\left[\sum_j X_j \sin\omega(t_j - \tau)\right]^2}{\sum_j \sin^2\omega(t_j - \tau)}\right\}, \tag{9}$$

where $\tau$ is defined as:

$$\tan(2\omega\tau) = \left(\sum_j \sin 2\omega t_j\right) \Big/ \left(\sum_j \cos 2\omega t_j\right). \tag{10}$$

An alternative version of the LS periodogram is the Generalized Lomb-Scargle periodogram (Zechmeister and Kürster 2009), which includes offsets to the data as well as different weights for the data points. It has been proven that it is more suitable to use in the cases of eccentric orbits in particular.

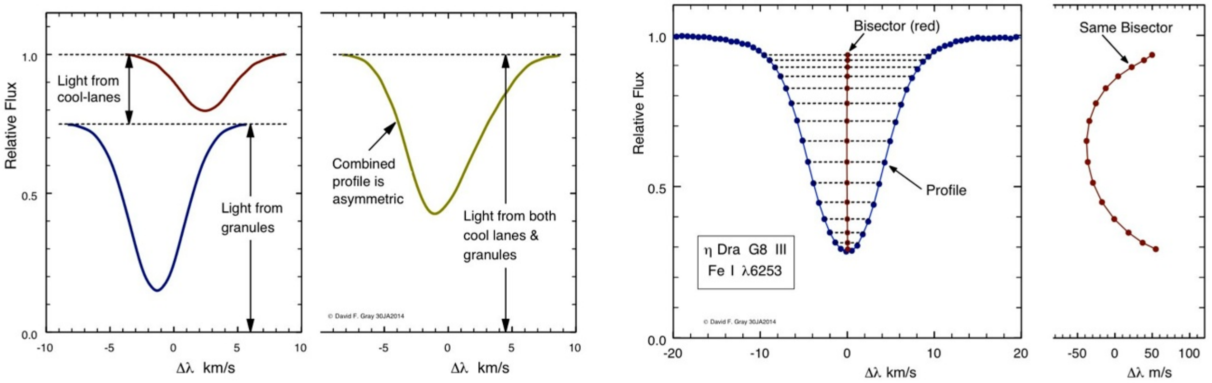

Figure 5: Left panel: Phenomena in the stellar photosphere producing line asymmetries. Right panel: Bisector measurement in a line profile. Both figures were taken from Gray (2005).

In order to assess the significance of the highest probability period from the periodogram, we need to measure what would be the probability of obtaining the desired signal period from noise. In this work, this is done by performing a bootstrap analysis, which consists of randomly interchanging the datapoints in time, maintaining the data set's time structure, and computing the periodogram $P$ each simulated data set. The probability of obtaining a certain period $p$, called the False Alarm Probability (FAP), is then obtained. A certain period $p_0$ is then only to be considered significant if $P(\omega_0)$ is higher than the 1% or 0.1% FAP level.

## Sources of jitter

Changes in the position of the absorption line centers in a stellar photosphere are not caused only by the radial motion of the star. The surface of the stars are not static, but they change over time, mostly due to the magnetic activity of the star, or the large-scale motions produced by convection. This will produce what is termed 'jitter', and it is an added source of noise to the measured radial velocities.

The magnetic activity on a star is produced by dynamos that generate magnetic fields, powered by the rotational velocity. These magnetic fields will interact with the stellar atmosphere and winds, and will cause surface brightness inhomogeneities, like bright and dark spots, which may cover a significant fraction of the stellar disk, and can be carried across it by the stellar rotation. As the star rotates, these spots (or plagues) will block (or enhance) part of the light approaching to us. This will result in an imbalance between the approaching (blueshifted) and the receding (redshifted) contributions to the absorption lines, creating asymmetries in the spectral lines (Vogt et al. 1987; Saar and Donahue 1997; Desort et al. 2007; Meunier et al. 2010; Dumusque et al. 2014), with periods similar to the rotational period of the star (Vanderburg et al. 2016). The mean activity level will depend on the stellar age, with young stars showing a larger level of magnetic activity compared to older stars (Baliunas et al. 1995; Mamajek and Hillenbrand 2008). Activity cycles have also been seen in several stars, like the Sun's 11-year cycle (Livingston et al. 2007), and have time-scales on the order of 2-10 years (Lovis et al. 2011; Gomes da Silva et al. 2011; Moutou et al. 2011; Ségransan et al. 2011). These cycles can also influence the radial velocities (Saar and Fischer 2000; Dumusque et al. 2011a). This is thought to happen because, during magnetic cycles, the fraction of the stellar envelop covered by spots increases, inhibiting convection inside these regions due to coupling of the gas plasma to the magnetic field (Cavallini et al. 1985; Brandt and Solanki 1990). The result of this magnetic coupling is to suppress the convective blueshift, making the spectral lines appear redder during active phases (Lovis et al. 2011).

Cool stars also have convective zones in their atmosphere, which will produce large-scale motions of material through the atmosphere. This effect is called granulation, and produces velocity fields in the photosphere which affects the material locally, producing spectral line asymmetries (left panel, Figure 5, see also Livingston 1982; Toner and Labonte 1990). Granulation is a stochastic process, and changes over time in a star, with time scales of $\sim$ 10 minutes for the Sun (Dravins 1990; Palle et al. 1995), and has been shown to produce radial velocity variations of the order of meters per second (Dumusque et al. 2011b). Granulation has also been shown to change with stellar evolution, increasing as the star evolves (Bastien et al. 2013, 2014). On top of granulation, stars have global oscillations, called p-mode oscillations, produced by turbulent convection. They have timescales of the order of a few minutes, and have amplitudes of a few m/s for F and G stars (Brown et al. 1998; Kjeldsen et al. 2005), to sub-m/s for K and M dwarfs (Berdiñas et al. 2017). They are usually averaged out of the data by taking long exposures, of over 15 minutes, or by binning the data (Dumusque et al. 2017, 2011b).

In order to identify magnetic activity or granulation in the stars, astronomers usually measure some indicators alongside the RV data. The most commonly used ones are:

- **Bisector analysis**. Line asymmetry, when not considered, can mimic RV shifts by moving the center of the spectral line. Line asymmetry is usually detected by measuring the line center position as a function of line depth (right panel, Figure 5), known as the line bisector. One of the most used diagnostics to measure the change of the bisector over time is the Bisector Inverse Slope (BIS, Queloz et al. 2001). It is defined as the difference between the bisector at the top and at the bottom of the line, and is usually measured in the star's CCF with a binary mask. It has been shown that, in active stars, the BIS is anti-correlated with the measured radial velocities (Queloz et al. 2001; Boisse et al. 2012). Other methods to measure line asymmetry have also been proposed (see Figueira et al. 2013).
- **FWHM**. The width of the lines, measured by their FWHM, can also be indicative of line shape differences over time. This is produced because the presence of spots will change the shape of the CCF (as mentioned previously), therefore the fit performed will change, either broadening or narrowing, which will change the FWHM of the line for different observations. The change in FWHM can also be produced by other sources like blended light from other stars (Santos et al. 2014), which would produce a broadening of the CCF with a period being given by the orbital period of the two unresolved sources.
- **Ca II H & K emission**. Magnetic fields heat the gas in the stellar photospheres, resulting in temperature inversion in the stellar chromospheres. This cools down by line emission, and is usually seen in spectra in the cores of the Ca II H& K lines (centered on 3968.47 Å and 3933.66 Å). The cores of these lines are so opaque that we cannot observed photons emitted deeper than the chromosphere ($\tau$ = 1, see equation 23), therefore all the flux we receive from them will come from the chromosphere rather than the photosphere. The amount of emission in these lines is then indicative of the stellar magnetic activity (Schrijver et al. 1989). The Mount Wilson $S_{\text{index}}$ (Wilson 1968) has been historically used to measure the amount of flux emitted in these lines, but it will depend on both the effective temperature and activity

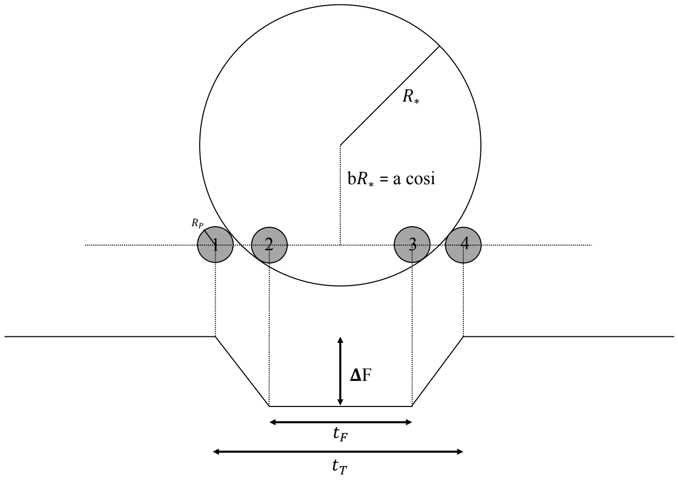

Figure 6: Diagram of a transit event. $t_T$, $t_F$, and $\Delta F$ are the transit total duration, transit duration between ingress and egress, and transit depth, respectively. The circles labelled 2 and 3 represent when the planet is in transit, and 1 and 4 when it is not in transit. This figure corresponds to a modified version of Figure 1 from Seager and Mallén-Ornelas (2003).

level of the star. In order to compare the activity of different types of stars, Noyes et al. (1984) introduced the $\log R'_{HK}$ index, which only measures the chromospheric component of the flux. These indices have been widely used to measure correlations of magnetic activity with radial velocities (e.g. Santos et al. 2014; Kane et al. 2016; Díaz et al. 2018), to detect long term activity cycles (Baliunas et al. 1995; Lovis et al. 2011), and to select quiet stars for exoplanetary detection samples[2] (e.g. Wright 2006; Jenkins et al. 2006, 2008, 2011b; Arriagada 2011). The Ca index has also been shown to be correlated with spots and plagues in the stellar photosphere (Meunier et al. 2010). Other indices have been used to measure chromospheric activity, such as the $H_\alpha$ line (Bonfils et al. 2007; Boisse et al. 2009), which shows emission in its core from the chromosphere for active M-dwarf stars (Walkowicz and Hawley 2009), and the He I line (Boisse et al. 2009), which is a tracer of solar plages and forms in the upper chromosphere (Saar et al. 1997). In this work, we choose to use only the Ca II H & K emission as the tracers for chromospheric activity, due to their historical relevance, which means their behaviours are generally well understood and characterisable.

### 0.1.4 Transit photometry

This method consists of measuring the dips in a star's light curve (flux versus time curve), produced by a planet crossing the stellar disk with an inclination that makes it favourable to block the star's light given our line of sight. This decrease in the flux is produced by the planet blocking part of the surface of the star for a short amount of time, and it will repeat with a period equal to the orbital period of the system. A schematic representation of a transit event in shown in Figure 6.

---

[2] As a reference, the Sun, during its quiet phase, has $\log R'_{HK} = -5.0$

One of the big advantages of this method is the amount of information we can retrieve from the system. The decrease in the flux when the planet is transiting the star, $\Delta F$, will be related to the ratio of sizes between the star and the planet:

$$\Delta F = \frac{F_{no\,transit} - F_{transit}}{F_{no\,transit}} = \left(\frac{R_p}{R_\star}\right)^2 , \tag{11}$$

where $F_{transit}$ and $F_{no\,transit}$ are the flux received from the star when the planet is in and out of transit, respectively (see Figure 1), and $R_p$ and $R_\star$ are the radius of the planet and the star, respectively. Equation 11 shows that larger planets will produced deeper transits, and will be easier to detect than small planets. The length of the transit is related to the separation between the star and the planet, and the inclination of the system, as was derived in Seager and Mallén-Ornelas (2003)

$$b \equiv \frac{a}{R_\star}\cos \mathrm{i} = \left[\frac{(1-\sqrt{\Delta F})^2 - [\sin^2(t_F\pi/P)/\sin^2(t_T\pi/P)](1+\sqrt{\Delta F})^2}{1-[\sin^2(t_F\pi/P)/\sin^2(t_T\pi/P)]}\right]^{1/2} , \tag{12}$$

$$\frac{a}{R_\star} = \left[\frac{(1+\sqrt{\Delta F})^2 - b^2(1-\sin^2(t_T\pi/P))}{\sin^2(t_T\pi/P)}\right]^{1/2} , \tag{13}$$

where $t_T$ and $t_F$ are total transit duration and the duration of the flat part of the light curve, $a/R_\star$ is the ratio between the semi-major axis and the radius of the star (also know as the scale of the system), i is the inclination of the system, and $b$ is known as the impact parameter, and its defined as the minimum projected distance between the planet and the center of the star, during the time of mid-transit.

By combining the geometric information from the previous equations, Seager and Mallén-Ornelas (2003) also shown that it was possible to obtain an estimate of the host star's density:

$$\frac{\rho_\star}{\rho_\odot} \equiv \frac{M_\star/M_\odot}{(R_\star/R_\odot)^3} = \left[\frac{4\pi^2}{P^2G}\right]\left[\frac{(1+\sqrt{\Delta F})^2 - b^2(1-\sin^2(t_T\pi/P))}{\sin^2(t_T\pi/P)}\right]^{3/2} . \tag{14}$$

These equations are valid to characterize systems with only one transiting object, and with no contamination from close-by stars. In the case where the later is happening, then the derived radius for the planet will be said to be diluted, and it will have to be corrected. When the contaminant flux comes from just one source ($F_{\mathrm{sec}}$), and the planet is orbiting the primary star (with flux $F_{\mathrm{prim}}$), then $\Delta m = m_{\mathrm{sec}} - m_{\mathrm{prim}} = -2.5\log(F_{\mathrm{sec}}/F_{\mathrm{prim}})$, and the corrected radius for the planet becomes:

$$R_{p,\mathrm{corr}} = R_p\sqrt{1+10^{-0.4\Delta m}}. \tag{15}$$

For the cases when there are more than one contaminant star, and/or the planet is not orbiting the primary star, we would have that the corrected planetary radius is:

$$R_{p,\mathrm{corr}} = R_p \frac{R_{\mathrm{sec}}}{R_*} \sqrt{10^{0.4\Delta m_c}\left(1 + \sum_{\mathrm{i}=1}^{N} 10^{-0.4\Delta m_{\mathrm{i}}}\right)}, \tag{16}$$

where $R_{\mathrm{sec}}$ is the radius of the secondary star around which the planet orbits, $R_*$ is the radius of the star when assumed to be a single star, $\Delta m_c$ is the magnitude difference between the secondary and primary magnitudes, and $m_{\mathrm{i}}$ is the magnitude difference of the $N$ companion stars with the primary. If there is only one contaminant star, and the planet is orbiting the primary source, then we recover equation 15. A full description of these two cases is found in Ciardi et al. (2015) and Furlan et al. (2017).

The previous equations represent systems with circular orbits (for eccentric orbits, please see Tingley et al. 2011), and neglect the limb darkening. Limb-darkening is produced by the non-uniform brightness of the stellar disk, and is seen during ingress and egress of the planet passing in front of the star (Figure 6). The limb-darkening can usually be parametrized following the relations:

$$I(\mu)/I(1) = 1 - u_1(1-\mu) \qquad \text{linear law} \tag{17}$$

$$I(\mu)/I(1) = 1 - u_1(1-\mu) - u_2(1-\mu)^2 \qquad \text{quadratic law} \tag{18}$$

$$I(\mu)/I(1) = 1 - u_1(1-\mu) - u_2(1-\sqrt{\mu}) \qquad \text{square-root law} \tag{19}$$

where $I(\mu)$ is the specific intensity of a star at $\mu = \cos\theta$, the cosine of the angle between the line of sight and the normal of the emerging intensity; $I(1)$ is the intensity at the centre of the star, and $u_{\mathrm{i}}$ are the limb-darkening coefficients, which change depending on the law used. Other parametrizations used are the logarithmic (Klinglesmith and Sobieski 1970) and exponential laws (Claret and Hauschildt 2003). Methods to chose the best law and fit for the coefficients for a transit have been proposed in the literature: Kipping (2013); Parviainen and Aigrain (2015); Espinoza and Jordán (2016). Usually, when modelling a real transit event, the methods derived by Mandel and Agol (2002) and Giménez (2006) are used.

### Detection of the transit signals

Usually, detection of planets using this method requires the monitoring of thousand of stars at the same time. It is not efficient to look at all the light curves produced by eye, and algorithms looking for periodic dips in the flux have been produced. One of the most used is the Box-fitting Least Squares (BLS, Kovács et al. 2002) periodogram. This method consists of setting two possible discrete values for the light curve, $H$ and $L$, where $L$ corresponds to the level of the transit. The time spent in the transit phase, $L$, is $qP_0$, where $P_0$ is the test period. For each test period, $P_0$, the light curve is phase folded and a box of length $q$ and depth $\delta = H - L$ is fitted to the data. The aim is then to find the model (with parameters $P_0$, $q$, $\delta$, and $t_0$, the epoch of the transit), that best fits the data.

The points in the dataset will be $\{x_{\mathrm{i}}\}$, each with an uncertainty given by $\sigma_{\mathrm{i}}$. We will define for each point a weight $w_{\mathrm{i}}$, with $w_{\mathrm{i}} = \sigma_{\mathrm{i}}^2[\sum_{j=1}^{n} \sigma_j^{-2}]^{-1}$. The phase-folded light curve, to a certain period,

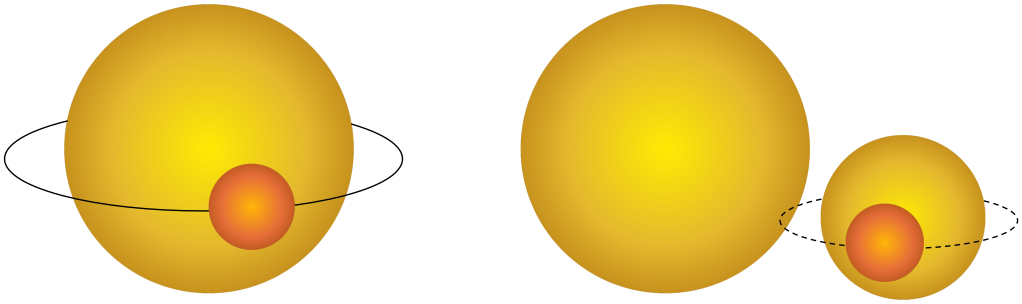

Figure 7: Different types of false positives.

will be denoted as $\{\tilde{x}_\mathrm{i}\}$. If we set the transit to occur between points $\mathrm{i}_1$ and $\mathrm{i}_2$, then $\hat{L}$ will be the level in $[\mathrm{i}_1, \mathrm{i}_2]$, and $\hat{H}$ will be the level in $[1, \mathrm{i}_1)$ and $(\mathrm{i}_2, n)$.

For any given $(\mathrm{i}_1, \mathrm{i}_2)$, the following expression is minimized:

$$\mathcal{D} = \sum_{\mathrm{i}=1}^{\mathrm{i}_1-1} \tilde{w}_\mathrm{i}(\tilde{x}_\mathrm{i} - \hat{H})^2 + \sum_{\mathrm{i}=\mathrm{i}_1}^{\mathrm{i}_2} \tilde{w}_\mathrm{i}(\tilde{x}_\mathrm{i} - \hat{L})^2 + \sum_{\mathrm{i}=\mathrm{i}_2+1}^{n} \tilde{w}_\mathrm{i}(\tilde{x}_\mathrm{i} - \hat{H})^2. \tag{20}$$

If we define $s = \sum_{\mathrm{i}=\mathrm{i}_1}^{\mathrm{i}_2} \tilde{w}_\mathrm{i}\tilde{x}_\mathrm{i}$ and $r = \sum_{\mathrm{i}=\mathrm{i}_1}^{\mathrm{i}_2} \tilde{w}_\mathrm{i}$, then the Box-fitting Least Squares frequency spectrum, for each trial period, will be:

$$SR = \max\left\{\left[\frac{s^2(\mathrm{i}_1, \mathrm{i}_2)}{r(\mathrm{i}_1, \mathrm{i}_2)[1 - r(\mathrm{i}_1, \mathrm{i}_2)]}\right]^{\frac{1}{2}}\right\}. \tag{21}$$

More details about this method, including its efficiency compared to other periodograms, are included in Kovács et al. (2002). Other detection methods have been proposed in Collier Cameron et al. (2006) and Régulo et al. (2007), and are not used in this work.

### False Positives

Transit-like shapes in light curves can be produced not only by a transiting planet, but also by other phenomena. When this happens, it is said to be a false positive. Two of the most common cases of false positives involve brown dwarfs. The first case consist of an eclipsing binary system, where one of the stars is a low-mass star or a brown dwarf (left panel, Figure 7). Because the sizes of brown dwarfs and planets are relatively similar, they would produce the same transit depth than if it were a planet. The second case consist of an unresolved triple-star system (or a fainter background star that is located angularly close to a foreground binary system on the sky), where a bright star has a dimmer nearby eclipsing binary system (right panel, Figure 7). The flux from the brightest star will dilute the transit produced by the eclipsing binary system, to the point where it will be as shallow as the one produced by a planet orbiting the brightest star. More examples of different types of false positives can been found in Brown (2003); Cameron (2012); Fressin et al. (2013).

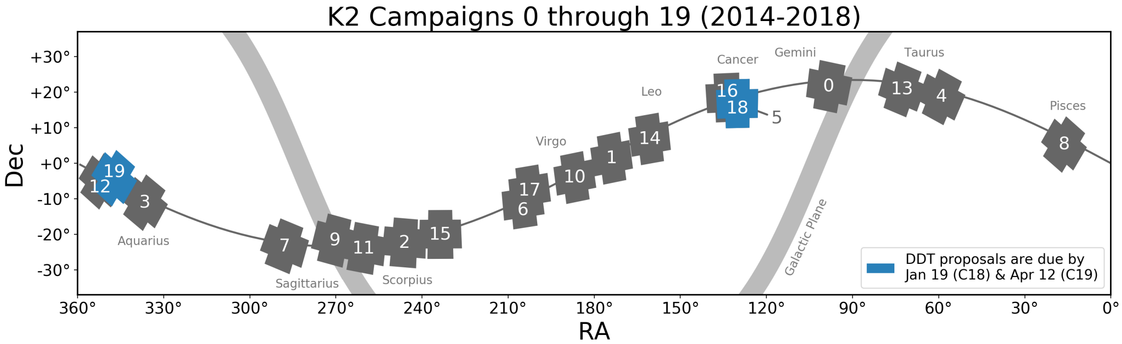

Figure 8: K2 campaigns, from 1 to 19.

One way to confirm the planetary nature of the transiting signal is to perform follow-up observations, consisting of follow-up photometry, different waveband photometry, spectroscopy to search for spectroscopic binaries, derivation of activity indicators (section 0.1.3), or high precision RV measurements to obtain the mass of the object, among others. The problem with this last approach is how expensive it is to obtain RV data for most targets from transit surveys, due to them being relatively faint in most of the cases. This has led people to come up with other methods to validate such systems, for example the centroid shifting method (Bryson et al. 2013; Günther et al. 2017), odd-versus-even numbered transit differences (Batalha et al. 2010), or machine-learning techniques (McCauliff et al. 2015). Another method is to estimate the probability that the observed signal is produced by a non-planetary phenomena. These methods take into account the number of transits measured and the galactic population surrounding the targets, among other factors. Some of them are described in Hartman et al. (2011a); Díaz et al. (2014); Torres et al. (2015); Morton et al. (2016).

### Photometric Surveys

The most efficient way of detecting planets using the transit method is to monitor thousands of stars at the same time. The most successful transit survey to-date is *Kepler* (Borucki et al. 2010). This space telescope was launched in 2011, and throughout its four year-long operation it detected over 1000 systems. The field of view of this mission, of 105 deg$^2$ centered on the Cygnus-Lyra region of the sky, allowed it to detect planets orbiting stars with a magnitude-limit of 17, with year-long orbital periods. After four years of operation, *Kepler* suffered the failure of one of its reaction wheels, which led to a change of the mission's observing strategy. *Kepler*, renamed K2 (Howell et al. 2014), would now focus on fields on the ecliptic for 80-day long campaigns (Figure 8). In chapter 2 I will show how we used data from K2 to detect two hot Jupiter planets.

Many other transit surveys have been carried out, or are in operation. Some of the most successful surveys are WASP (Pollacco et al. 2006), HATSouth (Bakos et al. 2013), and NGTS (Wheatley et al. 2018). Most recently the TESS (Ricker et al. 2015) mission was launched. After its six months commissioning phase, it will monitor some of the brightest stars in the sky, allowing for the detection of closer planetary systems than Kepler, meaning that follow-up efforts from Earth will be possible (like radial velocity follow-up, see next section).

## 0.2 Stellar characterization

As it was shown previously, we cannot (or at least not in most planet detections) directly observe a planet, but all our knowledge comes from observing the star. The mass and radius of the planet are derived from its comparison to the mass and radius of the host star, as well as the planet equilibrium temperature and semi-major axis. The activity level of the star will also depend on its spectral type and age, which is important to characterize in order to remove that signal from our data and correctly derive the planet parameters. Characterization of the host star is also useful to link formation theories with observations. One example of this is the correlation between planet occurrence and stellar metallicity (Gonzalez 1997; Fischer and Valenti 2005; Sousa et al. 2011a; Jenkins et al. 2017), which points at the core accretion model of planet formation (Lin et al. 1996). All of these points just show how important it is to first characterize the host star, before trying to focus on the planet characteristics.

Before beginning with the stellar characterization, an overview of stellar interiors and photospheres is necessary. This is intended just as a brief description of this subject. A more exhaustive description of the processes of stellar photospheres can be found in Gray (2005) and Niemczura et al. (2014).

### 0.2.1 Stellar photospheres

In order to understand the physics of stellar photospheres, it is necessary to understand how the radiation, produced in the center of the star, interacts with the stellar interior up to the atmosphere, from where it is emitted towards us.

#### Intensity and the line transfer equation

First, we will define the radiation intensity, which is the energy passing $\Delta E$, crossing an area $\Delta A$, oriented by the direction $\theta$, in the solid angle $\Delta\omega$, during a time $\Delta t$, in the wavelength interval $\Delta\nu$,

$$I_\nu = \lim_{\Delta\to 0} \frac{\Delta E}{\cos\theta\,\Delta A\,\Delta\omega\,\Delta t\,\Delta\nu} = \frac{\mathrm{d}E_\nu}{\cos\theta\,\mathrm{d}A\,\mathrm{d}\omega\,\mathrm{d}t\,\mathrm{d}\nu}. \tag{22}$$

Now, if this intensity passes through material where light only gets absorbed (by true absorption and/or scattering), and no radiation is emitted, then the change in intensity will be given by

$$\mathrm{d}I_\nu = -\kappa_\nu\,\rho\,I_\nu\,\mathrm{d}x = -I_\nu\,\mathrm{d}\tau_\nu, \quad \text{with} \quad \tau_\nu = \int_0^L \kappa_\nu\,\rho\,\mathrm{d}x, \tag{23}$$

where $\kappa_\nu$ is the absorption coefficient, $\rho$ is the density of the material, and $\tau_\nu$ is known as the optical depth of the material. From the above expression, the optical depth can be defined as the distance at which the intensity is reduced by a factor 1/e.

If we now consider the case where there is only emission of radiation and no absorption, then if $j_\nu$ is the emission coefficient of the material, then the change in intensity will be

$$\mathrm{d}I_\nu = j_\nu \rho \,\mathrm{d}x. \tag{24}$$

Combining both equations 23 and 24, we find that the change of radiation intensity when passing through a material which contributes to absorption and emission of radiation is $\mathrm{d}I_\nu = -\kappa_\nu \rho \, I_\nu \,\mathrm{d}x + j_\nu \rho \,\mathrm{d}x$. We can rewrite this equation as

$$\frac{\mathrm{d}I_\nu}{\mathrm{d}\tau_\nu} = -I_\nu + S_\nu, \tag{25}$$

known as the line transfer equation. $S_\nu = j_\nu/\kappa_\nu$ is the source function, and can be interpreted as the radiation intensity emitted in some point in a hot gas, and is proportional to the number of emitted photons per unit of optical depth.

In stellar surfaces, where $\tau_\nu = 0$, we have that equation 25 can be solved as

$$I_\nu(0) = \int_0^\infty S_\nu \, \mathrm{e}^{t_\nu \sec\theta} \sec\theta \,\mathrm{d}t_\nu. \tag{26}$$

The flux we measure will be the intensity over the whole stellar disk, and it can be defined as

$$F_\nu = \oint I_\nu \,\cos\theta \,\mathrm{d}\omega \; = \; 2\pi \int_0^\pi I_\nu \,\cos\theta \,\sin\theta \,\mathrm{d}\theta. \tag{27}$$

If we assume that the source function has no dependence over the direction (isotropic) and using equation 26, then at the stellar surface ($\tau_\nu = 0$) we'll have

$$F_\nu(0) \; = \; 2\pi \int_0^\infty S_\nu(t_\nu)\, E_2(t_\nu) \,\mathrm{d}t_\nu, \tag{28}$$

where $E_2$ is the exponential integral of second order. Equation 28 is the theoretical spectrum emitted from the stellar photosphere.

### Model atmosphere

As it is shown in equation 28, we must know how the source function varies with optical depth to solve that integral, which translates into understanding how the absorption and emission coefficients change though the stellar interior. Both coefficients will depend on the physical conditions of the atmospheric layers, which are a function of the temperature, pressure, number of ionized species and electrons, among others. The knowledge of how these parameters change as a function of $\tau_\nu$ is known as a model atmosphere. To obtain these, we require some conditional equations of stellar interiors.

First, we have the equation of hydrostatic equilibrium, which maps the change in pressure inside a star. If we consider the pressure to arise from different sources, the two dominant ones being the gas pressure, $P_\mathrm{gas}$, and the radiation pressure, $P_\mathrm{rad}$, then the hydrostatic equilibrium equation can be written as

$$\frac{\mathrm{d}P_\mathrm{gas}}{\mathrm{d}\tau_\nu} = \frac{g}{\kappa_\nu} - \frac{\mathrm{d}P_\mathrm{rad}}{\mathrm{d}\tau_\nu}. \tag{29}$$

It can be interpreted as the change in gas pressure, affected by the true gravity of the material pointing to the interior, plus the pressure produced by the radiation pointing outwards[3].

The distribution of temperature along the atmosphere can be obtained by assuming that the total flux is conserved (radiative equilibrium), and that the absorption coefficient will be a function of temperature and electron pressure $P_\mathrm{e}$, which in turn will depend on the chemical composition of the material.

For the case of absorption lines, each part of the line will be characterize by its own $\kappa_\nu$, following

$$\kappa_\nu^l = n_\mathrm{i}\, f_{\mathrm{i}j}\, \frac{\pi \mathrm{e}^2}{m\, c}\, \phi_\nu, \tag{30}$$

where $n_\mathrm{i}$is the level population at the atomic state i for a certain species, $f_{\mathrm{i}j}$ is the oscillator strength, and $\phi_\nu$ is the absorption line profile normalized to unity.

In the case of local thermodynamic equilibrium (LTE) conditions, in which the ionization and excitation of atoms depend only on the collisions among them, governed by the temperature of the material, then the level population $n_\mathrm{i}$ will be given by the Boltzmann and Saha equations:

$$\frac{N_n}{N} = \frac{g_n}{u(T)} 10^{-\log \mathrm{e}\, \chi_n/kT} \qquad \text{Boltzmann equation} \tag{31}$$

$$\frac{N_1}{N_0} = \frac{1}{P_\mathrm{e}} \frac{(2\pi m_\mathrm{e})^{3/2}(kT)^{5/2}}{h^3} \frac{2u_1(T)}{u_0(T)} \mathrm{e}^{-I/kT} \qquad \text{Saha equation} \tag{32}$$

where $k$ is the Boltzmann constant, $P_\mathrm{e}$ is the pressure due to the free electrons, $m_\mathrm{e}$ is the electron mass, $h$ is Planck's constant, $N_n$ is the number of electrons in the $n$ state, $N_1$ the number of ionized electrons, $g_n$ is the statistical weight of the $n$ state, $\chi$ is the excitation potential, $I$ is the ionization potential, $u(T) = \sum g_\mathrm{i} \mathrm{e}^{-\chi_\mathrm{i}/kT}$ is called the partition function, and $u_1/u_0$ is the ratio of ionic to neutral partition functions. In stellar photospheres, the absorption line profile, with its center at $\nu_0$, for most species can be approximated as

$$\phi_\nu = \frac{H(\mu, a)}{\sqrt{\pi}\, \Delta\nu_D}, \tag{33}$$

where $H(\mu, a)$ is the Voigt-Hjerting function, $\mu = (\nu - \nu_0)/\Delta\nu_D$, and $a = \gamma/(4\pi\Delta\nu_D)$.

This function is the product of the convolution of a Doppler and Lorentz profile, both contributing to the broadening of the line. The Doppler part is characterized by $\Delta\nu_D = \nu_0\, \sqrt{2kT/m + \xi_t^2}/c$, where $\xi_t$ is the microturbulence present in the stellar photosphere. The damping parameter of the Lorentz contribution is $\gamma = \gamma_R + \gamma_4 + \gamma_6$, where $\gamma_R$ is the radiative (natural) damping constant, $\gamma_4$ is the Stark damping, and $\gamma_6$ is the van der Waals damping. The last two coefficients will depend both on the temperature and pressure profiles inside the atmosphere.

---

[3] For small stars, like the Sun, the gas pressure is dominant, and for more massive stars the radiation pressure becomes more dominant.

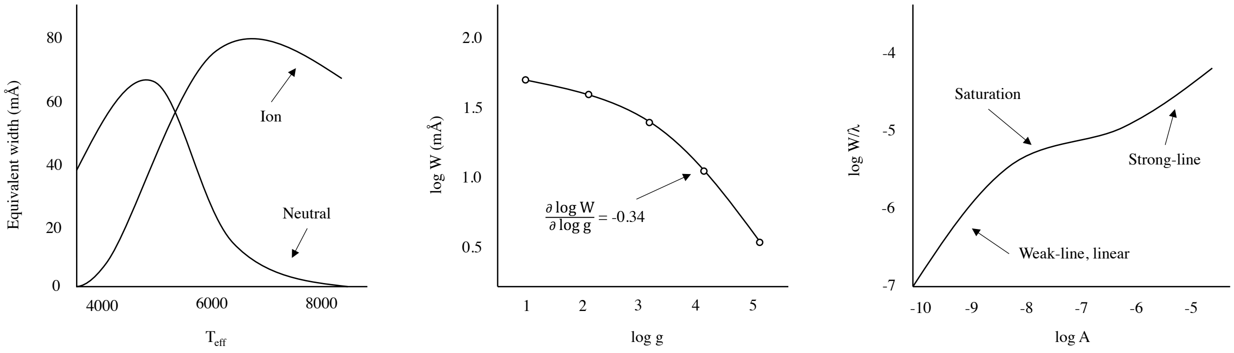

Figure 9: Equivalent width behaviour. From Gray (2005).

### 0.2.2 Derivation of stellar parameters with spectroscopy

The spectroscopic derivation of the stellar parameters is usually done following two methods: the spectral synthesis method, and the equivalent width method. The spectral synthesis method consists of computing a synthetic theoretical spectrum, with different atmospheric parameters, and then comparing it to the observed spectra, for a certain star. The best set of parameters will then be the ones used to synthesize the spectrum closest to the observation. This method is not the preferred one in this thesis work, so we point the reader to Valenti and Piskunov (1996); Gray (2005); Niemczura et al. (2014) for more information about it. The equivalent width method (used in this thesis work) consists of measuring the equivalent widths (EW) of a set of lines in a spectrum, and then, using model atmospheres and assuming several conditions for the stellar interiors, derive the individual abundances for each line.

The equivalent width of a line is defined as

$$W = \int_0^\infty \frac{F_\nu - F_c}{F_c}\,\mathrm{d}\nu, \tag{34}$$

where $F_\nu$ is the flux of the spectrum, $F_c$ is the flux of the continuum close to the line, and $\mathrm{d}\nu$ is the change in frequency. Theoretically, this can be computed using the approximation of the flux given by equation 28, without considering $k_\nu^l$ (the line absorption coefficient, defined in Equation 30) for the flux at the continuum.

Line strength (or EW) of an absorption will depend, as was seen in the previous section, on the temperature and pressure of the gas (left and middle panels of Figure 9, respectively), as well as the composition or abundance of the corresponding species producing the line. In the case of strong lines, the wings may also depend on the electron and gas pressure.

The abundance dependence of the equivalent widths is usually given by the curve of growth (right panel, Figure 9), and for weak lines its shape can be approximated as:

$$\log\left(\frac{W}{\lambda}\right) = \log C + \log A + \log\, g_n f \lambda - \theta_{\mathrm{ex}}\chi - \log \kappa_\lambda, \tag{35}$$

where $C$ is a constant for a certain ion and star, $A$ is the abundance, the same for all the lines of a certain species, $g_n$ is the statistical weight of the $n$ atomic level, $f$ is the oscillator strength, $\theta_{\mathrm{ex}} = 5040/T$, $\chi$ is the excitation potential, and $\kappa$ is the absorption coefficient.

The equivalent width method consists then of fitting previously observed equivalent widths to calculated ones from theory, with the use of model atmospheres with a certain set of atmospheric parameters, to derive the chemical abundance. This is an iterative process up until there is no correlation between the individual abundances computed for each line of the same species and the line's excitation potential and reduced equivalent width ($W/\lambda$), and there is no difference between the neutral and ionized abundances.

## 0.3 Thesis outline

This thesis work is separated into two independent, but related, themes. The first two chapters are focused on exoplanet detection, while the third chapter focuses on stellar characterization.

Chapter 1 describes the first work I did during the PhD on exoplanet detection. It involves the re-analysis of radial velocity data, in order to confirm or reject the existence of previously detected planets; a highly valuable endevour since the methodology used to detect a number of high impact planets was recently called into question. The work concluded with the confirmation of three planets, the rejection of three others, and the discovery of a new planetary candidate. This work was published in Soto et al. (2015).

The second chapter also deals with exoplanet discovery, but it was done during the last year of my PhD. It describes the work done to detect two hot Jupiter candidates, orbiting dwarf stars, detected using photometric data from the K2 survey (more details about this mission are given in chapter 2). RV data was used to confirm the planetary nature of the signals, and a full characterization of the systems was performed. One of these planets was also found to be inflated, meaning that its radius was larger than what is expected from theoretical models. This work has been accepted for publication in MNRAS, and is currently available at Soto et al. (2018).

The third chapter describes the code SPECIES, developed during the bulk of my PhD. This code characterizes stars by analyzing their spectra, and derives the main parameters that define them. It is mostly written in Python, and it is fully automated, requiring just minimum input from the user. This chapter was accepted for publication in A&A, and is currently available at Soto and Jenkins (2018). The code is also being integrated in the NGTS data flow, such that it will constitute the main stellar characterisation channel for this large international planet discovery project.

This thesis finishes with the final conclusions obtained from this work.

# Chapter 1

# RAFT: Reanalysis of archival FEROS spectra

During the last two decades, the quest of exoplanets has led to a huge improvement of instrumentation, calibration techniques, and signal detection methods, all which have made it possible to detect RV signals that confirm the existence of planets with masses approaching that of the Earth orbiting the nearest stars (Dumusque et al. 2012; Jenkins and Tuomi 2014; Anglada-Escudé et al. 2014, 2016). One of the instruments found to be useful in the exoplanet detection field is FEROS (section 1.1), which began its operations while mounted on the ESO 1.52m telescope, but was later moved to the 2.2m telescope, both located at the La Silla Observatory. From then on, FEROS has played a big role in the detection of new planetary candidates.

Due to the high precision required for radial velocities to detect planet-mass objects, it was later discovered that the reduction code was not operating optimally for such work. Müller et al. (2013) showed that the pipeline of the FEROS spectrograph used at that time performed an inaccurate barycentric velocity correction, since it does not include the Earth's precession, introducing a one-year period signal with an amplitude of $\sim$ 62 m s$^{-1}$ for $\tau$ Ceti (a known stable star at the few m s$^{-1}$ level, see Tuomi et al. 2013). In addition, the pipeline uses the initial time of the observation instead of the central time, which also introduces another uncertainty, especially for long exposure observations. This issue was also mentioned by Setiawan et al. (2000). This has led some groups to question the detections that were made using FEROS data before this problem was discovered, leading to the reanalysis of data taken with this instrument and the rejection of some systems (e.g. HIP 11952 in Desidera et al. 2013; Müller et al. 2013 and HIP 13044 in Jones and Jenkins 2014).

In this chapter I will present the reanalysis of archival FEROS data for the stars HD 11977, HD 47536, HD 70573, HD 110014 and HD 122430, all of which were observed with FEROS and are claimed to have at least one planet orbiting them. Four of these stars are G and K giants and one of them is a very young and nearby star, making them all interesting cases in the study of formation and evolution of planetary systems. This chapter was based on Soto et al. (2015), titled 'RAFT - I. Discovery of new planetary candidates and updated orbits from archival FEROS spectra', and published in MNRAS.

## 1.1 Observations and data reduction

The data were obtained using the Fiber-fed Extended Range Optical Spectrograph, FEROS (Kaufer et al. 1999), mounted on the 2.2m MPG/ESO telescope, at La Silla Observatory. The raw data are available in the ESO archive.[1] The extraction of the FEROS spectra was done with the ESO Data Reduction System (DRS), available for FEROS users. The DRS performs a bias subtraction, flat fielding, order tracing and extraction. The wavelength calibration was computed using two calibration lamps (one ThAr and one ThArNe), having different exposure times, allowing sufficient line coverage across all of the spectral range (~3500 - 9200 Å). The wavelength solution leads to a typical RMS of 0.005 Å from ~900 emission lines. Additionally, the reduction pipeline applies a barycentric correction to the extracted data, but this option was disabled and applied later using our own code.

### 1.1.1 Radial velocity calculation

The RVs were computed in a similar way as described in Jones et al. (2013), according to the following procedure. First, each order was separated into four chunks and the doppler shift was computed by applying a cross correlation (Tonry and Davis 1979) between the stellar spectrum and its corresponding template (high S/N spectrum of the same star). For this purpose the IRAF *fxcor* task (Fitzpatrick 1993) was used. Only 35 of the 39 orders available were used, rejecting one in the reddest part of the spectrum (because of the presence of telluric lines) and three in the bluest part of the spectrum (low S/N). That left us with a total of 140 chunks, and therefore 140 different velocities per observation. Then, for each RV dataset, the mean velocity was computed, rejecting every point more than 2.5 sigma from the mean. The RVs that were rejected constitute, on average, 17% of the total number of chunks for each epoch. These rejected chunks were the same for most of the datasets, at the very blue and red ends of the considered spectrum, therefore for most of the epochs we used the same chunks when computing the RVs. The principal cause for rejection of a chunk was because of the low S/N.

Similarly, we computed the cross correlation between the simultaneous calibration lamp (sky fiber) and one of the lamps that was used for the wavelength calibration of that night. The velocity we measured corresponds to the nightly drift that is produced mainly by small pressure and temperature variations inside the spectrograph. Finally, I applied the barycentric correction to the measured velocities using the central time of the exposure and the actual coordinates of the star. The final velocity for each epoch is then:

$$\mathrm{RV} = \mathrm{RV}_{\mathrm{obs}} + \mathrm{RV}_{\mathrm{drift}} + \mathrm{BC}, \tag{1.1}$$

where $\mathrm{RV}_{\mathrm{obs}}$ is the observed velocity, $\mathrm{RV}_{\mathrm{drift}}$ is the nightly drift, and BC is the barycentric correction.

To test this method, it was applied to the RV computation of 127 spectra of $\tau$ Ceti, taken from 2004 to 2013. The resulting velocities are shown in Figure 1.1. The RMS around zero is $\sim$10 m s$^{-1}$, which is higher than the $\sim$ 4 m s$^{-1}$ obtained by Jones et al. (2013) for the same star, however the difference is due to the limited data used in their work that spanned just over 3 years and were

---

[1] http://archive.eso.org/eso/eso_archive_main.html

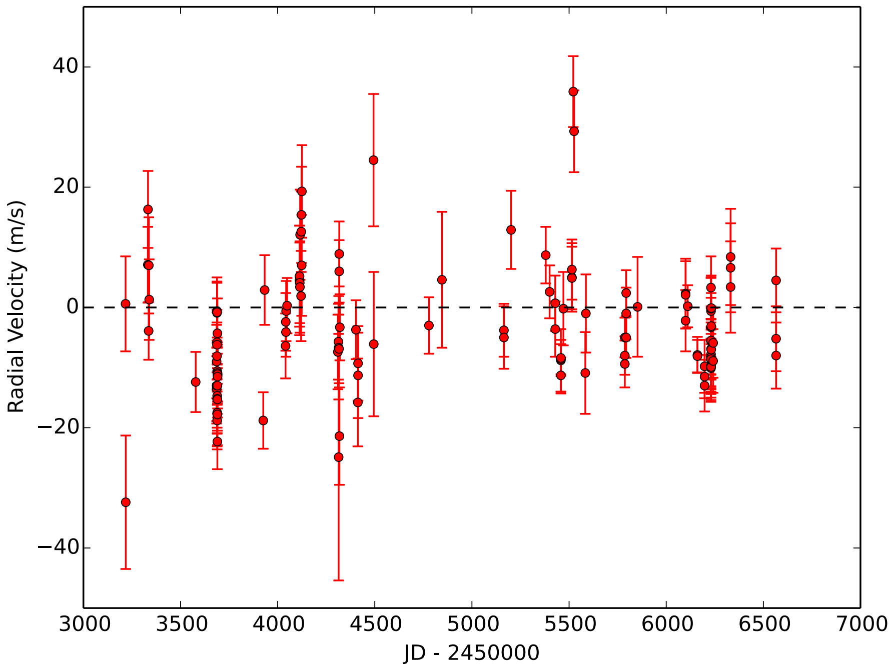

Figure 1.1: Radial measurements for $\tau$ Ceti from 2004 to 2013. The RMS of the data is 10 m $s^{-1}$.

observed after 2007. Prior to this date there was no standard calibration plan for FEROS, thus the wavelength solution was poorer.

### 1.1.2 Data from other instruments

In this work we also supplemented our data with spectra taken with other instruments, namely HARPS, CORALIE and CHIRON. The High Accuracy Radial velocity Planets Searcher, HARPS (Mayor et al. 2003), is located at the 3.6m ESO telescope at La Silla Observatory. Using this spectrograph, Müller et al. (2013) obtained a RMS of 6.9 m $s^{-1}$ for $\tau$ Ceti, proving the accuracy of its measurements. The data was obtained from the ESO Reduced Spectra.[2] The mean value of the RVs was subtracted from each HARPS data point, obtaining velocities distributed around zero m $s^{-1}$. We did this to later combine the HARPS RVs with data from other instruments, which were computed using a different template.

CORALIE (Queloz et al. 2000) is at the 1.2m Swiss telescope, located at the La Silla Observatory. In Ségransan et al. (2010), they show that 40% of the measurements made with this instrument reach a radial velocity accuracy of $\sim$ 6 m $s^{-1}$ or better, and 90% with an accuracy better than $\sim$ 10 m $s^{-1}$. We obtained the CORALIE RV's from the Systemic Console, which were mentioned in Setiawan et al. (2008b, hereafter S08) but were never published.

Finally, we used data from the CHIRON spectrograph (Tokovinin et al. 2013), located at the 1.5m telescope at Cerro Tololo Inter-American Observatory (CTIO). The extraction of the data was

---

[2] `http://archive.eso.org/wdb/wdb/adp/phase3_spectral/form`

Table 1.1: Updated and new orbital parameters for the planets analysed in this work.

| Parameter | HD11977 b | HD47536 b | HD110014 b | HD110014 c |
|---|---|---|---|---|
| $P$ (day) | 621.6 ± 2.4 | 434.9 ± 2.6 | 882.6 ± 21.5 | 130.0 ± 0.9 |
| $T_0$ (JD-2450000) | 2906.6 ± 10 | 3040.8 ± 30 | 3739.4 ± 50.2 | 4031.3 ± 3.78 |
| e | 0.3 ± 0.03 | 0.3 ± 0.1 | 0.26 ± 0.1 | 0.44 ± 0.2 |
| $\omega$ (deg) | 35.5 ± 5.8 | 268.6 ± 17.3 | 47.72 ± 15.5 | 307.6 ± 19.9 |
| $M_p \sin \mathrm{i}$ ($M_{\mathrm{Jup}}$) | 6.5 ± 0.2 | 4.0 ± 0.4 | 10.7 ± 1.0 | 3.1 ± 0.4 |
| $a$ (AU) | 1.89 ± 0.005 | 1.12 ± 0.005 | 2.31 ± 0.04 | 0.64 ± 0.003 |

done using the automatic reduction pipeline that is offered to CHIRON users. The velocities were obtained using the $I_2$ cell technique (Butler et al. 1996b). This consists of passing the stellar light through a cell that contains iodine vapor, that superimposes absorption lines in the region between 5000 Å and 6000 Å. These lines are then used as markers against which the doppler shift can be measured. More detail can be found in Jones et al. (2014). With this instrument, following our procedures, it is possible to reach a velocity precision of ~ 6 m s$^{-1}$.

The fits for the RV curves were made using the Systemic Console (Meschiari et al. 2009). We changed the objective function of the minimizer to be the RMS of the fit, instead of the $\chi^2$. This was done because of the difference between the uncertainties obtained in the measurements for each instrument. The HARPS data have uncertainties on the order of ~ 0.5 m s$^{-1}$, whereas for the other datasets they are generally higher than 5 m s$^{-1}$. When we tried to minimize the $\chi^2$, the HARPS data would dominate the fitting process, even when most of the RVs were computed from FEROS spectra. Minimizing the RMS prevents this from happening, making the fit more evenly distributed across all the datapoints. The uncertainties in the derived orbital parameters for each star were obtained using the boot strapping option available in the Systemic Console.

## 1.2 Radial velocity analysis

### 1.2.1 HD 11977

In Setiawan et al. (2005, hereafter S05), this star was classified as a G5III star, located in the "clump region". They derived a mass of 1.91 $M_\odot$, a rotational period of $P_{\mathrm{rot}}/\sin \mathrm{i}$ = 230-270 days, and a metallicity of [Fe/H] = -0.21. Assuming negligible mass loss during the red giant branch phase, it is likely a former main-sequence A-star. We will adopt a mass of 2.31 $M_\odot$ and metallicity of [Fe/H] = -0.16, which were derived in Mortier et al. (2013, hereafter M13). S05 also announced a planetary companion with an orbital period of P = 711 days, an eccentricity e = 0.4, and minimum mass $m_2 \sin \mathrm{i}$ =6.5 $M_{\mathrm{Jup}}$, being the first planet found orbiting an intermediate mass star (for $M_\star = 1.19 M_\odot$).

To test this Keplerian solution we used FEROS data of this star taken between 2001 and 2007. However, when testing the nights that were observed before 2004 we obtained a large scatter in the velocities for $\tau$ Ceti (~ 30 m s$^{-1}$), making those nights unreliable. Therefore, we only used the

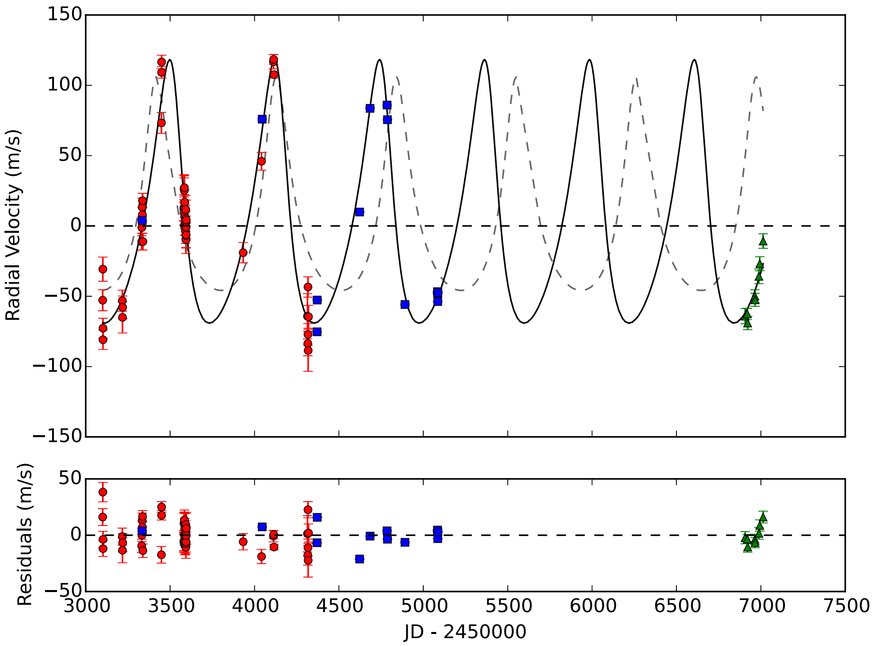

Figure 1.2: Top panel: Radial measurements for HD 11977 taken with FEROS (red circles), HARPS (blue squares), and CHIRON (green triangles). The back solid line corresponds to the RV curve found in this work, with a RMS of 11.2 m $s^{-1}$. The dashed grey line corresponds to the fit found in S05, which gives us a RMS of 33.8 m $s^{-1}$. Bottom planel: Residuals from our fit.

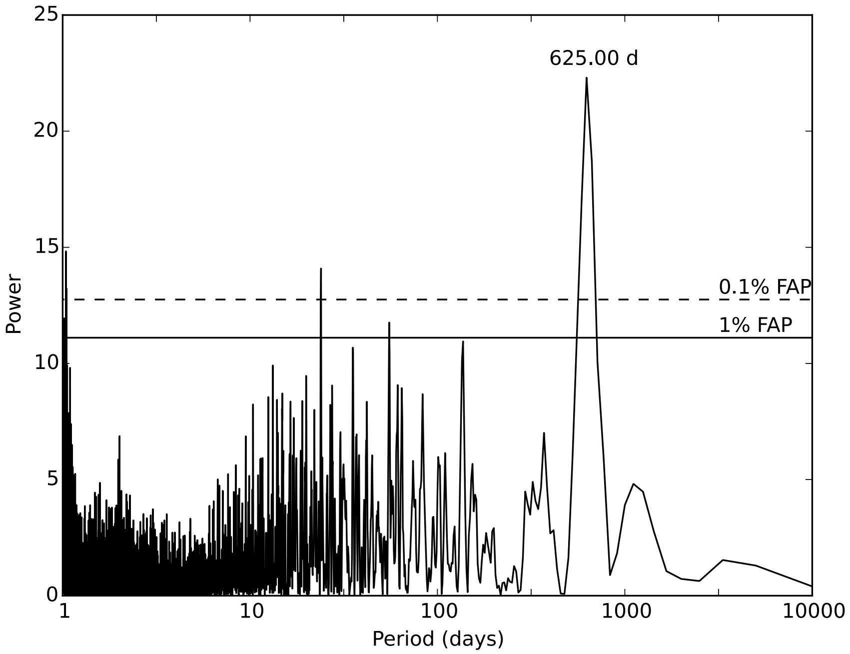

Figure 1.3: LS periodogram of our RV data for HD 11977. The two horizontal lines represent the 1% (solid line) and 0.1% (dashed line) FAP.

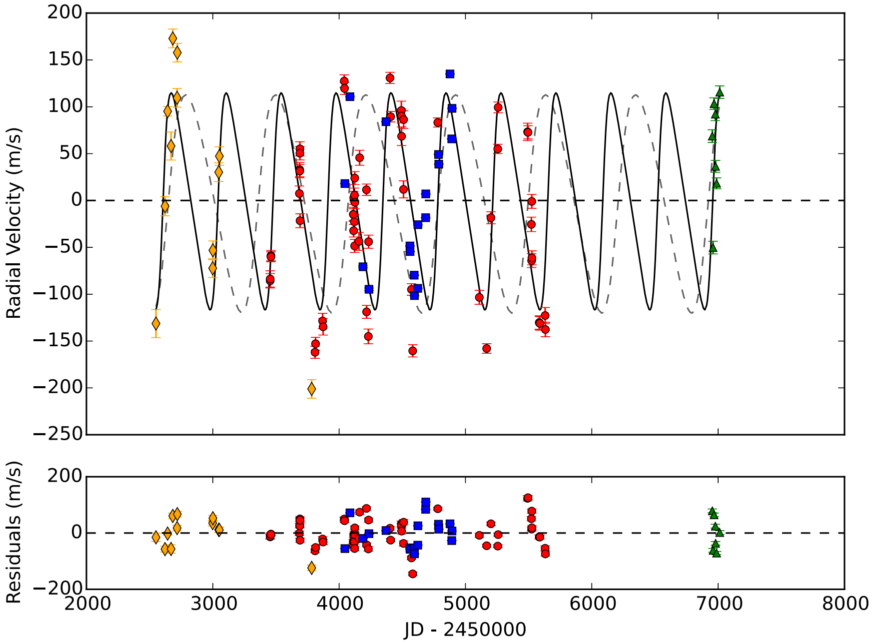

Figure 1.4: Top panel: Radial velocity measurements for HD 47536 from FEROS (red circles), CORALIE (orange diamonds), HARPS (blue squares), and CHIRON (green triangles). The back solid line corresponds to the RV curve found in this work. The RMS of this fit is 51.7 $ms^{-1}$. The dashed grey line corresponds to the fit found in Setiawan et al. (2003), with a RMS of 103.5 m $s^{-1}$. Bottom panel: Residuals from the fit found in this work.

nights from 2004 to 2007, which includes a total of 48 spectra. We also included 217 measurements taken with HARPS. Since many of these RV epochs were obtained during a single night, we decided to use the RV average in that night, leaving us with 13 RV epochs. We also included 8 observations made with CHIRON. Figure 1.2 shows the resulting RVs from FEROS (red circles), HARPS data (blue squares), and CHIRON (green triangles). When fitting the orbital solution found in S05, we got a RMS of 33.8 m $s^{-1}$, larger than the one published in S05 of 29.1 m $s^{-1}$. Figure 1.3 shows the LS periodogram of the data. As can be seen, there is a strong peak at 625 days. After close inspection, it was found that this period does not correspond to any peak in the periodogram of the sampling, however we did find that the second peak at 23 days is a product of the sampling of the data. We fitted a single-planet Keplerian solution to our data, starting from the 625 day period found in the periodogram. The best fit leads to the following parameters: P = 621 days, $M_p \sin \mathrm{i}$ = 6.5 $M_{\mathrm{Jup}}$, and an eccentricity of e = 0.3. The orbital parameters are listed in Table 1.1. This solution leads to a RMS of 11.2 m $s^{-1}$, almost a factor three better than the 29.1 m $s^{-1}$ uncertainty found in S05.

### 1.2.2 HD 47536

The second star in our sample is HD 47536, a very metal-poor K1-III star. Setiawan et al. (2003) derived a mass of 1.1-3.0 $M_{\odot}$, a rotational period of $P_{\mathrm{rot}}/\sin \mathrm{i}$ = 619 days, and a metallicity of [Fe/H]= -0.68 dex. It was first studied using data from 1999 to 2002 taken with FEROS, and

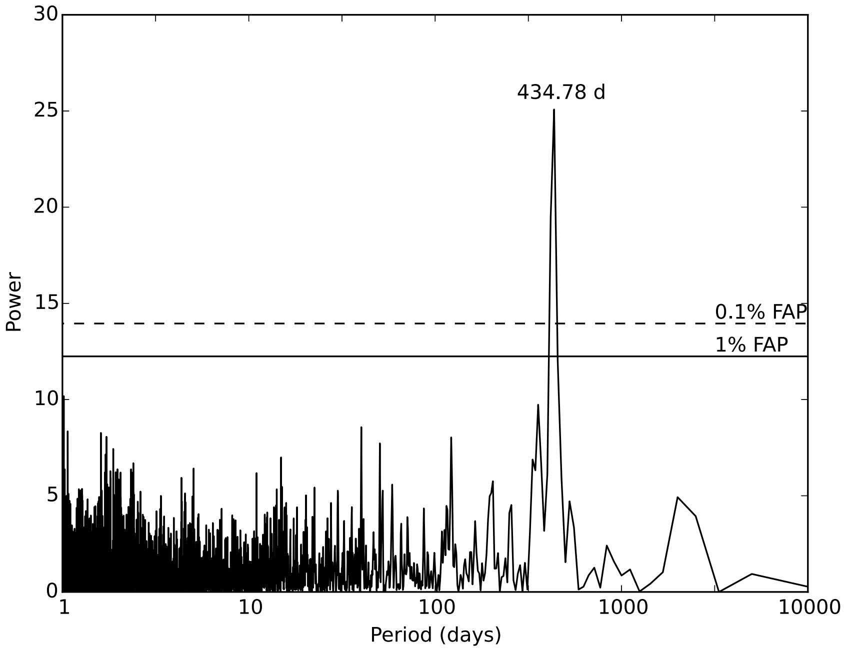

Figure 1.5: Lomb-Scargle periodogram of the HD 47536 RV measurements. The two horizontal lines represent the 1% (solid line) and 0.1% (dashed line) FAP.

one night with CORALIE in October 2002. They reported the discovery of one companion with a period of 712 days and a minimum mass of 5.0 $M_{\rm Jup}$. Later, S08 did a revision of the orbital solution including new data from 2004. They claimed that the star actually hosts two planets with the following orbital parameters: P ~430 days and $M_p$ ~5 $M_{\rm Jup}$ for the inner planet, and a P ~2500 days and a $M_p$ ~7 $M_{\rm Jup}$ for the outer object. It is worth mentioning that they did not publish the exact results from the two-planet solution, the values we quote came from an unrefereed conference proceeding.

We analyzed 56 FEROS spectra of HD 47536, taken from 2005 to 2011. We did not include the data taken before 2005 because of the large RV scatter we obtained for $\tau$ Ceti, as was the case for the nights before 2004 for HD 11977. Additionally, we included 12 RV epochs obtained with CORALIE, 6 data points obtained with CHIRON, and 18 RVs computed from HARPS spectra. The resulting RV measurements are shown in Figure 1.4. The red circles, orange diamonds, blue squares, and green triangles correspond to FEROS, CORALIE, HARPS, and CHIRON data, respectively. We also used the mass and metallicity derived by M13 for this star, corresponding to $M_\star = 0.98 M_\odot$ and [Fe/H]=-0.65 dex. The LS periodogram of the RVs (Figure 1.5) shows a strong peak at 434 days. Starting from this period we fit a Keplerian solution to the data, which leads us to the following orbital parameters: P=434.9 days, e = 0.3 and $M_P$ = 4.0 $M_{\rm Jup}$. The orbital solution is overplotted in Figure 1.4 (solid line) and we obtain a RMS around the fit of 51.7 ms$^{-1}$. The orbital parameters are listed in Table 1.1.

In Figure 1.6 the periodogram for the window function and the data are shown. We see that there is a peak in the sampling, at 454 days, very close to the peak found in Figure 1.5. In order to discard the possibility that the 434-days period is not a product of the sampling of the data, we measured its power in the periodogram as we add data points. If the period is from a true signal

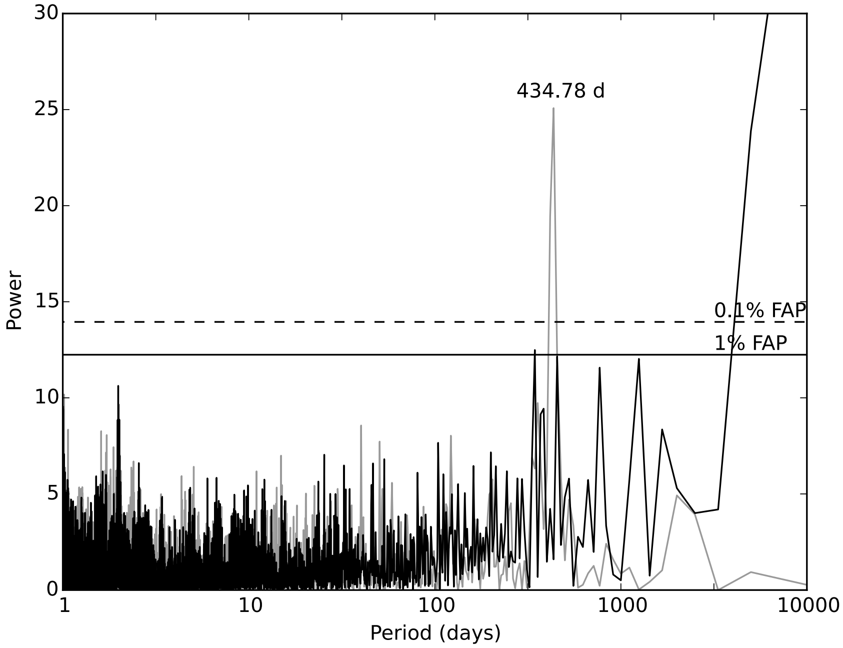

Figure 1.6: Lomb-Scargle periodogram of the sampling window (black line) and the data (grey line) for HD 47536. The peak at 434.78 days corresponds to the peak found in Figure 1.5.

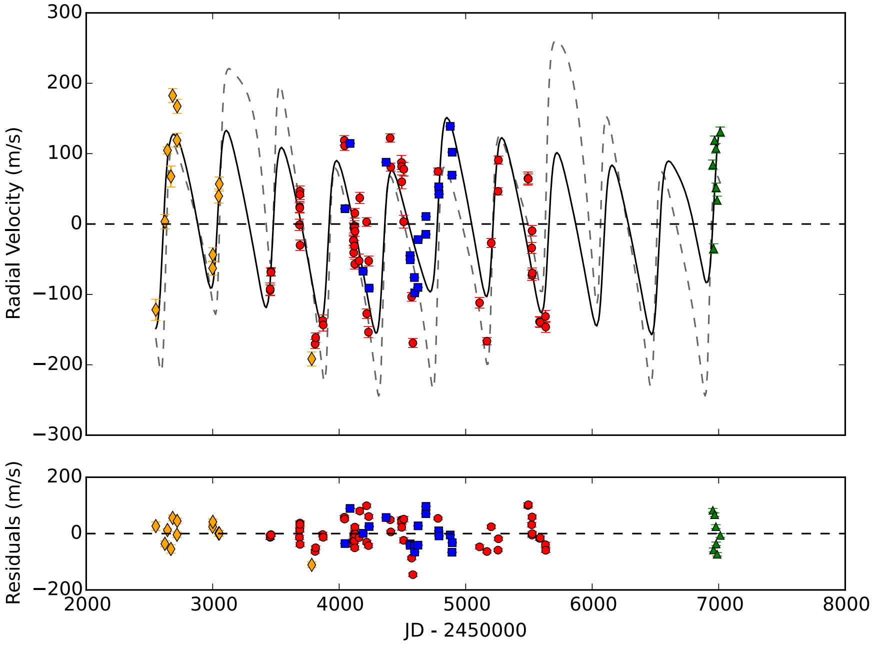

Figure 1.7: Top panel: Radial velocity for HD 47536 from FEROS (red circles), CORALIE (orange diamonds), HARPS (blue squares), and CHIRON (green triangles). The black solid line corresponds to the RV curve found in this work for a 2-planet fit, with a RMS of 48.9 m s$^{-1}$. The dashed grey line corresponds to the fit found in S08, with a RMS of 58.8 m s$^{-1}$. Bottom planel: Residuals from the fit found in this work.

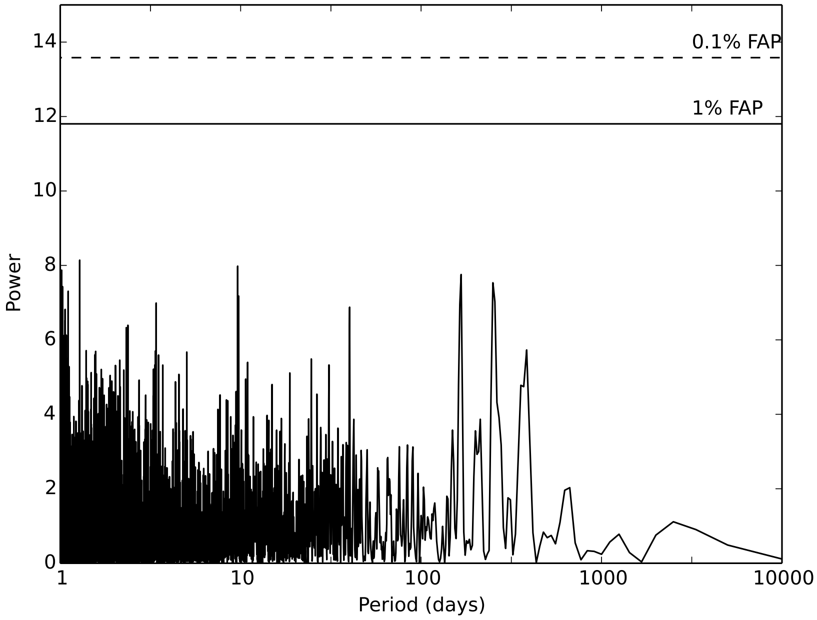

Figure 1.8: Periodogram of the residuals of HD 47536 after fitting the one-planet solution. The two horizontal lines represent the 1% (solid line) and 0.1% (dashed line) FAP.

from the star, then we expect that it should become stronger as we add more RV measurements, in a monotonic fashion. If it is a product of the sampling, its power could stop growing and will decline in regions. We found that the power grows as we add more data points more or less monotonically, instead of decreasing, which helps to confirm that the 434-days period is produced by a true signal from the system.

We then tried to fit a two-planet solution using as initial guesses the values for the period and mass of the planets found in S08 (limiting the eccentricity of the outer planet to be smaller than 0.5 otherwise the system might be highly unstable). We found a mass for the outer planet of $\sim 2.0\ M_{\rm Jup}$, with a period of 2013 days and eccentricity of 0.5. This two-planet fit is shown in Figure 1.7. The RMS of the solution is 48.9 m $s^{-1}$, which is slightly better than the one-planet fit. We performed an F-test between these two solutions and found that the two-planet solution is not statistically superior to the one-planet fit (probability of 70 %).

When looking again at the periodogram of the data, we were not able to find any other significant peak that could justify another signal. The periodogram of the residuals from the one-planet fit (Figure 1.8) does not show a significant peak neither. Therefore, we can rule out the existence of a second statistically significant signal in the current RV data of this star.

### 1.2.3 HD 110014

HD 110014 is a K2III star with an absolute magnitude $M_v$ = -0.11, color $(B-V)$ = 1.24, and metallicity [Fe/H]=0.14 dex (M13). In de Medeiros et al. (2009, hereafter M09) the authors estimated

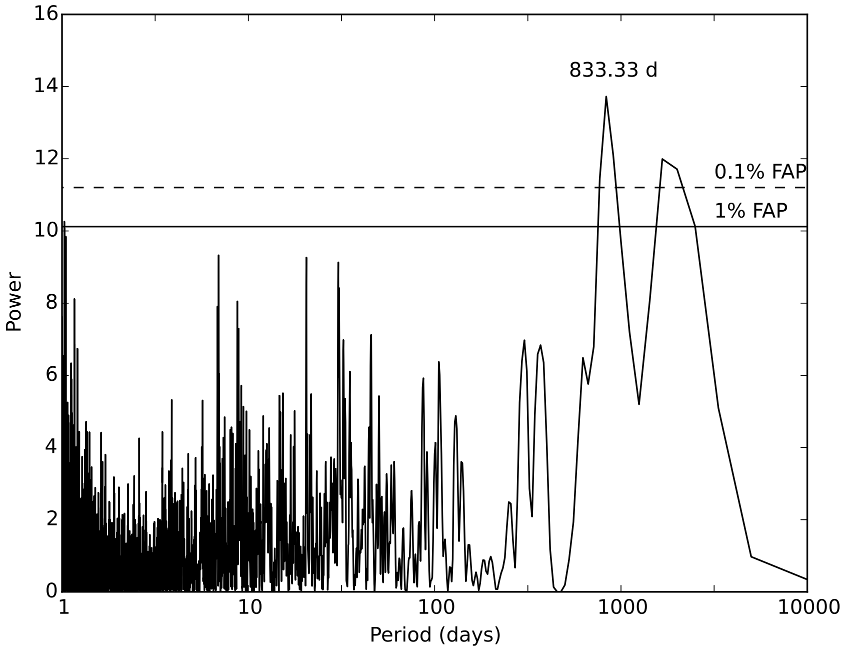

Figure 1.9: LS periodogram of HD 110014. The two horizontal lines represent the 1% (solid line) and 0.1% (dashed line) FAP.

the upper limit of the rotational period as $P_{\mathrm{rot}}/\sin \mathrm{i} \sim 513$ days. They also estimated the mass and age of this star by its position in the color-magnitude diagram, using the process explained in da Silva et al. (2006). According to their solution, HD 110014 could be either a 1.9 $M_{\odot}$ star at the end of its core helium phase, or a 2.4 $M_{\odot}$ star in its first-ascent of the RGB, close to the core helium flash. In this chapter we will adopt the mass of 2.09 $M_{\odot}$, as derived by M13. In M09 this star was observed using FEROS from 1999 to 2007, plus a few nights with HARPS and CORALIE. They claim the detection of a planet with a period of 835.5 days, a minimum mass of 11.1-9.5 $M_{\mathrm{Jup}}$ (for $M_{\star} = 1.9 - 2.4\ M_{\odot}$), and an eccentricity of 0.46.

We analyzed spectra taken with FEROS from 2004 to 2011, corresponding to 21 nights and a total of 25 data points. We also used 116 data points taken with HARPS, but as with HD 11977, many of them were taken in the same night and so we took the average velocity per night. That left us with 17 HARPS data points.

We tried to fit the solution found in M09 to our data, obtaining a RMS of 63.13 m s$^{-1}$, larger than the one published of only 45.8 m s$^{-1}$. When trying to find another orbital solution we looked at the periodogram of the data in Figure 1.9, which shows an emerging peak at 833 days. Beginning with that initial period and minimizing all the orbital parameters, we obtained the solution for a planet with orbital period $P$ = 936.4 days, e = 0.06, and $M_p \sin \mathrm{i} = 13.67\ M_{\mathrm{Jup}}$. The RMS of this fit is 44.64 m s$^{-1}$, and is shown in Figure 1.10. The period of this possible companion, of 936 days, is slightly larger than the 833-days period found in Figure 1.9. The periodogram of the residuals (Figure 1.11) shows a possible peak at 133 days and is comfortably above the 0.1% FAP. When a new signal with a period of 133 days is added to our previous one-planet solution, we find a new model as shown in Figure 1.12, and this leads to the orbital parameters listed in Table 1.1. The

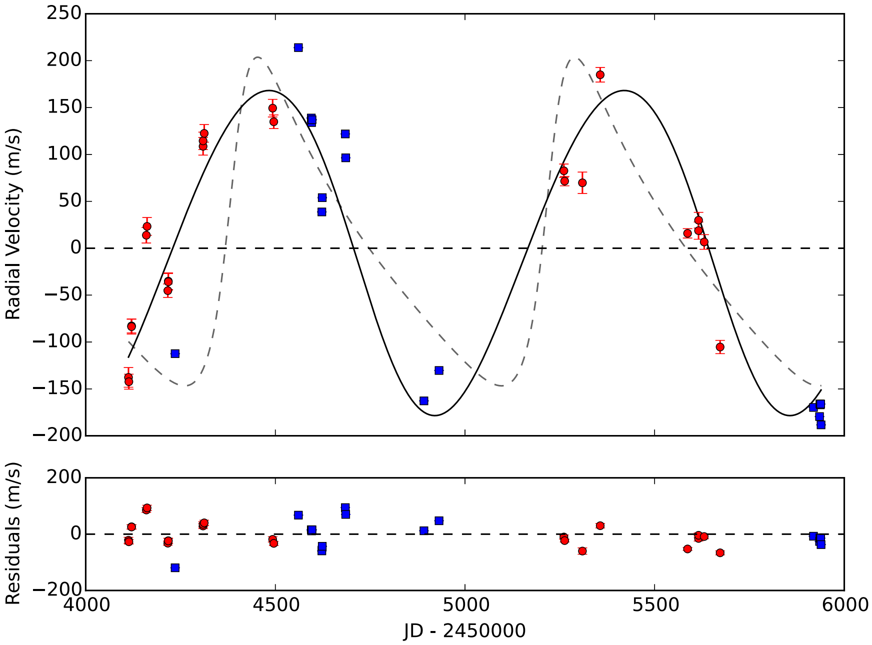

Figure 1.10: Top panel: Radial measurements for HD 110014 from FEROS (red circles) and HARPS (blue squares). The back solid line corresponds to the RV curve for one planet found in this work, with a RMS of 44.6 m s$^{-1}$. The dashed grey line correspond to the fit found in M09, which gives us a RMS of 63.13 m s$^{-1}$. Bottom panel: Residuals from the fit.

RMS of this two-planet solution is 19.4 m s$^{-1}$, significantly lower than the one found in M09 of 45.8 m s$^{-1}$ and our own one-planet solution.

We performed a F-test between the one-planet solution and the two-planet solution and found that they are significally different (probability of ~0% that they are both statistically similar). We also looked at the periodogram of the sampling (Figure 1.13) and we find that there is no peak corresponding to the 133-days period. This helps us to rule out the possibility that the signal we see is due to the sampling of the data.

In M09 a periodicity of 130-days was also detected in the residuals of their fit. They performed several tests in order to discard the possibility that the signal is intrinsic to the star. They could not find any correlation between those tests and the measured velocities, nor with the fit residuals, yet, they could not find enough evidence to be sure that the signal is produced by the presence of a second companion. The RMS they obtain after fitting the orbital solution of the second planet is 32.9 m s$^{-1}$, significantly higher than the 19.4 m s$^{-1}$ RMS we got with our fit.

The 130-days period could be caused, not only by a planetary companion, but also by a cool spot on the surface of the star. It has been shown that RV signals caused by rotational modulation of star spots can mimic Doppler signals, causing possible misinterpretation of the measurements (e.g. Setiawan et al. 2008a; Huélamo et al. 2008), particularly when the star is at low inclination since some activity indicators, like the bisector inverse slope (BIS), are insensitive in this regime (Desort et al. 2007). In order to test this possibility, we first computed the spot filling factor from Hatzes (2002). This is the percentage of the surface of the star that a spot should have to cover in order

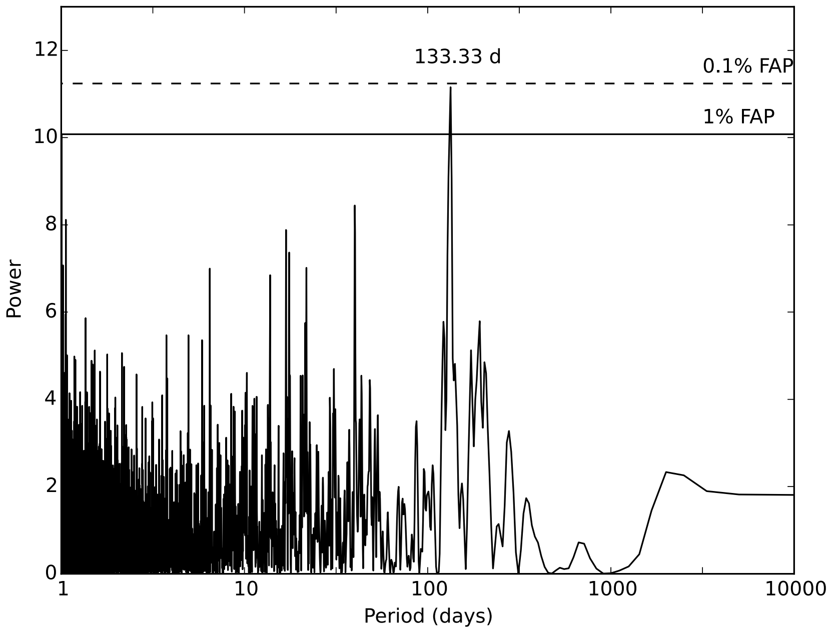

Figure 1.11: Lomb-Scargle periodogram of the residuals of HD 110014, after fitting the one-planet solution. The two horizontal lines represent the 1% (solid line) and 0.1% (dashed line) FAP.

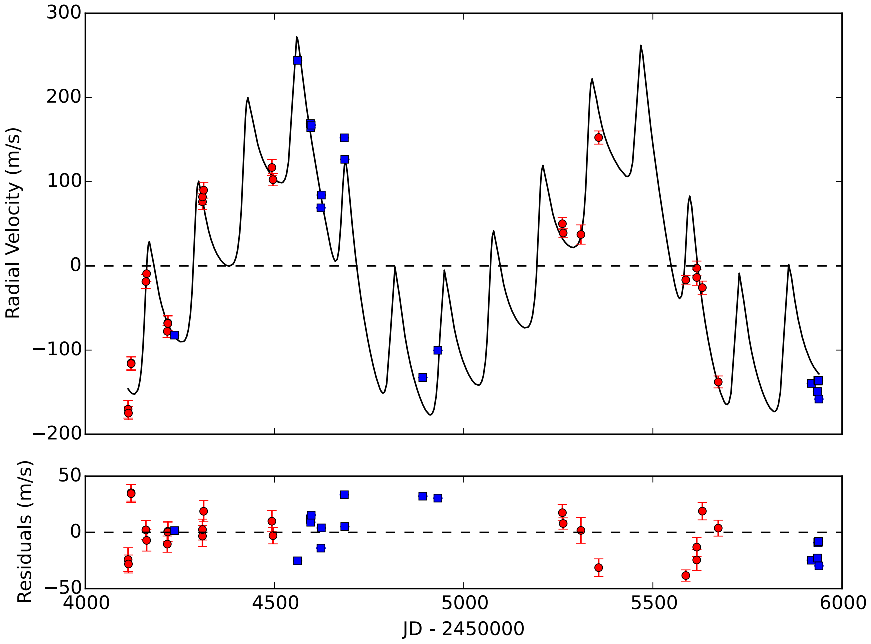

Figure 1.12: Top panel: Radial velocity measurements for HD 110014 from FEROS (red circles) and HARPS (blue squares). The back solid line corresponds to the RV curve found for a two-planets system. The RMS of this fit is 19.4 m $s^{-1}$. Bottom panel: Residuals from the fit.

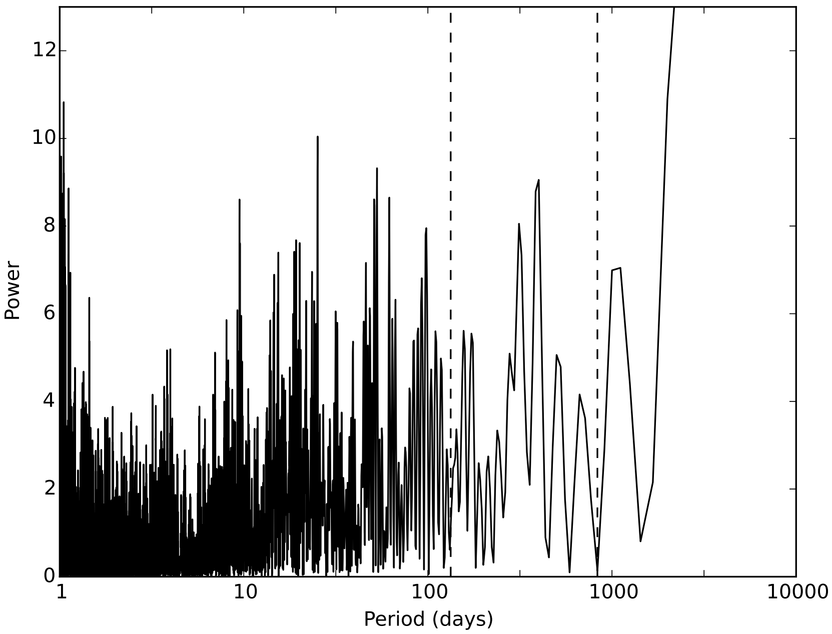

Figure 1.13: Lomb-Scargle periodogram of the sampling of the data for HD 110014. The vertical dashed lines represent the location of the 833-days period and the 133-days period found in the periodograms of Figures 1.9 and 1.11.

to produce a RV signal with the same amplitude as the one measured. We used $V = v \sin \mathrm{i} = 1.1$ km s$^{-1}$, derived in De Medeiros et al. (2014), as the rotational velocity of the star, and $K_2 = 83.5$ m s$^{-1}$ as the RV amplitude produced by the 130-days signal. We obtained a filling factor of 13.8%. In section 1.3.2, we discuss the analysis of available photometry for this star, to test if we can find signals that could be due to spots with this level of spot coverage.

### 1.2.4 HD 122430

HD 122430 is a giant star (K2III) with metallicity of [Fe/H] = -0.09 dex and a mass of 1.68 $M_{\odot}$ (data from M13). A planet orbiting this star was reported in Setiawan (2003), using data from FEROS and CORALIE. The orbital parameters correspond to a planet with a period of 344 days, eccentricity of 0.68, and minimum mass $M_p \sin \mathrm{i}$ = 3.71-6.04 $M_{\mathrm{Jup}}$ (for $M_{\star}$=1.2-2.5 $M_{\odot}$). The RMS of this solution is reported to be 27.2 m s$^{-1}$.

We used spectra taken with FEROS from 2004 to 2010, totaling 42 data points. We also used 6 velocities computed with HARPS as a check on our solution. When trying to fit the values for the orbital parameters found by Setiawan (2003, hereafter S03) we found a RMS of 63.4 m s$^{-1}$. From the periodogram (Figure 1.14) we could not find any significant peak that would lead us to a starting period for a fit. We then let the console minimize the orbital parameters with starting values given by the orbital parameters found in S03. This leads us to a new solution with a period of 455.1 days, an eccentricity of 0.6, a minimum mass of 2.1 $M_{\mathrm{Jup}}$ and a RMS of 29.3 m s$^{-1}$. The fit

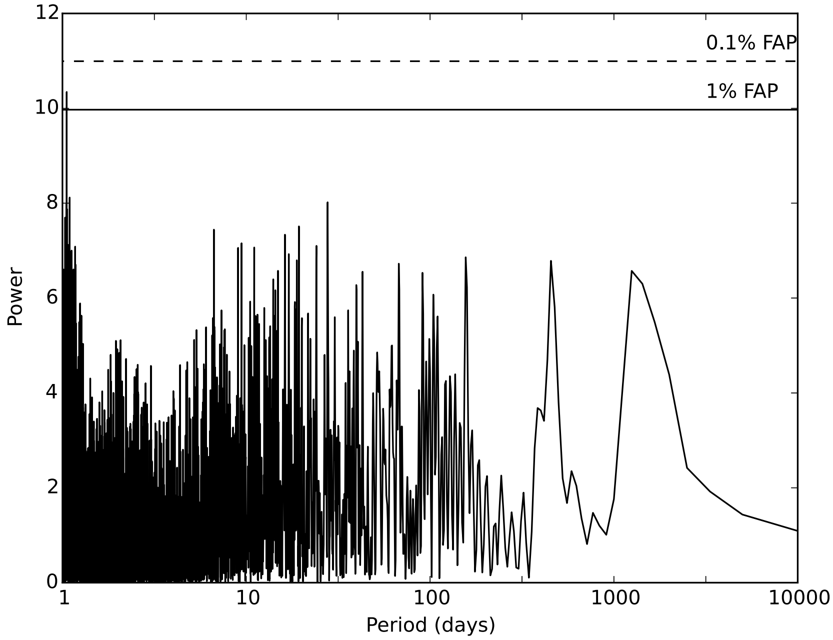

Figure 1.14: Lomb-Scargle periodogram of HD 122430. The two horizontal lines represent the 1% (solid line) and 0.1% (dashed line) FAP.

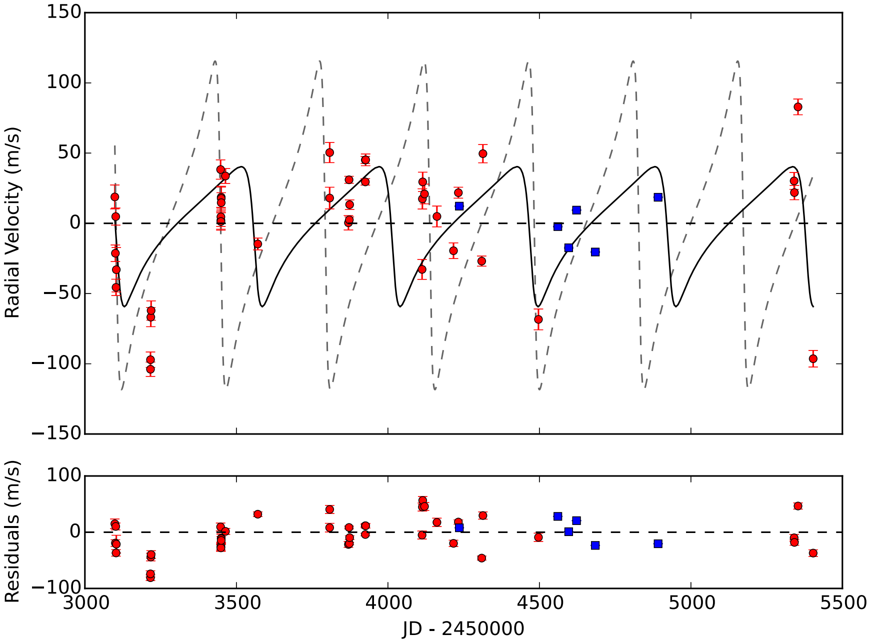

Figure 1.15: Top panel: Radial velocity measurements for HD 122430 from FEROS (red circles) and HARPS (blue squares). The back solid line corresponds to the RV curve found in this work and has a RMS of 29.3 m s$^{-1}$. The grey dashed line is the solution found in Setiawan (2003) and gives a RMS of 63.4 m s$^{-1}$. Bottom panel: Residuals from the fit.

is shown in Figure 1.15 as the black solid line, where the red circles and the blue squares represent the FEROS and HARPS data, respectively. Even though the RMS of S03 is still lower than the one obtained for HD 47536 and HD 110014 (one-planet fit), their periodograms showed at least one period with a significant peak close to the 1% and 0.1% FAP, which helped us prove that there was a signal within the RV data. This is not the case for HD 122430, and after finding a RMS of 29 m $s^{-1}$ for our best solution, we cannot support the existence of this planet based on our data. Indeed, a mean noise model fit to the data returns an RMS of 40 m $s^{-1}$, only ∼ 10 m $s^{-1}$ larger than the one-planet solution.

In order to check if we missed the signal in the LS periodogram because of its high eccentricity, we also calculated the Generalized Lomb-Scargle Periodogram (GLS, Zechmeister and Kürster 2009). This periodogram is more suited to detecting signals arising from bodies on eccentric orbits ($e > 0.5$). We found no peak above the noise level, meaning that the high eccentricity was not the only reason no peak was found in the LS periodogram. Therefore, if a planet does exist orbiting this star, we do not have the necessary data yet to make this claim.

### 1.2.5 HD 70573

The last star in our sample is HD 70573, a young lithium bearing star classified as a member of the Local Association (Pleiades moving group) by Montes et al. (2001). The age is therefore estimated to be between 78-125 Myr (only 3%-6% the age of the Sun, where moving groups are thought to be associations of young stars, see Murgas et al. 2013). It has a spectral type of G1-1.5 V and a mass of 1.0 $M_{\odot}$, according to Setiawan et al. (2007, hereafter S07). Henry et al. (1995) measured photometric variations of HD 70573 and found a rotational period of 3.296 days.

This star was studied in S07, in which they claimed the detection of a companion with a period of 852 days and a minimum mass ($M_p \sin i$) of 6.1 $M_{\mathrm{Jup}}$. To verify this detection we analyzed data taken with FEROS between 2004 and 2008, corresponding to a total of 41 nights and 55 data points. Since this is a young star some parts of its spectrum contain very few lines or heavily blended lines (because of line broadening from rapid rotation). This leads to an inaccurate correlation between the spectra and the template for some orders, and in turn in noisy results for the velocities. To deal with this, we had to modify the orders that we were considering to calculate the RVs. After visually inspecting each order for different observations of this star, we decided to consider only from orders 9 to 31, instead of using information from orders 2 to 36 like we did for the above stars.

When we fit a companion with the orbital parameters as given by S07 to our data we arrived at a RMS of 78.78 m $s^{-1}$, much higher than the published RMS of 18.7 m $s^{-1}$. The fit is shown in Figure 1.16 as the grey solid line, and the red circles represent the FEROS RV's. The periodogram of the data (Figure 1.17) does not show any significant peak at high periods, like it did in S07. Only one peak above the 0.1% FAP can be seen, corresponding to a period of 3.296 days, the same as the rotational period of the star found in Henry et al. (1995). We tried to fit a curve with a period of 3.296 days to model the rotational effects of the star on the RVs. The fit is shown in Figure 1.18 and has an associated RMS of 36.4 m $s^{-1}$. The periodogram of the sampling (Figure 1.19) shows that one of the peaks correspond to a 833-day period, close to the 852-days period proposed by S07. This indicates that the previously published orbital solution might be due to a sampling alias combined with noisy data.

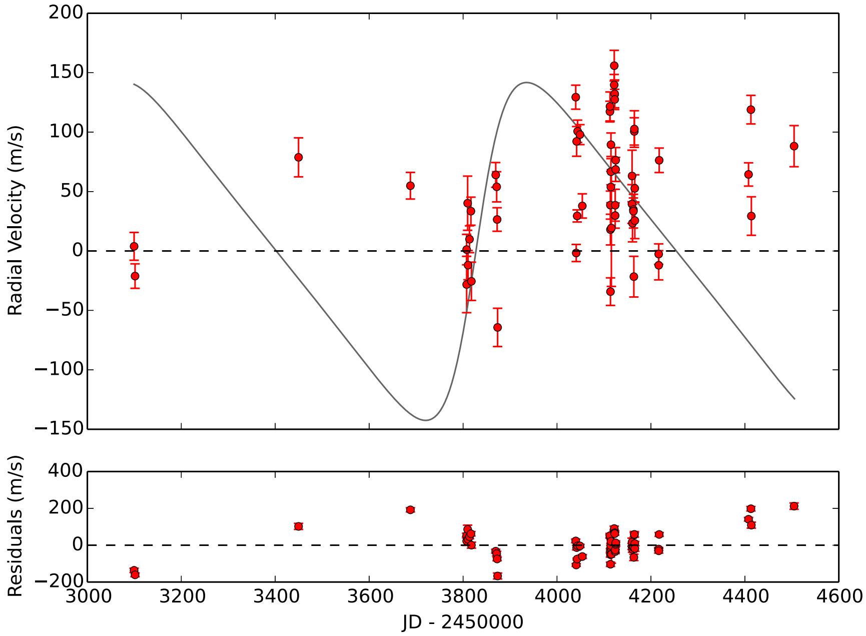

Figure 1.16: Top panel: Radial velocities measured by FEROS for HD 70573 (red dots). The grey line correspond to the orbital solution found in S07. The RMS of this fit is 78.8 m $s^{-1}$. Bottom panel: Residuals from the fit. A long period variation can be seen in the residuals.

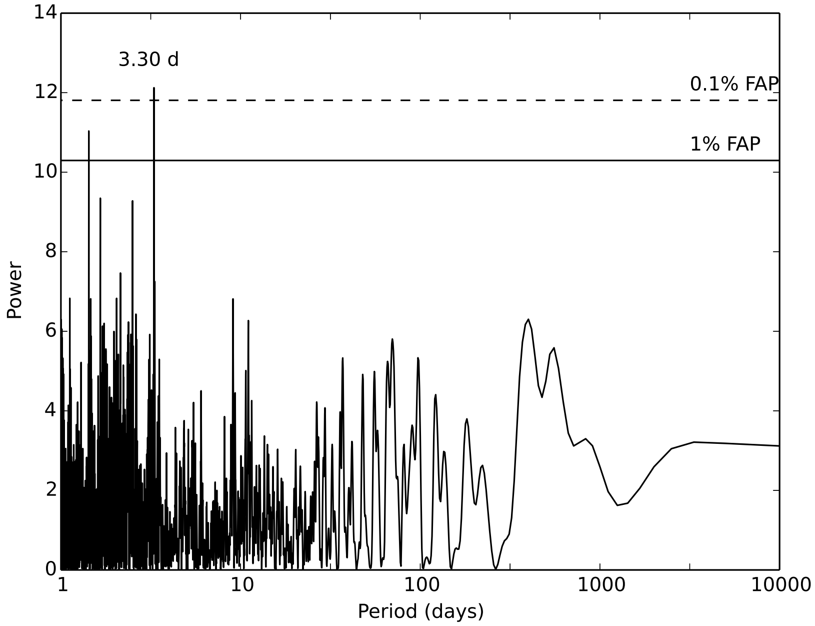

Figure 1.17: LS periodogram of HD 70573. The two horizontal lines represent the 1% (solid line) and 0.1% (dashed line) FAP. Only one significant peak, above the 0.1% FAP, is seen, corresponding to 3.296 days.

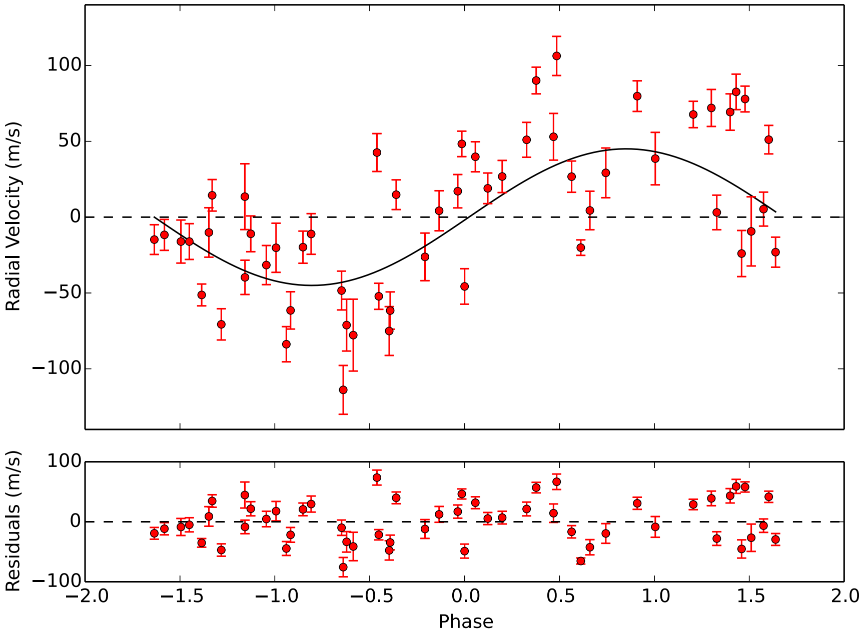

Figure 1.18: Top panel: Phase-folded RV curve for HD 70573 (red dots), and fit to the data (solid line).The RMS of this fit is 36.4 m s$^{-1}$. Bottom panel: Residuals from the fit.

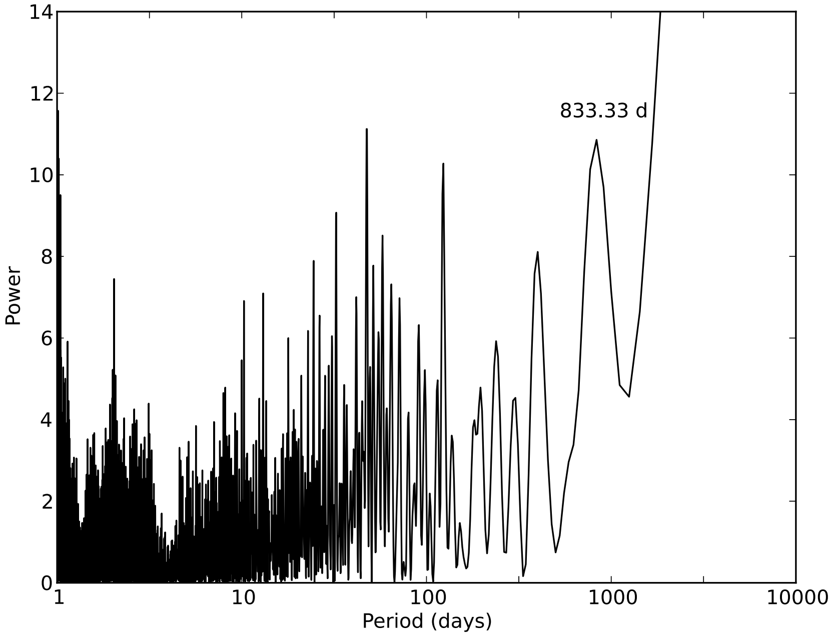

Figure 1.19: LS periodogram of the sampling window for HD 70573. The peak corresponding to 833 days, close to the period of 852-days found by S07, is shown.

## 1.3 Activity

### 1.3.1 S-index and Bisector Velocity Span

As was mentioned in the introduction, it has been shown that intrinsic stellar phenomena such as magnetic activity can produce a periodic radial velocity signal that can be misinterpretated as a substellar companion (Queloz et al. 2001). We performed three tests to our data to verify if this is the case for the stars we are studying. First, we measured the change in the flux from the Ca II HK lines over time by calculating the S-index for each epoch (the process is described in Jenkins et al. 2008, 2011a). The second test we used was the bisector analysis (Toner and Gray 1988), aimed at detecting asymmetries in the line profiles caused by intrinsic stellar phenomena. We measured the bisector velocity span (BVS) for each epoch, which essentially corresponds to the velocity difference between the bottom and top thirds of the cross correlation function (CCF, see Jones et al. 2013). Finally, the third test we used to parameterize line asymmetries was analysis of the CCF full width at half maximum (FWHM).

Our aim was to test if these activity indicators were correlated with the RV at each epoch. To measure the level of the correlation we computed the Pearson rank correlation coefficient, which is a measure of the linear correlation between two variables, where 1 is a total positive correlation, 0 is no correlation, and -1 is total negative correlation. When computing the Pearson correlation coefficient all the data points have the same weight, meaning that one point lying very far away from the mean is going to affect the final result, even if it has a large uncertainty. That is why we only used the points that were closer than $2.5\sigma$ from the mean value of the distribution.

For most of the stars no correlation was found between the activity indicators and the velocities, with $r \sim 0$, where $r$ is the Pearson correlation coefficient. Plots of the indices vs RV for each star can be found in the Appendix. There were some cases that required further analysis. One of them is HD 47536. The RVs obtained for this star showed a lot of jitter, even after fitting a one-planet solution ($\sim 50$ m s$^{-1}$), leaving us with a RMS of 51.7 m s$^{-1}$ which could not be significantly improved by adding a new component to the system. In the left panels of Figure 1.20 we show the activity indicators versus the measured RV, and in the right panels the same activity indicators but this time versus the residuals left over after fitting our one-planet solution. There are no significant correlations in any of the plots versus the RVs, with $r$ indices equal to -0.3, 0.3 and -0.02. From the $\chi^2$ test between the indices and a mean noise model fit, we found that the probability of these being fit by a horizontal line is $\sim 90\%$. This means that it is unlikely that the velocities are a product of the stellar activity, and are likely produced by an external source. Also, we find no correlation in any of the plots versus the residual RV (right panel), which might indicate that the jitter in the residuals is not due to magnetic activity nor rotationally modulated spots on the star. We computed the velocity oscillation amplitude for this star from the relations in Kjeldsen and Bedding (1995). We used $M = 0.98\ M_\odot$ from M13 and $L = 175.19\ L_\odot$ from Anderson and Francis (2012). We obtained $v_{\rm osc} = (41.8 \pm 2.5)$ m s$^{-1}$. This is only 10 m s$^{-1}$ lower than our RMS of 51.7 m s$^{-1}$, meaning that the residuals from our 1-planet fit could be explained by the expected "jitter" for this giant star.

In Figure 1.21 we can see the same plots as before, but this time for the star HD 110014. In the left panels we show the activity indices versus the measured RV, and in the right panels are

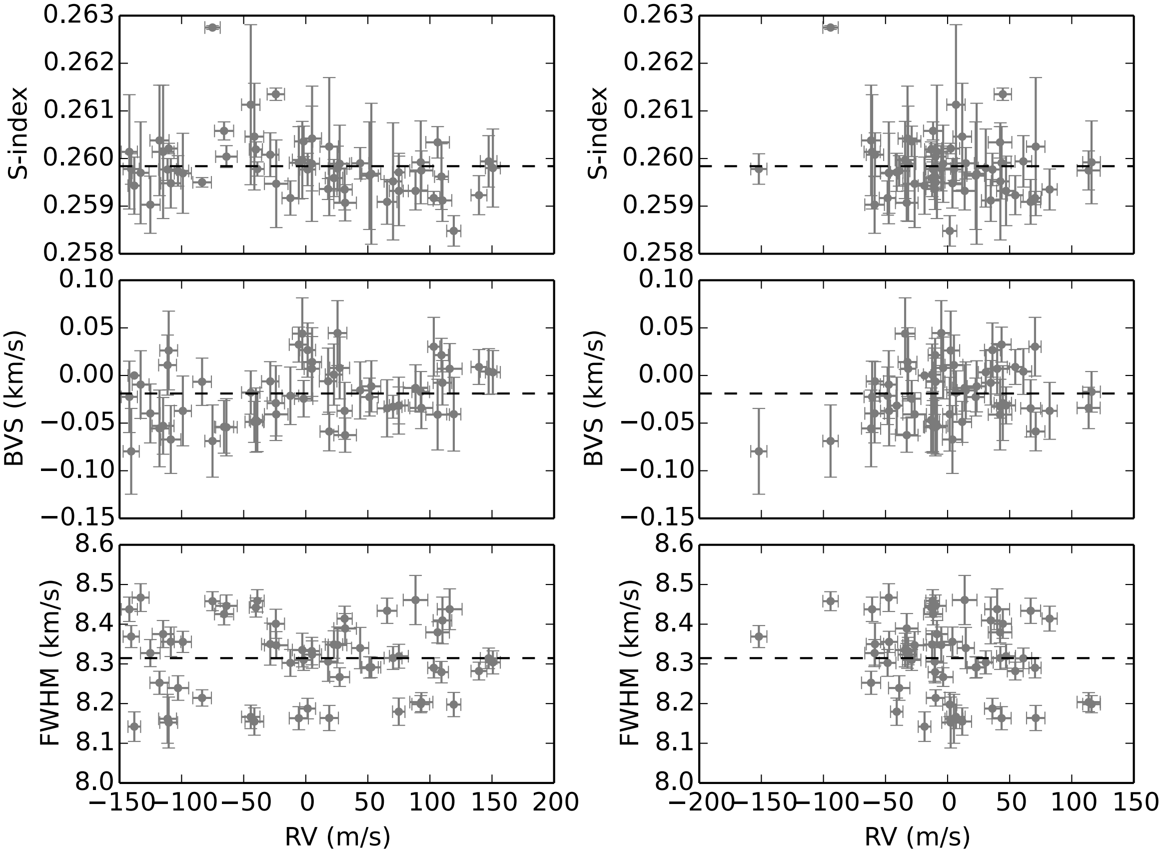

Figure 1.20: S-index (upper panel), bisector velocity span (middle panel), and FWHM of the CCF (lower panel) versus the measured RV (left panel) and versus the residual RV for HD 47536, after fitting the one-planet solution. Only the values for the activity indices laying $2.5\sigma$ from the mean value of the distribution were considered. The correlation coefficients for the plots in the left panels are $r$= -0.3, 0.3 and -0.02, and for the right panels are $r = -0.2$, 0.24 and -0.23 for the S-index, BVS and FWHM versus the residual velocity, respectively. Horizontal dashed lines correspond to the mean of the distribution for each plot.

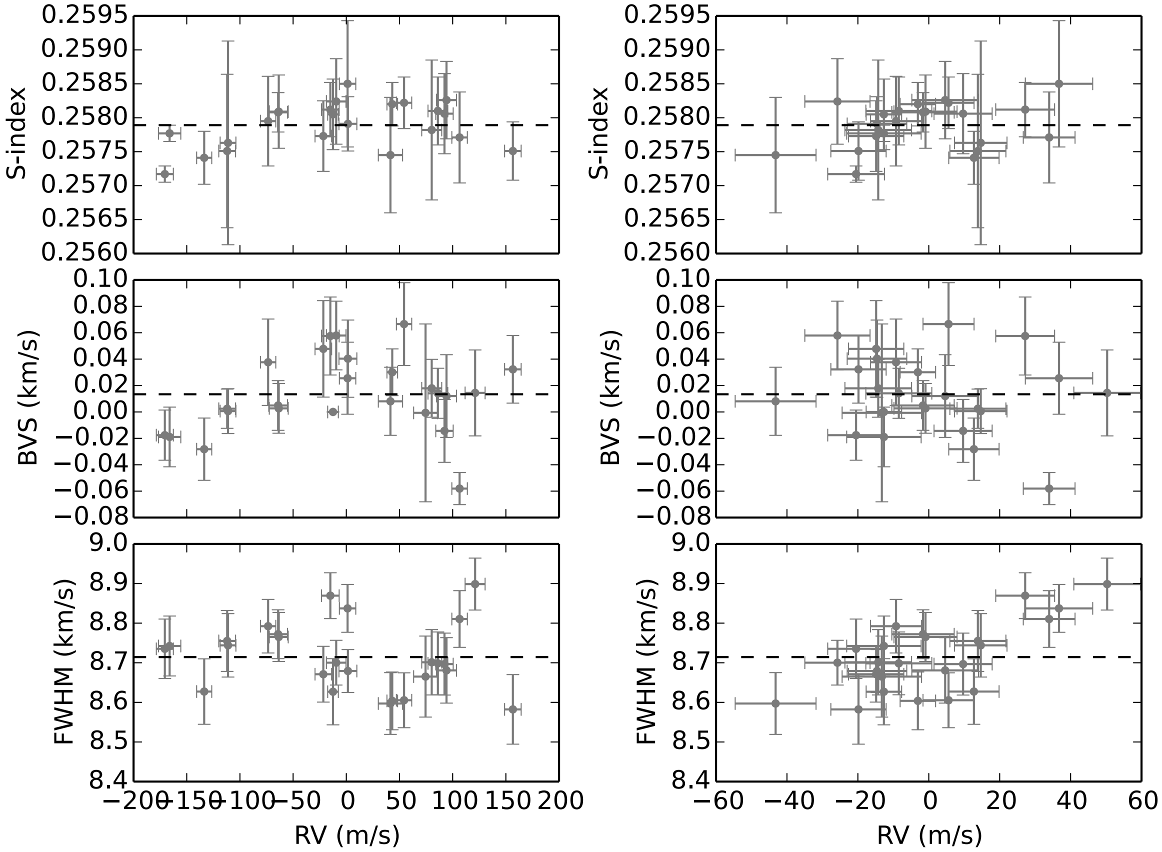

Figure 1.21: S-index (upper panel), bisector velocity span (middle panel), and FWHM of the CCF (lower panel) versus the measured RV (left panel), and versus residual RV (right pannel) for HD 110014, after fitting the two-planet solution. Only the values for the activity indices laying $2.5\sigma$ from the mean value of the distribution were considered. The correlation coefficients for the plots in the left panel are $r$=0.36, 0.19 and -0.17, and in the right panel are $r$ = 0.3, -0.18 and 0.68 for the S-index, BVS and FWHM versus the velocity, respectively. Horizontal dashed lines correspond to the mean of the distribution for each plot.

the same activity indices but versus the residual velocity left after fitting the two-planet solution we are proposing in this work. We found that the $r$ values for the activity indices and velocity in the left panels plots are $r$=0.36, 0.19 and -0.17 for the S-index, BVS and FWHM, respectively. This indicates that activity in the star is not the cause of the velocities we observe and supports our argument that they are produced by two planets orbiting the star. In the right panels, the $r$ indices are $r$ = 0.3, -0.18 and 0.68 for the S-index, BVS and FWHM versus the residual velocity, respectively, suggesting that part of the jitter we were left with after fitting our two-planet solution may be caused by activity in the atmosphere of the star.

The last case is for HD 70573. One interesting result is that, when we studied the periodogram of the BVS (Figure 1.22), we found a signal corresponding to the orbital period of the star of 3.296 days, just like we did with our RVs. Even though this peak is not nearly as significant as it is in Figure 1.17, it is present and it supports our result that the observed velocities contain a signal

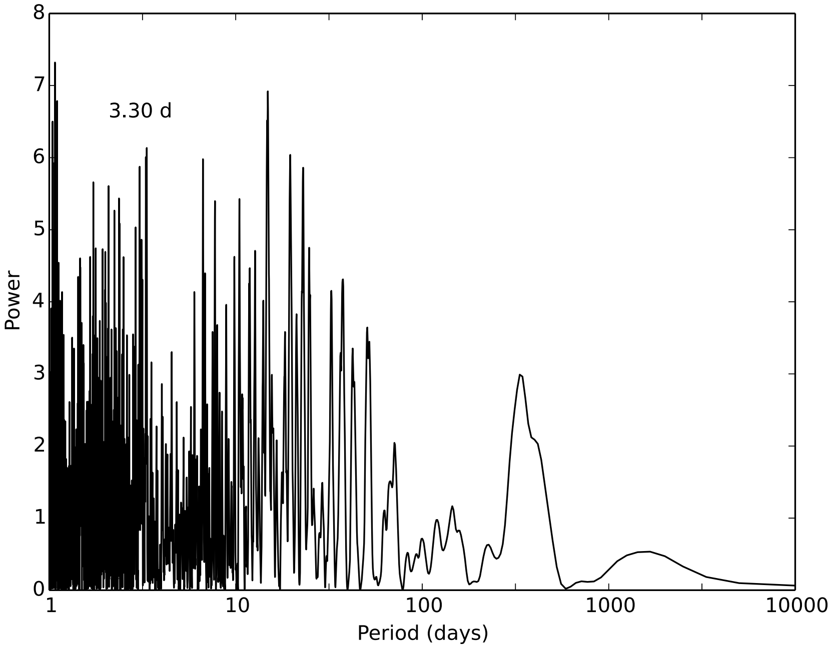

Figure 1.22: LS periodogram of the bisector velocity span for HD 70573.

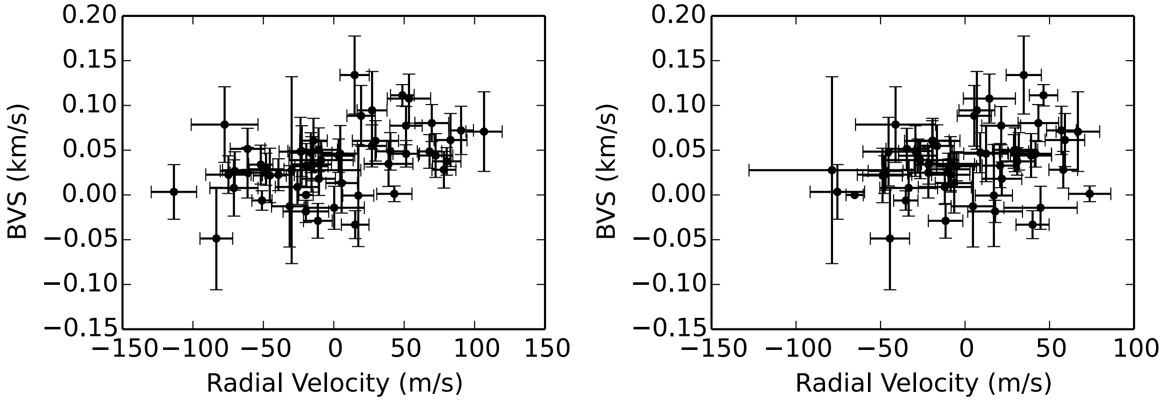

Figure 1.23: BVS vs measured RV (left panel) and vs residual velocity after removing the rotational solution (right panel) for the star HD70573. The *r* coefficients are 0.44 (left panel) and 0.26 (right panel).

that is due to features on the star modulated by its rotation. The S-index and FWHM of the CCF do not show correlation with the RV, with $r$ indices less than 0.2. However, for the case of the BVS (Figure 1.23), we have a correlation coefficient of $r = 0.44$ for this index vs the measured RVs, which is suggestive of correlation. The $r$ value decreases to $r = 0.26$ when considering just the residual velocities after fitting the rotational period of the star. This strongly suggests that the rotation of the star is likely the cause of the variation seen in the bisector.

### 1.3.2 Photometry

We looked for any period variation in the visual magnitude that could mimic the results we show in this work. We analyzed the $V$-band photometry from the All Sky Automated Survey (Pojmanski 1997) for the stars HD 11977, HD 47536 and HD 110014. The precision from this data is on the order of 1%. The magnitude versus time are plotted in Figure 1.24. Superimposed on each plot are the long-period fits, with periods of $P$ = 2114, 1962 and 1687 days for HD 11977, HD 47536 and HD 110014, respectively. Because these are evolved stars, this long-period variation could be caused by magnetic cycles in the photosphere of the stars. These periods are not present in the velocities so we can conclude that this photometric variation is not the cause of the signals in the RV data.

For HD 110014 we analyzed the photometry in order to search for any signals from cool spots on surface of the star that could cause the RV signal we found (see section 1.2.3). We could not find any period above the noise level that could correspond to the periods of the planets detected. We also looked at the Hipparcos photometry (Perryman et al. 1997) for this star but we found no significant peak with a period longer than 2 days. The precision of the data for this star is ~0.1%. As previously mentioned, the filling factor of a spot on the surface would need to be 13.8% to produce this level of RV signal, and therefore it is likely that this level of spot coverage would not be detectable in this dataset, meaning a spot origin for the signal can not be ruled out with any degree of certainty. However, we do note that we studied the power of the periodogram peak as a function of time, as we did for HD 47536 in section 1.2.2. We found that, in general, the signal peak rising almost monotonically. This lends some weight to the planetary hypothesis for the second signal in the RV data of this star.

## 1.4 Conclusions and Discussion

We computed precise radial velocities using archival FEROS spectra for stars HD 11977, HD 47536, HD 70573, HD 110014 and HD 122430. From this data we can conclude the following:

- There is a companion around HD 11977 with a period of 621.6 days and minimum mass of 6.5 $M_{\mathrm{Jup}}$.
- We can confirm the presence of one companion around HD 47536, with a period of 434.9 days and minimum mass of 4.0 $M_{\mathrm{Jup}}$. We cannot confirm the existence the second companion proposed by S08.
- We confirm the existence of a companion around HD 110014, with a period of 882.6 days and

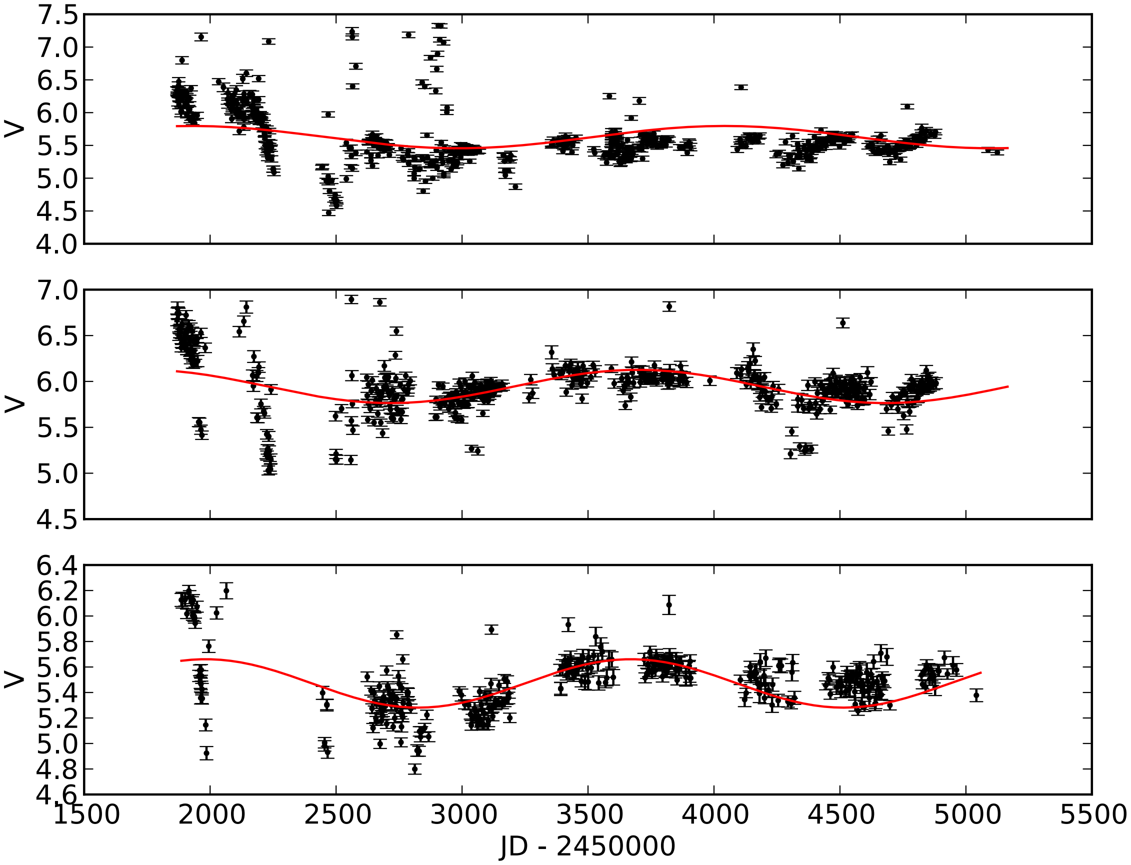

Figure 1.24: V-magnitude variation for HD 11977 (upper panel), HD 47536 (middle panel) and HD 110014 (lower panel). In each plot a long-period variation was found (red lines), with $P$ = 2114 days for HD 11977, $P$ = 1962 days for HD 47536, and $P$ = 1687 days for HD 110014.

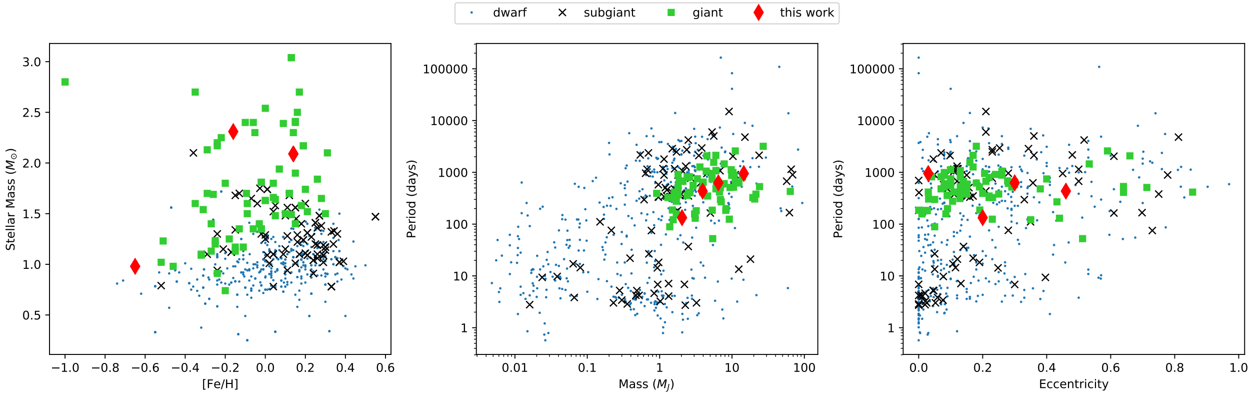

Figure 1.25: Stellar mass versus stellar metallicity (left panel), period versus mass (middle panel) and period versus eccentricity (right panel) for all confirmed planets with known values for the stellar type, mass and metallicity, and for known values of planetary mass, eccentricity and period. There is a total of 317 planets around dwarf stars, 76 around sub-giant stars, and 67 around giant stars (including the ones in this work).

minimum mass of 10.7 $M_{\mathrm{Jup}}$. We also found evidence of a second companion around this star with a period of 130.0 days and minimum mass of 3.1 $M_{\mathrm{Jup}}$. A more extensive photometric analysis has to be done to confirm that this signal corresponds to a second companion and not to a cold spot on the star's surface.

- There is no signal significant enough to confirm the presence of any companion around HD 122430.
- We found no evidence of the planet orbiting HD 70573 proposed in S07, nor evidence of any other companion. The only signal present corresponds to the rotational period of the star.
- There is no correlation between the activity indices and the RVs for the stars HD 11977, HD 47536, HD 110014 and HD 122430, supporting our hypothesis that the observed velocity signals are Doppler signals. We find a small yet not significant correlation between the activity indices and the measured RVs for HD 70573, but it decreases after removing the rotation of the star. We find a higher level of correlation in the activity indices versus the residual velocities after removing the two-planet fit for HD 110014. This could explain the jitter in the residual RVs as a product of activity within the star.
- We observe a periodic variation in the photometric data for three of the stars in our sample (HD 11977, HD 46536 and HD 110014), but with periods different than the ones of the companions we found. We conclude that the signals in HD 11977 and HD 47536 data cannot be explained by intrinsic photometric variation in the stars. For HD 110014 we could not find evidence of any photometric signal with periods equal to the one of the RV signals, supporting our argument of the existence of this second planet orbiting this star.

Finally, in Figure 1.25 we can see that the planets found in this work follow similar trends to the previously detected planets around giant stars. The left and middle panels show that these planets are mostly clustered around periods from ∼ 100 to 1000 days, and with masses from ∼ 1 to 30 $M_{\mathrm{Jup}}$. The right panel of Figure 1.25 is similar to Figure 2 in Reffert et al. (2015, hereafter R15) which shows the distribution of metallicity and stellar mass for planets around giant stars. HD 110014 b and c fall in the region corresponding to a 20.8% probability of the star having a planet, and

HD 11977 b falls in the block with probability of 6.9%. Both stars are in the range of masses for giant stars for which we can expect the highest number of planets (~2 $M_{\odot}$ according Figure 2 and 5 of R15). HD 110014 is also the star with the highest metallicity in our sample, and in turn is the one with the most currently detected planets (two found in this work). This follows the notion that the higher the metallicity of a star, the higher the probability of finding a planet orbiting them. This result was discussed in R15 and mimics the trend and discoveries of planets orbiting the most metal-rich lower-mass stars (Fischer and Valenti 2005; Sousa et al. 2011b; Jenkins et al. 2013b).

One special case is that of HD 47536b. This planet is orbiting a very metal poor giant star ([Fe/H]=-0.65 dex), making HD 47536 the second most metal-poor star known to host a planet (the most metal-poor star was thought to be BD+20 2457, with [Fe/H]=-1.0 dex, but it was recently shown to be an unstable system; see Horner et al. 2014). Actually, the probability of finding a planet around such a metal poor star is almost 0% (according to Figure 4 and 7 of R15). The confirmation of a planet orbiting HD 47536 is a very interesting case to consider in the study of the formation of these systems.

# Chapter 2

# Discovery of two hot Jupiters from K2 photometry

Since the detection of the first transiting exoplanet (HD 209458 b, Charbonneau et al. 2000), the anomalously large radii of many hot Jupiters have been puzzling astronomers trying to understand the formation and composition of these close-in systems. Inflated giant planets have radii larger than what theoretical models predict for their masses (Burrows et al. 2007; Fortney et al. 2007), and are often found orbiting their host stars at short periods. Many groups have been working on different theories to explain this phenomena, most of which place stellar insolation as the most important factor driving planetary inflation. Here, a fraction of the absorbed stellar flux is transported by some mechanism deep within the atmosphere, near to the radiative-convective boundary. This flux would then prevent the contraction of these planets, explaining their large radius. The mechanisms proposed for the flux transportation within the planetary atmosphere, as well as other proposed theories to explain planetary inflation, not based on its insolation, are reviewed in Weiss et al. (2013). Based on observational evidence, an insolation limit of $F > 2 \times 10^8\,\mathrm{erg\,s^{-1}\,cm^{-2}}$ has been set to trigger the expansion of the planet (Miller and Fortney 2011; Demory and Seager 2011).

The launch of the *Kepler* space mission meant an exponential growth in the number of exoplanets detected, with over 1000 system confirmed and over 3000 candidates awaiting confirmation. Unfortunately, most of the detections made by *Kepler* were too faint for further follow-up studies. Also, the observations carried out by Kepler were made in the celestial northern hemisphere, out of reach from some of the largest telescopes in the world. After the failure of one of its reaction wheels, Kepler was renamed K2, and changed its field of view to campaigns in the ecliptic, which meant that some of this fields would be visible from the Southern hemisphere, allowing astronomers to carry out follow-up efforts. Because ultracool dwarfs and gas giant planet more or less share a common radius (especially when said giant planets are inflated), dynamical mass measurements are required to determine whether a transit signal originates from a planet or an ultracool dwarf. For single-planet systems, this is possible through the radial velocity method, which also provides the high resolution spectra required for the characterization of the host star and, in consequence, the planet.

Currently, researchers working in Chilean institutions have privileged access to state of the art instrumentation for follow-up observation of planetary candidates through radial velocity. This led us to create a Chilean-based K2 project (K2CL), focused on the task of selection of planetary candidates through photometry from the K2 mission, and later follow up using high resolution spectrographs. Exciting results have already been published since the project was started (see Espinoza et al. 2016; Brahm et al. 2016; Jones et al. 2017; Brahm et al. 2018).

In this chapter I will explain the discovery of two hot Jupiter planets, orbiting two dwarf stars that represent two different cases of the hot Jupiter-type planets. K2-237 is an 11.6 magnitude F star visible from the southern hemisphere (Table 2.1). It was observed during Campaign 11 of the K2 mission, and the planet was found to have a mass of $1.60^{+0.11}_{-0.11}\,M_{\rm Jup}$, but a radius of $1.65^{+0.07}_{-0.08}\,R_{\rm Jup}$, making it a highly inflated hot Jupiter. The next planet, K2-238 *b*, was found using data from Campaign 12 of K2 to be orbiting a G type star. For this planet, we found a mass of $0.86^{+0.13}_{-0.12}\,M_{\rm Jup}$, and radius of $1.30^{+0.15}_{-0.14}\,R_{\rm Jup}$. Even though the planet is in the hot Jupiter regime and receives a flux above the inflation threshold, it does not show inflation characteristics.

This chapter is organized as follows: in Section 2.1 we present the data obtained for each star, including photometric and spectroscopic observations. In Section 2.2 we analyze and derive the atmospheric parameters and obtain estimates for their stellar parameters such as age, mass, metallicity, effective temperature and rotational velocity. We also model both the radial velocity observations and the light curves, and derive the physical characteristics for each planetary system. In Section 2.3 we show the evidences which imply that K2-237 *b* corresponds to a highly inflated hot Jupiter, while K2-238 *b* appears to be consistent with a hydrogen/helium dominated planet with some metal content. Finally, in Section 2.4, we present a summary of our findings. This work has been accepted by MNRAS, under the title 'EPIC 229426032 *b* and EPIC 246067459 *b*: discovery and characterization of two new inflated hot Jupiters from K2, and it is available at Soto et al. (2018).

## 2.1 Data

### 2.1.1 Photometry

We analyzed photometric data from Campaign 11 (K2-237) and Campaign 12 (K2-238) of the *K2* mission. We downloaded the Target Pixel Files (TPF) from the Mikulski Archive for Space Telescopes (MAST), extracted the photometry, and detrended it with an implementation of the EVEREST algorithm (Luger et al. 2017). The candidates were selected after running a BLS periodogram. The remaining long-term variations were removed following a similar procedure than the one described in Giles et al. (2017a). We locally fit a third-order polynomial to sections of 0.5 days of the light curve, using a window of 10 days over the surrounding data. We repeat this process over the whole light curve. An outlier rejection was performed before fitting the data, making sure that the transit was not removed. The light curves obtained after detrending and removing the long term variations are shown in Figs. 2.1 & 2.2. For the case of K2-237, this is not the final light curve we used to derive the planet parameters. The data we used for that analysis is shown in Figure 2.7, and the process we followed to process it is explained in section 2.2.2.

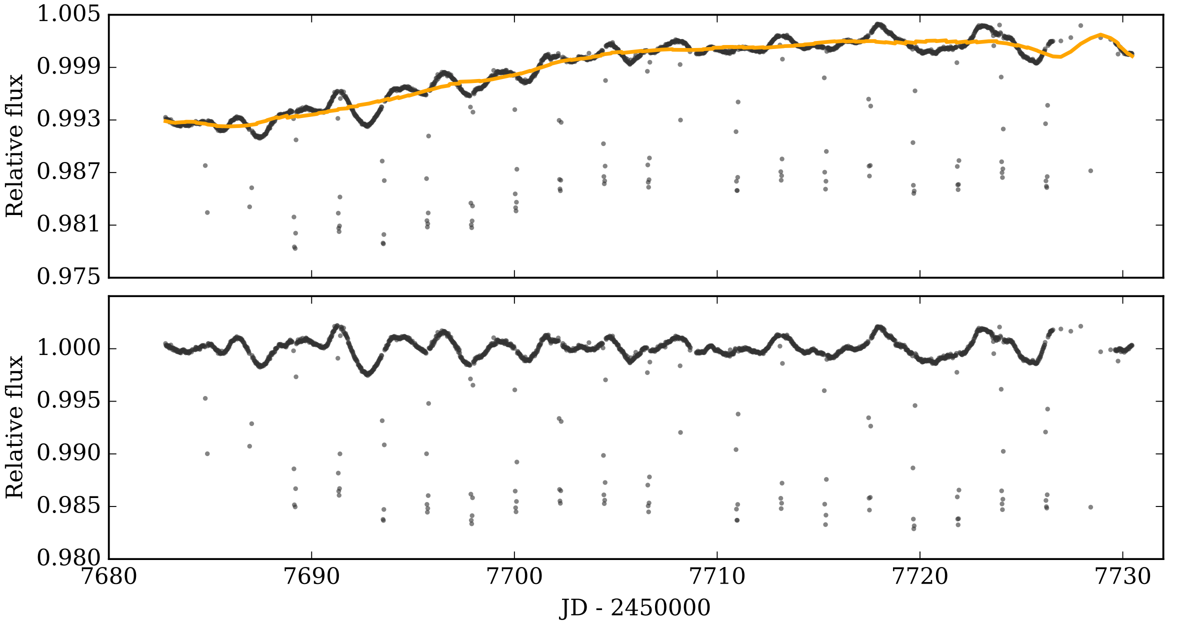

Figure 2.1: Top panel: Light curve of K2-237 (black), after detrend it with the EVEREST algorithm. The orange line represents the long term variations detected using the polynomial fitting explained in section 2.1.1. Bottom panel: Final light curve, with the long term variations removed.

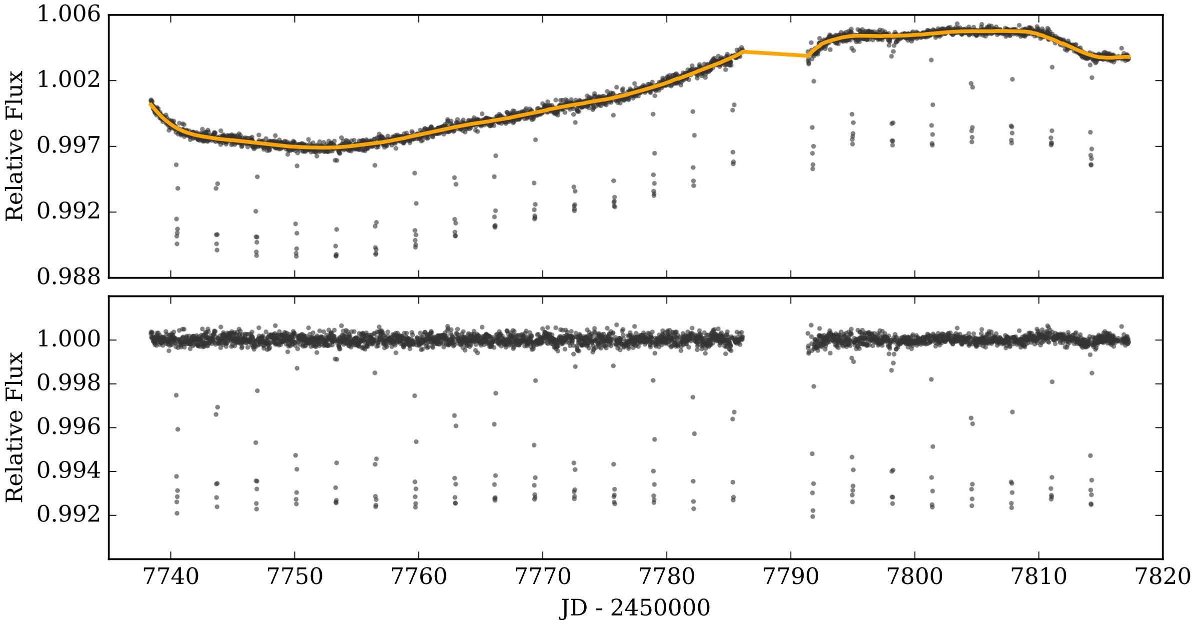

Figure 2.2: Top panel: Light curve of K2-238 (black), after detrend it with the EVEREST algorithm. The orange line represents the long term variations detected using the polynomial fitting explained in section 2.1.1. Bottom panel: Final light curve, with the long term variations removed.

Table 2.1: Stellar Parameters for both stars.

| Parameter | K2-237 | K2-238 | Source |
|---|---|---|---|
| R.A. (J2000) | 16:55:04.5 | 23:10:49.042 | |
| Dec. (J2000) | -28:42:38 | -07:51:27.00 | |
| $B$ | 12.19 ± 0.07 | 14.61 ± 0.10 | |
| $V$ | 11.60 ± 0.05 | 13.75 ± 0.02 | |
| $J$ | 10.51 ± 0.02 | 12.46 ± 0.03 | 2MASS |
| $H$ | 10.27 ± 0.02 | 12.10 ± 0.04 | 2MASS |
| $K$ | 10.22 ± 0.02 | 12.03 ± 0.03 | 2MASS |
| Distance (pc) | $458^{+196}_{-118}$ | $453^{+72}_{-46}$ | |
| Spectral type | F6V | G2V | |
| Mass ($M_{\odot}$) | $1.28^{+0.03}_{-0.04}$ | $1.19^{+0.08}_{-0.08}$ | $Y^2$ isochrones |
| Radius ($R_{\odot}$) | $1.43^{+0.06}_{-0.07}$ | $1.59^{+0.16}_{-0.16}$ | $Y^2$ isochrones |
| Density ($\rho_{\odot}$) | $0.102^{+0.012}_{-0.010}$ | $0.0550^{+0.0003}_{-0.0002}$ | $Y^2$ isochrones |
| $T_{\rm eff}$ (K) | 6257 ± 100 | 5630 ± 78 | ZASPE |
| [Fe/H] | 0.14 ± 0.05 | 0.34 ± 0.04 | ZASPE |
| $\log g$ (cm s$^{-2}$) | 4.24 ± 0.10 | 4.11 ± 0.07 | ZASPE |
| Age (Gyr) | $2.55^{+0.38}_{-0.44}$ | $5.63^{+1.05}_{-1.97}$ | $Y^2$ isochrones |
| $P_{\rm rot}$ (days) | 5.07 ± 0.02 | | Autocorrelation function |
| $v \sin i$ (km s$^{-1}$) | 11.76 ± 0.90 | 3.78 ± 0.57 | |

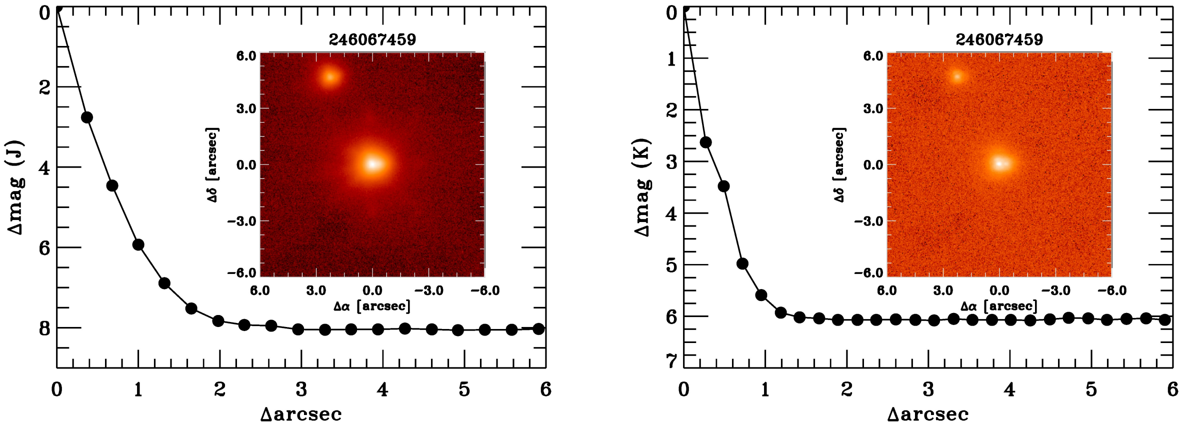

Figure 2.3: Contrast sensitivity curves obtained for K2-238, in the *J* (left panel) and *K* (right panel) bands, using ShaneAO at the Lick 3-m telescope. The plot represents the $5\sigma$ contrast limits, in $\Delta$ magnitude, plotted against angular separation in arcseconds. The insets in both figures show the image of the target.

### 2.1.2 Radial Velocity follow-up

Radial velocity follow-up data for K2-237 was acquired using the CORALIE spectrograph (Queloz et al. 2000), mounted on the 1.2m Euler Swiss Telescope at La Silla Observatory.

We obtained 9 observations between July 7th and July 11th 2017. For each one of the 4 consecutive nights, we acquired two observations of 1800 seconds each, achieving a signal-to-noise (S/N) ratio of $\sim$ 20. The spectra were reduced and analyzed using the CERES automated pipeline (Brahm et al. 2017a). The mean radial velocity uncertainty achieved for this target was $\sim 38\,\mathrm{m\,s^{-1}}$. The obtained radial velocities for each epoch are listed in Table B.1.

We also acquired 4 additional radial velocity data points using HARPS (Mayor et al. 2003), which is mounted on the ESO 3.6m telescope at La Silla Observatory. The data were taken during four consecutive nights, with one 1800 seconds exposure per night. The S/N achieved for these data is $\sim$ 32. The observations were later processed using the CERES pipeline, obtaining an uncertainty in the radial velocities of $\sim 25\,\mathrm{m\,s^{-1}}$. The HARPS velocities are listed in Table B.2.

For K2-238, 6 radial velocity measurements were obtained using FEROS (Kaufer et al. 1999), mounted on the 2.2m ESO/MPG Telescope at La Silla Observatory. The data was taken during five nights between November 6th and November 9th 2017, using exposures of 1500 seconds, and achieving S/N$\sim$ 32. The CERES automated pipeline was used to reduce and extract the radial velocities. The mean radial velocity uncertainty achieved with FEROS for this target is $16.5\,\mathrm{m\,s^{-1}}$. The velocities are listed in Table B.3.

### 2.1.3 High-resolution AO Imaging

Observations on the $J$ and $K$ bands for K2-238 (Figure 2.3) were taken on August 30, 2017, using the ShaneAO (Gavel et al. 2014) at the Lick 3-m Shane Telescope. A PSF of 0.328” and 0.236” were obtained for the $J$ and $K$ bands, respectively. The contrast measured at 0.5” from the center is of Δ2.76 and Δ3.48 magnitudes for both bands, respectively. A companion star is seen in both images at around $\sim 2.8''$ from our target (Figure 2.3).

The photometry was extracted for the resolved companion on both bands, with which we were able to estimate magnitude differences of $\Delta J = 2.2009 \pm 0.0015$ and $\Delta K = 2.0009 \pm 0.0053$ with respect to the brighter source, implying $J - K = 0.631 \pm 0.043$. Using this color, we use the Casagrande et al. (2010) color-temperature relations in order to derive a temperature of $T_{\text{eff}} = 4750 \pm 192$ K for the resolved companion, where the error incorporates the uncertainty on the metallicity of the companion (propagated assuming an uniform distribution for it between the validity of the color-temperature relation), the error on our color estimation and the dispersion on the relation itself, which includes uncertainty on the unknown value of $\log(g)$, and which assumes the companion is a dwarf or sub-giant star. We could also detect a second companion at 0.35” from our target. We used aperture photometry to deblend the K-band photometry, obtaining $K = 12.47 \pm 0.05$ and $13.2 \pm 0.1$ for the primary star and the companion, respectively. Deblending in the J-band was not possible to perform.

Using the relations from Howell et al. (2012), we transformed the 2MASS photometry for both stellar companions to the Kepler bandpass, obtaining a magnitude difference with respect to our target of $\Delta K_p = 2.9 \pm 0.8$ and $4.2 \pm 0.6$, for the stars at 0.35” and 2.8” away, respectively. We estimate a dilution correcting factor, using equation 15, of $1.04 \pm 0.03$ for the radius of the planet orbiting the primary star. This factor will be applied to the inferred radius, obtained after combining the light curve and radial velocity information.

We do not find any close companions to K2-237 at 5” from the source.

## 2.2 Analysis

### 2.2.1 Stellar Parameters

The atmospheric parameters ($T_{\text{eff}}$, logg and metallicity) for both stars we computed using the Zonal Atmospheric Parameters Estimator (ZASPE, Brahm et al. 2017b) code. ZASPE matches the observed stellar spectrum with a set of synthetic spectra generated from the ATLAS9 (Castelli and Kurucz 2004) model atmospheres. This procedure is performed via a global $\chi^2$ minimization, in a set of selected spectral regions. For K2-237 we used the co-added CORALIE spectrum, after correcting each individual spectrum by its radial velocity. We used the CORALIE spectra, over the co-added HARPS spectrum, due to the higher S/N obtained. For K2-238 we used the co-added FEROS spectra.

The physical parameters and evolutionary stages of both stars were obtained by interpolating

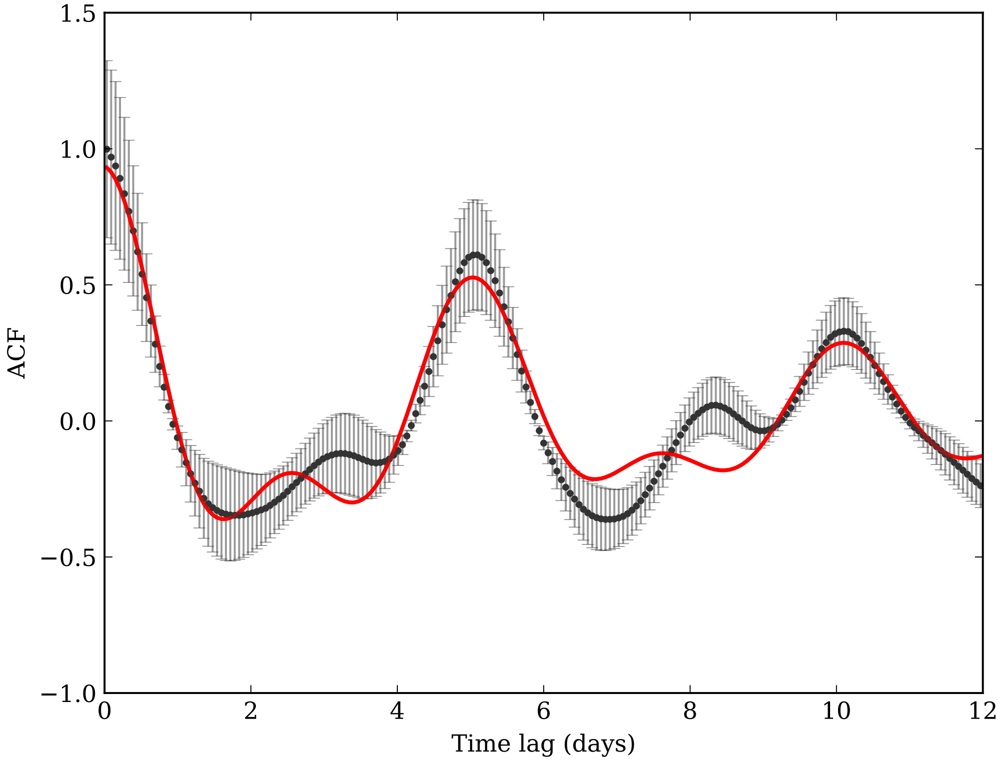

Figure 2.4: Autocorrelation function of the light curve (black dots), along with its uSHO fit (red line), in which the rotation period equals to 5.07 days.

through a grid of Yonsei-Yale isochrones (Demarque et al. 2004). We ran a Markov-Chain Monte Carlo (MCMC), using the `emcee1` Python package, to explore the parameter space, given by the observed properties of each star (Table 2.1). Using the metallicity value derived with ZASPE, we found the posterior distributions for the stellar age and mass. As observed parameters, we use the spectroscopic $T_{\text{eff}}$ and the $a/R_{\star}$ value obtained from the light curves (see section 2.2.3), which is a more precise proxy for the stellar luminosity than the spectroscopic $\log(g)$ (Sozzetti et al. 2007). The derived stellar parameters are listed in Table 2.1. Both stars have similar masses and are $\approx 25\%$ more massive than the Sun. While the parameters of K2-237 are consistent with being in the main sequence, the temperature, radius, and log(g) values of K2-238 show that it is slightly evolved. Additionally, both stars, in particular K2-238 ([Fe/H]=+0.34), are enriched in metals compared to the sun.

### 2.2.2 Rotational Period

For highly active stars, it is possible to measure the rotational period of a star from its light curve. If one assumes that the star's surface contains spots blocking part of its flux, then a periodic signal will be produced in its light curve, with a period related to the star's rotational period, and time scale of the order of the spots's mean lifetime. This effect, known as rotational modulation, can be spotted in the data of K2-237, easily seen in the light curve from Figure 2.1. The rotational period can then be measured by using the autocorrelation function (ACF), defined as the correlation of a signal with a delayed copy of itself, as a function of delay or time lapse. The autocorrelation is used in different field to detect periodic signals within noisy data. This method has been used with Kepler data in the literature (e.g. McQuillan et al. 2013; López-Morales et al. 2016; Giles et al. 2017b). For this analysis we used the final light curve obtained from Section 2.1.1, after detrending and removing the long term variation.

We produced the ACF by following the method described in Edelson and Krolik (1988), which allows for its computation with discrete and unevenly sampled data. In Edelson and Krolik (1988), the autocorrelation between two datapoints ($y_\mathrm{i}$, $y_j$), associated with the time lag $\Delta t_{\mathrm{i}j} = t_j - t_\mathrm{i}$, is computed as:

$$\mathrm{ACFi}, j = \frac{(y_\mathrm{i} - \hat{y})(y_j - \hat{y})}{\sqrt{\sigma_\mathrm{i}^2 \sigma_j^2}}, \tag{2.1}$$

where each datapoint has uncertainty $\sigma_\mathrm{i}$, and $\hat{y}$ is the inverse-variance weighted average of the dataset, defined as:

$$\hat{y} = \left(\sum_{\mathrm{i}=1}^{n} y_\mathrm{i}/\sigma_\mathrm{i}^2\right) / \left(\sum_{\mathrm{i}=1}^{n} 1/\sigma_\mathrm{i}^2\right) \tag{2.2}$$

This method is implemented in `astroML`[1] for Python-based computations. López-Morales et al. (2016) showed that the ACF follows a behaviour similar to that of an under-damped simple harmonic oscillator (uSHO):

$$y(t) = \mathrm{e}^{-t/\tau_\mathrm{AR}} \left[A \cos\left(\frac{2\pi t}{P}\right) + B \cos\left(\frac{4\pi t}{P}\right)\right] + y_0, \tag{2.3}$$

where $\tau_\mathrm{AR}$ is the spots decay timescale, $P$ is the stellar rotation period, both in units of days, and $y_0$ is a constant. In the equation are considered spots that are located in the opposite side of the star, and become visible at half the rotation period.

We fit equation 2.3 to our ACF using a least-square minimization, and obtained the following solutions: $\tau_{AR} = 9.0 \pm 0.6$ days, $P = 5.07 \pm 0.02$ days, $A = 0.59 \pm 0.02$, $B = 0.32 \pm 0.02$, and $y_0 = 0.02 \pm 0.01$. Therefore, these results provide a stellar rotational period of $P = 5.07 \pm 0.02$ days. The result is shown in Figure 2.4.

Before further analysis of the light curve to search for transit signals, we had to remove the effect of rotational modulation from the data. This was done through Gaussian Process (GP) analysis. A Gaussian process consists of a non-parametric approach to fitting a dataset, where multidimensional Gaussian distributions are used. GPs are used to study data with red noise components, meaning that there is a correlation among the datapoints. This correlation can be described by a kernel **K**.

**K** is a $n \times n$ matrix usually referred to as the covariance matrix, and each point $K_{\mathrm{i}j}$ describes the covariance between two points $y_\mathrm{i}$ and $y_j$. The probability distribution of a dataset, with each point

---

[1] `http://www.astroml.org/modules/generated/astroML.time_series.ACF_EK.html`

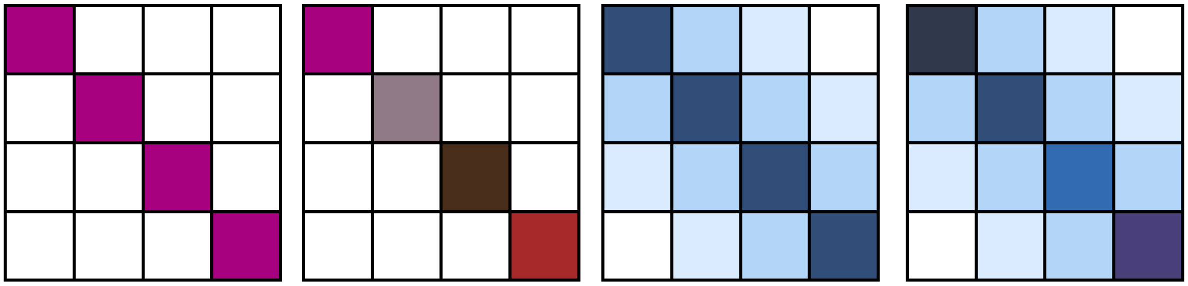

Figure 2.5: Four different examples of covariance matrices. From left to right: white noise with a constant variance, white noise with varying variance, red noise and constant variance, red noise and variable variance. From Haywood (2015), Figure 2.5.

related to the other by an amount described by the covariance matrix, will be:

$$P(y|\mathbf{K}) = \left(\frac{1}{2\pi}\right)^{n} \cdot \frac{1}{\sqrt{\det \mathbf{K}}} \cdot \exp\left[\frac{1}{2}(y-\mu)^{T}\,\mathbf{K}^{-1}(y-\mu)\right]. \tag{2.4}$$

Examples of different types of covariance matrices are shown in Figure 2.5. The diagonal of **K** describes the correlation of each point with itself, and will be given by the uncertainty of each measurement $\sigma_\mathrm{i}$. In the case where all the points $y_\mathrm{i}$ are independent from each other (white noise), then $K_{\mathrm{i}j}$ is a diagonal matrix, where $K_{\mathrm{i}j} = 0$ for $\mathrm{i} \neq j$ are zero, and the joint probability is then:

$$P(y) = \prod_{\mathrm{i}=1}^{n} P(y_\mathrm{i}), \quad \text{where } P(y_\mathrm{i}) = \frac{1}{\sigma_\mathrm{i}\sqrt{2\pi}} \exp\left[\frac{-(y_\mathrm{i}-\mu_\mathrm{i})^2}{2\sigma_\mathrm{i}^2}\right]. \tag{2.5}$$

A more extensive explanation of Gaussian Process regression, as well as the different types of kernels available, can be found in Rasmussen and Williams (2006) and Haywood (2015). Several works (e.g. Vanderburg et al. 2015; Aigrain et al. 2016; Angus et al. 2018) have shown that a Quasi-Periodic kernel can model sinusoidal variations in a dataset, with decay components. The Quasi-Periodic kernel is defined as:

$$k(t,t') = a^2 \exp\left[-\frac{(t-t')^2}{\theta_1^2} - \frac{1}{\theta_2^2}\sin^2\left(\frac{\pi(t-t')}{P}\right)\right], \tag{2.6}$$

where $a$ is the amplitude of the covariance function, $\theta_1$ is the time scale of the exponential decay, $\theta_2$ and $P$ are the amplitude and period of the sinusoidal component. We also included a white noise component to the kernel, of the form $\sigma_n^2\,\delta_{t,t'}$, where $\delta_{t,t'}$ is the Kronecker delta. The values obtained from the ACF analysis were used as priors for $P$ and $\theta_1$ (Haywood et al. 2014; López-Morales et al. 2016). The amplitude was set to be constrained by the amplitude of the data, and $\theta_2$ to be within 0.05 and 5.0, following Jeffers and Keller (2009). The priors and best-fit values for each quantity are listed in Table 2.2.

We used the `george`[2] implementation of GP analysis, along with the `emcee` package, to adjust this kernel to our data by performing a MCMC sampling. The posterior distributions for each

---

[2] `http://dan.iel.fm/george/current/`

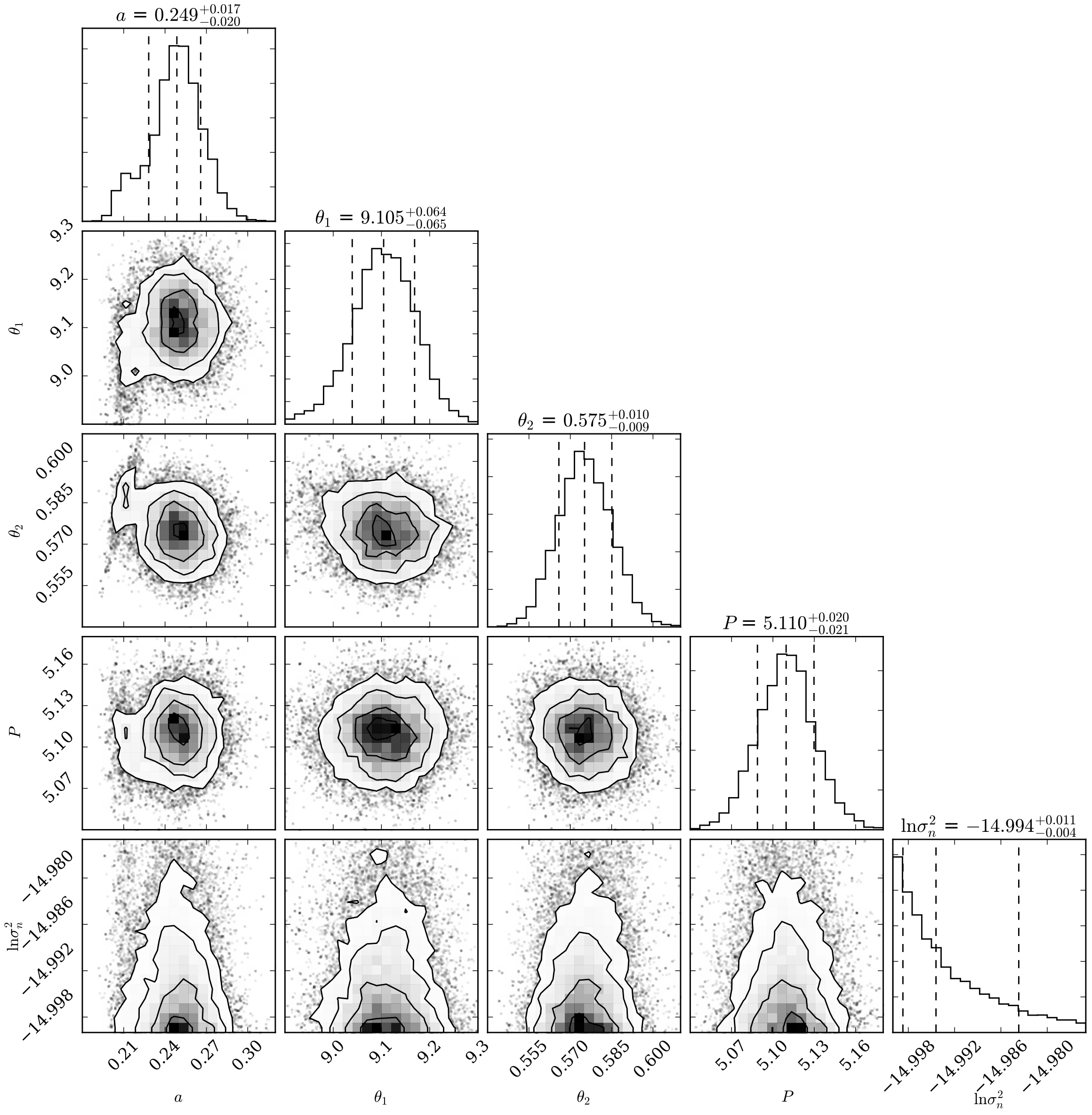

Figure 2.6: Posterior distributions of the parameters from the Quasi-periodic kernel (Equation 2.6). $a$ is the amplitude of the covariance function, $\theta_1$ is the time scale of the exponential decay, and $\theta_2$ and $P$ are the amplitude and period of the sinusoidal component. $\sigma_n$ corresponds to the amplitude of the white noise component.

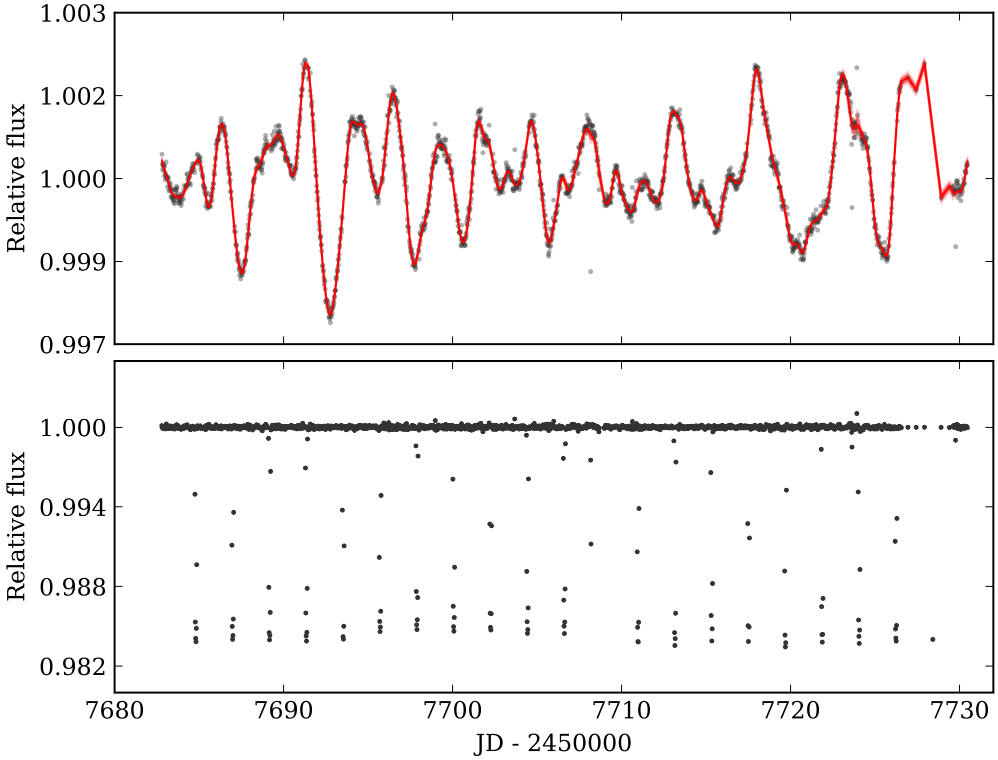

Figure 2.7: Top panel: Detrended light curve, with the transits masked out (black points). The red line represents the GP adjusted to the data, using the most probable hyper-parameters from the MCMC. Bottom panel: Final light curve, with the most probable GP fit removed.

Table 2.2: Priors and best-fit results obtained for the quasiperiodic kernel parameters. $\mathcal{N}(\mu, \sigma)$ represents a normal prior with with mean $\mu$ and standard deviation $\sigma$. $\mathcal{J}(a, b)$ represents a Jeffrey's prior with limits $a$ and $b$.

| Parameter | Prior | Best-fit value |
|---|---|---|
| $a$ | $\mathcal{J}(0.0001, 0.5)$ | $0.249^{+0.017}_{-0.020}$ |
| $\theta_1$ | $\mathcal{N}(9.0, 0.6)$ | $9.105^{+0.064}_{-0.065}$ |
| $\theta_2$ | $\mathcal{N}(0.5, 0.05)$ | $0.575^{+0.010}_{-0.009}$ |
| $P$ | $\mathcal{N}(5.07, 0.02)$ | $5.11^{+0.02}_{-0.02}$ |
| $\ln \sigma_n^2$ | $\mathcal{J}(-15, -6)$ | $14.994^{+0.011}_{-0.004}$ |

parameter of the Quasi-periodic kernel are shown in Figure 2.6. The final fit to the light curve is shown in Figure 2.7. The resulting light curve, without the effect of stellar rotation, was then used to derive the planet parameters for this star. Using the rotational period, with the stellar radius and the projected rotational velocity from Table 2.1, we obtain the rotational velocity and star inclination to be $v_{\rm rot} = 14.31^{+0.59}_{-0.67}\,{\rm km\,s^{-1}}$ and $\mathrm{i} = 51.56^{+3.73}_{-2.80}$ degrees. For K2-238, we could not measure the rotational period using this method because the signal from the stellar rotation embedded in the light curve was not as strong as with the other star. This might be due to it being a less active star.

### 2.2.3 Joint Analysis

In order to obtain a global solution for both systems, combining the photometry and radial velocity information, we used the `exonailer` code (Espinoza et al. 2016). `exonailer` is a tool that fits transit light curves, as well as radial velocity information, using a Bayesian approach to derive the most probable solution, for a given system, by using a set of priors for each one of the orbital and transit model parameters. For the case of the light curve, it uses the model from Mandel and Agol (2002), implemented in the batman[3] package (Kreidberg 2015). We used the quadratic limb-darkening law on both stars, which is the optimal one in our case following the algorithms and method detailed in Espinoza and Jordán (2016). As a remainder, the quadratic limb-darkening law is defined as:

$$I(\mu)/I(1) = 1 - u_1(1-\mu) - u_2(1-\mu)^2, \tag{2.7}$$

where $I(\mu)$ is the specific intensity of a star at $\mu = \cos\theta$, the cosine of the angle between the line of sight and the normal of the emerging intensity; $I(1)$ is the intensity at the centre of the star, and $u_{\rm i}$ are the limb-darkening coefficients.

The coefficients were sampled using the relations from Kipping (2013) for the quadratic law, where they define the new coefficients $q_1 = (\mu_1 + \mu_2)^2$ and $q_2 = \mu_1/(2(\mu_1 + \mu_2))$, both ranging from 0.0 to 1.0, and the limb-darkening coefficients can be recovered as $\mu_1 = 2\sqrt{q_1}q_2$ and $\mu_2 = \sqrt{q_1}(1 - 2q_2)$. We fitted for the limb-darkening coefficients instead of using modelled values, which has been shown to lead to important biases in the transit parameters (Espinoza and Jordán 2015). For the radial velocities, exonailer fits a Keplerian model, using the implementation from the radvel[4] package (Fulton et al. 2018). We fitted the data of K2-237 with both circular (e = 0.0) and non-circular (e >= 0.0) models, and obtained that the eccentricity of the non-circular model was consistent with zero. The Bayesian information criterium (BIC, Schwarz 1978) obtained for the circular orbit (BIC = -20.54) was also smaller compared with the non-circular one (BIC = -15.17), leading us to finally adopt a circular orbit for the system. The same was done for K2-238, where we also adopted a circular model. The priors used and the obtained distributions for each parameter, as well as the limb-darkening sampling coefficients $q_1$ and $q_2$, represented by the 16, 50, and 84% percentiles, are listed in Table 2.3. For K2-237, we used the light curve obtained in section 2.2.2, and shown in the bottom panel of Figure 2.7, with the effect of stellar rotation and long term variations removed. For K2-238, we used the detrended light curve obtained in section 2.1.1, and shown in the bottom panel of Figure 2.2. The transit and radial velocity solutions, given the posterior values from Table 2.3, are shown in Figure 2.8 and 2.9 for K2-237 and K2-238, respectively.

---

[3] `https://github.com/lkreidberg/batman`

[4] `http://radvel.readthedocs.io/en/latest/`

Table 2.3: Physical and orbital parameters for both planets, derived from the results from the `exonailer` run.

| | | K2-237 *b* | | K2-238 *b* | |
|---|---|---|---|---|---|
| Parameter | Unit | Prior[a] | Best-fit value[b] | Prior[a] | Best-fit value[b] |
| Period | days | $\mathcal{N}(2.18057, 0.1)$ | $2.18056^{+0.00002}_{-0.00002}$ | $\mathcal{N}(3.20466, 0.1)$ | $3.20466^{+0.00003}_{-0.00003}$ |
| $T_0$ - 2450000 | days | $\mathcal{N}(7684.8101, 0.1)$ | $7684.8101^{+0.0001}_{-0.0001}$ | $\mathcal{N}(7740.5036, 0.1)$ | $7740.5036^{+0.0004}_{-0.0004}$ |
| $a/R_\star$ | | $\mathcal{U}(1, 300)$ | $5.50^{+0.15}_{-0.11}$ | $\mathcal{U}(1, 300)$ | $6.27^{+0.66}_{-0.52}$ |
| $R_\mathrm{P}/R_\star$ | | $\mathcal{U}(0.001, 0.5)$ | $0.118^{+0.001}_{-0.002}$ | $\mathcal{U}(0.001, 0.5)$ | $0.080^{+0.003}_{-0.002}$ |
| i | deg | $\mathcal{U}(0, 90)$ | $84.3^{+0.7}_{-0.4}$ | $\mathcal{U}(0, 90)$ | $84.5^{+1.8}_{-1.5}$ |
| $q_1$[c] | | $\mathcal{U}(0, 1)$ | $0.15^{+0.10}_{-0.04}$ | $\mathcal{U}(0, 1)$ | $0.53^{+0.29}_{-0.22}$ |
| $q_2$[c] | | $\mathcal{U}(0, 1)$ | $0.69^{+0.21}_{-0.26}$ | $\mathcal{U}(0, 1)$ | $0.28^{+0.30}_{-0.15}$ |
| $\sigma_w$ | ppm | $\mathcal{J}(10, 500)$ | $128.2^{+2.8}_{-2.6}$ | $\mathcal{J}(10, 500)$ | $369.9^{+4.6}_{-4.6}$ |
| $K$ | $\mathrm{km\,s^{-1}}$ | $\mathcal{N}(0.3, 0.1)$ | $0.21^{+0.01}_{-0.01}$ | $\mathcal{N}(0.1, 0.1)$ | $0.10^{+0.01}_{-0.01}$ |
| e | | fixed | 0.0 | fixed | 0.0 |
| $\omega$ | deg | fixed | 90 | fixed | 90 |
| $\mu_\mathrm{CORALIE}$ | $\mathrm{km\,s^{-1}}$ | $\mathcal{N}(-22.3, 0.05)$ | $-22.27^{+0.03}_{-0.03}$ | | - |
| CORALIE jitter | $\mathrm{km\,s^{-1}}$ | $\mathcal{J}(0.0001, 1)$ | $0.09^{+0.03}_{-0.02}$ | | - |
| $\mu_\mathrm{HARPS}$ | $\mathrm{km\,s^{-1}}$ | $\mathcal{N}(-22.3, 0.05)$ | $-22.26^{+0.01}_{-0.02}$ | | - |
| HARPS jitter | $\mathrm{km\,s^{-1}}$ | $\mathcal{J}(0.0001, 1)$ | $0.002^{+0.015}_{-0.002}$ | | - |
| $\mu_\mathrm{FEROS}$ | $\mathrm{km\,s^{-1}}$ | | - | $\mathcal{N}(8.22, 0.05)$ | $8.26^{+0.01}_{-0.01}$ |
| FEROS jitter | $\mathrm{km\,s^{-1}}$ | | - | $\mathcal{J}(0.0001, 0.1)$ | $0.03^{+0.01}_{-0.01}$ |
| $M_\mathrm{P}$ | $M_\mathrm{Jup}$ | | $1.60^{+0.11}_{-0.11}$ | | $0.86^{+0.13}_{-0.12}$ |
| $R_\mathrm{P}$[d] | $R_\mathrm{Jup}$ | | $1.65^{+0.07}_{-0.08}$ | | $1.30^{+0.15}_{-0.14}$ |
| $\rho_\mathrm{P}$ | $\mathrm{g\ cm^{-3}}$ | | $0.44^{+0.08}_{-0.06}$ | | $0.56^{+0.25}_{-0.16}$ |
| $a$ | AU | | $0.037^{+0.002}_{-0.002}$ | | $0.046^{+0.007}_{-0.006}$ |
| $T_\mathrm{eq.}$ | K | | $1884^{+37}_{-36}$ | | $1587^{+75}_{-76}$ |
| $<F>$ | $10^9\ \mathrm{erg\,s^{-1}\ cm^{-2}}$ | | $2.86^{+0.23}_{-0.21}$ | | $1.44^{+0.29}_{-0.26}$ |
| $H$ | $10^8$ cm | | $1.06^{+0.13}_{-0.12}$ | | $0.93^{+0.21}_{-0.22}$ |

[a] $\mathcal{N}(\mu, \sigma)$ represents a normal prior with with mean $\mu$ and standard deviation $\sigma$. $\mathcal{U}(a, b)$ represents an uniform prior with limits $a$ and $b$. $\mathcal{J}(a, b)$ represents a Jeffrey's prior with limits $a$ and $b$.

[b] The values are shown as $B^{C-B}_{B-A}$, where $A$, $B$ and $C$ correspond to the 16, 50 and 84% percentiles.

[c] $q_1$ and $q_2$ are the sampling coefficients to fit for a quadratic limb-darkening law, defined in Kipping (2013).

[d] The planet radius for K2-238 *b* considers the transit depth and the dilution produced by nearby stars (section 2.1.3). The uncorrected radius was found to be $1.24^{+0.13}_{-0.14}\,R_\mathrm{Jup}$.

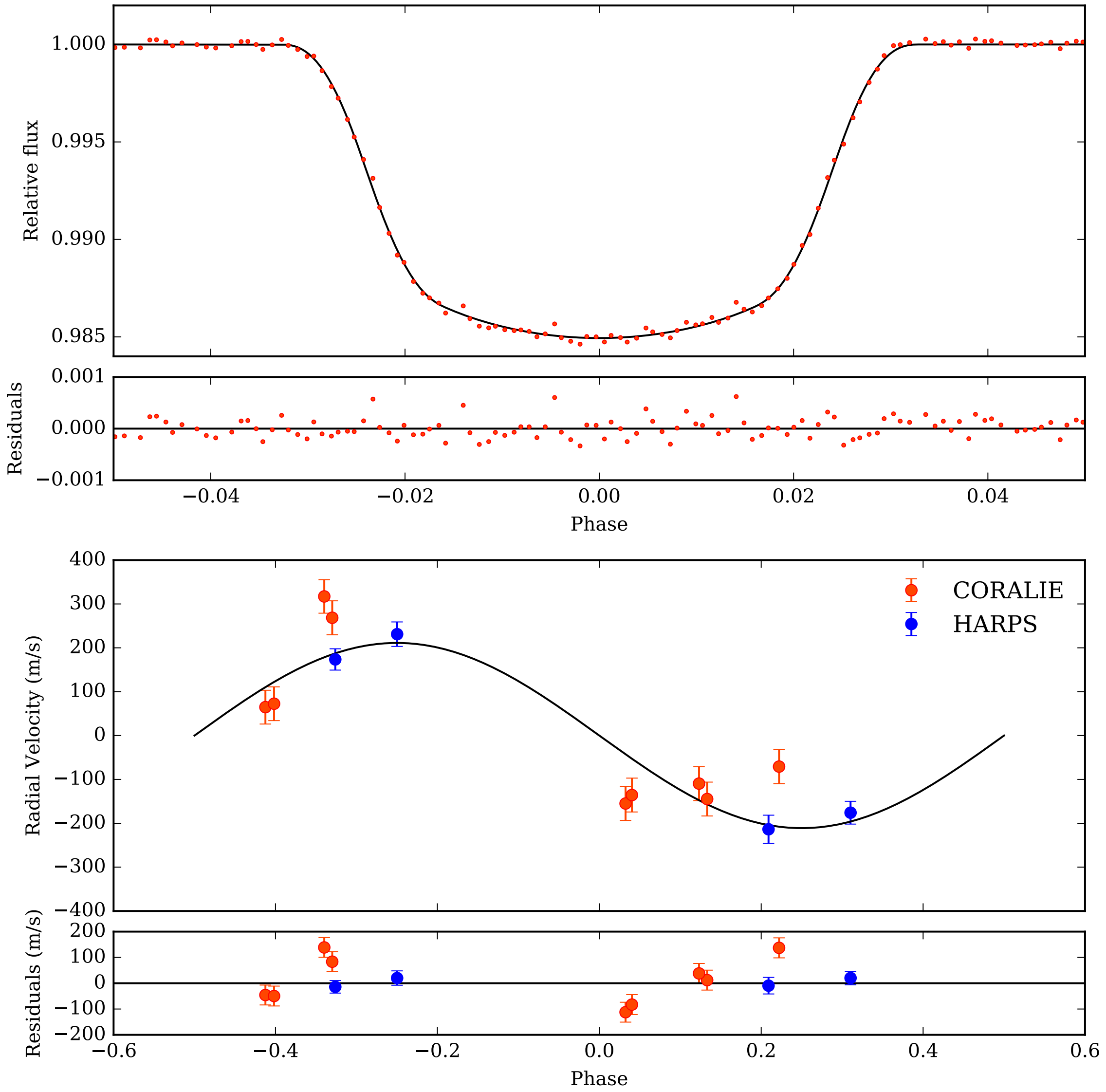

Figure 2.8: `exonailer` fit for K2-237. Top panel: Relative flux vs. orbital phase. Bottom panel: Radial Velocity data vs. phase, where red points represent Coralie, and blue points HARPS data. For both plots, the black lines represent the models with the most probable solution for the `exonailer` fit, with parameters listed in Table 2.3.

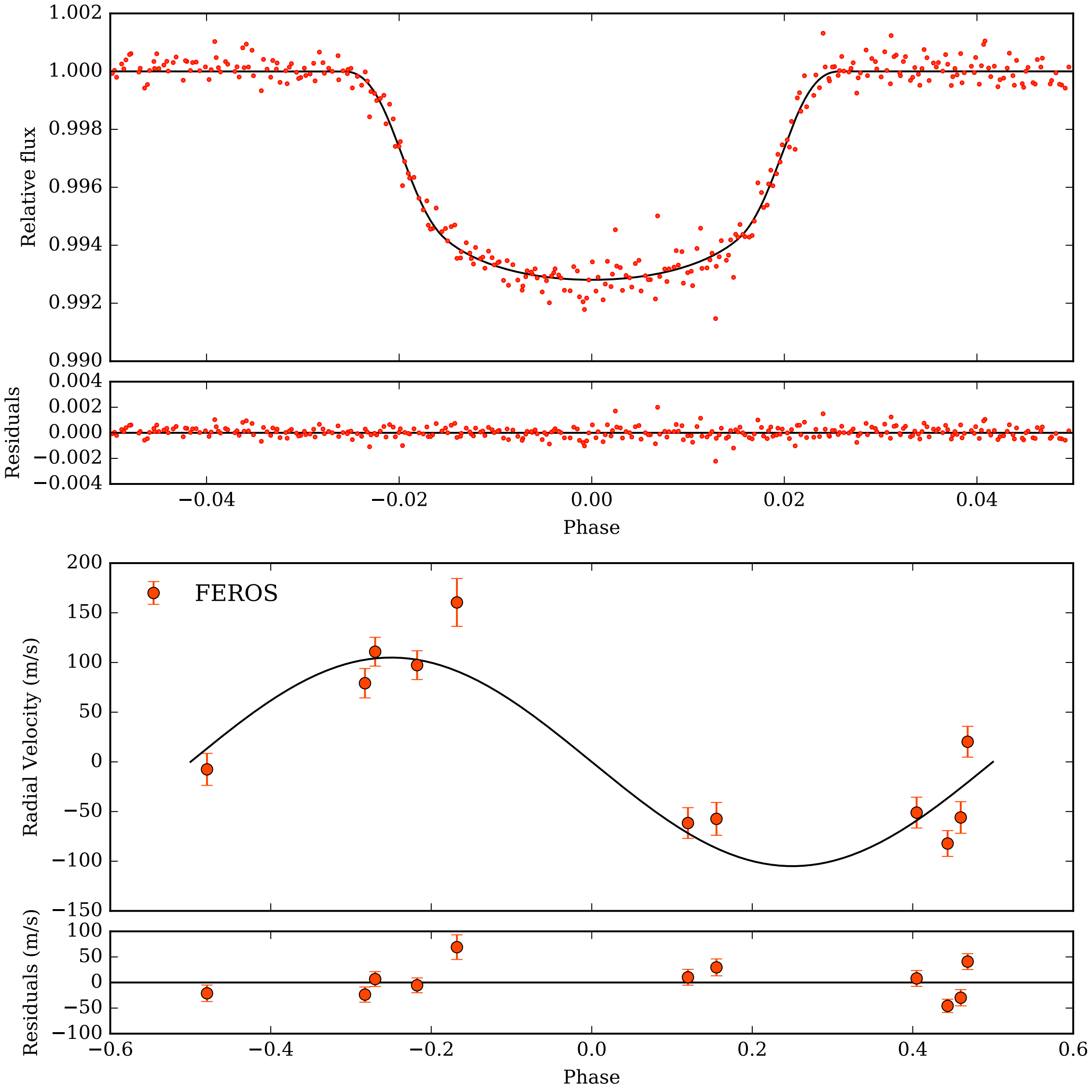

Figure 2.9: `exonailer` fit for K2-238. Top panel: Relative flux vs. orbital phase. Bottom panel: Radial Velocity data vs. phase, where red points represent FEROS data. For both plots, the black lines represent the models with the most probable solution for the `exonailer` fit, with parameters listed in Table 2.3.

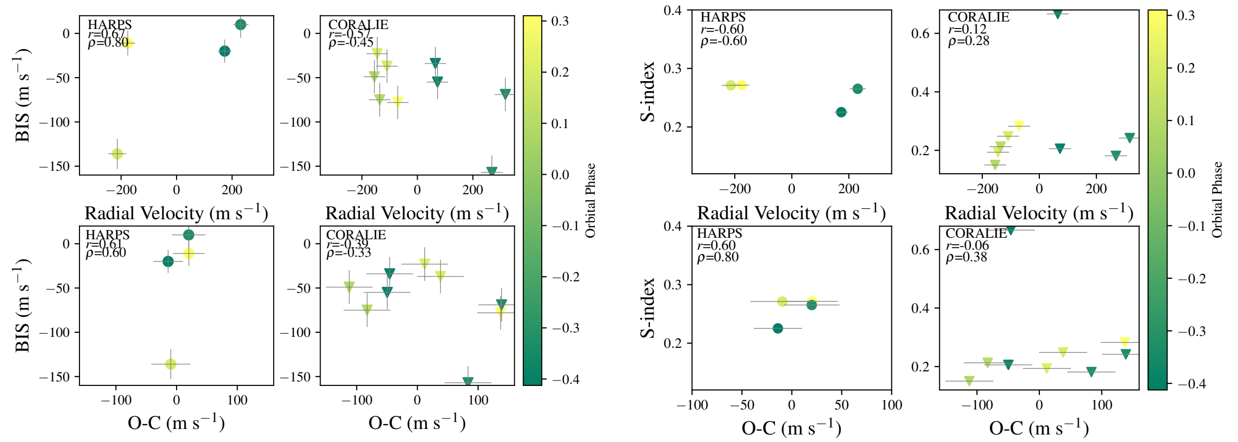

Figure 2.10: Correlations between the RVs (top panels) and the activity indices available from both HARPS (left panels) and CORALIE (right panels) for K2-237. The lower panels show the same correlations for the residuals from the fit. The colors represent the orbital phase of the RV and residuals. $r$ and $\rho$ are the Pearson and Spearman correlation coefficients, respectively.

Using the stellar mass and radius computed in Section 2.2.1, along with the values from Table 2.3, we estimate the planet mass and radius to be $1.60^{+0.11}_{-0.11}\,M_{\mathrm{Jup}}$ and $1.65^{+0.07}_{-0.08}\,R_{\mathrm{Jup}}$, respectively, for K2-237 *b*. For K2-238 *b*, we also had to consider the dilution in the transit depth produced by the two detected nearby companions. After correcting by this factor, we found the planet mass and radius to be $0.86^{+0.13}_{-0.12}\,M_{\mathrm{Jup}}$ and $1.30^{+0.15}_{-0.14}\,R_{\mathrm{Jup}}$, respectively. The orbit averaged stellar insolation was computed following

$$\langle F \rangle = \sigma T_{\mathrm{eff}}^4 \frac{R_\star^2}{a^2}\sqrt{\frac{1}{1-\mathrm{e}^2}}, \tag{2.8}$$

where $R_\star$ is the stellar radius, $T_{\mathrm{eff}}$ is the effective stellar temperature, $a$ is the semimajor axis, and e is the orbital eccentricity. The equilibrium temperature of the planet can be inferred as

$$T_{\mathrm{eq}} = T_{\mathrm{eff}}\sqrt{\frac{R_\star}{2a}}. \tag{2.9}$$

Here we have assumed zero Bond albedo and total planet redistribution of the stellar flux absorbed. The planetary atmospheric scale heigh is defined as

$$H = \frac{k\,T_{\mathrm{eq}}}{\mu\, m_H\, g}, \tag{2.10}$$

where $k$ is the Boltzmann's constant, $m_H$ is the mass of the hydrogen atom, $g$ is the planet's surface gravity, and $\mu$ is the average mass of an atmospheric particle, in units of hydrogen atom mass. In this work we assume that a hydrogen dominated composition. These quantities, along with other parameters, are summarized in Table 2.3.

### 2.2.4 Activity indicators

We measured a set of stellar activity indicators for both stars, in order to further confirm the planetary nature of the transit and radial velocity signals. For K2-237, we measured the Bisector Inverse

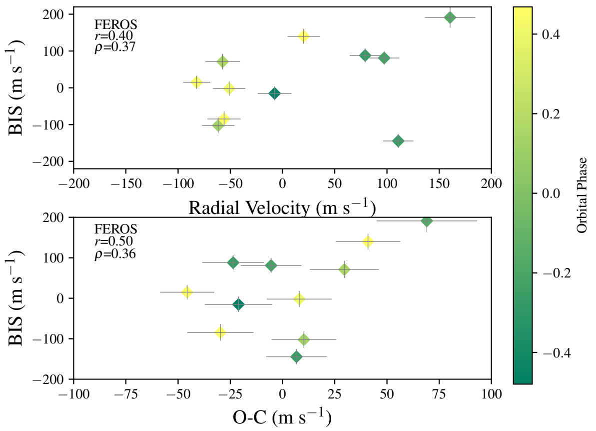

Figure 2.11: Correlations between the radial velocities (top panel) and the residuals from the planetary fit (bottom panel), with the BIS from FEROS for K2-238. The colors represent the orbital phase of the RV and residuals. $r$ and $\rho$ are the Pearson and Spearman correlation coefficients, respectively.

Span (BIS, Toner and Gray 1988; Queloz et al. 2001), and the Ca II H and K S-index (Jenkins et al. 2008, 2011b). We used two coefficients to determine the level of correlation between the activity indices and the radial velocities for each instrument, the Pearson ($r$) and Spearman ($\rho$) correlation coefficients. The difference between them is that the Spearman coefficient assesses how well two variables can be described using a monotonic function, which can be a linear or a non-linear relation, while the Pearson coefficient only assesses the correlation with a linear relationship. For both quantities, the standard limits set for weak, moderate, and strong correlation between two quantities are $|r_c| < 0.5$, $0.5 \leq |r_c| \leq 0.7$, and $0.7 < |r_c|$, respectively.

For the HARPS data, we obtain $(r, \rho)_{\mathrm{BIS}} = (0.67, 0.80)$, and $(r, \rho)_{\text{S-index}} = (0.60, 0.60)$, for the correlation between the BIS and the S-index with the RVs, respectively (Figure 2.10). These results would suggest that both coefficients are correlated with the RVs, but the number of points considered is too small to make any robust conclusions. We performed the same analysis with the residuals from the planetary fit (see Figure 2.8), and obtained $(r, \rho)_{\mathrm{BIS}} = (0.61, 0.60)$, and $(r, \rho)_{\text{S-index}} = (0.60, 0.80)$. This would also hint again at correlation with the activity indices, but as before, the number of points is too low to conclude whether this means there is moderate correlation between the quantities or not.

For the Coralie data, we find $(r, \rho)_{\mathrm{BIS}} = (-0.57, -0.45)$, and $(r, \rho)_{\text{S-index}} = (0.12, 0.28)$. For the BIS, the coefficients would suggest weak to moderate correlation with the RVs. We find that this correlation is powered only by one point (RV = 270 m s$^{-1}$, BIS = -157 m s$^{-1}$), and if we remove it, the correlation drops to $(r, \rho)_{\mathrm{BIS}} = (-0.24, -0.29)$. This reality is confirmed by a jacknife-like analysis that moved through the data, removing individual points and re-performing the correlation tests, highlighting that only when this outlying data point is removed does the correlation coefficient change. Too much statistical weight is being given to this one outlier. In fact, when we combine the HARPS and Coralie measurements, the coefficients also drop into the weakly correlated category, showing that stellar activity may be impacting the RVs, but only by adding random noise.

In the case of the correlation with the residuals from the planet fit we obtain $(r, \rho)_{\mathrm{BIS}} = (-0.39, -0.33)$, and $(r, \rho)_{\text{S-index}} = (-0.06, 0.38)$, which indicates no correlation among these quantities. These results, for the HARPS and Coralie data, can be seen in Figure 2.10, with the activity indices listed in Table B.1 and B.2.

We also performed the bisector analysis on K2-238, and found $(r, \rho)_{\text{BIS}} = (0.40, 0.37)$, which would indicate no correlation between the BIS and the FEROS RVs. For the residuals we found $(r, \rho)_{\text{BIS}} = (0.50, 0.36)$, also indicative of no strong correlation. The results are shown in Figure 2.11, and listed in Table B.3. We did not include the S-index due to the low S/N spectra obtained with FEROS, which prohibited us from measuring them reliably.

### 2.2.5 Planet scenario validation

In order to confirm the planetary nature of our photometric and spectroscopic measurements, we performed a blend analysis using the algorithms described in Hartman et al. (2011b,a), which model the observations taking into account the possibility that they could be generated by either a planet, stellar companions physically associated with our target star or by various blend scenarios, including blended eclipsing binary and hierarchical triple systems.

K2-237b is confirmed to be a planet based solely on the photometry; it is practically impossible for the best-fit blend scenarios to fit the observed photometry in any of the cases consistent with the spectroscopic information. For K2-238b, the planetary interpretation is also favored by the data: although there is a detected close-by companion in the Lick 3m AO data, the lightcurve is not consistent with the transit/eclipses arising from the neighbor, as all the simulated lightcurve signatures imply $J - K$ colors much less than the observed $J - K = 0.631 \pm 0.043$. Considering that the brighter source could still itself be a blend, we can reject all the blend scenarios at 2.5 sigma-confidence based on the photometry. However, none of them are able to produce the observed 100 m/s sinusoidal RV variation. The best-fit blend scenarios to the photometry also yield large bisector span variations in excess of 1 km/s, which are clearly ruled out by our measurements (see Figure 2.11). We consider thus both planets to be statistically validated given our photometric and spectroscopic measurements.

### 2.2.6 Searching for additional signals in the photometry

We reach for additional signals in our K2 light curves, produced by other companions, orbital phase variations, or secondary eclipses.

The search of signals from one or more companions was done by performing a BLS periodogram[5] on the light curves, with the transits of the detected planets removed. We find no significant peak in the BLS for both stars, which limits the transit depth of the possible additional companions to be less than 220 ppm and 250 ppm for K2-237 and K2-238, respectively, for a $3\sigma$ detection. We could not detect secondary eclipses in neither of the light curves. For K2-237 we had placed an upper limit for the depth of the eclipse to be $(R_{\text{p}}/a)^2 < 478$ ppm, so the fact we could not detect it points at the geometric albedo to be $A_{\text{g}} < 0.46$. This is in agreement with

---

[5] An implementation of this method, written in Python, is available at `https://github.com/dfm/python-bls`

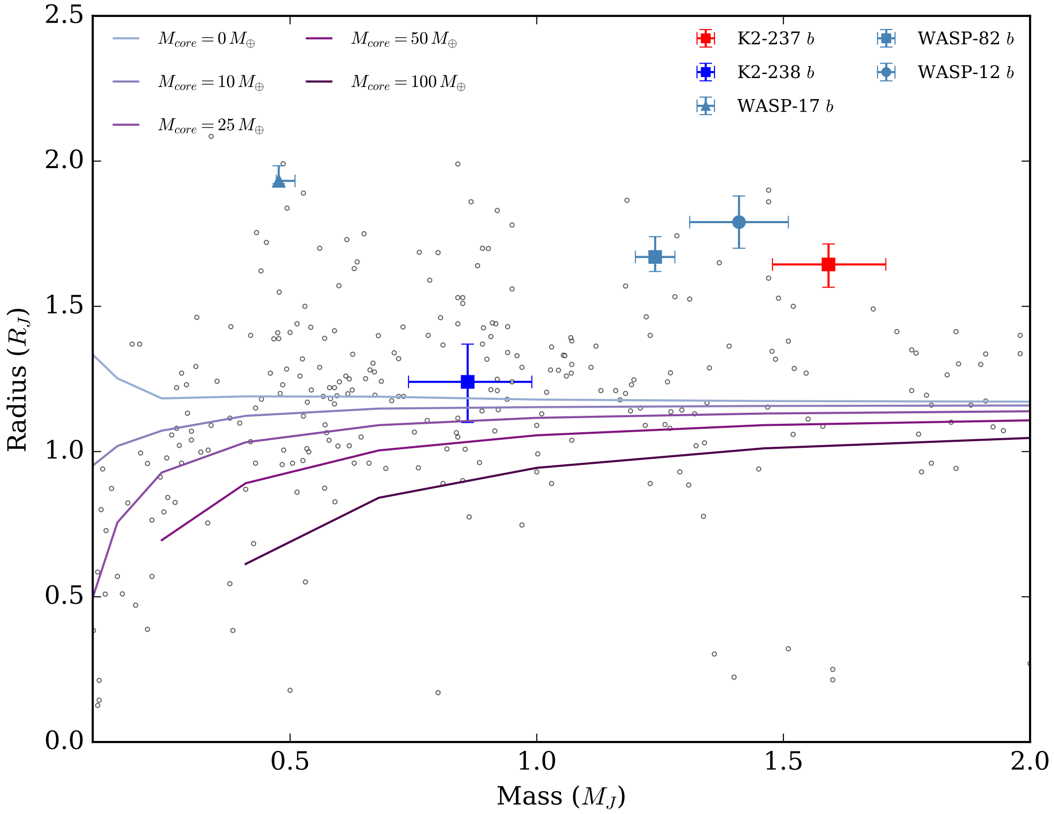

Figure 2.12: Mass-radius diagram. The red and blue squares represent the planets detected in this work. The lines represent models from Fortney et al. (2007), for hydrogen-helium dominated planets, at 0.02 AU from the parent star, and different values of core mass. Light blue symbols represent inflated and very dense hot Jupiters mentioned in the text. The white circles represent planets from the NASA Exoplanet archive, with known mass and radius values, orbital period less than 10 days, and masses within 0.1-2.0 $M_{\mathrm{Jup}}$.

what has been found for hot Jupiters (Heng and Demory 2013; Esteves et al. 2015). For K2-238, it comes to no surprise that we could not detect its eclipse, given that its depth would have been $(R_\mathrm{p}/a)^2 < 163$ ppm, which is bellow the limit detection in the data. We could not detect orbital phase variations in neither of the light curves.

## 2.3 Discussion

We compared the mass and radius of both planets with the models from Fortney et al. (2007), for hydrogen-helium dominated planets, with different amounts of metal compositions (represented by the core mass). We found for K2-237 *b* that the radius is significantly higher than expected for the given mass (0.5 $R_{\mathrm{Jup}}$ larger than the model for a 4.5 Gyr-old planet with semi-major axis of 0.02 AU and no core). This is shown in Figure 2.12. We looked at the confirmed planets list from the NASA

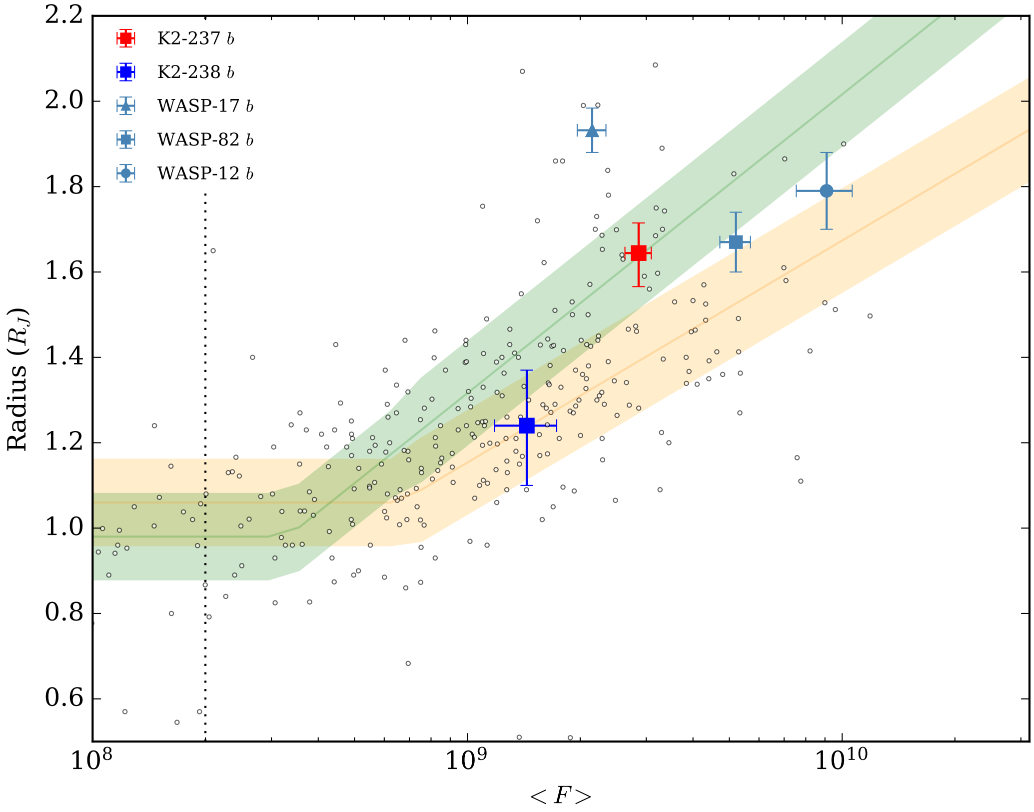

Figure 2.13: Radius vs. planet incident flux. The red and blue squares represent the planets detected in this work. The light blue markers and white circles represent the same systems as in Figure 2.12. The vertical dotted line represents the flux threshold $2 \times 10^8$ erg s$^{-1}$ cm$^{-2}$, above which planets have been found to be inflated. The shaded areas represent the relations from Sestovic et al. (2018) for $M = 0.37 - 0.98\,M_{\rm Jup}$ (green) and $M = 0.98 - 2.50\,M_{\rm Jup}$ (orange), and their $1\sigma$ confidence levels.

Exoplanet Archive[6], and found that K2-237 *b* falls into a region of highly inflated hot Jupiters that is as yet not very well populated. We also compared the planet with other cases of highly inflated hot Jupiters, like WASP-17 *b* (Anderson et al. 2010), WASP-82 *b* (West et al. 2016), and WASP-12 *b* (Hebb et al. 2009). These planets have shown to be good cases to perform atmospheric studies, which makes K2-237 *b* a good laboratory for studying the atmospheres of highly inflated planets as well. For K2-238 *b*, we find its radius to be consistent with the models of Fortney et al. (2007) for a hydrogen and helium dominated planet with a core mass up to 25 $M_\oplus$, at the $1\sigma$ level.

As was mentioned in the introduction, some studies trying to detect the source of planetary inflation point at correlations between the planet's incident flux and radius (e.g. Demory and Seager 2011; Laughlin et al. 2011), and have detected an incident flux threshold $F_\mathrm{i} = 2 \times 10^8\,\mathrm{erg\,s^{-1}\,cm^{-2}}$, above which inflation is found to happen. Both of our planets fall above this threshold as shown in Figure 2.13, which suggests inflation is shaping the observed radius of our newly discovered exoplanets. We see that K2-237 b is considerably larger than what theoretical models predict for a H/He dominated planet, receiving high radiation levels. In the case of K2-238 *b*, its mass and radius seem to be consistent with it not-being inflated, even though it receives a high incident flux (Fig. 2.13). We also compared the two planets from this work with the models of radius against incident flux and mass by Sestovic et al. (2018). Here we see again see that K2-237 b appears to be even more inflated than what the model from Sestovic et al. (2018) predicts ($M_\mathrm{p}$ = 0.98–2.50 $M_\mathrm{Jup}$, orange area in Figure 2.13). We also find that the scale height estimated for this planet (see Table 2.3) is comparable to those of systems currently targeted for atmospheric characterization (e.g., WASP-12b, with $H \sim 1100$ km, Burton et al. 2015). The latter, and given that the planet orbits a bright host star, again makes K2-237 b appear to be an excellent candidate for follow-up studies. For K2-238 *b*, we see that its radius is consistent with a non-inflated planet of mass within $0.37 - 0.98\,M_\mathrm{Jup}$ within $1\sigma$ (represented by the flat part of the green region in Figure 2.13).

Jenkins et al. (2017) show that gas giant planets with orbital periods less than 100 days orbit stars that are significantly more metal-rich than their counterparts that host longer period giant planets. Furthermore, they also discovered a difference in the host star metallicity of Jupiter-mass planets and super-Jupiters, whereby the Jupiter-mass planets orbit stars significantly more metal-rich than those with significantly higher masses. This result was later confirmed at higher statistical significance by Santos et al. (2017). The very short period systems detected in this work also seem to orbit very metal-rich stars, and although the less massive of the two, K2-238 *b*, is still classed as a Jupiter-mass gas giant for the purposes of the metallicity-mass relationship discovered by Jenkins et al., it is intriguing that it orbits a significantly more metal-rich star than K2-237 *b*.

## 2.4 Summary

We present the discovery of two new hot Jupiters from our Chilean K2 project that aims to detect new planets in the southern fields of the K2 mission. For K2-237 *b*, our best solution is consistent with a hot Jupiter planet with a $R = 1.65\,R_\mathrm{Jup}$, orbiting its host star in a period of 2.2 days. Its radius makes it a highly inflated hot Jupiter, and when coupled with the brightness of the host, it makes an excellent candidate for further atmospheric studies.

---

[6] `https://exoplanetarchive.ipac.caltech.edu/index.html`

K2-238 *b*, on the other hand, appears to have a mass similar to that of Jupiter, a radius of $R = 1.30\,R_{\rm Jup}$, and orbital period of 3.2 days. Even though this planet is in the regime where planetary inflation is important, it was found to have a radius consistent with theoretical models for H/He dominated objects.

# Chapter 3

# SPECIES: Spectroscopic Parameters and atmosphEric ChemIstriEs of Stars

The characterisation of exoplanetary systems has become a booming field of study in astronomy over the last 20 years, thanks to the large amount of detections provided by different surveys from different telescopes and instruments (CORALIE, Keck, HARPS, AAT, WASP, Kepler, K2, etc). Unfortunately, the low surface brightness and size of planets compared to their host star, makes them extremely difficult to study directly, therefore it is necessary to study the behaviour and physical parameters of the host stars in order to better characterise their planetary companions. These parameters include the temperature, metallicity, surface gravity, mass, and age, which in turn gives us an estimate of their evolutionary stages.

Calculation of the stellar bulk parameters, like temperature, metallicity and mass, is vital to derive the physical characteristics of the companions. Just as was mentioned in the introduction, the minimum mass of the planetary candidates can be obtained by the amplitude of the star's radial velocity, which in turn depends on the mass of the host star, among other parameters. Planetary sizes can be inferred by studying the decrease in brightness of the host star when the planet transits, which in turn depends on the diameter of the star. By knowing the mass and physical size of a planetary companion, it is possible to understand its chemical composition, since the planet bulk density can be calculated. This information, combined with the knowledge of the stellar effective temperature ($T_{\mathrm{eff}}$) and the orbital distance of the planet, allows a probability to be placed on the likelihood that the planet has liquid water in its atmosphere, and/or on its surface. Knowledge of the stellar parameters is also needed in order to study the formation of planetary companions (Fischer and Valenti 2005; Buchhave et al. 2012; Jenkins et al. 2013a), how the system has evolved to its current stage (Ida and Lin 2004, 2005; Mordasini et al. 2012), and how the subsequence evolution of the host star will affect the planetary system (Villaver and Livio 2009; Kunitomo et al. 2011; Jones et al. 2016).

The derivation of stellar parameters is not something new in astrophysics. Many works have dealt with this task, employing different methods in order to obtain them. The most common methods in the literature are using equivalent width (EW) measurements (e.g. Edvardsson et al. 1993; Feltzing and Gustafsson 1998; Santos et al. 2004; Bond et al. 2006; Neves et al. 2009), and the spectral synthesis approach (e.g. Valenti and Fischer 2005; Jenkins et al. 2008; Pavlenko et al.

2012). The results produced by different methods show significant systematic differences (Torres et al. 2012; Ivanyuk et al. 2017), which then can affect the physical characteristics of any detected companions. When the values for the stellar parameters are retrieved from different sources, it can lead to problems when studying populations of stars. This is often necessary because not all catalogues of stellar parameters have all the quantities needed, or uncertainties in the values are not listed, making it difficult to implement them in other studies (e.g. see the analysis presented in Jenkins et al. 2017). Another barrier that one finds when studying stellar parameters is that most works are limited to the stars included in their resulting catalogues, making it difficult to compute parameters for new stars in a homogeneous way. All of these issues were behind the development of the SPECIES code, an open source method that can compute stellar parameters for large numbers of stars in a homogeneous and self-consistent fashion, and crucially, that is publicly available to the scientific community[1].

The SPECIES code is written mostly in the python programming language, making use of some previously developed software (e.g. `MOOG`, Sneden 1973; `ARES`, Sousa et al. 2007) that allows automatic calculations of specific jobs to be performed, with the goal of increasing the speed of the process whilst subsequently decreasing the user input for the derivation of the stellar parameters. The code is automated in the computation of all the parameters, and the only input from the user is a high resolution spectrum of the desired star. It can be used with only one star at a time, or several stars at once running in parallel. This makes it possible to derive the parameters for large samples of stars, a necessity in this new era of exoplanet surveys (e.g. NGTS, ESPRESSO, TESS, etc), with the number of planetary candidates increasing each month.

The structure of this chapter is as follows. Section 3.1 explains the inputs needed to run the code, and its final output. Here we also list the atomic lines used (subsection 3.1.1), we explain in detail the derivation of the atmospheric parameters and their corresponding uncertainties (subsections 3.1.4 and 3.1.5, respectively), the stellar mass, radii and age (subsection 3.1.6), the chemical abundances of different elements (subsection 3.1.7), and the computation of the macroturbulence and rotational velocity (subsection 3.1.8). Section 3.2 shows the results obtained using our code for a sample of 522 stars, how those values compare to others in the literature (subsection 3.2.2), and the difference obtained when using spectra from different instruments (subsection 3.2.4). In subsection 3.2.3 we show the correlations between the parameters that we find in our results. Finally, in Section 3.3 we give a summary of the characteristics and use of SPECIES and how we plan to continue to develop the code in the future.

The work presented in this chapter has been accepted for publication in A&A, and is available at Soto and Jenkins (2018).

## 3.1 Stellar parameter computation

SPECIES is an automatic code that computes stellar atmospheric parameters in a self-consistent and homogeneous way: effective temperature, surface gravity, metallicity with respect to the Sun, and microturbulent velocity ($T_{\rm eff}$ , $\log g$ , [Fe/H], and $\xi_t$ respectively). Our code also derives chemical abundances for 11 additional atomic elements, rotational and macroturbulence velocity, along with

---

[1] `https://github.com/msotov/SPECIES/`

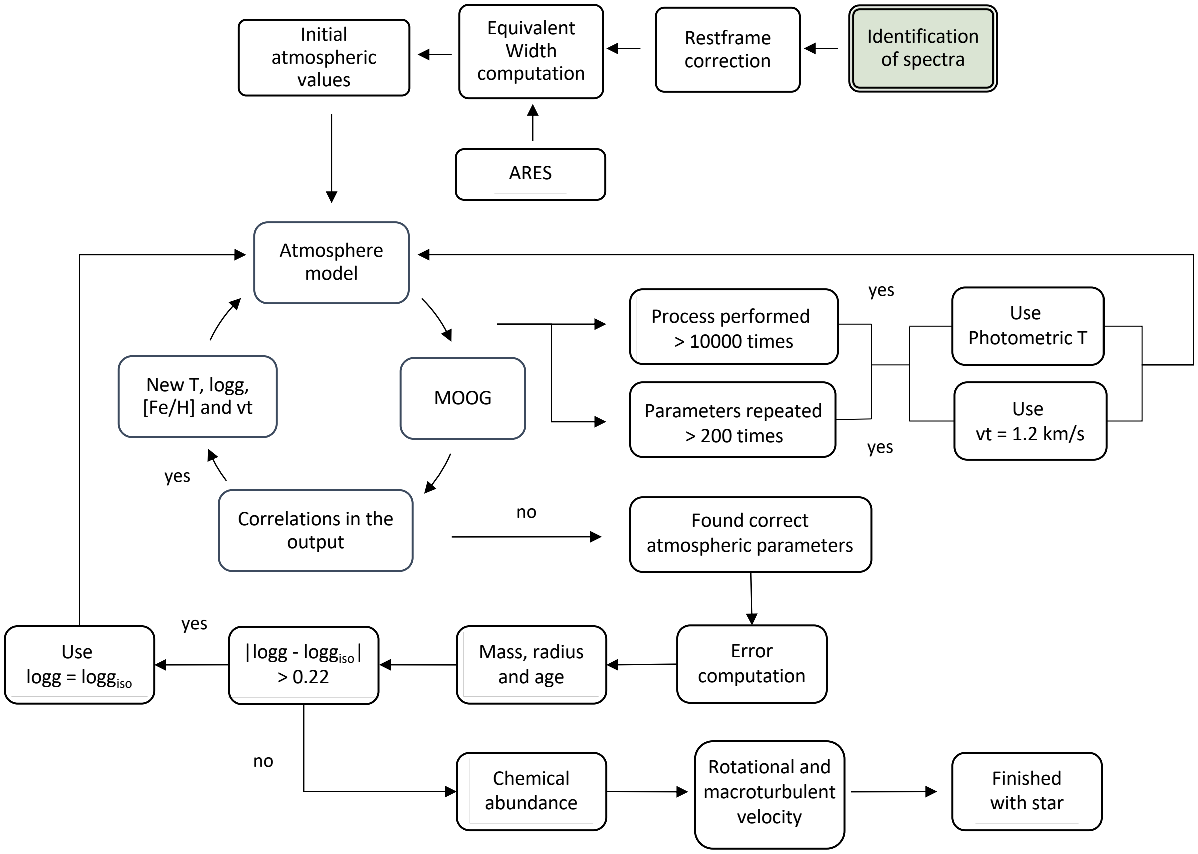

Figure 3.1: Flow diagram showing the process sequence of SPECIES. Each step is explained in Section 3.1. The green box represents the beginning of the diagram.

stellar mass, age, radius, and photometric log g . The uncertainties of each parameter are also computed in a consistent way, dealing with parameter correlations and propagation of uncertainties, all of which will be discussed in the following sections.

The inputs needed for our code to perform all computations are:

- A high resolution (R > 40000) spectrum. It handles spectra acquired with HARPS (High Accuracy Radial velocity Planet Searcher Mayor et al. 2003), FEROS (Fiber-fed Extended Range Optical Spectrograph, Kaufer et al. 1999), UVES (Ultraviolet and Visual Echelle Spectrograph, Dekker et al. 2000), HIRES (High Resolution Echelle Spectrometer Vogt et al. 1994), AAT (Anglo-Australian Telescope, Tinney et al. 2001) and Coralie instruments (Queloz et al. 2000). The spectra do not need to be normalised, because then will be locally normalised when measuring the equivalent widths (section 3.1.2). The optimal wavelength range should go from 5500 to 6500 Å, or cover most of this range. It is not necessary for the spectra to have continuous wavelength coverage, except for the regions where included iron lines are located (Table C.1). A minimum of 15 Fe I lines and 5 Fe II lines should be present in the input spectrum.

- Coordinates. They can be input by the user, retrieved from the fits header of the spectra, or retrieved from the following catalogues: 2MASS (Cutri et al. 2003), GAIA DR2 (Gaia Collaboration et al. 2016), the Hipparcos catalogue (van Leeuwen 2007), or the Tycho-2 Catalogue (Hog et al. 2000).

- Parallax data. It can be input by the user, but otherwise it will be automatically retrieved from the GAIA DR1 (Gaia Collaboration et al. 2016), or from the Hipparcos catalogue (van Leeuwen 2007).

- Apparent magnitudes for each star. These can be either given by the user, or they can be retrieved from the following catalogues: 2MASS (Cutri et al. 2003) for the $JHKs$ bands, Tycho-2 Catalogue (Hog et al. 2000) for the Tycho-2 $(BV)t$ magnitudes, Hauck and Mermilliod (1998) or Holmberg et al. (2009) for Strömgren $b-y$, $m_1$, and $c_1$, and Koen et al. (2010), Casagrande et al. (2006), Beers et al. (2007), or Ducati (2002) for the Johnson $BV(RI)c$ magnitudes.

All the data from these catalogues were obtained using Vizier[2]. Other files used by SPECIES, like the atomic line list and binary masks are included in the SPECIES package.

A diagram showing a representation of the process followed by SPECIES to derive all the stellar parameters is shown in Figure 3.1. Each step of the computation will be explained in the next sections.

---

[2] `http://vizier.u-strasbg.fr`

### 3.1.1 Atomic line selection

We selected all of the lines used in our analysis from the Vienna Atomic Line Database version 3 (VALD3, Piskunov et al. 1995; Kupka et al. 1999; Ryabchikova et al. 2011). The lines were selected based on comparing the line database to a HARPS solar spectrum to ensure they appeared strong and clearly detectable at the resolution offered by HARPS (we note that the macroturbulence of the solar envelope ensures that the spectra have an effective resolution $R$ of around 70'000). We also note that the lines were cross-validated by literature searches, since each of the lines has previously been employed in atomic abundance calculations by other teams using different methods. The parameters drawn from the VALD3 catalogue for each of these lines are the excitation potential ($\chi_l$), central rest wavelengths, and oscillator strengths (loggf). The final line lists contain 149 Fe I lines and 21 Fe II lines, along with 6 (Na I), 4 (Mg I), 3 (Al I), 22 (Si I), 14 (Ca I), 22 (Ti I), 3 (Ti II), 37 (Cr I), 8 (Mn I), 52 (Fe I), 15 (Fe II), 24 (Ni I), 4 (Cu I), and 1 (Zn I) lines. We show all data for the iron lines used in the computation of the atmospheric stellar parameters in Table C.1, and for the lines used in the computation of the chemical abundances in Table C.2.

### 3.1.2 Equivalent width computation

The EWs were measured using the ARES code (Sousa et al. 2007, 2015). The input required by ARES is a one-dimensional spectrum and a line list. For each line, the code performs a local normalisation, over a window of 4Å across the line centre. The normalisation is done by adjusting a third-order polynomial to that portion of the spectrum, and selecting only the points laying above $rejt$ times the obtained fit. This process is repeated three times, and the final local continuum is subtracted from the data. $rejt$ is computed per spectrum, and depends on the signal-to-noise of the data, where large ($\sim 1$) values would correspond to high S/N. We use the S/N given in the image header, and when that is not provided, we compute it as the median of the S/N for different portions of the spectra, free of absorption lines. More information about this parameter can be found in Sousa et al. (2007). For the computation of the atmospheric parameters, we only consider lines with EWs in the range $10 \leq \text{EW} \leq 150$ mÅ, in order to avoid lines too weak that could be affected by the continuum fitting, and lines too strong for which the LTE approximation might no longer be valid. We also discarded the lines for which $\sigma_{\text{EW}}/\text{EW} > 1$, where $\sigma_{\text{EW}}$ is the error in the EW measured with ARES. We note that for these rejected lines, the Gaussian fit performed by ARES is not accurate enough, leading to an incorrect computation of the stellar parameters. We also perform a restframe correction in all our spectra before computing the EW of the lines. This was done by cross-correlating (Tonry and Davis 1979) a portion of the spectrum, between 5500 Å and 6050 Å, with a G2 binary mask within the same wavelength range. The wavelength was then scaled as $\lambda = \lambda_o/(1 + v/c)$, where $\lambda_o$ is the observed wavelength, $v$ is the derived velocity of the star that SPECIES computes using a cross-correlation method, and $c$ is the speed of light. This spectrum will be used for the rest of the calculations. One example of this cross-correlation function (CCF) and subsequent velocity correction is shown in Figure 3.2. We have made sure that the instruments accepted by our code have a wavelength coverage that is wide enough so that the region of the spectra used for the restframe correction is included.

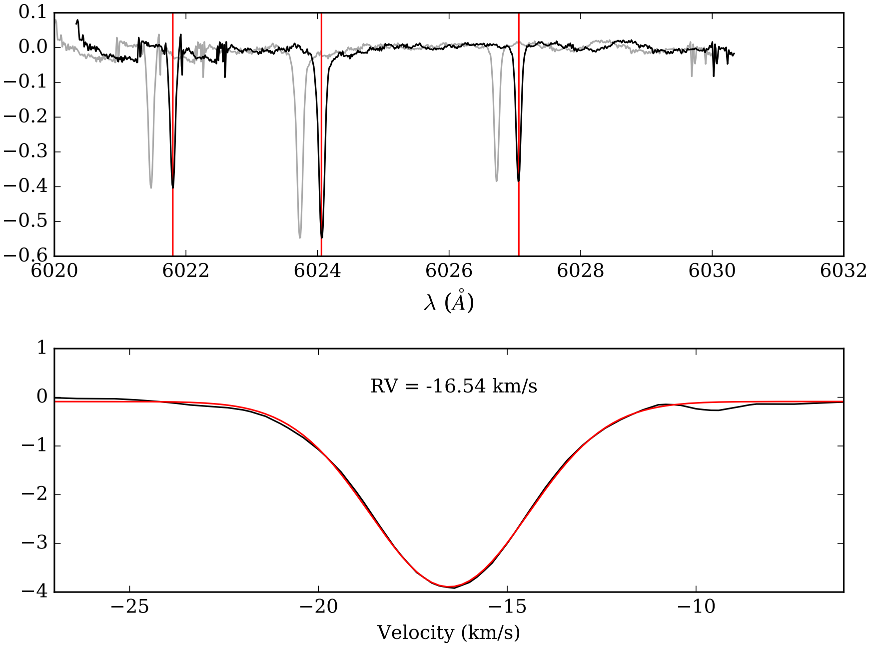

Figure 3.2: Restframe correction applied to HD10700. Top panel: Original spectra (grey), corrected spectra (black), and three reference lines at 6021.8, 6024.06, and 6027.06 Å (red). Bottom panel: Cross-correlation function (CCF) between the binary mask and the spectra. The red line corresponds to the Gaussian fit to the CCF, with a mean equal to -16.54 km $s^{-1}$.

### 3.1.3 Initial conditions

Initial values for the atmospheric parameters ($T_{\mathrm{eff}}$ , log g , [Fe/H]) are needed for their subsequent derivation through SPECIES, in a manner which will be explained in the next section. The initial conditions can be input by the user, or can be derived from the photometric information for each star.

In the case that the photometric magnitudes are retrieved from existing catalogues, they first should be corrected for interstellar extinction. We use the coordinates and parallax, along with the interstellar maps from Bovy et al. (2016, which are a combination of the maps from Drimmel et al. 2003; Marshall et al. 2006; Green et al. 2015), to obtained $E(B-V)$. In the cases when no parallax information is available, we use the maps from Schlegel et al. (1998). The extinction in each band, $A_\lambda$, was obtained using $R_V = 3.1$ and the re-scaling from Schlafly and Finkbeiner (2011, Table 6). The corrected magnitudes for each band is then obtained as $m_{\lambda,C} = m_{\lambda,O} - A_\lambda$, where $m_{\lambda,O}$ is the magnitude retrieved from the catalogue, and $m_{\lambda,C}$ is the extinction corrected magnitude.

#### Luminosity class

Before deriving the initial conditions, it is necessary to classify the star as a dwarf or giant. That is done by using the JHK magnitudes, and the intrinsic colours of dwarfs and giants, for different spectral types, from Bessell and Brett (1988). We first converted the JHK magnitudes to the Bessel

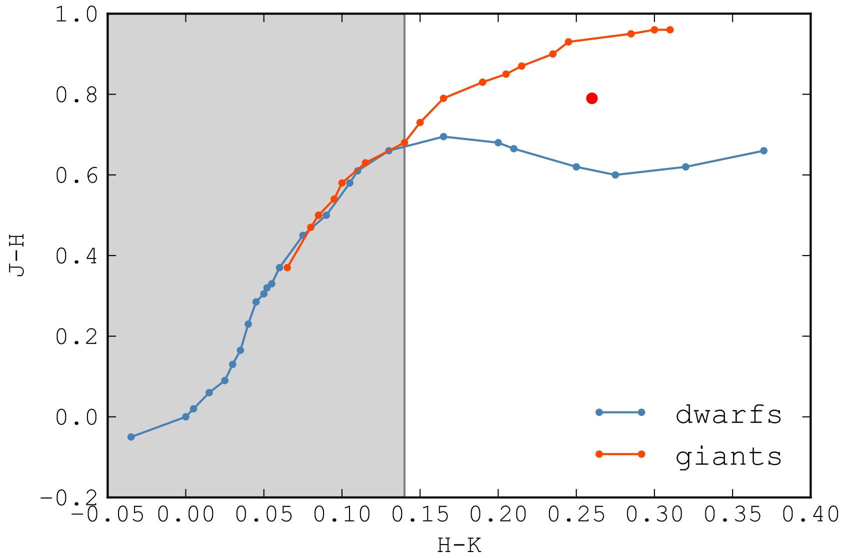

Figure 3.3: Intrinsic JHK colours for dwarf (blue line) and giant (red line) stars, from Bessell and Brett (1988). The red point represents a star with $H - K = 0.26$ and $J - H = 0.79$. The distance between the point to the giant curve is 0.08 dex, and to the dwarf curve is 0.13 dex, therefore the star is classified as giant. The shaded area represents the $H - K$ range for which the curves overlap, and no classification can be correctly performed. In those cases, the star is classified as dwarf.

and Brett system using the relations from Carpenter (2001)[3]. We then computed the distance to the dwarf and giant evolutionary models, and classify the star from the curve for which the distance is the shortest. This procedure, as well as the dwarf and giant curves from Bessel and Brett, are shown in Figure 3.3. If the JHK magnitudes are missing, the star is classified as a dwarf. This procedure is also performed only when $H - K > 0.14$, which is when the dwarf and giant curves no longer overlap. For stars with $H - K < 0.14$, they are classified as dwarfs.

### Metallicity

The metallicity is derived from Equation 1 of Martell and Laughlin (2002), using the Strömgren coefficients $b - y$, $m_1$, and $c_1$. This relation is valid for $-2.0 < \text{[Fe/H]} < 0.5$. In the case the Strömgren coefficients are missing, or the derived metallicity is outside of the permitted ranges, then [Fe/H] is set to zero.

### Temperature

The derivation of the initial effective temperature ($T_{\text{i}ni}$) will depend of the luminosity class. In the case of dwarf stars, the photometric relations from Casagrande et al. (2010, hereafter C10), or Mann et al. (2015, hereafter M15) are used. The difference between both relations is that the one from M15 is optimised for M dwarf stars, and the relations from C10 are applicable for FGK stars.

---

[3] `http://www.astro.caltech.edu/~jmc/2mass/v3/transformations/`

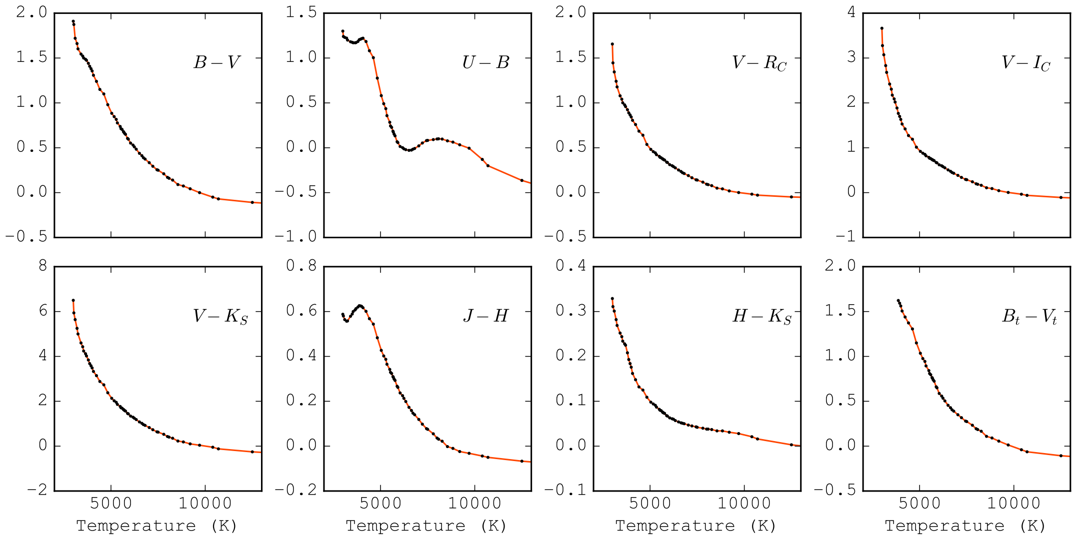

Figure 3.4: Photometric colours of main sequence stars, for different effective temperatures, from Pecaut and Mamajek (2013). Red lines represent the spline approximation for each curve. The temperature for a given colour is computed as the root of the ($m_1$ - $m_2$) - ($m_{1,\star}$ - $m_{2,\star}$) curve, where $m_1 - m_2$ is the chosen colour, and $m_{1,\star}$, $m_{2,\star}$ are the star's colours.

In order to infer which type of star we are dealing with, we use its apparent magnitudes and the intrinsic colours for each spectral type derived in Pecaut and Mamajek (2013, hereafter P13). If the colours are in agreement with a K07 star or later, we use the M15 relations. If the photometric colours are outside of the permitted ranges for the C10 or M15 relations, we then infer the initial temperature by interpolating from the photometric colours and temperatures from P13. The colour in different bands and temperatures, along with the spline representation of each curve, are shown in Figure 3.4.

In C10, M15 and P13, several relations are available for different photometric colours. For each star, we compute the average of the temperature derived for each photometric colour, weighted by their uncertainty.

If the star is classified as a giant, then the relations from González Hernández and Bonifacio (2009) are used. Just like for C10 and M15, different temperatures are derived for each photometric colour, and the final value corresponds to the average of the individual temperatures for each colour, weighted by their uncertainty.

The initial temperature will also set the boundaries of the parameter space through which SPECIES will search for the final temperature. These boundaries are set to be 200 K from $T_{\rm ini}$. In section 3.2.1 we will show the reasons for choosing 200 K as the window over $T_{\rm ini}$. This can be disabled by the user at any time.

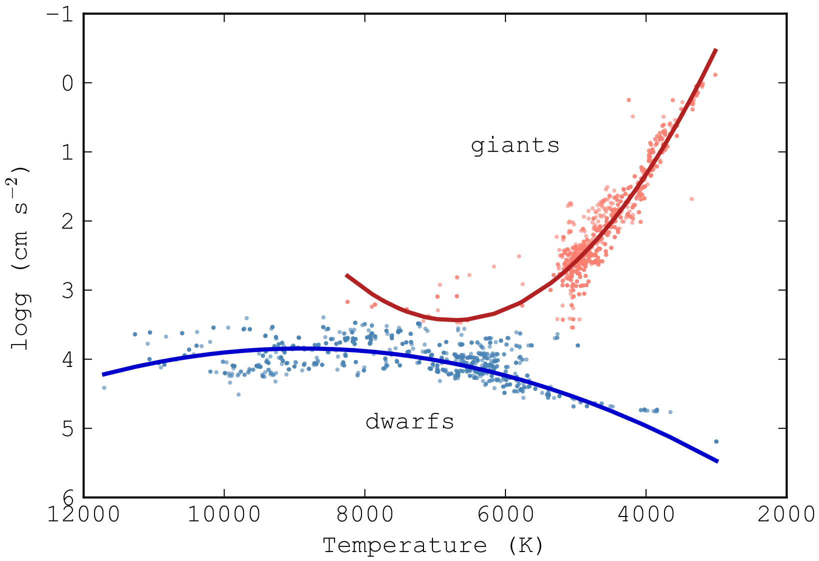

Figure 3.5: logg vs temperature for several stars in the literature. Red points represent giant stars, and blue points dwarf stars. The solid lines are the polynomials adjusted to each group, showed in Equation 3.1.

**Surface gravity**

The initial surface gravity is derived by comparing log g and $T_{\rm eff}$ obtained for stars in the literature with different luminosity classes. We used the sample of stars from the NASA Exoplanet Archive[4], and separated the points into two classes: dwarf ($\log g \gtrsim 4.0$) or giants ($\log g \lesssim 4.0$). Then, we adjusted a second order polynomial to each group, obtaining the following relations, depending on the luminosity class:

$$\mathrm{logg} = \begin{cases} 4.68 \times 10^{-8}\, T^2 - 8.33 \times 10^{-4}\, T - 7.547 & \text{dwarf,} \\ -2.8 \times 10^{-7}\, T^2 + 3.79 \times 10^{-3}\, T - 9.335 & \text{giant,} \end{cases} \tag{3.1}$$

## 3.1.4 Atmospheric parameters

The atmospheric parameters ($T_{\rm eff}$, log g, [Fe/H], and $\xi_t$) are derived using equivalent widths (EWs) for the set of Fe I and Fe II lines discussed above. These EW values, along with an appropriate atmosphere model obtained by interpolating through a grid of ATLAS9 atmosphere models (Castelli and Kurucz 2004), are given to the 2017 version of the MOOG code (Sneden 1973), using the driver *abfind*, which solves the radiative transfer equation assuming local thermodynamic equilibrium (LTE) conditions. The atmospheric parameters are then derived through an iterative process that stops when no correlation is found to a tolerance level of 0.02 dex between the abundance of each individual Fe I line and both the excitation potential and the reduced equivalent width ($\log EW/\lambda$),

---

[4] `https://exoplanetarchive.ipac.caltech.edu`

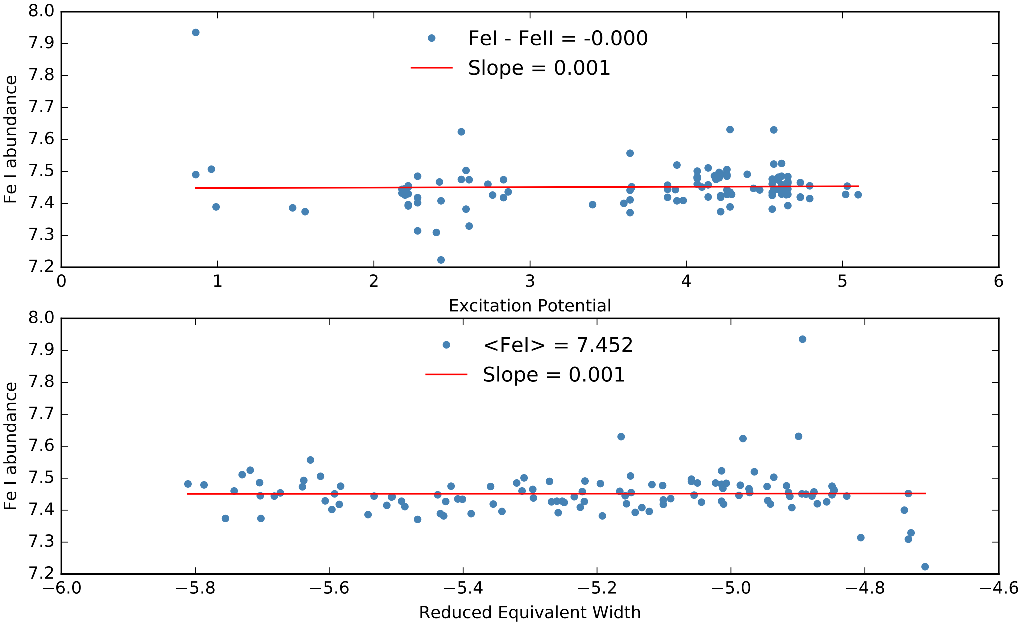

Figure 3.6: Example of the output from MOOG, when the correct atmospheric parameters are found: there is no correlation between the individual Fe I abundances, the excitation potential and the reduced equivalent width (represented by the slope of the linear regression between the quantities), the abundance difference between the neutral and ionized Fe is zero, and the iron abundance of the input model is the same as from the MOOG output. The values used for this model are: $T_{\mathrm{eff}}$ = 5750, log g = 4.40, [Fe/H] = -0.02, and $\xi_t$ = 0.66.

Table 3.1: Estimate of the uncertainties for the stellar parameters, separated in ranges of stellar temperature, for dwarf stars.

| Parameter uncertainty | 4500 - 5125 (K) | 5125 - 5750 (K) | 5750 - 6375 (K) | 6375 - 7000 (K) |
|---|---|---|---|---|
| $\sigma_T$ | 53 | 31 | 32 | 75 |
| $\sigma_{\log \mathrm{g}}$ | 0.31 | 0.27 | 0.24 | 0.75 |
| $\sigma_{[\mathrm{Fe/H}]}$ | 0.12 | 0.07 | 0.06 | 0.12 |
| $\sigma_{\xi_t}$ | 0.05 | 0.02 | 0.03 | 0.06 |

and also when the average abundances for Fe I and Fe II are equal to the iron abundance given to the atmosphere model at the level of 0.02%. Figure 3.6 shows an example of the output from MOOG, when the conditions for finding the correct atmospheric parameters are found.

The ranges in parameters accepted by the code are [3500 – 15000 K] for the temperature, [-3.0 – +1.0 dex] for the metallicity, [0.0 – 5.0] for the logarithm of the surface gravity in $\mathrm{cm\,s^{-2}}$, and [0.0 – 2.0 $\mathrm{km\,s^{-1}}$] for the microturbulent velocity. If, during the iterative process, all four parameters are outside of those ranges, or the same values are repeated more than 200 times, the computation stops. This last case would mean that SPECIES is stuck in one section of the parameter space, prolonging the time the code runs, without reaching final convergence. From our experience using SPECIES, we find that after the same parameters are repeated over 200 times, the code is not able to search the rest of the parameters space. For those cases, it is recommended that the user specifies the initial conditions, or fixes one of the parameters to a certain value. If no convergence was reached, we perform the derivation another time but now setting the temperature to be equal to $T_{\mathrm{i}ni}$, and keeping it fixed. SPECIES also has an option to set the microturbulence to a fixed value through the computation. We found that, for some stars, all the atmospheric parameters would reach convergence except for the microturbulence, therefore for those stars we set $\xi_t = 1.2\,\mathrm{km\,s^{-1}}$. These options to fix the temperature or/and the microturbulence are only used when there was no convergence on the atmospheric parameters, and can be disabled by the user.

### 3.1.5 Uncertainty estimation

An important facet of the SPECIES code is the handling of uncertainties for each of the calculated parameters. A number of the parameters derived by SPECIES are heavily correlated, such as temperature and iron abundance, due to them being derived simultaneously with MOOG via the curve of growth analysis. The code tries to take into consideration these correlations to return a more representative uncertainty estimate for each of the elements, and to consider the uncertainty in the EW (derived with ARES) in the equation. In order to do so, we took as a reference the uncertainty estimation method used in Gonzalez and Vanture (1998) and Santos et al. (2000). In Table 3.1 we show the typical uncertainties obtained for each atmospheric parameter, separated in ranges of stellar temperature.

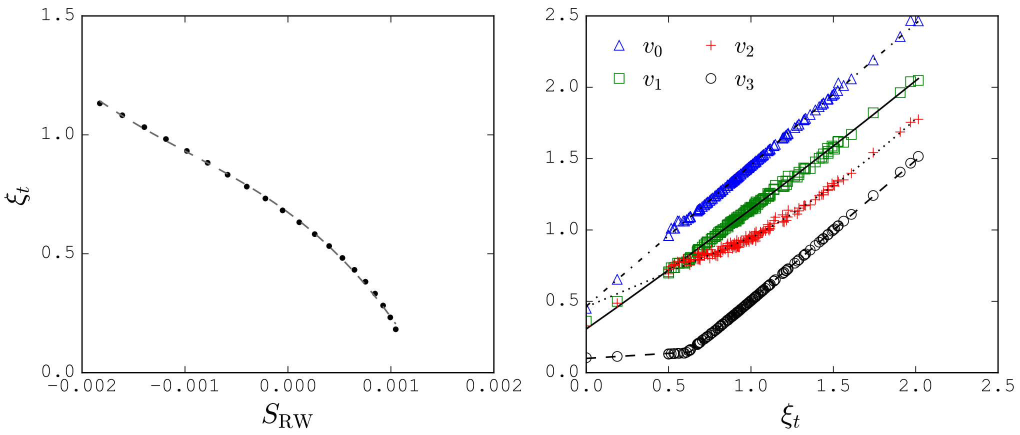

Figure 3.7: Top panel: $\xi_t$ vs $S_{RW}$ for a Solar spectrum. Bottom panel: Fit of the spline coefficients as a function of microturbulence.

### Microturbulence

The microturbulence is computed as the value for which the slope of the linear fit performed between the individual Fe I abundances and the reduced equivalent width reaches zero. This value will be referred to as $S_{RW}$. Therefore, the resulting uncertainty will depend on this slope, resulting in:

$$\sigma^2_{\xi_t} = \left( \frac{\partial \xi_t}{\partial S_{RW}} \bigg|_{S_{RW}=0} \right)^2 \sigma^2_{S_{RW}}, \tag{3.2}$$

where $\sigma_{S_{RW}}$ corresponds to the uncertainty in $S_{RW}$.

We computed this uncertainty for 160 stars from the sample studied in Sousa et al. (2008), and for 10 solar spectra, all taken using HARPS (more details about this sample of stars will be given in Section 3.2.2). We found that, for each case, there was a dependency of $\xi_t$ with $S_{RW}$, which can be adjusted with a cubic spline,

$$\xi_t = Y(v_0, v_1, v_2, v_3, S_{RW}), \tag{3.3}$$

where $Y$ represents a cubic spline, with coefficients $v_{\rm i}$. The coefficients are a function of microturbulence velocity, shown in Figure 3.7, and have the following dependence:

$$\begin{aligned}
v_0 &= 0.99 \cdot \xi_t \ + \ 0.466, \\
v_1 &= 0.03 \cdot \xi_t^2 \ + \ 0.81 \cdot \xi_t \ + \ 0.306, \\
v_2 &= \begin{cases} 0.49 \cdot \xi_t \ + \ 0.46 & \xi_t < 1.04, \\ 0.19 \cdot \xi_t^2 \ + \ 0.26 \cdot \xi_t \ + \ 0.49 & \xi_t \geq 1.04, \end{cases} \\
v_3 &= \begin{cases} 0.07 \cdot \xi_t \ + \ 0.1 & \xi_t < 0.63, \\ 0.98 \cdot \xi_t \ - \ 0.47 & \xi_t \geq 0.63. \end{cases}
\end{aligned} \tag{3.4}$$

Another way SPECIES computes the uncertainty in the microturbulence is explained in the appendix, section C.2, and although we performed this method on all our stars, it is not the preferred final value. We note however that it does appear in the SPECIES catalogue as `err_vt2`.

### Temperature

The temperature is obtained when the slope of the dependence between the individual Fe I abundances, and the excitation potential, is zero. We will call this slope as $S_{\mathrm{EP}}$. Since all the atmospheric parameters are derived simultaneously, the microturbulence will have an effect on the final temperature, and its uncertainty. The final expression for the error in the temperature is then:

$$\sigma_T^2 = \left( \frac{\partial T}{\partial \xi_t} \bigg|_{\xi_t} \right)^2 \sigma_{\xi_t}^2 + \left( \frac{\partial T}{\partial S_{\mathrm{EP}}} \bigg|_{S_{\mathrm{EP}}=0} \right)^2 \sigma_{S_{\mathrm{EP}}}^2, \tag{3.5}$$

where $\partial T / \partial \xi_t$ is evaluated at the microturbulence derived by our code, $\sigma_{\xi_t}$ is its uncertainty, and $\sigma_{S_{\mathrm{EP}}}$ is the uncertainty in $S_{\mathrm{EP}}$, when the temperature reaches convergence.

In order to find the first term, we computed the value of the temperature after fixing $\xi_t$ to a specific value. We obtained a quadratic fit, which is shown in the top-left panel of Figure 3.8. For the second term, we followed a similar procedure to the one discussed for the microturbulence, and computed the temperature we would obtain as a function of $S_{\mathrm{EP}}$. In this case, the dependence could be fitted by a quadratic curve, and is shown in the top-right panel of Figure 3.8.

As we did before, to find the values for the coefficients of the dependence between $T$ and $\xi_t$, and between $T$ and $S_{\mathrm{EP}}$, we computed the uncertainties for the same sample of stars than in the previous section. The coefficients corresponding to the relation between $T$ and $\xi_t$ are plotted in the bottom-left panel of Figure 3.8, and depend on $T$ in the following way:

$$\begin{aligned} T &= t_0 \cdot \xi_t^2 + t_1 \cdot \xi_t + t_2, \\ t_0 &= -8.7 \times 10^{-3} \cdot T + 81.74, \\ t_1 &= -5.4 \times 10^{-2} \cdot T + 580.5, \\ t_2 &= 0.88 \cdot T + 405.8. \end{aligned} \tag{3.6}$$

For the relation between $T$ and $S_{\mathrm{EP}}$, the coefficients are plotted in the bottom-right panel of Figure 3.8, and have the following dependency with $T$:

$$\begin{aligned} T &= t_3 \cdot S_{\mathrm{EP}}^2 + t_4 \cdot S_{\mathrm{EP}} + t_5, \\ t_3 &= 7.4 \cdot T - 4 \times 10^4, \\ t_4 &= -8.77 \times 10^{-4} \cdot T^2 + 8.8 \cdot T - 2.74 \times 10^4, \\ t_5 &= T - 41. \end{aligned} \tag{3.7}$$

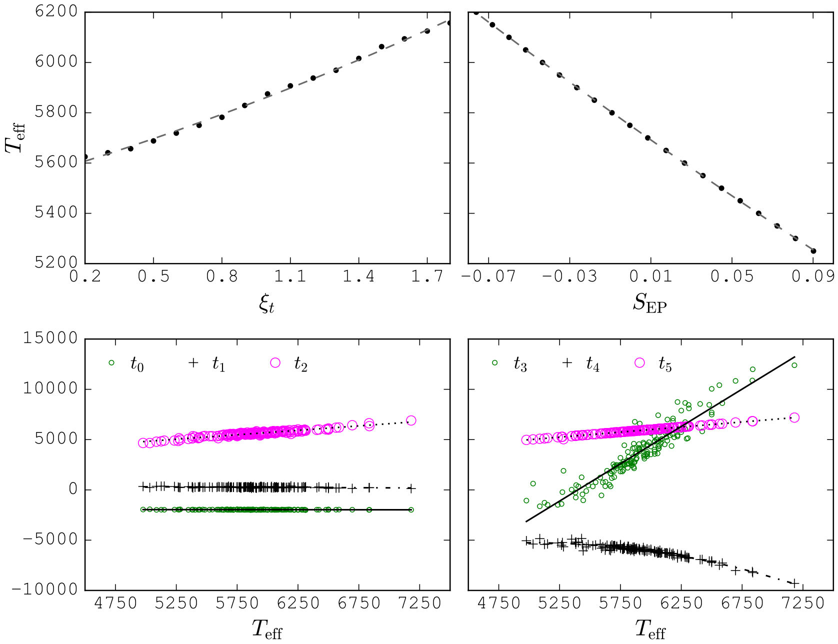

Figure 3.8: Top panel: Dependence of temperature with microturbulence (left) and $S_{\rm EP}$ (right), for a Solar spectrum. Bottom panel: Coefficients of the fit between $T$ and $\xi_t$ (left), and between $T$ and $S_{\rm EP}$ (right).

Again we highlight a second way to compute the uncertainty in temperature that is explained in the appendix. We performed it for all our stars but it is used mainly as a cross-check and is again not the preferred value. It appears in the catalogue as `err_T2`.

### Metallicity

The final value for the metallicity is reached when the average of the individual Fe I abundances matches the one from the input model atmosphere, and will depend on the scatter found in the Fe I abundances. As was mentioned previously, the final metallicity will also depend on the rest of the atmospheric parameters, and in this case, it will depend on the temperature and the surface gravity. The final expression for the uncertainty in the metallicity will be:

$$\sigma^2_{\rm [Fe/H]} = \left( \left.\frac{\partial {\rm [Fe/H]}}{\partial \xi_t}\right|_{\xi_t} \right)^2 \sigma^2_{\xi_t} + \left( \left.\frac{\partial {\rm [Fe/H]}}{\partial T}\right|_{T} \right)^2 \sigma^2_T + \sigma^2_{\rm Fe\,I}, \tag{3.8}$$

where $\partial{\rm [Fe/H]}/\partial\xi_t$ and $\partial{\rm [Fe/H]}/\partial T$ are evaluated at $\xi_t$ and $T$ derived by our code, respectively, and $\sigma_{\rm Fe\,I}$ is the scatter over the abundances of each Fe I lines.

We computed the metallicity for different values of the temperature and microturbulence, and obtained the following relation:

$$ {\rm [Fe/H]} = (m_0 \cdot \xi_t + m_1) \cdot T + (m_2 \cdot \xi_t + m_3), \tag{3.9}$$

which can also be seen in the top panels of Figure 3.9.

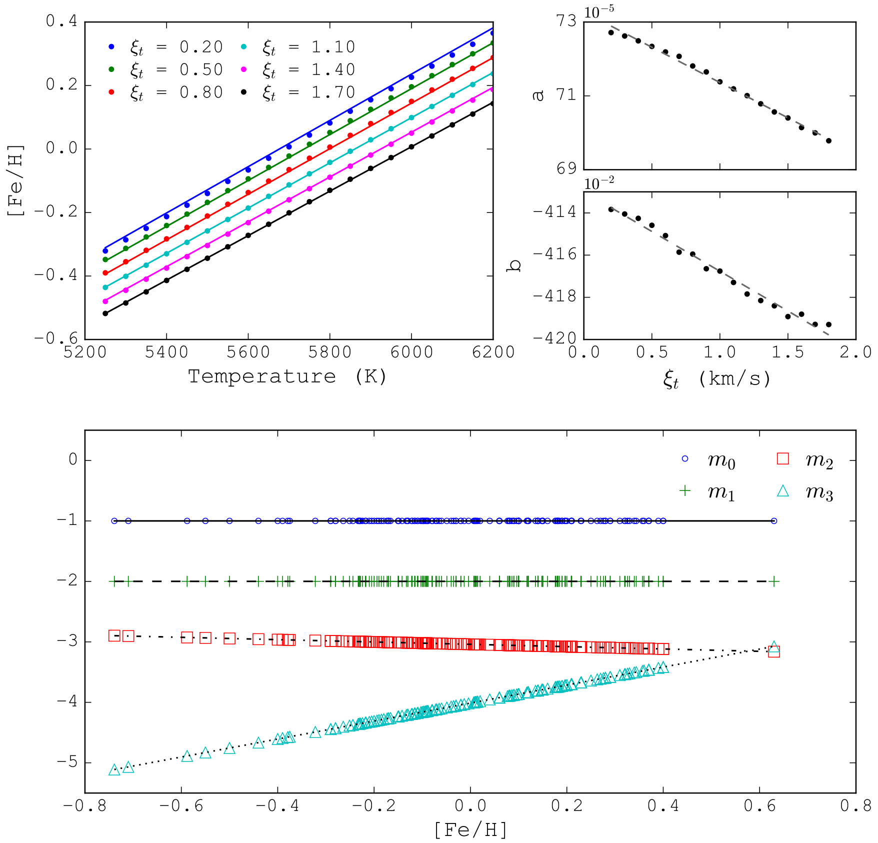

Figure 3.9: Top panel: (left) Dependence of metallicity with temperature for several values of microturbulence, (right) dependence of the coefficients $a$ and $b$ with $\xi_t$, so that [Fe/H] = $a \cdot T + b$. Bottom panel: Coefficients of the fit of [Fe/H] with $T$ and $\xi_t$, so that $a = m_0 \cdot \xi_t + m_1$ and $b = m_2 \cdot \xi_t + m_3$. A vertical offset was applied to each coefficient for plotting purposes.

We followed the same procedure than in the previous sections to find the dependence of the fit coefficients with the metallicity. The fits we obtained are plotted in the bottom panel of Figure 3.9, and correspond to

$$
\begin{aligned}
m_0 &= 2.02 \times 10^{-5} \cdot [\mathrm{Fe/H}] \ - \ 1.8 \times 10^{-5}, \\
m_1 &= -9.57 \times 10^{-5} \cdot [\mathrm{Fe/H}] \ + \ 7.03 \times 10^{-4}, \\
m_2 &= -0.2 \cdot [\mathrm{Fe/H}] \ - \ 0.04, \\
m_3 &= 1.49 \cdot [\mathrm{Fe/H}] \ - \ 4.01.
\end{aligned}
\tag{3.10}
$$

### Surface gravity

The surface gravity depends on the average abundance obtained for the Fe II lines, as well as on the final temperature from the iterative process. Therefore, the uncertainty in log g will be given by:

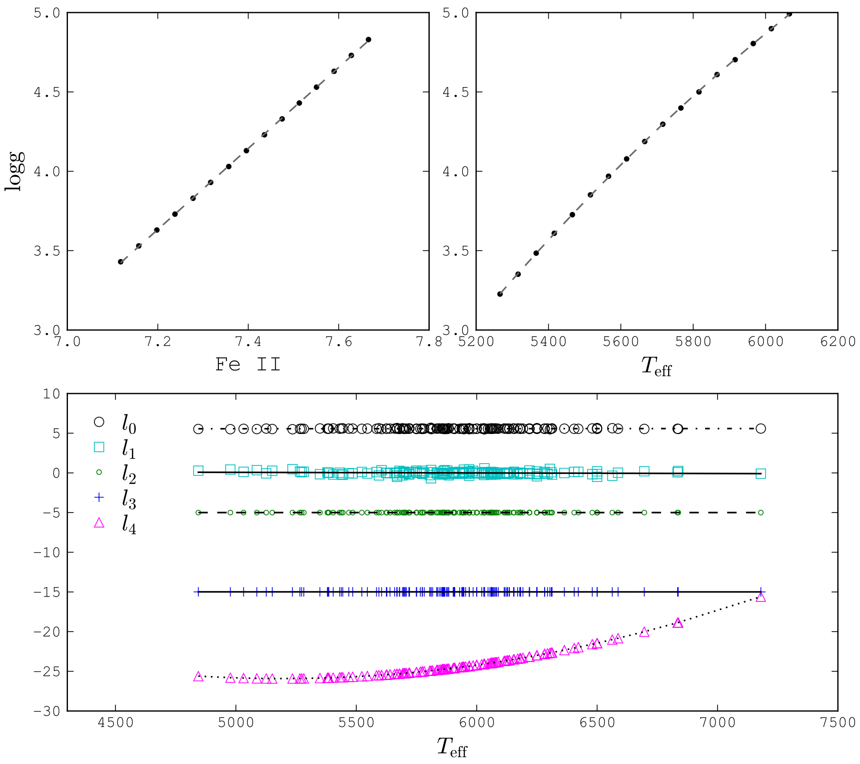

Figure 3.10: Top panel: (left) Dependence of surface gravity (log g ) with individual Fe II abundance, (right) dependence of log g with temperature. Bottom panel: Coefficients of the fits between log g with Fe II , and between log g with $T_{\rm eff}$ , as shown in Equation 3.12. A vertical offset was applied to each coefficient for plotting purposes.

$$\sigma^2_{\log g} = \left( \frac{\partial \log g}{\partial T} \bigg|_T \right)^2 \sigma^2_T + \left( \frac{\partial \log g}{\partial \,\mathrm{Fe\,II}} \bigg|_{\mathrm{Fe\,II}} \right)^2 \sigma^2_{\mathrm{Fe\,II}}, \tag{3.11}$$

where $\partial \log g/\partial T$ and $\partial \log g/\partial\,\mathrm{Fe\,II}$ are evaluated for $T$ and [Fe/H] found by our code, respectively.

As for the previous parameters, we found that $\log g = l_0 \cdot \mathrm{Fe\,II} + l_1$, and $\log g = l_2 \cdot T^2 + l_3 \cdot T + l_4$. Both of these relations are plotted in the top panel of Figure 3.10. The coefficients $l_0, l_1, l_2, l_3$, and $l_4$ all depend on the temperature and are shown in the bottom panel of Figure 3.10. The relations and coefficient values are as follows:

$$\begin{aligned}
l_0 &= 8.3 \times 10^{-5} \cdot T \;+\; 2.1, \\
l_1 &= -5.36 \times 10^{-4} \cdot T \;-\; 11.8, \\
l_2 &= 9.2 \times 10^{-10} \cdot T \;-\; 5.83 \times 10^{-6}, \\
l_3 &= -2.23 \times 10^{-6} \cdot T \;+\; 2.1 \times 10^{-2}, \\
l_4 &= 2.61 \times 10^{-6} \cdot T^2 \;-\; 2.71 \times 10^{-2} \cdot T \;+\; 44.4.
\end{aligned} \tag{3.12}$$

### 3.1.6 Mass, age, and radius

SPECIES uses the python package `isochrones`[5] (Morton 2015) in order to derive the mass, age, and radius for each star. It uses the previously derived [Fe/H], $\log g$, and $T_{\mathrm{eff}}$, and the MESA Isochrones and Stellar Tracks (MIST, Dotter 2016). The package performs a MCMC fit, with priors given by the [Fe/H], $\log g$, and $T_{\mathrm{eff}}$ input values, plus their uncertainties. The samples generated correspond to the mass, age, and radius, evaluated at each chain link. The resulting values will be given by the median and standard deviation of the posterior distributions. It is also possible to input photometric data as priors. This data corresponds to apparent magnitude in several bands, as well as parallax in mas, and can either be given by the user, or retrieved from catalogues. The list of catalogues used, as well as the allowed magnitudes, are given in section 3.1. Figure 3.11 shows an example posterior distribution obtained for one of our solar spectra.

Another value measured from the isochrones interpolation is the surface gravity a star would have for the mass, age, and radius derived previously. This quantity, which we will referred to as $\log g_{\mathrm{iso}}$, should match the input $\log g$ (referred to as the spectroscopic $\log g$ within the text), and it does so in most cases, but we do find some exceptions. When using SPECIES on a sample of dwarf stars (which will be further explained in section 3.2.2), we find that for some cases the value of $\log g$ is $< 4.0$. We also find better agreement between $\log g_{\mathrm{iso}}$ and the surface gravity from the literature (for the description of the catalogues used for the comparison, see section 3.2.2), than when using the spectroscopic $\log g$ (section 3.2.2, Figure 3.19). This leads us to conclude that $\log g_{\mathrm{iso}}$ is a better tracker of the true surface gravity than the $\log g$ obtained from the iterative process explained in section 3.1.4. In order to incorporate this result into the computation, we studied the distribution of $\log g$ -$\log g_{\mathrm{iso}}$ (Figure 3.12), and we found that it follows a Gaussian distribution centred around zero, and with a standard deviation equal to 0.11. Most of the stars are found contained within $2\sigma$ of this distribution. For the cases when the discrepancy between both $\log g$ measurements is larger than $2\sigma$, which translates into 0.22 dex, we perform a second iteration to derive the atmospheric parameters, following the same procedure than in section 3.1.4, but setting $\log g = \log g_{\mathrm{iso}}$ as the correct value. This option can be disabled when running SPECIES (section 3.2).

It is important to mention that $\log g_{\mathrm{iso}}$ not only seems to provide a better estimate of the true surface gravity of a dwarf star, but it also agrees for evolved stars. This is shown in section 3.2.2, where we use SPECIES to derive the parameters for a sample of dwarf and evolved stars, and we find agreement between our values and those from the literature.

### 3.1.7 Chemical abundances

SPECIES allows the computation of chemical abundances for 11 elements (Na, Mg, Al, Si, Ca, Ti, Cr, Mn, Ni, Cu, Zn) and to test the level to which the code performs these measurements, we compared the SPECIES values with the solar values already studied in the literature, where we used the values for $T_{\mathrm{eff}}$, $\log g$, [Fe/H], and $\xi_t$ computed previously. We used the line list used in Ivanyuk et al. (2017, we refer the reader to that work for a detailed description of the line selection), and the solar abundances from Asplund et al. (2009). The EW were measured using the ARES code, and

---

[5] `https://github.com/timothydmorton/isochrones`

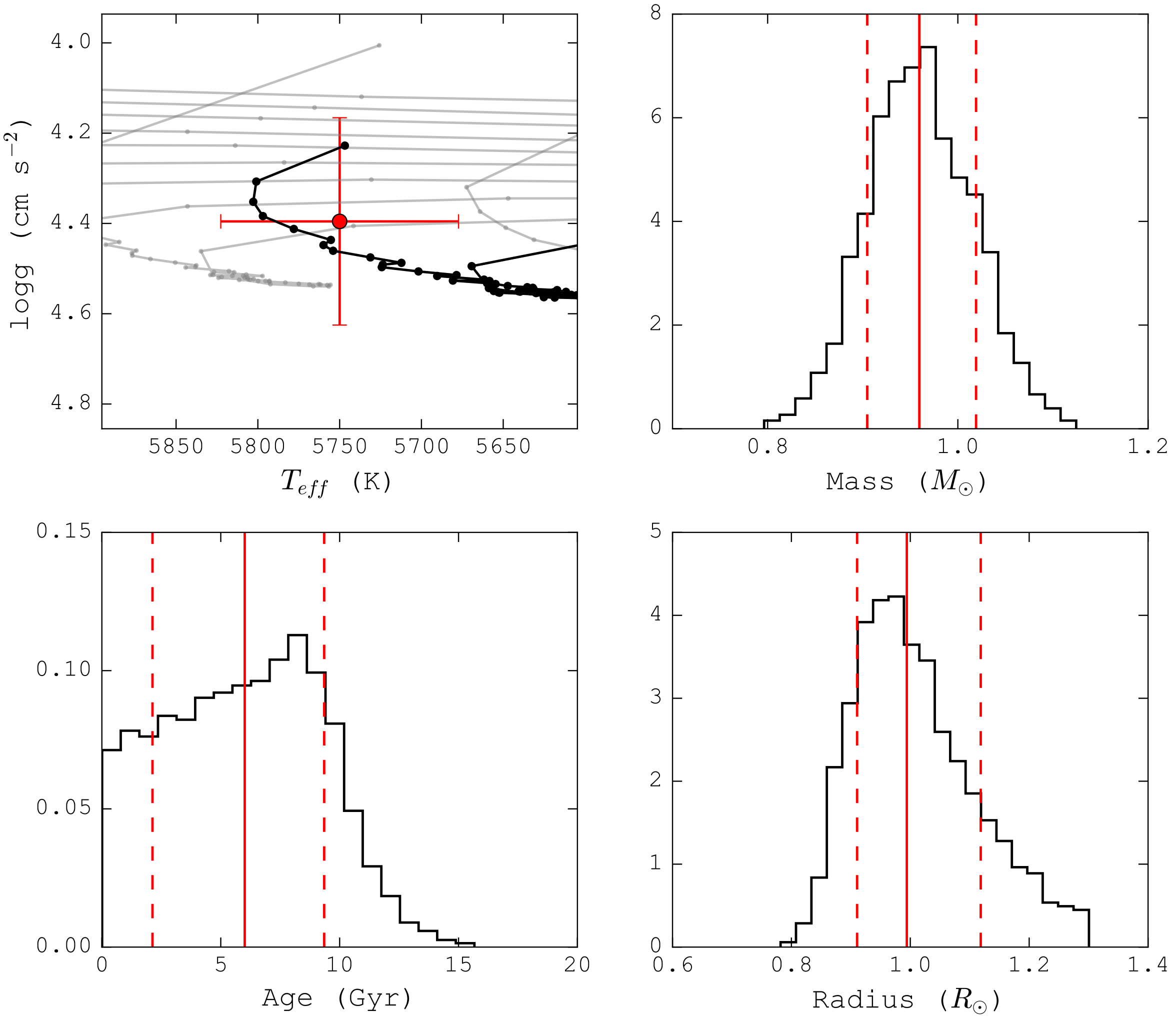

Figure 3.11: Results obtained for one of the solar spectrum used in SPECIES. First panel: log g - $T_{\mathrm{eff}}$ space diagram. The red point represents the position of the Sun, with the final values obtained using our code (T = 5776 ± 73 K, [Fe/H] = 0.0± 0.1 dex, log g = 4.5 ± 0.2 cm s$^{-2}$). Dotted lines represent the evolutionary tracks for stars with masses from 0.5 to 1.5 $M_{\odot}$, and [Fe/H] = 0.0. The black line is the track for a 1.0 $M_{\odot}$ star. Each point in the lines represent a different age. Remaining panels: Distribution of the mass, age, and radius, for one of our HARPS solar spectra. The red dashed-solid-dashed lines represent the (16, 50, 84) quantiles, respectively. The results for this spectrum are listed in Table 3.3 as `sun03`.

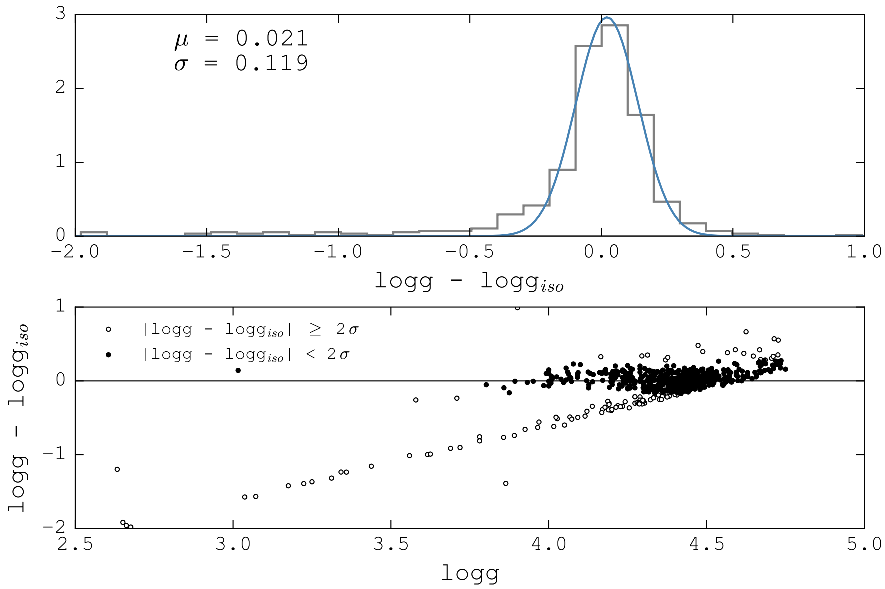

Figure 3.12: Top panel: histogram of the difference between $\log g$ and $\log g_{\mathrm{iso}}$. The blue line corresponds to the Gaussian distribution fit performed, with mean and sigma equal to $\mu = -0.004$ and $\sigma = 0.112$, respectively. Bottom panel: Difference between $\log g$ and $\log g_{\mathrm{iso}}$ vs $\log g$. Filled circles are the stars laying within $2\sigma$ of the Gaussian fit performed to the histogram. Empty circles are the points laying beyond the $2\sigma$ level, for which the computation was performed a second time, but setting $\log g = \log g_{\mathrm{iso}}$.

for the analysis only lines with $10 < \mathrm{EW} \leq 150$ were used, as explained before.

For each element, we considered only the lines for which the individual abundance was within 1.5 $\sigma$ of the mean value. This was done in order to avoid the lines that deviate too much (more than 2 dex in some cases) from the abundance given by the rest of the lines for that element. The final abundance for each element was computed as the average abundance from each individual line, after the sigma-clipping, and its uncertainty was taken as the standard deviation over the average. We weighted the abundance of each line as $1/\sigma_{\mathrm{EW}}$. When only one line per element is available, the uncertainty is taken to be the average error for the other elements used, and no sigma-clipping was performed.

For all the elements, except for Ti, only lines from neutral species were used. In the case of Ti, we list the abundances obtained for both Ti I and Ti II. We also include in the output the abundances for Fe I and Fe II.

Currently, it is not possible to quickly modify the line list, nor add new species to the computation.

### 3.1.8 Macroturbulence and rotational velocity

In order to compute the macroturbulence ($v_{mac}$) and rotational ($v \sin i$) velocities, we followed the procedure described in dos Santos et al. (2016). It consist of measuring both quantities individually

Table 3.2: Line list used to measure the rotational velocity for each star. $v_{macro,\odot}$ is the macroturbulence velocity found for the Sun in dos Santos et al. (2016)

| Wavelength (Å) | Z | Ion | Exc. pot. (eV) | log($gf$) | $v_{macro,\odot}$ (km s$^{-1}$) |
|---|---|---|---|---|---|
| 6027.050 | 26 | Fe II | 4.076 | -1.09 | 3.0 |
| 6151.618 | 26 | Fe I | 2.176 | -3.30 | 3.2 |
| 6165.360 | 26 | Fe I | 4.143 | -1.46 | 3.1 |
| 6705.102 | 26 | Fe I | 4.607 | -0.98 | 3.6 |
| 6767.772 | 28 | Ni I | 1.826 | -2.17 | 2.9 |

for five different absorption lines, and then compares the results to those from the Sun. The lines used, as well as their atomic characteristics, are mentioned in Table 3.2.

The macroturbulent velocity was obtained from Eq. 1, dos Santos et al. (2016):

$$\begin{aligned} v_{macro,\lambda} = v^{\odot}_{macro,\lambda} &- 0.00707\,T + 9.2422 \times 10^{-7} T^2 \\ &+ 10.0 + k_1(\log \mathrm{g} - 4.44) + k_2, \end{aligned} \tag{3.13}$$

where $v^{\odot}_{macro,\lambda}$ are the velocities obtained for each line in the solar spectra, shown in Table 3.2. $k_1$ and $k_2$ are constants equal to -1.81 ± 0.26 and -0.05 ± 0.03, respectively. All the quantities mentioned were computed by dos Santos et al. (2016). This relation is also very similar to the one used in Valenti and Fischer (2005). The uncertainty in $v_{mac,\lambda}$ for each line is given by:

$$\begin{aligned} \sigma^2_{v_{mac,\lambda}} = \sigma^2_{v^{\odot}_{mac,\lambda}} &+ (1.848 \times 10^{-6}\,T - 0.00707)^2 \sigma^2_T \\ &+ k_1^2 \sigma^2_{\log \mathrm{g}} + (\log g - 4.44)^2 \sigma^2_{k_1} + \sigma^2_{k_2}, \end{aligned} \tag{3.14}$$

where the error in $v^{\odot}_{mac,\lambda}$ is reported to be ± 0.1 km s$^{-1}$. The temperature and surface gravity, along with their uncertainties, are the ones produced by SPECIES. The final $v_{mac}$ corresponds to the average of the individual results, weighted by their uncertainties.

The rotational velocity for each line was obtained by comparing the line profiles with synthetic ones produced by the MOOG driver *synth*. The driver receives a model atmosphere, obtained from the ATLAS 9 grids and the atmospheric values found by SPECIES, and the line abundance, found by measuring the EW of the line with ARES (following the same settings described in section 3.1.2), and using the MOOG driver *abfind*. It also receives the macroturbulent velocity found previously, and the width of the line produced by the instrument resolution. The synthetic profile is then convolved with a rotational profile (Gray 2005) for a certain $v \sin \mathrm{i}$ value. This was performed using the PoWeRS[6] code, which was modified and optimised in order to fit into SPECIES. The code creates grids of different values for $v \sin \mathrm{i}$ and line abundance, and finds the values (abundance, $v \sin \mathrm{i}$) for which the synthetic profile best matches the original line profile. This is measured by

---

[6] `https://github.com/RogueAstro/PoWeRS`

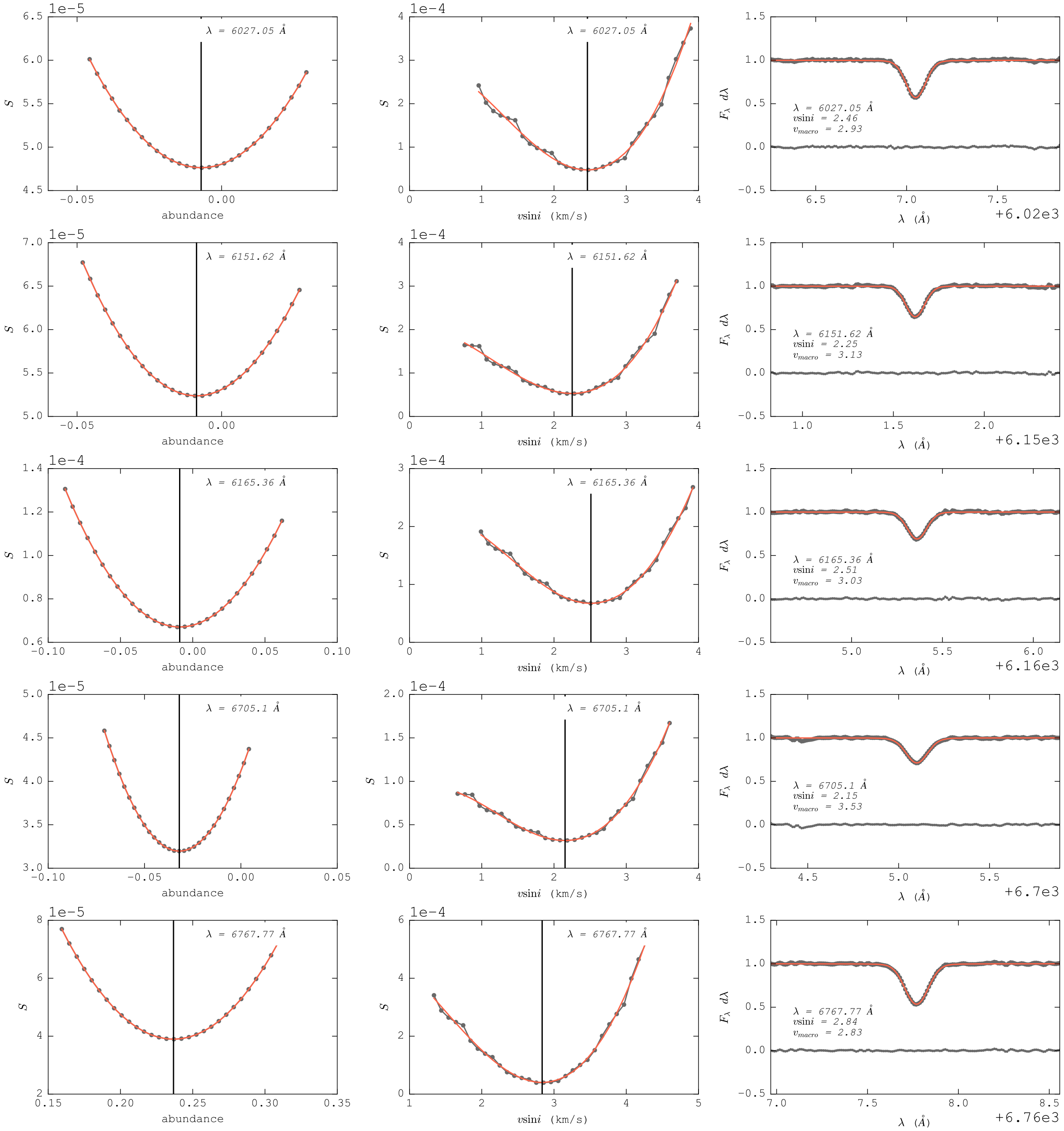

Figure 3.13: Change of $S$ versus abundance (left panels) and rotational velocity (middle panels), for each line of the solar spectra. The red lines represent the cubic spline fit performed over the data, and the vertical line shows the values where the minimum of $S$ is reached. The right panels show the line profiles, along with the final fit (red line) combining the instrumental profile, macroturbulence and rotational velocity. The horizontal black line around zero represents the residuals of the fit.

Table 3.3: Stellar parameters found for a sample of Solar spectra, taken using HARPS.

| Name | [Fe/H] | Temperature | logg | $\xi_t$ | Mass | Radius | Age | vsini | $v_{mac}$ |
|---|---|---|---|---|---|---|---|---|---|
| ceres01 | -0.0 ± 0.1 | 5766 ± 37 | 4.4 ± 0.2 | 0.67 ± 0.03 | 0.97 ± 0.04 | 1.02 ± 0.14 | 6.0 ± 3.7 | 2.2 ± 0.2 | 3.2 ± 0.2 |
| ceres02 | -0.0 ± 0.1 | 5778 ± 32 | 4.4 ± 0.2 | 0.85 ± 0.03 | 0.97 ± 0.04 | 1.00 ± 0.12 | 5.8 ± 3.7 | 2.0 ± 0.2 | 3.1 ± 0.2 |
| ceres03 | -0.0 ± 0.1 | 5707 ± 63 | 4.3 ± 0.2 | 0.78 ± 0.05 | 0.94 ± 0.05 | 1.01 ± 0.16 | 7.7 ± 4.7 | 2.1 ± 0.2 | 3.2 ± 0.2 |
| moon01 | 0.0 ± 0.1 | 5782 ± 48 | 4.4 ± 0.2 | 0.66 ± 0.04 | 0.98 ± 0.05 | 1.01 ± 0.14 | 5.4 ± 3.6 | 2.9 ± 0.3 | 3.1 ± 0.3 |
| ganymede01 | -0.0 ± 0.1 | 5782 ± 57 | 4.5 ± 0.2 | 0.84 ± 0.05 | 0.97 ± 0.05 | 1.00 ± 0.13 | 5.4 ± 3.6 | 2.0 ± 0.3 | 3.2 ± 0.3 |
| sun01 | -0.1 ± 0.1 | 5735 ± 37 | 4.3 ± 0.2 | 0.70 ± 0.03 | 0.94 ± 0.04 | 1.00 ± 0.13 | 7.0 ± 4.3 | 2.3 ± 0.2 | 3.2 ± 0.2 |
| sun02 | 0.0 ± 0.1 | 5766 ± 62 | 4.4 ± 0.3 | 0.44 ± 0.04 | 0.97 ± 0.05 | 1.01 ± 0.16 | 6.0 ± 3.8 | 2.4 ± 0.3 | 3.1 ± 0.3 |
| sun03 | -0.0 ± 0.1 | 5750 ± 73 | 4.4 ± 0.2 | 0.66 ± 0.06 | 0.96 ± 0.06 | 1.00 ± 0.14 | 6.0 ± 3.9 | 2.4 ± 0.2 | 3.1 ± 0.2 |
| sun04 | -0.0 ± 0.1 | 5735 ± 63 | 4.3 ± 0.3 | 0.52 ± 0.04 | 0.96 ± 0.05 | 1.00 ± 0.16 | 6.5 ± 4.2 | 2.3 ± 0.3 | 3.2 ± 0.3 |
| sun05 | -0.0 ± 0.1 | 5735 ± 39 | 4.4 ± 0.3 | 0.58 ± 0.03 | 0.95 ± 0.04 | 0.99 ± 0.14 | 6.5 ± 4.2 | 2.4 ± 0.2 | 3.1 ± 0.2 |

the quantity $S$, which measures the goodness of the fit, and is given by

$$S = \frac{1}{N}\sum_{\mathrm{i}=0}^{N}(y_{o,\mathrm{i}} - y_{s,\mathrm{i}})^2,$$

with $\mathrm{i} = \{0, ..., N\}$ the number of points in the line profile, which is considered from $\lambda - 0.5$ to $\lambda + 0.5$. $y_o$ represents the measured line profile, and $y_s$ the synthetic one. The code performs a cubic spline fit to the value of $S$ vs. the abundance and rotational velocity, and finds the values for which the minimum of $S$ is reached. A minimum of four iterations are performed, refining the abundance and velocity grids by shifting the grid centre to match the values with the best goodness of fit, and making the delta between grid points smaller. This is done in order to obtain the most precise results (minimum of $S$). In Figure 3.13 we show the changes in $S$ for a grid of line abundances and rotational velocities, and the final fits obtained for each line, for a solar spectrum. The final $v \sin \mathrm{i}$ corresponds to the average of the individual values found for each line, and its uncertainty is estimated as $\sigma^2_{v \sin \mathrm{i}} = \sum(S^2_\lambda + \sigma^2_{v_{mac},\lambda})$, where the sum is performed over all the lines.

The stellar parameters obtained for the Sun, using 10 different solar spectra taken with the HARPS instrument[7], are listed in Table 3.3. The final values found, after performing a weighted average with the S/N of each solar spectrum, are T = 5754.2 ± 23.3 K, [Fe/H] = -0.02 ± 0.02 dex, log g = 4.38 ± 0.05 cm $\mathrm{s}^{-2}$, $\xi_t$ = 0.68 ± 0.11 km $\mathrm{s}^{-1}$, $\mathrm{v}_{mac}$ = 3.15 ± 0.06 km $\mathrm{s}^{-1}$, vsini = 2.35 ± 0.27 km $\mathrm{s}^{-1}$, mass = 0.96 ± 0.01 $M_\odot$, radii = 1.00 ± 0.01, and age = 6.17 ± 0.7 Gyr.

## 3.2 Results obtained with SPECIES

Currently, the SPECIES catalogue has 72 columns with the stellar parameters, described in section C.4. In order to test the accuracy of the results obtained with SPECIES, we derived the parameters for a sample of 584 dwarf stars, targeted by the HARPS GTO projects (parameters derived in Sousa et al. 2008) and the Calan-Hertfordshire Extrasolar Planet Search (CHEPS) programme (Jenkins et al. 2009, stellar parameters derived in Ivanyuk et al. 2017). They cover a wide range in temperature and metallicity, from 4300 to 6500 K, and -0.9 to 0.6 dex, respectively. We selected the highest S/N spectra taken with HARPS (given that it is the highest resolution instrument currently accepted

---

[7] `https://www.eso.org/sci/facilities/lasilla/instruments/harps/inst/monitoring/sun.html`

Table 3.4: Mean of the Gaussian fits (in K) performed on the distribution of differences between the temperatures derived by SPECIES, and from using the colour relations from C10. Values inside the parenthesis are the number of points used for each colour and instrument.

| Colour | HARPS | FEROS | HIRES | UVES |
|---|---|---|---|---|
| $B - V$ | 36 (71) | 8 (19) | 207 (9) | 16 (17) |
| $V - R_C$ | 6 (59) | -18 (10) | 208 (8) | -33 (8) |
| $R_C - I_C$ | -47 (59) | -53 (11) | 83 (8) | -8 (8) |
| $V - I_C$ | -15 (58) | -40 (10) | 145 (8) | -26 (8) |
| $V - J$ | -81 (458) | -103 (82) | -60 (48) | -83 (88) |
| $V - H$ | -46 (466) | -77 (84) | -15 (49) | -31 (88) |
| $V - K_S$ | -38 (468) | -43 (83) | -7 (50) | -4 (89) |
| $J - K_S$ | 25 (562) | 27 (94) | 115 (61) | 125 (91) |
| $B_t - V_t$ | -15 (573) | -16 (96) | 16 (61) | -14 (92) |
| $V_t - J$ | -76 (561) | -100 (94) | -42 (60) | -90 (91) |
| $V_t - H$ | -43 (567) | -76 (95) | -4 (61) | -42 (91) |
| $V_t - K_S$ | -39 (570) | -42 (95) | -12 (62) | -21 (92) |
| $b - y$ | -89 (458) | -67 (85) | -27 (47) | -48 (89) |

Table 3.5: Mean of the Gaussian fits (in K) performed on the distribution of differences between the temperatures derived by SPECIES, and from using the colour relations from M15. Values inside the parenthesis are the number of points used for each colour and instrument.

| Colour | HARPS | FEROS | HIRES | UVES |
|---|---|---|---|---|
| $V - I_C$ | 152 (60) | 275 (11) | 320 (8) | 472 (8) |
| $V - J$ | 25 (462) | 11 (84) | 39 (50) | 41 (88) |

by SPECIES), and compare them with what is obtained with photometric relations and other catalogues in the literature. Unless stated otherwise, the results presented here were computed using the temperature from photometry and/or fixing $\xi_t = 1.2$ km s$^{-2}$ when convergence is not reached in the atmospheric parameters, and setting $\log g_{\rm iso}$ as the correct value for the surface gravity when their differences are larger than 0.22 dex. If different options were used in the computation, it will be specified within the text and in the captions of the figures and/or tables.

A sample of the catalogue is shown in Table C.3.

### 3.2.1 Comparison with photometric relations

The first comparison we performed was to analyse the differences between the temperatures derived from our code and from the photometric relations explained in Section 3.1.3. As was mentioned in Section 3.1.3 and 3.1.4, we used the temperatures derived from photometry (for the cases when that information was available) as an initial value for SPECIES, and in the cases when our code could not converge to a valid result for the atmospheric parameters.

In order to check that the temperature from photometry is in agreement with that from SPECIES,

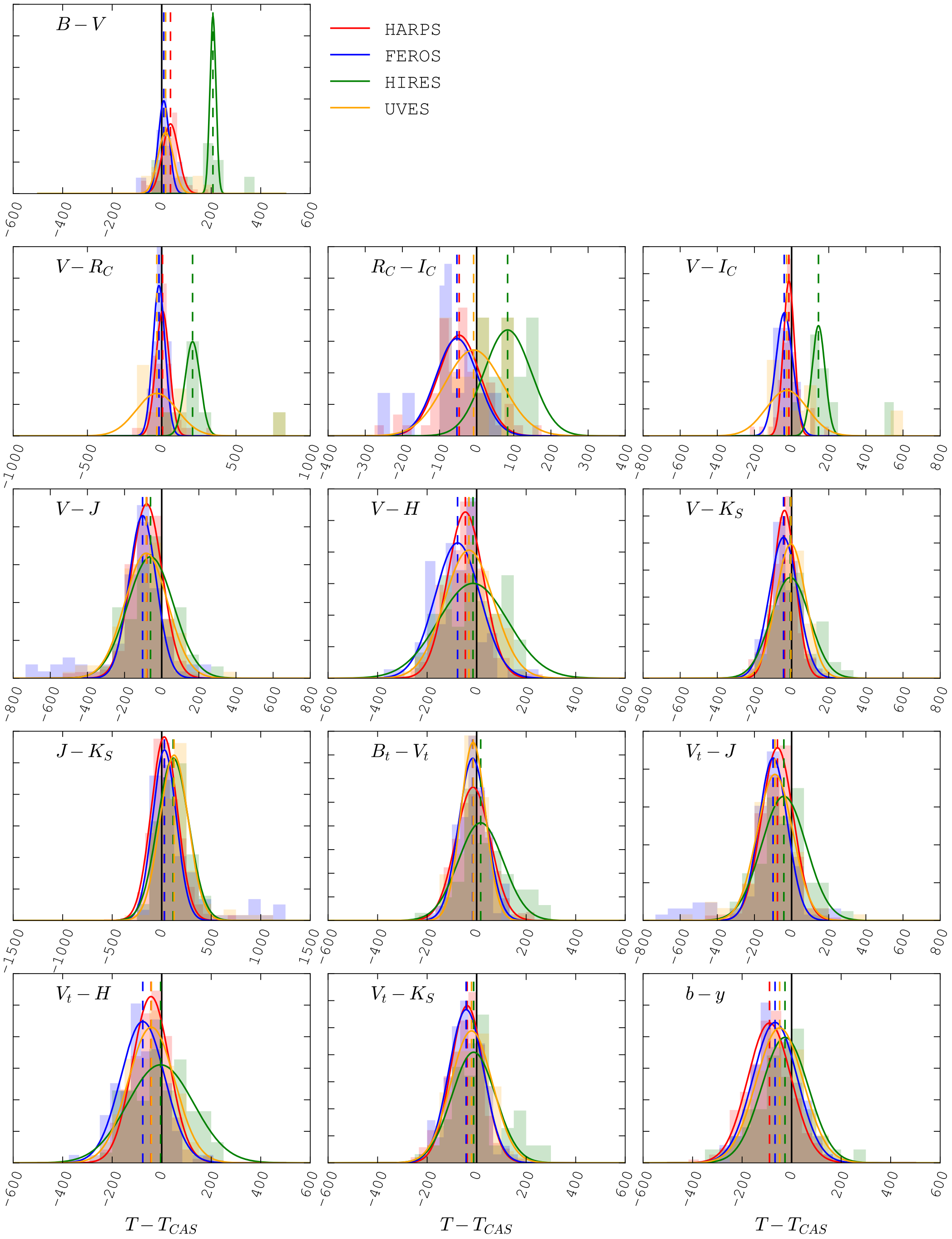

Figure 3.14: Histograms of the difference between the temperature computed by SPECIES, and those using the colour relations from C10. The lines correspond to Gaussian distributions adjusted to the histograms, with mean values listed in Table 3.4. Each colour represents a different instrument: red for HARPS, blue for FEROS, green for HIRES, and orange for UVES. The different panels show the temperatures computed using different photometric colours, mentioned in Section 3.1.

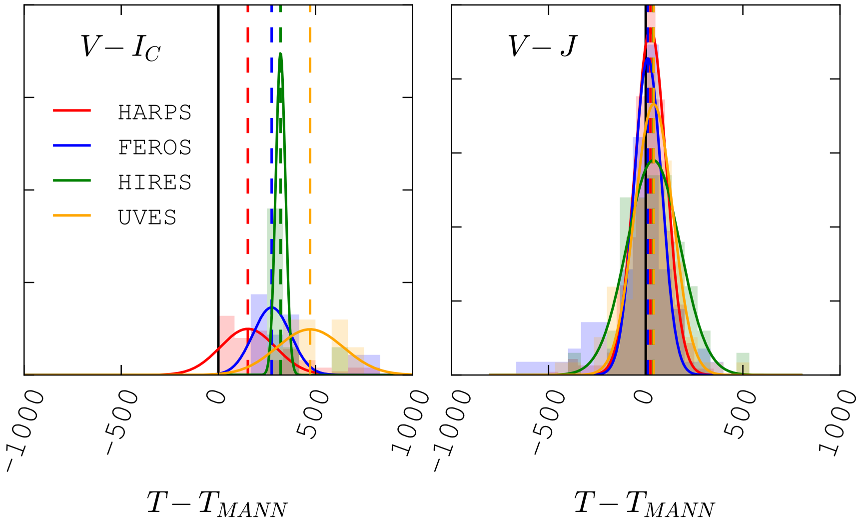

Figure 3.15: Histograms of the difference between the temperature computed by SPECIES, and by using the colour relations from M15. The lines correspond to the Gaussian fits for each distribution, and the colours represent the same instruments as in Figure 3.14. The mean of the Gaussian fits are shown in Table 3.5.

Table 3.6: Mean of the Gaussian distribution (in K) adjusted to the histograms of the different between the temperature from SPECIES, and from interpolating between the models of P13. Values inside the parenthesis are the number of points used for each distribution.

| Colour | HARPS | FEROS | HIRES | UVES |
|---|---|---|---|---|
| $B-V$ | 17 (73) | 11 (19) | 143 (9) | 70 (17) |
| $V-R_C$ | 31 (59) | -6 (10) | 274 (8) | -40 (8) |
| $V-I_C$ | -18 (59) | -57 (10) | 200 (8) | -106 (8) |
| $V-K_S$ | -41 (469) | -39 (84) | -5 (50) | 0 (90) |
| $J-H$ | -13 (562) | -41 (94) | 91 (61) | 26 (93) |
| $H-K_S$ | 349 (538) | 298 (89) | 202 (57) | 237 (87) |
| $B_t-V_t$ | 43 (579) | 36 (97) | 96 (62) | 77 (93) |

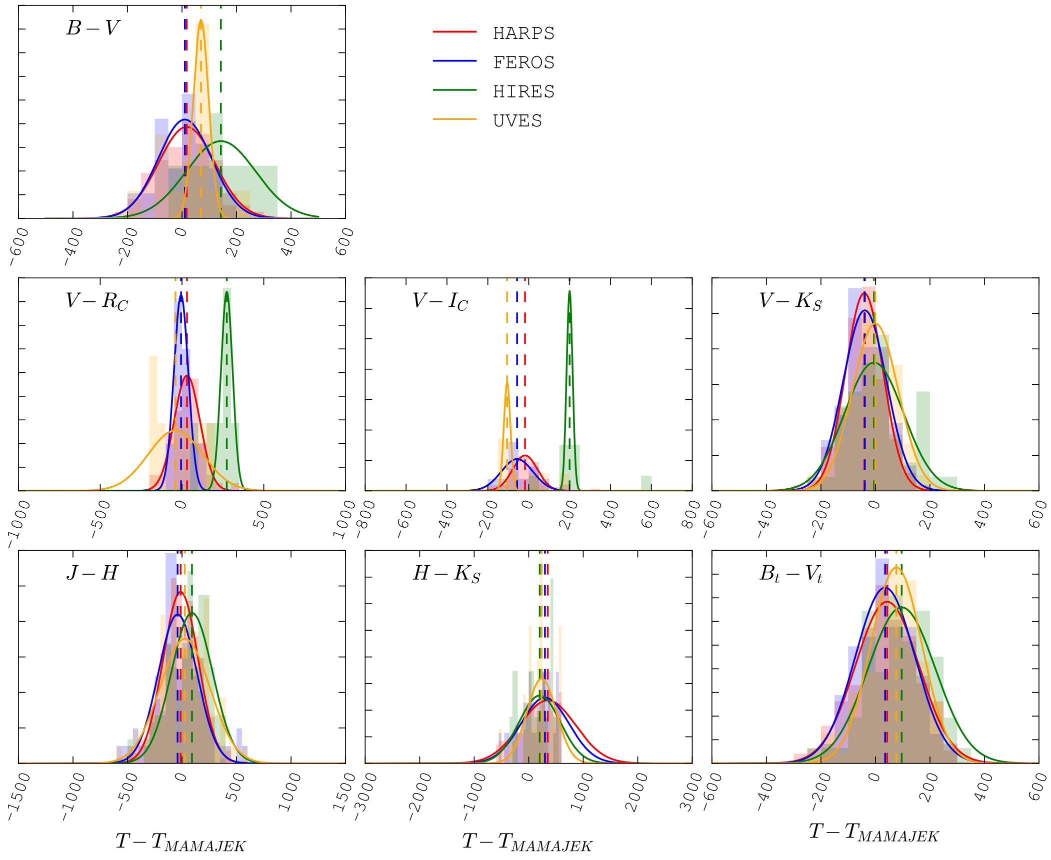

Figure 3.16: Histograms of the difference between the temperature computed by SPECIES, and those obtained by interpolating through the models of P13. The lines correspond to Gaussian distributions adjusted to the histograms, with mean values listed in Table 3.4. The mean of each Gaussian distribution is listed in Table 3.6. The colours represent the same instruments as in Figure 3.14.

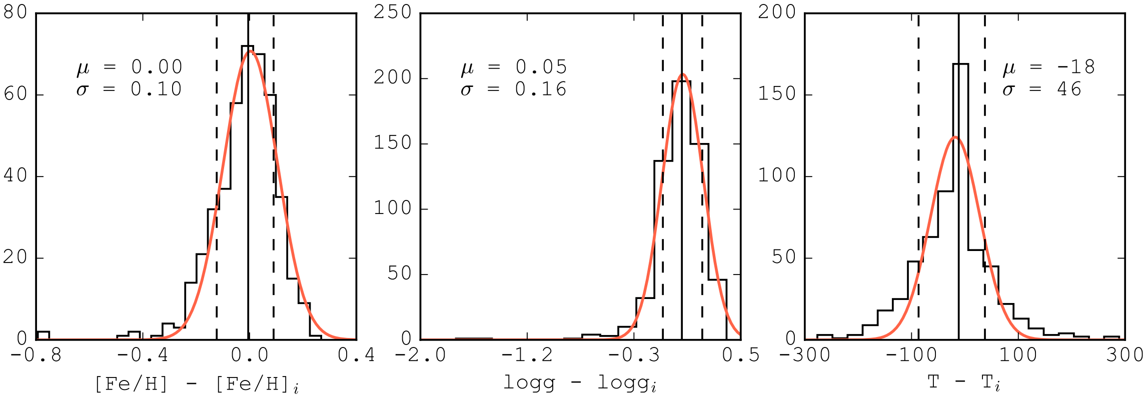

Figure 3.17: Histograms of the difference between the metallicity (left panel), surface gravity (middle panel) obtained with SPECIES, and from using the photometric relations from sections 3.1.3 and 3.1.3 (right panel). The vertical lines correspond (from left to right) to the 16, 50 and 84 percentiles.

we compared both results for our sample of FGK dwarfs stars, observed with HARPS, FEROS, HIRES, and UVES. We considered only the cases when it was not necessary to set the temperature from photometry as the correct value to reach converge in the derivation of the atmospheric parameters. For each star we retrieved the photometric information from Vizier, using the catalogues mentioned in Section 3.1, and computed the temperature using the relations from Section 3.1.3.

We computed the difference between the temperature from SPECIES, and from using each photometric relation, for spectra taken with different instruments. We then adjusted Gaussian models to the distributions obtained, and define the mean of the model as the offset between each temperature measurement. This was done for every relation described in Section 3.1.3, except when using González Hernández and Bonifacio (2009), due to the small number of stars in our sample which met the requirement of being classified as giants. Instead of adjusting Gaussian models to the distribution, we just computed the mean of the difference, setting that value as the offset between both temperature measurements. The results from the comparisons are shown in Figures 3.14, 3.15, and 3.16, and Tables 3.4, 3.5, and 3.6, for the relations from Casagrande et al. (2010), Mann et al. (2015), and Pecaut and Mamajek (2013).

We use these offsets to correct the temperatures obtained using the photometric relations (section 3.1.3), to match the values with those obtained by SPECIES. For the case of the relations from González Hernández and Bonifacio (2009), we did not perform this comparison because we had no giants in our test.

Finally, we compared the final metallicity, surface gravity and temperatures obtained with SPECIES, and the initial values derived from photometry in section 3.1.3, 3.1.3, and 3.1.3. The distributions we obtain for the difference between both quantities are shown in Figure 3.17. For all three parameters we find them to be distributed around zero (median of the distributions around -0.0001 and 0.02 for the metallicity and surface gravity, respectively), meaning excellent agreement. We find only a few cases that the values from SPECIES are smaller than from the photometric relations.

Table 3.7: Parameters of the Gaussian distributions adjusted to the difference of stellar parameters from SPECIES and from the literature. $\mu$ and $\sigma$ correspond to the mean and standard deviation of the distributions, respectively.

| Parameter | Sousa et al. (2008) | | Brewer et al. (2016) | | Bond et al. (2006) | | Bensby et al. (2014) | | Ivanyuk et al. (2017) | |
|---|---|---|---|---|---|---|---|---|---|---|
| | $\mu$ | $\sigma$ | $\mu$ | $\sigma$ | $\mu$ | $\sigma$ | $\mu$ | $\sigma$ | $\mu$ | $\sigma$ |
| $M$ ($M_\odot$) | 0.04 | 0.06 | 0.04 | 0.11 | | | 0.01 | 0.04 | | |
| Age (Gyr) | | | -0.46 | 1.77 | | | -0.41 | 2.24 | | |
| $R$ ($R_\odot$) | | | 0.00 | 0.03 | | | | | | |
| $T$ (K) | 26 | 53 | 55 | 55 | 110 | 92 | 51 | 65 | 100 | 65 |
| [Fe/H] | 0.03 | 0.03 | 0.04 | 0.03 | 0.11 | 0.06 | 0.02 | 0.05 | 0.14 | 0.06 |
| log g | 0.00 | 0.09 | 0.02 | 0.11 | 0.04 | 0.16 | 0.00 | 0.12 | 0.01 | 0.10 |
| $\xi_t$ (km s$^{-1}$) | -0.17 | 0.09 | | | -0.38 | 0.15 | -0.17 | 0.13 | -0.25 | 0.12 |
| $v \sin i$ (km s$^{-1}$) | | | 0.46 | 0.89 | | | | | -1.02 | 0.45 |
| $v_{mac}$ (km s$^{-1}$) | | | -0.22 | 0.25 | | | | | | |

Notes: The offset for each catalogue is taken to be $\mu$ from this table.

### 3.2.2 Comparison with other catalogues

In order to test the accuracy of SPECIES, we compared the spectral parameters for a set of stars obtained with our code, with ones listed in the literature. We chose five different catalogues for this comparison, since each had analysed a large sample of stars and they all used differing methods to compute the stellar parameters, providing a robust test of the SPECIES automatic calculations. The samples are briefly described as follows:

- Brewer et al. (2016, hereafter SPOCS2), a continuation of Valenti and Fischer (2005, SPOCS), in which stellar parameters were presented for ~ 1000 stars. They used the spectral synthesis method to derive the atmospheric parameters, and interpolation using Yonsei-Yale (Y2) isochrones (Demarque et al. 2004) to obtain mass and age measurements. They set the microturbulence velocity to 4 km/s through their calculation, and derive a formula for the macroturbulence velocity very similar to the one used in this work (Eq 3.13). In SPOCS2, the abundances list was increased, as well as the number of stars in their sample (~ 1600 stars).

- Sousa et al. (2008, hereafter S08), in which they used the same method as we did to compute the atmospheric parameters ($T_{\text{eff}}$, log g , [Fe/H], and $\xi_t$), that is by computing the EWs using ARES for a set of iron lines and then using MOOG to derive their stellar parameters. In the case of the abundances for other chemical elements, we used the values from Adibekyan et al. (2012, hereafter A12), which uses the atmospheric parameters derived in S08.

- Bond et al. (2006, hereafter B06), where the procedure used to derive their parameters also relied on the measurement of EWs, assuming LTE to derive the atmospheric parameters. There are considerable differences between their method and ours. First, they measured the EWs of their lines by direct integration, instead of Gaussian fitting, as is done in this work. Second, the temperatures were derived using the star colours, following the relation from

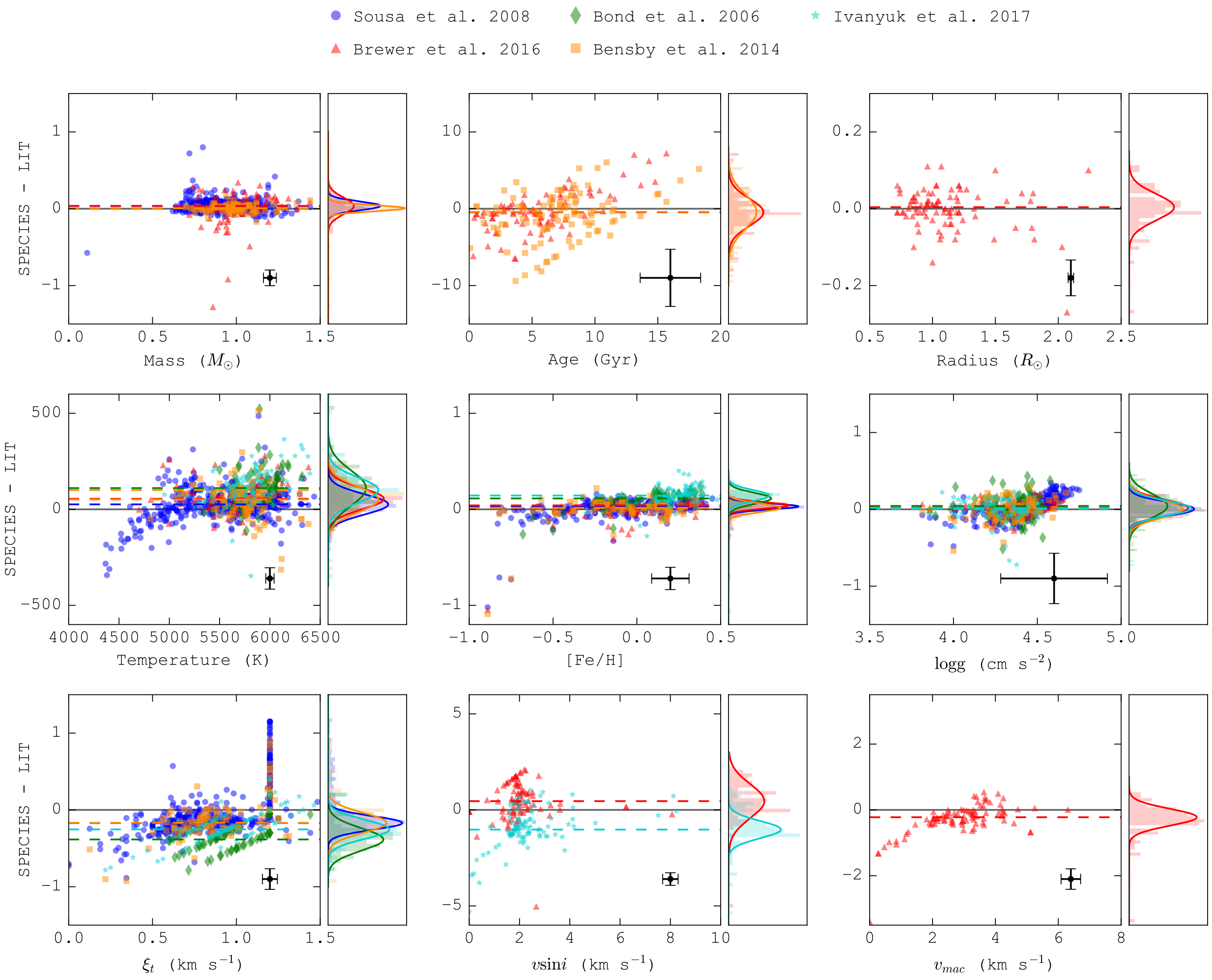

Figure 3.18: Comparison between the values for different parameters obtained with our code and from literature. The y-axis in the plots correspond to the difference between both measurements, represented by different symbols and colours: blue circles to Sousa et al. (2008), red triangles to Brewer et al. (2016), green diamonds to Bond et al. (2006), orange squares to Bensby et al. (2014), and cyan stars to Ivanyuk et al. (2017). The black points in the bottom right of each plot represents the average uncertainty in the points. The histograms in the right panels of each of the plots show the distribution of the results, fitted by Gaussian functions, with parameters given in Table 3.7.

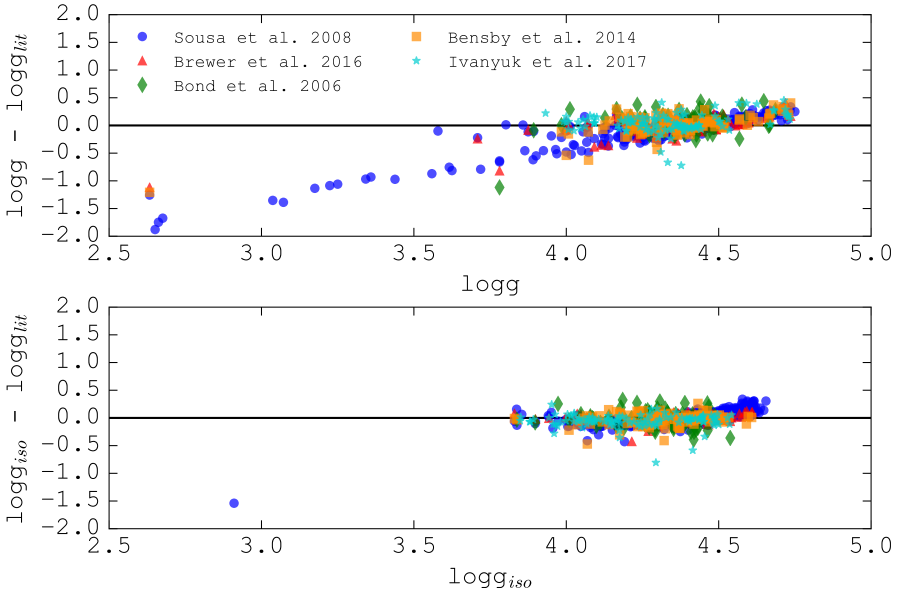

Figure 3.19: Comparison between the surface gravity from SPECIES, and from the literature. In the top panel, the surface gravity from SPECIES corresponds to the results obtained from the convergence of the atmospheric parameters (section 3.1.4), without the option of recomputing using log $g_{iso}$ . In the bottom panel, the surface gravity from SPECIES corresponds to the log $g_{iso}$ obtained for the same stars (section 3.1.6).

Table 3.8: Parameters of the Gaussian distributions adjusted to the difference of atomic abundance from SPECIES and from the literature. $\mu$ and $\sigma$ correspond to the mean and standard deviation of the distributions, respectively.

| Element | Adibekyan et al. (2012) | | Brewer et al. (2016) | | Bond et al. (2006) | | Bensby et al. (2014) | | Ivanyuk et al. (2017) | |
|---|---|---|---|---|---|---|---|---|---|---|
| | $\mu$ | $\sigma$ | $\mu$ | $\sigma$ | $\mu$ | $\sigma$ | $\mu$ | $\sigma$ | $\mu$ | $\sigma$ |
| [Na/H] | -0.06 | 0.07 | 0.13 | 0.07 | -0.00 | 0.05 | 0.14 | 0.07 | 0.06 | 0.06 |
| [Mg/H] | 0.04 | 0.06 | 0.12 | 0.05 | | | 0.06 | 0.07 | 0.03 | 0.09 |
| [Al/H] | 0.00 | 0.05 | 0.14 | 0.04 | 0.22 | 0.05 | 0.09 | 0.07 | 0.20 | 0.04 |
| [Si/H] | 0.01 | 0.07 | 0.07 | 0.08 | 0.04 | 0.07 | 0.04 | 0.08 | 0.07 | 0.10 |
| [Ca/H] | 0.07 | 0.06 | 0.24 | 0.06 | 0.14 | 0.07 | 0.12 | 0.06 | 0.14 | 0.09 |
| [Ti/H] | -0.02 | 0.08 | 0.10 | 0.08 | 0.01 | 0.09 | 0.06 | 0.09 | 0.14 | 0.09 |
| [Cr/H] | 0.04 | 0.05 | 0.08 | 0.07 | | | 0.05 | 0.05 | 0.14 | 0.07 |
| [Mn/H] | 0.35 | 0.08 | 0.16 | 0.07 | | | | | 0.04 | 0.08 |
| [Ni/H] | 0.00 | 0.06 | 0.02 | 0.05 | 0.06 | 0.06 | 0.01 | 0.06 | 0.01 | 0.07 |

Notes: The offset for each catalogue is taken to be $\mu$ from this table.

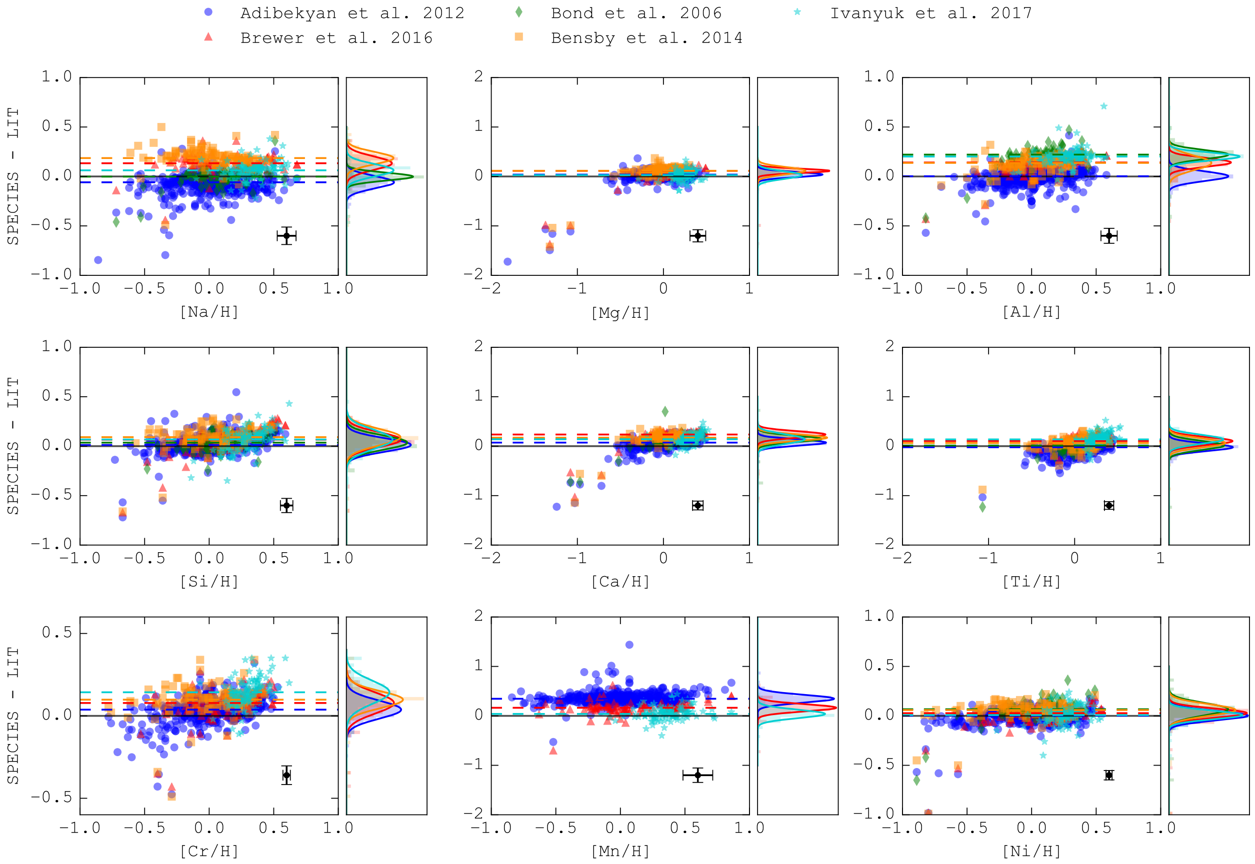

Figure 3.20: Comparison between the abundances for different elements obtained with our code and from literature. The y-axis in the plots correspond to the difference between both measurements, represented by different symbols: blue circles to Sousa et al. (2008), red triangles to Brewer et al. (2016), green squares to Bond et al. (2006), orange squares to Bensby et al. (2014), and cyan stars to Ivanyuk et al. (2017). The black points in the bottom right of each plot represents the average uncertainty in the points. The histograms at the right panels of each plots show the distribution of the results, fitted by Gaussian functions.

Smith (1995). Finally, they derived the metallicity with two different methods, one using Strömgren *uvby* colours (Strömgren 1966), and the other using the measured EW. For this comparison, we are using the metallicity values derived through spectroscopy.

- Bensby et al. (2014, hereafter B14), in which they also used EW measurements, along with LTE model stellar atmospheres, in order to determine the parameters. The differences between their method and ours are that in B14 they used the MARCS code (Gustafsson et al. 1975) to solve the radiative transfer equations, computed the EW for each line using the IRAF task SPLOT, and used Y2 isochrones to derive the mass and age of each star.

- Ivanyuk et al. (2017, hereafter I17), where they used the Infrared Flux Method (IRFM Blackwell and Lynas-Gray 1994) calibration to derive effective temperatures, and the modified numerical scheme developed by Pavlenko (2017) in order to compute the iron abundance, surface gravity, microturbulent and rotational velocity, from high S/N HARPS spectra observed as part of the Calan-Hertfordshire Extrasolar Planet Search (CHEPS) programme (Jenkins et al. 2009). These values were then used to derive the atomic abundances for several elements.

We selected the highest S/N spectra taken with HARPS (given that it is the highest resolution instrument currently accepted by SPECIES) for each star we wanted to analyse, which left us with 95 stars for SPOCS2, 435 stars for S08, 67 stars for B06, 99 stars for B14, and 103 stars for I17

The comparison between the atmospheric parameters (plus mass and age) from each catalogue and ours are shown in Figure 3.18. In Figure 3.20 the same comparison is shown for the chemical abundances (only the elements we had in common with each catalogue).

#### Fundamental physical parameters

In order to study the agreement between our results for the fundamental parameters ($T_{\rm eff}$, [Fe/H], log g, $\xi_t$, $v \sin$ i, $v_{mac}$, mass, age, and radius), with that of the literature, we computed the difference between both measurements, obtaining for each parameter and catalogue a distribution of differences around zero. Then, for each distribution we adjusted a Gaussian function obtaining the mean ($\mu$) and standard deviation ($\sigma$) of the difference of results. For the analysis performed in the following sections, we consider the mean of the distribution as the offset between our results and the literature, and the significance of that offset will be given by the width of the distribution, and how far away from zero it is located. The difference in parameters, as well as the adjusted Gaussian distributions, are shown in Figure 3.18, and the Gaussian parameters ($\mu$, $\sigma$) are shown in Table 3.7.

We find that, overall, the measurements are in good agreement ($\mu \leq 1.5\sigma$) among the different catalogues, albeit with a few exceptions. These are found for the following quantities: for the temperature, $\mu = 1.55\sigma$ against I17. For the metallicity, $\mu = 1.80\sigma$ and $2.30\sigma$ against the values from B06 and I17, respectively. For the microturbulence, we find $\mu = 1.89\sigma$, $2.50\sigma$, and $2.1\sigma$ against S08, B06, and I17, respectively. Finally, for the rotational velocity, we find that $\mu = 2.30\sigma$ for the distribution of our results against the ones from I17.

The largest discrepancies are found against the values from B06 and I17. Those catalogues are the only ones that only use photometric calibrations to derive the stellar temperatures (as explained above). In order to check if the temperature is the source of the discrepancies, we fixed the temperature to the values listed in B06 and I17, and then recomputed the rest of the parameters, for the stars we had in common with those catalogues. We find that, while the offsets with metallicity are significantly improved (0.0 and 0.04 with respect to B06 and I17, respectively), the other parameters do not improve. We conclude that the differences in temperature against what was obtained in B06 and I17 produce the offsets in metallicity, but are not responsible for the discrepancies with the rest of the parameters. The results for the rotational velocity are also very different between SPECIES and I17. The SPECIES results are smaller than for I17, except for very few exceptions. We believe this is caused by considering the line broadening as the contribution from rotational and macroturbulence velocities, instead of taking into account only the rotational contribution (as was done in I17). This manifests into lower rotational velocities than in I17.

As for the offsets seen with the other catalogues, these can be due to the different method and calibrations used to derive the parameters, and can be corrected with respect to the ones obtained with SPECIES by applying the values in Table 3.7.

We looked again at the differences with $\log g$ and $\log g_{\rm iso}$. In section 3.1.6, we stated that $\log g_{\rm iso}$ (the surface gravity a star would have for the mass, age and radius derived from isochrones) is a better indication of the true $\log g$ than the spectroscopic value. We now compare the surface gravities from the literature against those that SPECIES would obtain without the option to recompute the stellar parameters with $\log g = \log g_{\rm iso}$, and against $\log g_{\rm iso}$. This is shown in Figure 3.19. We obtain large discrepancies between $\log g$ and the literature for $\log g < 4.0$, but this difference disappears when using the $\log g_{\rm iso}$ value. This supports the statement we made in section 3.1.6, that $\log g_{\rm iso}$ is a better representation of the true surface gravity of a star in a lot of cases. SPECIES will use $\log g_{\rm iso}$ as the correct results for the cases when $\log g - \log g_{\rm iso} > 0.22$ dex.

### Atomic abundances

For the analysis of the atomic abundances from SPECIES, we followed the same procedure as in the previous section. We obtained the differences between the measurements from SPECIES and from the same catalogues already described and adjusted Gaussian distributions to the results. The results of this are shown in Figure 3.20, and the parameters of the Gaussian distributions ($\mu$, $\sigma$) are shown in Table 3.8. Different abundances for the sun were used as references in each of the works, so we first need to correct the results in the literature for the differences between their reference solar abundances and the scale used in this work (solar chemical composition from Asplund et al. 2009). We also remind the reader that the abundances for the S08 stars are listed in Adibekyan et al. (2012, hereafter A12).

We find that the largest discrepancies are seen against the results of SPOCS2, and I17. For SPOCS2, $\mu = 1.86\sigma$, $2.4\sigma$, $3.5\sigma$, $4\sigma$, and $2.29\sigma$ for Na, Mg, Al, Ca, and Mn, respectively. For I17, $\mu = 5\sigma$, $1.56\sigma$, $1.56\sigma$, and $2\sigma$ for Al, Ca, Ti, and Cr, respectively. We checked if the differences with I17 are again a consequence of the method they used to derive the temperature, by recomputing the abundances using the temperature from I17. We find a decrease in the offsets with respect to Ca and Ti ($\mu < 1.5\sigma$), but almost no change in the results for Al and Cr. The improvement in the differences for some of the elements was expected, given that in the previous section we found that

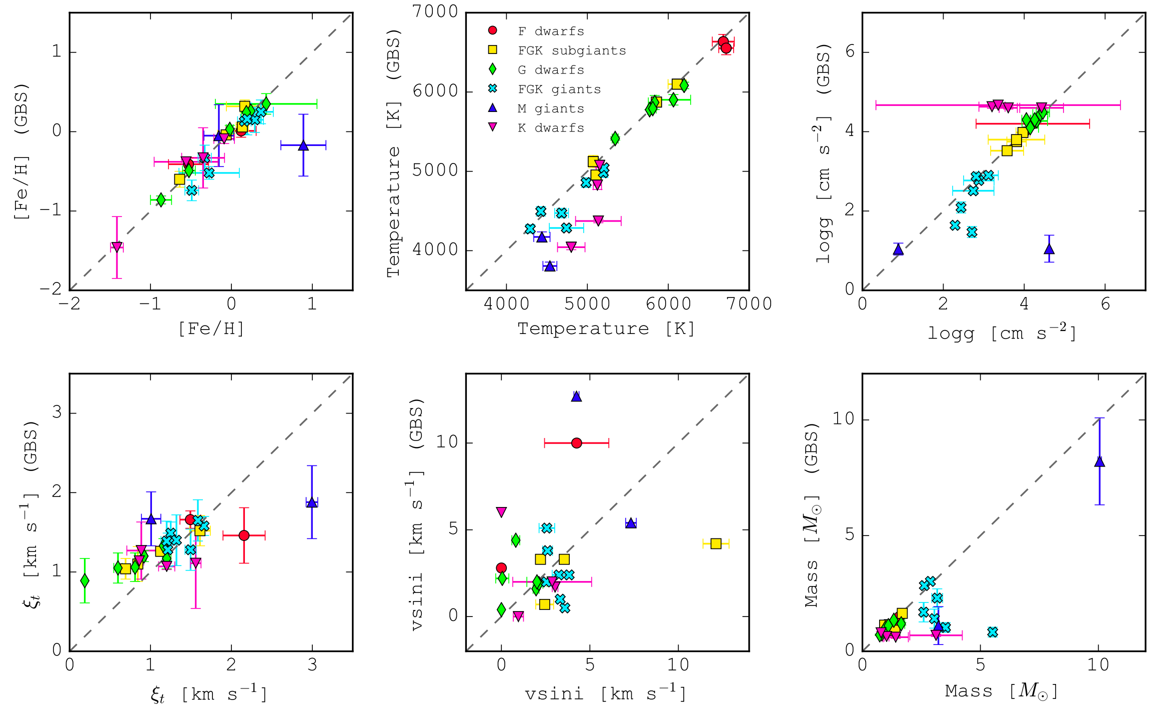

Figure 3.21: Results for the stellar parameters, obtained with SPECIES (x-axis), compared with what was found in the literature (y-axis), for the GBS sample. The different symbols denote different spectral types. The dashed line represents the 1:1 relation.

the discrepancy with the metallicity is significantly decreased when using the temperature from I17, which thus will affect the final chemical abundance. By seeing no improvement in Al and Cr, we can conclude that those elements are less affected by temperature and metallicity than the rest of the species analysed. We performed the same analysis but using the temperature from SPOCS2, to see if there are changes with the chemical abundance. We find that the discrepancies with Na and Mn decreases, falling below the 1.5 $\sigma$ level, but for Mg, Al, and Ca we do not see such improvements, with the offsets still above the 1.5 $\sigma$ level. This shows that differences in the temperature obtained between this work and SPOCS2 are not the source of the large abundance differences for Mg, Al, and Ca. I17 also compared their abundances against results from other catalogues (some of them included in this work) and even though they found similar trends in abundance versus metallicity, they do see offsets between them. One of the explanations they find includes selection effects and differences in atomic line data.

Other large discrepancies we find are: $\mu_{B14} = 2\sigma_{B14}$ for Na, $\mu_{B06} = 4.4\sigma_{B06}$ for Al, $\mu_{B06} = 2\sigma_{B06}$ and $\mu_{B14} = 2\sigma_{B14}$ for Ca, and $\mu_{A12} = 4.4\sigma_{A12}$ for Mn. These can be explained by the differences in method used to derive the abundances, and differences in the line list used.

### Results for the Gaia Benchmark Stars sample

Finally, we compared the results obtained with SPECIES for the Gaia Benchmark Stars (GBS) sample. This sample consists of 34 FGK stars, presented in Jofré et al. (2014), spanning a wide

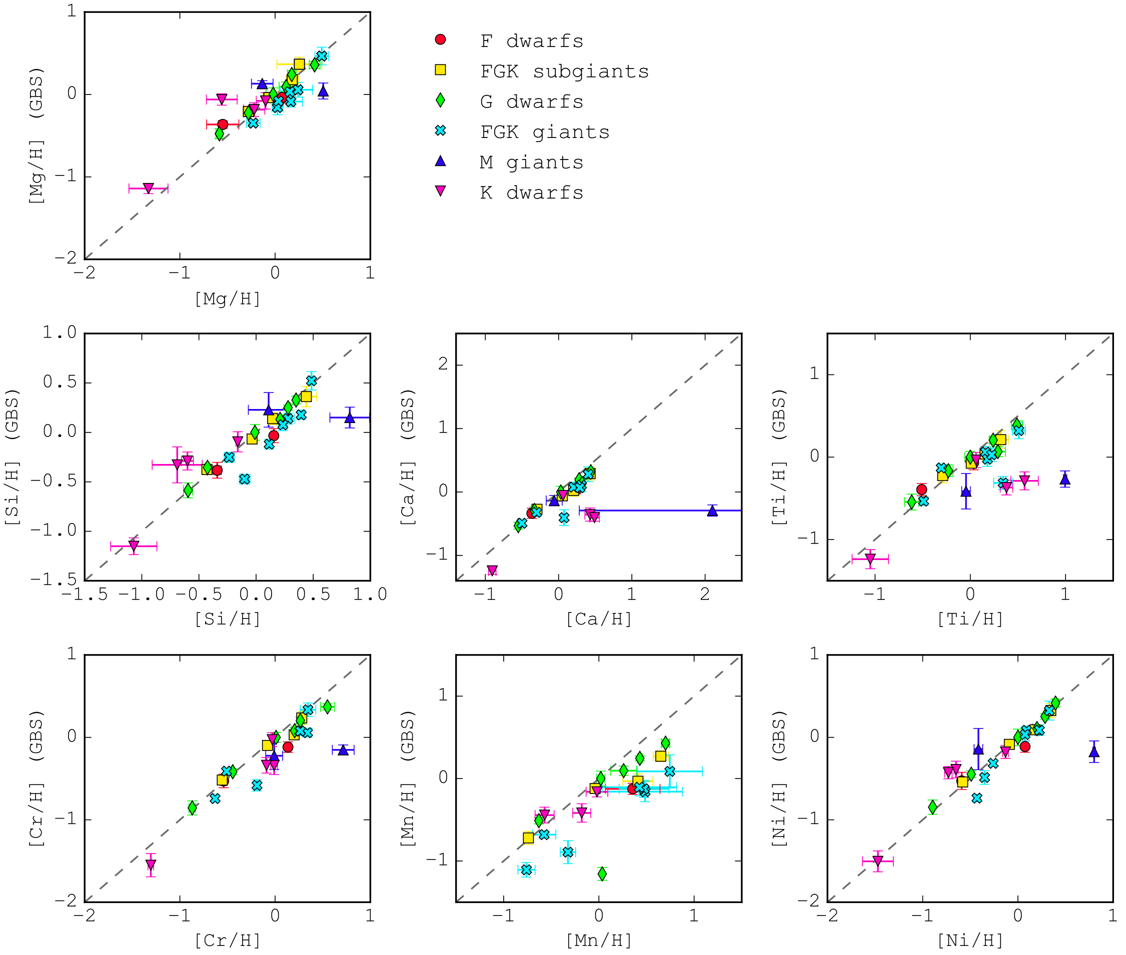

Figure 3.22: Results for the chemical abundance of $\alpha$ and iron peak elements, obtained with SPECIES (x-axis), compared with what was found in the literature (y-axis), for the GBS sample. The different symbols denote different spectral types. The dashed line represents the 1:1 relation.

range of metallicities and gravities, which translates into different evolutionary stages.

The GBS sample was presented and studied in several works: Jofré et al. (2014) for the determination of metallicity, Heiter et al. (2015) for the effective temperature and surface gravity, and Jofré et al. (2015) for chemical abundance of $\alpha$ and iron peak elements. In those papers, the parameters for each star were computed using different methods (except for the rotational velocity, for which they extract values from the literature). The input spectra were obtained from Blanco-Cuaresma et al. (2014), and correspond to HARPS data. The results obtained with SPECIES for the GBS sample are shown in Figure 3.21, for the atmospheric parameters, as well as rotational velocity and mass, and in Figure 3.22 for chemical abundance. It is important to note that SPECIES could not converge to correct solutions for every star. Those corresponded, in most of the cases, to stars with very few spectral lines (mostly giant stars), or stars that are part of a spectroscopic binary system, where line blending was present in the spectra. The results obtained for each star are listed on Table C.4 and C.5.

We find that the results from SPECIES are systematically larger than the ones from the literature, for all the parameters analysed. In term of the spectral types, we find good agreement with the FGK subgiant, giant, and G dwarf samples (mean of difference for each parameter between SPECIES and the literature is less than $1\sigma$ the mean uncertainty from SPECIES), with the exception of the mass and Mn abundance of FGK giants, where SPECIES obtained values larger than $1\sigma$ from the mean uncertainty. It is not possible to draw more conclusions for the other spectral types (F dwarfs, M giants, and K dwarfs), due to the low number of stars for each type ($<$ 3 stars for each case). We also looked at the $\log \mathrm{g}_{\mathrm{iso}}$ obtained for the Gaia stars, and found them to be very similar to the surface gravity from Heiter et al. (2015). This favours the statement we made in sections 3.1.6 and 3.2.2, in which $\log \mathrm{g}_{\mathrm{iso}}$ is a good representation of the true $\log \mathrm{g}$ for a lot of cases, now including stars in different evolutionary stages, with $\log \mathrm{g} < 4.0$ dex.

### 3.2.3 Correlation between parameters

We studied whether there were strong correlations between the stellar parameters, by plotting each quantity against the rest, considering only points within $3\sigma$ of the mean. We find that the majority of the parameters derived using this code show no strong correlations between each other, as can be seen in Figure 3.25, even though we do find some exceptions. We find that the mass, radius, temperature and macroturbulent velocities show correlations among each other, as is shown in Figure 3.23. We adjusted the following relations to those correlations:

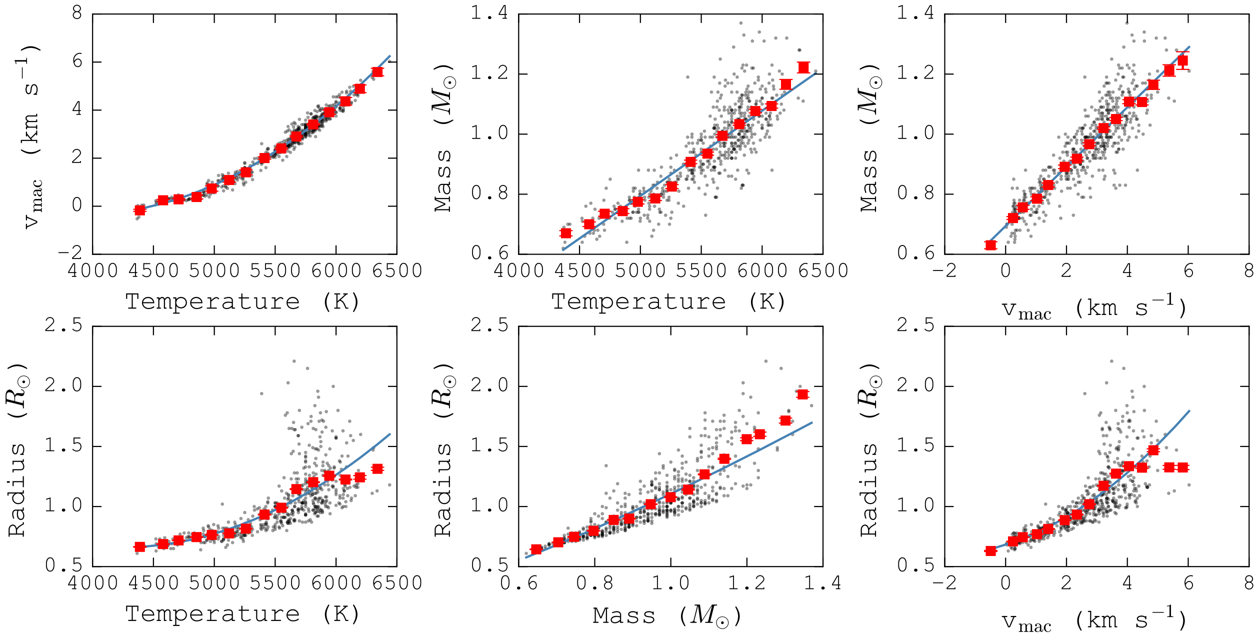

Figure 3.23: Correlations between the stellar parameters computed by SPECIES. The red squares are the binned data points, and the blue lines correspond to the fits described in Equation 3.15. The data used correspond to points within $3\sigma$ of their corresponding distribution.

$$
\begin{aligned}
v_{mac} &= \frac{(T-5777)^2}{9.3\times10^5} + \frac{(T-5777)}{251} + 3.54,\\
M &= \frac{(T-5777)}{3371} + 1.03,\\
M &= 0.10\,v_{mac} + 0.66,\\
R &= \frac{(T-5777)^2}{5.84\times10^6} + \frac{(T-5777)}{1802} + 1.1,\\
R &= 1.08\,M^{1.28},\\
R &= 0.01\,v_{mac}^2 + 0.08\,v_{mac} + 0.66.
\end{aligned}
\tag{3.15}
$$

All these relations are shown as the blue lines in Figure 3.23.

The mass correlation with temperature reflects the known mass-luminosity relationship for stars (Kuiper (1938)), for which $L \propto M^{\alpha}$. Dwarf stars increase in luminosity for higher temperatures, therefore the relation can be interpreted as larger mass for higher surface temperature. The correlation between macroturbulence velocity and temperature is produced by the method we used to derive $v_{mac}$, following equation 3.13 (Section 3.1.8), and the increased depth of the convective envelope with decreasing temperature. In the equation for instance, the metallicity dependence is not as strong as the temperature dependence, which explains why we do not see such a strong correlation between macroturbulence velocity and metallicity (Figure 3.25). The relation between stellar mass and radius has been well studied over the years, and for main sequence stars, Demircan and Kahraman (1991) found that where $R = 1.06\,M^{0.945}$, for $M < 1.66M_\odot$. The fit we performed to the SPECIES results is in agreement with the previous relation.

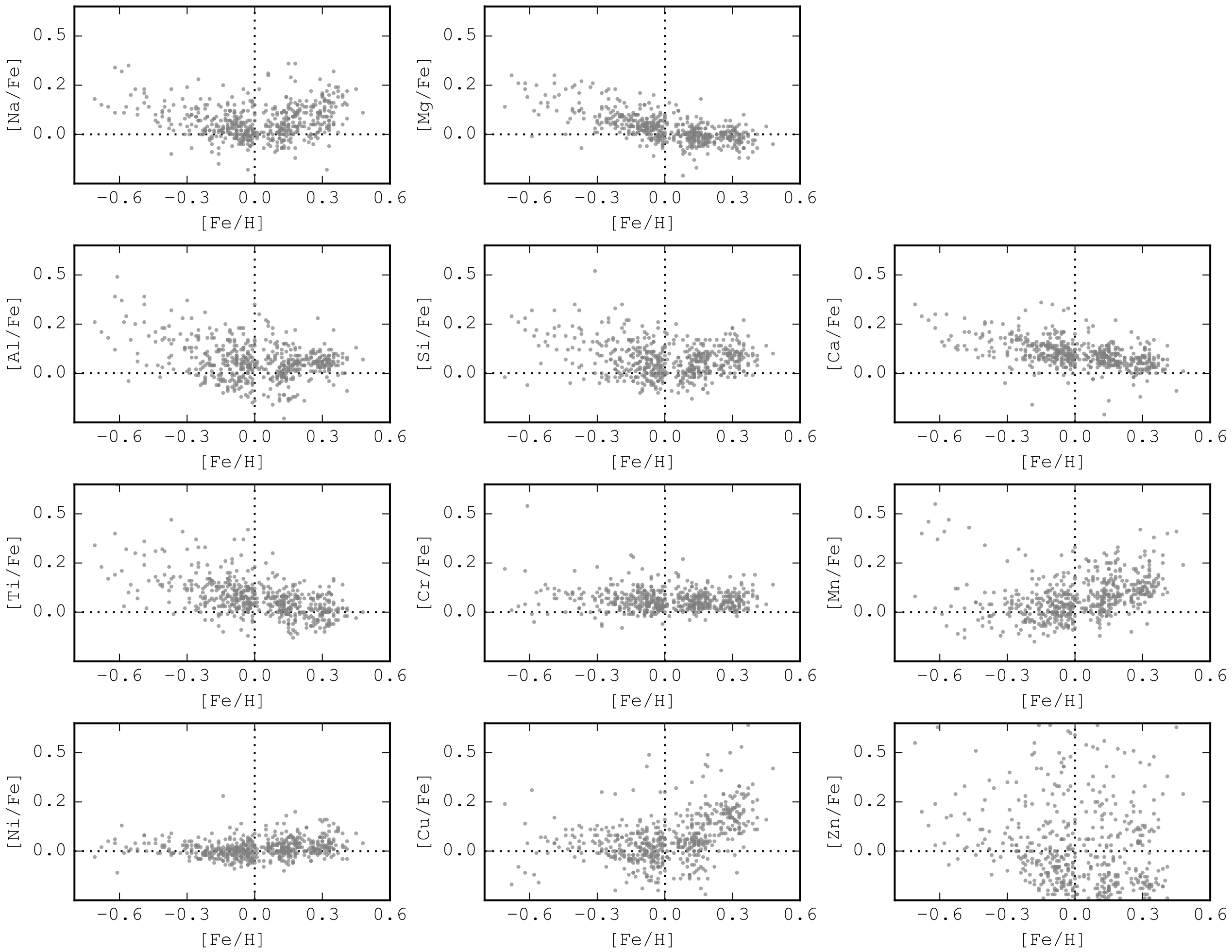

Figure 3.24: Abundances for the 11 elements analysed by SPECIES with respect to iron, versus metallicity. This includes all the stars studied in section 3.2.2, as well as from the Gaia benchmark sample (section 3.2.2).

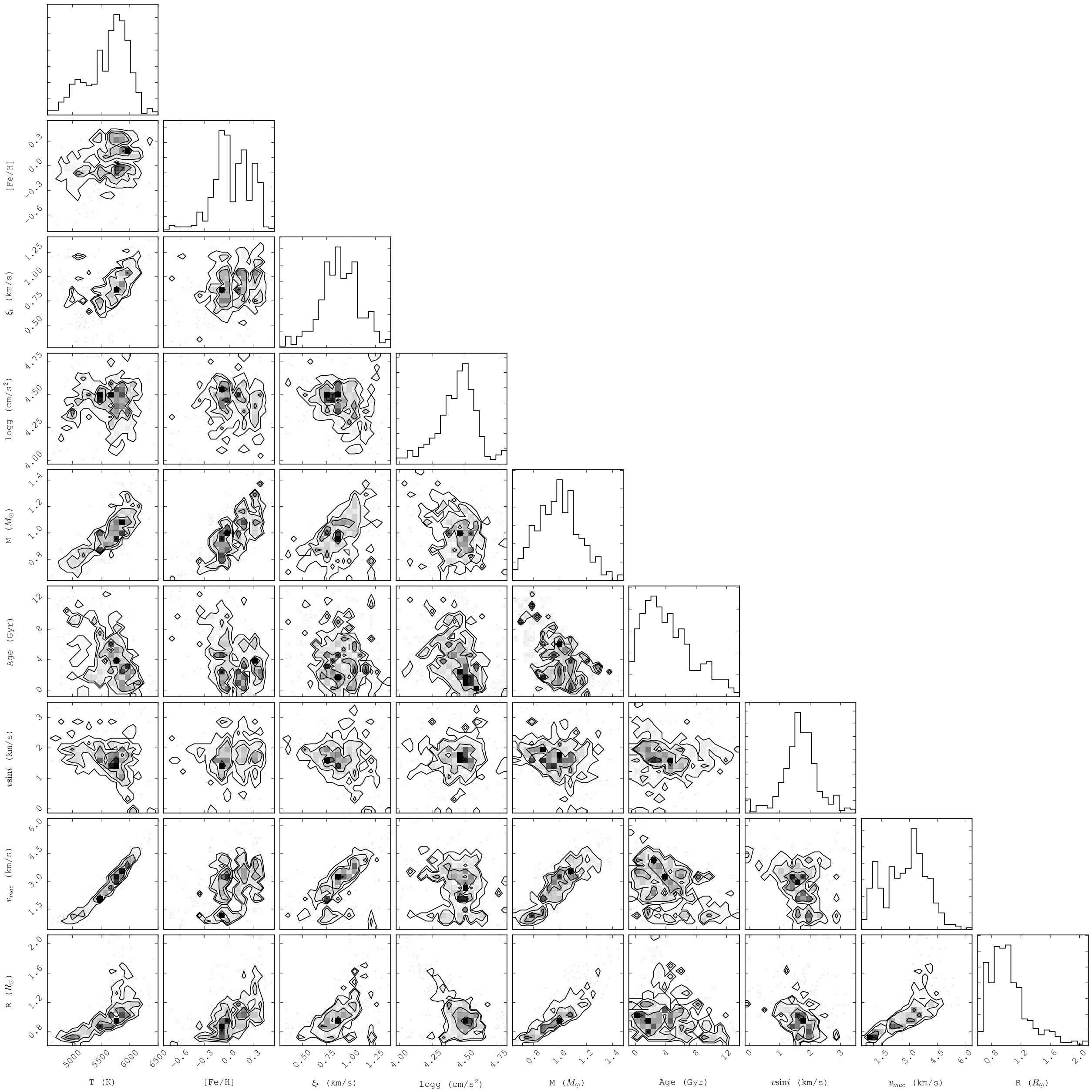

Figure 3.25: Correlation between the atmospheric parameters, as well as the mass and age for each stars, derived by this code for HARPS spectra. The histograms the the top of each column show the distribution of every single quantity. For log g , $\xi_t$, and age, the points farther than $3\sigma$ from the mean of the distribution were not included.

Table 3.9: Gaussian distribution parameters ($\mu$, $\sigma$) obtained for the difference between stellar parameters from HARPS, and from other instruments.

| Parameter | FEROS | | UVES | | HIRES | |
|---|---|---|---|---|---|---|
| | $\mu$ | $\sigma$ | $\mu$ | $\sigma$ | $\mu$ | $\sigma$ |
| $M$ ($M_\odot$) | 0.00 | 0.02 | 0.00 | -0.02 | 0.00 | 0.03 |
| Age (Gyr) | -0.04 | 1.16 | 0.27 | 0.93 | 0.33 | 1.15 |
| $R$ ($R_\odot$) | 0.00 | 0.01 | 0.01 | 0.01 | 0.01 | 0.01 |
| $T$ (K) | 10 | 50 | -11 | 61 | -21 | 39 |
| [Fe/H] | 0.02 | 0.06 | 0.01 | 0.04 | 0.04 | 0.08 |
| log g | 0.05 | 0.11 | 0.01 | 0.08 | -0.01 | 0.09 |
| $\xi_t$ (km s$^{-1}$) | -0.12 | 0.17 | -0.02 | 0.11 | -0.07 | 0.15 |
| $v \sin$ i (km s$^{-1}$) | 0.84 | 0.76 | 0.18 | 0.34 | -0.21 | 0.69 |
| $v_{mac}$ (km s$^{-1}$) | -0.01 | 0.15 | 0.06 | 0.02 | 0.09 | 0.16 |

Notes: The distributions are shown in on top of the histograms in Figure 3.26.

The rest of the strong correlations seen in Figure 3.23 are a consequence of the relations mentioned previously. The relation between mass and microturbulence is due to the relation between microturbulence and temperature, and of mass with temperature. The macroturbulence with microturbulence is also due to the relation between both quantities and temperature. Finally, the relation between macroturbulence and mass is produced by the effect temperature has on both parameters.

When looking at the chemical compositions, we studied its abundance with respect to iron, versus the star's overall metallicity. This is shown in Figure 3.24. We find that, for most of the elements, their abundance is greater than iron in metal-poor stars, and resembles (Mg, Al, Ca, Ti, Cr, Ni) or is greater (Na, Mn, Cu) than iron for metal-rich ([Fe/H] ≥ 0.0) stars. This behaviour is very similar to that of Ivanyuk et al. (2017), where they also compare their results with catalogues in the literature (some of them are also included in this work). We cannot make any conclusions about the behaviour of Zn, given that the spread in the results is too large.

### 3.2.4 Offsets between different instruments

In order to use this code with spectra from different instruments, it is necessary to understand any offsets that are present between the parameters computed with spectra taken from different spectrographs. We compared the results we obtained for the stars used in the previous section, using four of the available instruments accepted by our code (HARPS, FEROS, UVES, and HIRES). The results of this comparison are shown in Figure 3.26 for the atmospheric parameters and in Figure 3.27 for the abundances. It is important to point out that not all the stars were observed with all instruments, therefore the number of stars compared per instrument varies, with 118 for FEROS, 115 for UVES, and 89 for HIRES.

We followed the same procedure used in the previous sections to analyse the significance of the

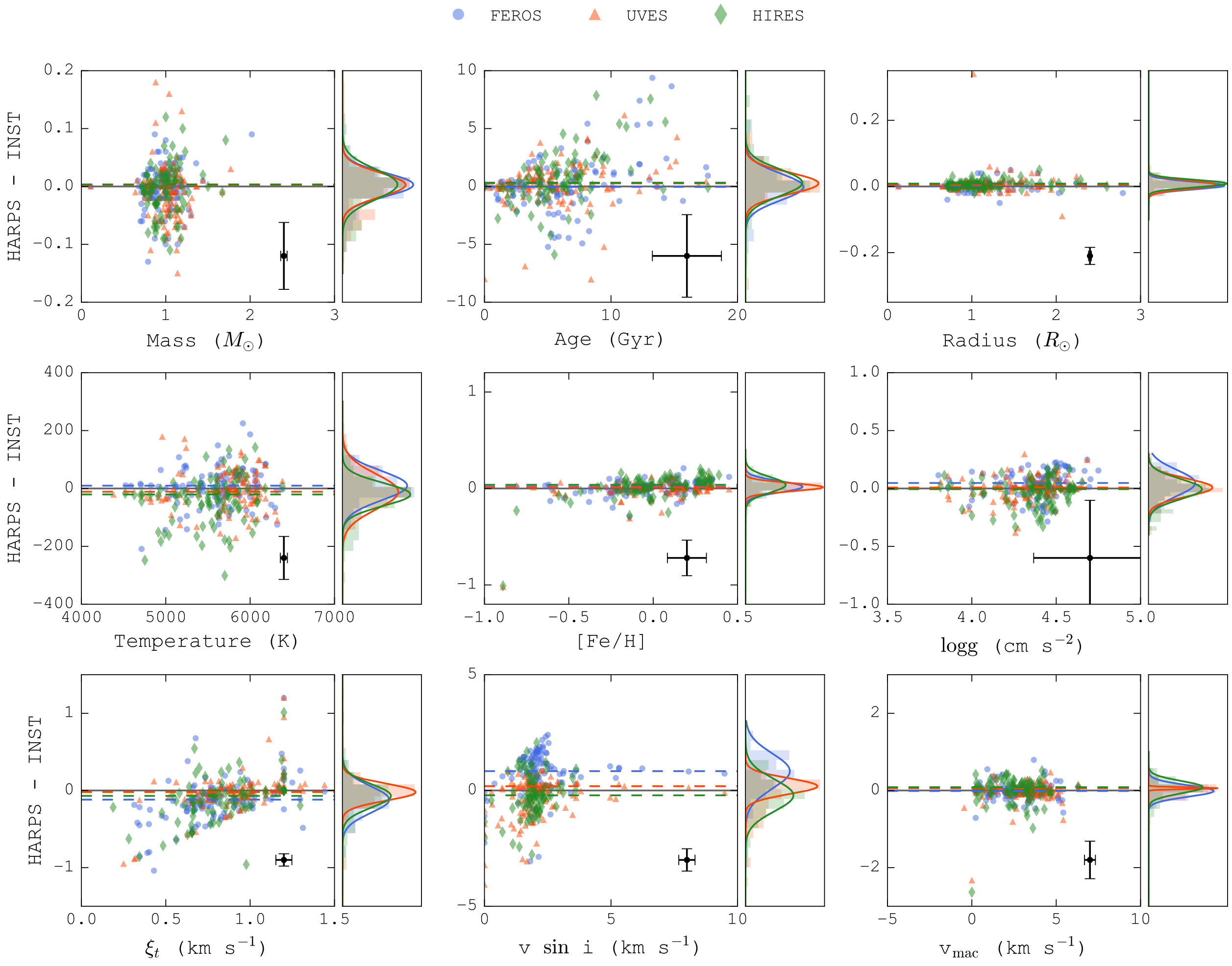

Figure 3.26: Comparison between the stellar parameters obtained using spectra from different instruments, with respect to the ones obtained with HARPS. The y-axis for each plot corresponds to the difference between the parameters. Blue dots correspond to FEROS data, red triangles to UVES data, and green diamonds to HIRES data. For each panel, the right-hand plot corresponds to the distribution of the values, and solid line to the Gaussian distribution adjusted to each histogram. The black points in the bottom right of each plot represents the average uncertainty in the points.

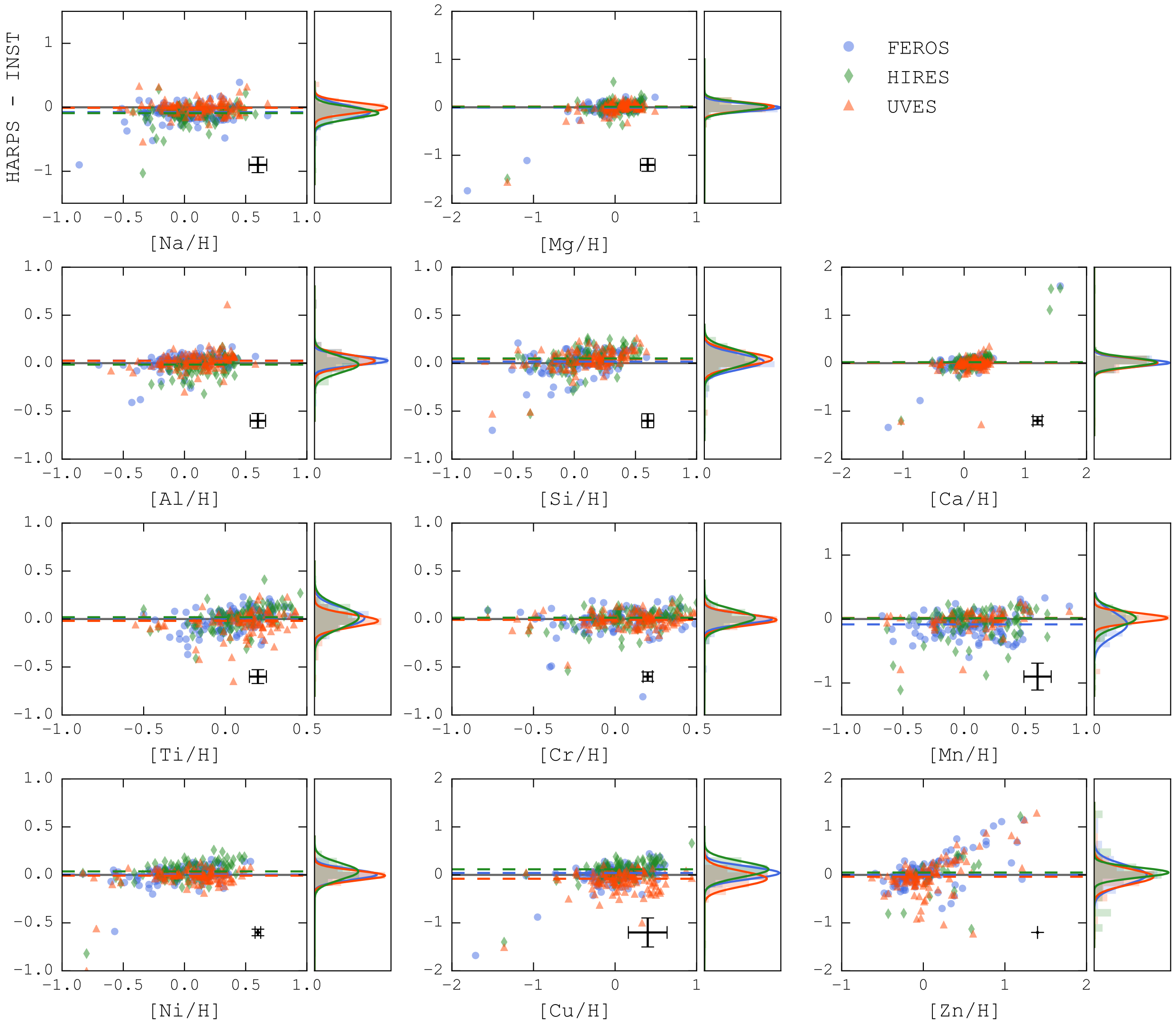

Figure 3.27: Comparison between the abundances obtained with spectra from different instruments, with respect to the values obtained with HARPS spectra. The y-axis for each panel corresponds to the difference between the values from HARPS, and from FEROS (blue squares), UVES (red triangles), and HIRES (green diamonds). The right-hand plots show the distribution of the values, along with their Gaussian distribution fit. The black points in the bottom right of each plot represents the average uncertainty in the points.

Table 3.10: Gaussian distribution parameters ($\mu$, $\sigma$) obtained for the difference between atomic abundances from HARPS, and from other instruments.

| Element | FEROS | | UVES | | HIRES | |
|---|---|---|---|---|---|---|
| | $\mu$ | $\sigma$ | $\mu$ | $\sigma$ | $\mu$ | $\sigma$ |
| [Na/H] | -0.08 | 0.11 | -0.01 | 0.08 | -0.09 | 0.09 |
| [Mg/H] | -0.01 | 0.08 | 0.02 | 0.08 | 0.01 | 0.09 |
| [Al/H] | 0.03 | 0.05 | 0.02 | 0.06 | -0.02 | 0.08 |
| [Si/H] | 0.02 | 0.08 | 0.04 | 0.07 | 0.05 | 0.09 |
| [Ca/H] | 0.01 | 0.08 | 0.01 | 0.09 | 0.02 | 0.09 |
| [Ti/H] | 0.01 | 0.10 | -0.02 | 0.07 | 0.02 | 0.11 |
| [Cr/H] | 0.00 | 0.05 | -0.01 | 0.06 | 0.01 | 0.08 |
| [Mn/H] | -0.08 | 0.19 | 0.02 | 0.07 | 0.01 | 0.13 |
| [Ni/H] | 0.00 | 0.05 | -0.01 | 0.05 | 0.04 | 0.09 |
| [Cu/H] | 0.04 | 0.13 | -0.08 | 0.16 | 0.12 | 0.16 |
| [Zn/H] | -0.00 | 0.20 | -0.04 | 0.16 | 0.05 | 0.10 |

Notes: The distributions are shown in on top of the histograms in Figure 3.27.

differences in results. In this case, the comparison was done with respect to the HARPS results. The parameters for the Gaussian distributions adjusted to the difference in results are listed in Tables 3.9 and 3.10, for the atmospheric parameters and atomic abundance, respectively.

From both tables, it can be seen that all the quantities are in good agreement among all the instruments, with $\mu < 1.5\sigma$ for each of them. This shows that SPECIES delivers consistent results with spectra from different high resolution spectrographs. We do want to mention that the only quantity with an offset larger than $1\sigma$ is seen in $v \sin \mathrm{i}$, with respect to FEROS, with $\mu = 1.15\sigma$. We believe this is caused mainly because of the lower spectral resolution ($R$ = 48000) of FEROS, with respect to the rest of the instruments ($R$ = 115000, 110000, and 67000 for HARPS, UVES, and HIRES, respectively, as it appears in their documentation). This produces larger instrumental broadening, which, together with the macroturbulence contribution, dominate the absorption line profiles. In those cases, the rotational broadening has to be larger than ~2 km s$^{-1}$in order to make a contribution to the line profile that is measurable with FEROS (Murgas et al. 2013). This is also the reason behind the almost constant increase in difference for larger HARPS $v \sin \mathrm{i}$, for low rotational velocities (up to 2 km s$^{-1}$). For those low values, the line profiles measured with FEROS are still dominated by macroturbulence and instrumental broadening, resulting in a constant $v \sin \mathrm{i}$ for FEROS. This leads us to then set a minimum limit for the rotational velocity measured using FEROS spectra of 2 km s$^{-1}$. For stars with slower rotation, the FEROS spectral resolution makes it difficult to obtain accurate results. In the future, we will perform the same comparison, but using spectra from the other instruments accepted by SPECIES that are not included in this analysis (i.e. Coralie, AAT).

## 3.3 Summary and conclusions

In this chapter we have presented a new code to derive stellar parameters in an automated way, using high resolution stellar spectra and minimal photometric inputs. The parameters calculated by SPECIES agree with previously published values at the $1\sigma$ level, for works using the same method as the one used in this work (EW measurements), as well as others (synthetic spectra). The code presented here computes all the stellar parameters in a self-consistent way, and we include in our values the rotational and macroturbulence velocity for each star, which is not present in most of the major catalogues that employ the EW method.

We also show the methods we used to derive the uncertainties for the atmospheric parameters, by providing analytic formulas that can be later used by others in the study of correlations between each parameter. We have listed the correlations present in our values, which can be linked to the physics that govern stars, or to the methods we use to derive them. We recommend the use of SPECIES for FGK dwarf and subgiant stars, for which we had tested it against a large sample of stars, and to use it with caution for giant stars, which will be tested more in future works. SPECIES has been used in Bluhm et al. (2016), Jones et al. (2017), Díaz et al. (2018), and Pantoja et al. (2018, submitted to MNRAS).

In future works we will apply the SPECIES code to accept spectra from more instruments, we will study a wide range of stars across a large evolutionary range to probe in detail the underlying nature of element production, and also we aim to include a module in SPECIES that will allow the calculation of precise parameters for M dwarf stars, where dust and molecules play a significant role.

Finally we note that SPECIES takes of the order of five minutes on a standard iMac desktop with a 3.2Gb processor to obtain all the parameters for a single stellar spectrum. It can be run in single spectra mode or in parallel to simultaneously analyse large data sets.

# Conclusions and future work

In this work we show results obtained in the area of exoplanet detection and stellar characterization during the course of this thesis.

We analyzed radial velocity data from the FEROS spectrograph, using a different pipeline than the one previously available, and compared our results with those already published in the literature. We concluded that the new pipeline produced more precise radial velocities than what was previously measured. We also combined the FEROS data with measurements from other spectrographs, and after performing Keplerian fits to the radial velocities, we could confirm the presence of three exoplanets previously detected orbiting three different giant stars. We also rejected the existence of another three exoplanets that were published as bonefide discoveries, and we finally reported the discovery of a new planetary companion to a giant star HD 110014b.

In the next stage of the work, we used radial velocity data from HARPS, FEROS, and Coralie, and combined it with photometric data taken with the K2 space mission, to report the detection of two new hot Jupiters orbiting the stars K2-237 and K2-238. Based on the Keplerian solutions adjusted to both the radial velocity and photometric data, we concluded that K2-237b corresponds to a highly inflated planet, which makes an excellent candidate for further atmospheric studies, and that K2-238b is consistent with a H/He gaseous planet with some significant metal content.

Finally, this thesis work concludes with discussing a third part of the project, which was the development of the SPECIES code. SPECIES is now being used to characterize stellar sources using high-resolution echelle spectra, allowing the primary stellar bulk parameters to be measured, along with a detailed profile of the chemical abundance patterns of stars. The results we obtained with SPECIES for over 400 test stars, are in good agreement with what has been found in the literature, even when different methods were used to derive them. We also provide analytic relations that can be later used by others in the study of correlations between each atmospheric parameter. We conclude that SPECIES is an excellent tool for stellar characterization, given that it computes a large number of parameters in an homogeneous and automatic fashion, and therefore it is now being used as the primary stellar characterisation tool for the Next Generation Transit Survey.

Looking forward, in the future we would like to conduct the second part of the RAFT project, consisting of a new reanalysis of the FEROS radial velocities using the CERES pipeline for the data reduction, and see how much our results might change, along with studying new systems that were part of the same large survey we scrutinised in detail in this work. We will also work on the expansion and improvement of SPECIES, which will include the addition of modules for the computation of activity indicators, along with the computation of stellar parameters for M dwarfs and M giant stars.

# Bibliography

V. Z. Adibekyan, S. G. Sousa, N. C. Santos, E. Delgado Mena, J. I. González Hernández, G. Israelian, M. Mayor, and G. Khachatryan. Chemical abundances of 1111 FGK stars from the HARPS GTO planet search program. Galactic stellar populations and planets. *A&A*, 545:A32, Sept. 2012. doi: 10.1051/0004-6361/201219401.

S. Aigrain, H. Parviainen, and B. J. S. Pope. K2SC: flexible systematics correction and detrending of K2 light curves using Gaussian process regression. *MNRAS*, 459:2408–2419, July 2016. doi: 10.1093/mnras/stw706.

D. R. Anderson, C. Hellier, M. Gillon, A. H. M. J. Triaud, B. Smalley, L. Hebb, A. Collier Cameron, P. F. L. Maxted, D. Queloz, R. G. West, S. J. Bentley, B. Enoch, K. Horne, T. A. Lister, M. Mayor, N. R. Parley, F. Pepe, D. Pollacco, D. Ségransan, S. Udry, and D. M. Wilson. WASP-17b: An Ultra-Low Density Planet in a Probable Retrograde Orbit. *ApJ*, 709:159–167, Jan. 2010. doi: 10.1088/0004-637X/709/1/159.

E. Anderson and C. Francis. XHIP: An extended hipparcos compilation. *Astronomy Letters*, 38: 331–346, May 2012. doi: 10.1134/S1063773712050015.

G. Anglada-Escudé, P. Arriagada, M. Tuomi, M. Zechmeister, J. S. Jenkins, A. Ofir, S. Dreizler, E. Gerlach, C. J. Marvin, and A. Reiners. Two planets around Kapteyn's star: a cold and a temperate super-Earth orbiting the nearest halo red dwarf. *MNRAS*, 443:L89–L93, Sept. 2014. doi: 10.1093/mnrasl/slu076.

G. Anglada-Escudé, P. J. Amado, J. Barnes, Z. M. Berdiñas, R. P. Butler, G. A. L. Coleman, I. de La Cueva, S. Dreizler, M. Endl, B. Giesers, S. V. Jeffers, J. S. Jenkins, H. R. A. Jones, M. Kiraga, M. Kürster, M. J. López-González, C. J. Marvin, N. Morales, J. Morin, R. P. Nelson, J. L. Ortiz, A. Ofir, S.-J. Paardekooper, A. Reiners, E. Rodríguez, C. Rodríguez-López, L. F. Sarmiento, J. P. Strachan, Y. Tsapras, M. Tuomi, and M. Zechmeister. A terrestrial planet candidate in a temperate orbit around Proxima Centauri. *Nature*, 536:437–440, Aug. 2016. doi: 10.1038/nature19106.

R. Angus, T. Morton, S. Aigrain, D. Foreman-Mackey, and V. Rajpaul. Inferring probabilistic stellar rotation periods using Gaussian processes. *MNRAS*, 474:2094–2108, Feb. 2018. doi: 10.1093/mnras/stx2109.

P. Arriagada. Chromospheric Activity of Southern Stars from the Magellan Planet Search Program. *ApJ*, 734:70, June 2011. doi: 10.1088/0004-637X/734/1/70.

M. Asplund, N. Grevesse, A. J. Sauval, and P. Scott. The Chemical Composition of the Sun. *ARA&A*, 47:481–522, Sept. 2009. doi: 10.1146/annurev.astro.46.060407.145222.

G. Á. Bakos, Z. Csubry, K. Penev, D. Bayliss, A. Jordán, C. Afonso, J. D. Hartman, T. Henning, G. Kovács, R. W. Noyes, B. Béky, V. Suc, B. Csák, M. Rabus, J. Lázár, I. Papp, P. Sári, P. Conroy, G. Zhou, P. D. Sackett, B. Schmidt, L. Mancini, D. D. Sasselov, and K. Ueltzhoeffer. HATSouth: A Global Network of Fully Automated Identical Wide-Field Telescopes. *PASP*, 125:154, Feb. 2013. doi: 10.1086/669529.

S. L. Baliunas, R. A. Donahue, W. H. Soon, J. H. Horne, J. Frazer, L. Woodard-Eklund, M. Bradford, L. M. Rao, O. C. Wilson, Q. Zhang, W. Bennett, J. Briggs, S. M. Carroll, D. K. Duncan, D. Figueroa, H. H. Lanning, T. Misch, J. Mueller, R. W. Noyes, D. Poppe, A. C. Porter, C. R. Robinson, J. Russell, J. C. Shelton, T. Soyumer, A. H. Vaughan, and J. H. Whitney. Chromospheric variations in main-sequence stars. *ApJ*, 438:269–287, Jan. 1995. doi: 10.1086/175072.

A. Baranne, D. Queloz, M. Mayor, G. Adrianzyk, G. Knispel, D. Kohler, D. Lacroix, J.-P. Meunier, G. Rimbaud, and A. Vin. ELODIE: A spectrograph for accurate radial velocity measurements. *A&AS*, 119:373–390, Oct. 1996.

F. A. Bastien, K. G. Stassun, G. Basri, and J. Pepper. An observational correlation between stellar brightness variations and surface gravity. *Nature*, 500:427–430, Aug. 2013. doi: 10.1038/nature12419.

F. A. Bastien, K. G. Stassun, J. Pepper, J. T. Wright, S. Aigrain, G. Basri, J. A. Johnson, A. W. Howard, and L. M. Walkowicz. Radial Velocity Variations of Photometrically Quiet, Chromospherically Inactive Kepler Stars: A Link between RV Jitter and Photometric Flicker. *AJ*, 147: 29, Feb. 2014. doi: 10.1088/0004-6256/147/2/29.

N. M. Batalha, J. F. Rowe, R. L. Gilliland, J. J. Jenkins, D. Caldwell, W. J. Borucki, D. G. Koch, J. J. Lissauer, E. W. Dunham, T. N. Gautier, S. B. Howell, D. W. Latham, G. W. Marcy, and A. Prsa. Pre-spectroscopic False-positive Elimination of Kepler Planet Candidates. *ApJ*, 713: L103–L108, Apr. 2010. doi: 10.1088/2041-8205/713/2/L103.

T. C. Beers, C. Flynn, S. Rossi, J. Sommer-Larsen, R. Wilhelm, B. Marsteller, Y. S. Lee, N. De Lee, J. Krugler, C. P. Deliyannis, A. T. Simmons, E. Mills, F.-J. Zickgraf, J. Holmberg, A. Önehag, A. Eriksson, D. M. Terndrup, S. Salim, J. Andersen, B. Nordström, N. Christlieb, A. Frebel, and J. Rhee. Broadband UBVR$_C$I$_C$ Photometry of Horizontal-Branch and Metal-poor Candidates from the HK and Hamburg/ESO Surveys. I. *ApJS*, 168:128–139, Jan. 2007. doi: 10.1086/509324.

T. Bensby, S. Feltzing, and M. S. Oey. Exploring the Milky Way stellar disk. A detailed elemental abundance study of 714 F and G dwarf stars in the solar neighbourhood. *A&A*, 562:A71, Feb. 2014. doi: 10.1051/0004-6361/201322631.

Z. M. Berdiñas, C. Rodríguez-López, P. J. Amado, G. Anglada-Escudé, J. R. Barnes, J. MacDonald, M. Zechmeister, and L. F. Sarmiento. High-cadence spectroscopy of M-dwarfs - II. Searching for stellar pulsations with HARPS. *MNRAS*, 469:4268–4282, Aug. 2017. doi: 10.1093/mnras/stx1140.

M. S. Bessell and J. M. Brett. JHKLM photometry - Standard systems, passbands, and intrinsic colors. *PASP*, 100:1134–1151, Sept. 1988. doi: 10.1086/132281.

D. E. Blackwell and A. E. Lynas-Gray. Stellar effective temperatures and angular diameters determined by the infrared flux method (IRFM): Revisions using improved Kurucz LTE stellar atmospheres. *A&A*, 282:899–910, Feb. 1994.

S. Blanco-Cuaresma, C. Soubiran, P. Jofré, and U. Heiter. The Gaia FGK benchmark stars. High resolution spectral library. *A&A*, 566:A98, June 2014. doi: 10.1051/0004-6361/201323153.

P. Bluhm, M. I. Jones, L. Vanzi, M. G. Soto, J. Vos, R. A. Wittenmyer, H. Drass, J. S. Jenkins, F. Olivares, R. E. Mennickent, M. Vučković, P. Rojo, and C. H. F. Melo. New spectroscopic binary companions of giant stars and updated metallicity distribution for binary systems. *A&A*, 593:A133, Oct. 2016. doi: 10.1051/0004-6361/201628459.

I. Boisse, C. Moutou, A. Vidal-Madjar, F. Bouchy, F. Pont, G. Hébrard, X. Bonfils, B. Croll, X. Delfosse, M. Desort, T. Forveille, A.-M. Lagrange, B. Loeillet, C. Lovis, J. M. Matthews, M. Mayor, F. Pepe, C. Perrier, D. Queloz, J. F. Rowe, N. C. Santos, D. Ségransan, and S. Udry. Stellar activity of planetary host star HD 189 733. *A&A*, 495:959–966, Mar. 2009. doi: 10.1051/0004-6361:200810648.

I. Boisse, F. Pepe, C. Perrier, D. Queloz, X. Bonfils, F. Bouchy, N. C. Santos, L. Arnold, J.-L. Beuzit, R. F. Díaz, X. Delfosse, A. Eggenberger, D. Ehrenreich, T. Forveille, G. Hébrard, A.-M. Lagrange, C. Lovis, M. Mayor, C. Moutou, D. Naef, A. Santerne, D. Ségransan, J.-P. Sivan, and S. Udry. The SOPHIE search for northern extrasolar planets. V. Follow-up of ELODIE candidates: Jupiter-analogs around Sun-like stars. *A&A*, 545:A55, Sept. 2012. doi: 10.1051/0004-6361/201118419.

I. A. Bond, A. Udalski, M. Jaroszyński, N. J. Rattenbury, B. Paczyński, I. Soszyński, L. Wyrzykowski, M. K. Szymański, M. Kubiak, O. Szewczyk, K. Żebruń, G. Pietrzyński, F. Abe, D. P. Bennett, S. Eguchi, Y. Furuta, J. B. Hearnshaw, K. Kamiya, P. M. Kilmartin, Y. Kurata, K. Masuda, Y. Matsubara, Y. Muraki, S. Noda, K. Okajima, T. Sako, T. Sekiguchi, D. J. Sullivan, T. Sumi, P. J. Tristram, T. Yanagisawa, P. C. M. Yock, and OGLE Collaboration. OGLE 2003-BLG-235/MOA 2003-BLG-53: A Planetary Microlensing Event. *ApJ*, 606:L155–L158, May 2004. doi: 10.1086/420928.

J. C. Bond, C. G. Tinney, R. P. Butler, H. R. A. Jones, G. W. Marcy, A. J. Penny, and B. D. Carter. The abundance distribution of stars with planets. *MNRAS*, 370:163–173, July 2006. doi: 10.1111/j.1365-2966.2006.10459.x.

X. Bonfils, M. Mayor, X. Delfosse, T. Forveille, M. Gillon, C. Perrier, S. Udry, F. Bouchy, C. Lovis, F. Pepe, D. Queloz, N. C. Santos, and J.-L. Bertaux. The HARPS search for southern extra-solar planets. X. A m sin i = 11 $M_\oplus$ planet around the nearby spotted M dwarf GJ 674. *A&A*, 474: 293–299, Oct. 2007. doi: 10.1051/0004-6361:20077068.

W. J. Borucki, D. Koch, G. Basri, N. Batalha, T. Brown, D. Caldwell, J. Caldwell, J. Christensen-Dalsgaard, W. D. Cochran, E. DeVore, E. W. Dunham, A. K. Dupree, T. N. Gautier, J. C. Geary, R. Gilliland, A. Gould, S. B. Howell, J. M. Jenkins, Y. Kondo, D. W. Latham, G. W. Marcy,

S. Meibom, H. Kjeldsen, J. J. Lissauer, D. G. Monet, D. Morrison, D. Sasselov, J. Tarter, A. Boss, D. Brownlee, T. Owen, D. Buzasi, D. Charbonneau, L. Doyle, J. Fortney, E. B. Ford, M. J. Holman, S. Seager, J. H. Steffen, W. F. Welsh, J. Rowe, H. Anderson, L. Buchhave, D. Ciardi, L. Walkowicz, W. Sherry, E. Horch, H. Isaacson, M. E. Everett, D. Fischer, G. Torres, J. A. Johnson, M. Endl, P. MacQueen, S. T. Bryson, J. Dotson, M. Haas, J. Kolodziejczak, J. Van Cleve, H. Chandrasekaran, J. D. Twicken, E. V. Quintana, B. D. Clarke, C. Allen, J. Li, H. Wu, P. Tenenbaum, E. Verner, F. Bruhweiler, J. Barnes, and A. Prsa. Kepler Planet-Detection Mission: Introduction and First Results. *Science*, 327:977, Feb. 2010. doi: 10.1126/science.1185402.

F. Bouchy, F. Pepe, and D. Queloz. Fundamental photon noise limit to radial velocity measurements. *A&A*, 374:733–739, Aug. 2001. doi: 10.1051/0004-6361:20010730.

J. Bovy, H.-W. Rix, G. M. Green, E. F. Schlafly, and D. P. Finkbeiner. On Galactic Density Modeling in the Presence of Dust Extinction. *ApJ*, 818:130, Feb. 2016. doi: 10.3847/0004-637X/818/2/130.

R. Brahm, M. Jones, N. Espinoza, A. Jordán, M. Rabus, F. Rojas, J. S. Jenkins, C. Cortés, H. Drass, B. Pantoja, M. G. Soto, and M. Vučković. An Independent Discovery of Two Hot Jupiters from the K2 Mission. *PASP*, 128(12):124402, Dec. 2016. doi: 10.1088/1538-3873/128/970/124402.

R. Brahm, A. Jordán, and N. Espinoza. CERES: A Set of Automated Routines for Echelle Spectra. *PASP*, 129(3):034002, Mar. 2017a. doi: 10.1088/1538-3873/aa5455.

R. Brahm, A. Jordán, J. Hartman, and G. Bakos. ZASPE: A Code to Measure Stellar Atmospheric Parameters and their Covariance from Spectra. *MNRAS*, 467:971–984, May 2017b. doi: 10.1093/mnras/stx144.

R. Brahm, N. Espinoza, A. Jordán, F. Rojas, P. Sarkis, M. R. Díaz, M. Rabus, H. Drass, R. Lachaume, M. G. Soto, J. S. Jenkins, M. I. Jones, T. Henning, B. Pantoja, and M. Vučković. K2-232 b: a transiting warm Saturn on an eccentric P = 11.2 days orbit around a V = 9.9 star. *MNRAS*, Mar. 2018. doi: 10.1093/mnras/sty795.

P. N. Brandt and S. K. Solanki. Solar line asymmetries and the magnetic filling factor. *A&A*, 231: 221–234, May 1990.

J. M. Brewer, D. A. Fischer, J. A. Valenti, and N. Piskunov. Spectral Properties of Cool Stars: Extended Abundance Analysis of 1,617 Planet-search Stars. *ApJS*, 225:32, Aug. 2016. doi: 10.3847/0067-0049/225/2/32.

T. M. Brown. Expected Detection and False Alarm Rates for Transiting Jovian Planets. *ApJ*, 593: L125–L128, Aug. 2003. doi: 10.1086/378310.

T. M. Brown, R. Kotak, S. D. Horner, E. J. Kennelly, S. Korzennik, P. Nisenson, and R. W. Noyes. A Search for Line Shape and Depth Variations in 51 Pegasi and $\tau$ Bootis. *ApJ*, 494:L85–L88, Feb. 1998. doi: 10.1086/311168.

S. T. Bryson, J. M. Jenkins, R. L. Gilliland, J. D. Twicken, B. Clarke, J. Rowe, D. Caldwell, N. Batalha, F. Mullally, M. R. Haas, and P. Tenenbaum. Identification of Background False Positives from Kepler Data. *PASP*, 125:889, Aug. 2013. doi: 10.1086/671767.

L. A. Buchhave, D. W. Latham, A. Johansen, M. Bizzarro, G. Torres, J. F. Rowe, N. M. Batalha, W. J. Borucki, E. Brugamyer, C. Caldwell, S. T. Bryson, D. R. Ciardi, W. D. Cochran, M. Endl, G. A. Esquerdo, E. B. Ford, J. C. Geary, R. L. Gilliland, T. Hansen, H. Isaacson, J. B. Laird, P. W. Lucas, G. W. Marcy, J. A. Morse, P. Robertson, A. Shporer, R. P. Stefanik, M. Still, and S. N. Quinn. An abundance of small exoplanets around stars with a wide range of metallicities. *Nature*, 486:375–377, June 2012. doi: 10.1038/nature11121.

A. Burrows, I. Hubeny, J. Budaj, and W. B. Hubbard. Possible Solutions to the Radius Anomalies of Transiting Giant Planets. *ApJ*, 661:502–514, May 2007. doi: 10.1086/514326.

J. R. Burton, C. A. Watson, P. Rodríguez-Gil, I. Skillen, S. P. Littlefair, S. Dhillon, and D. Pollacco. Defocused transmission spectroscopy: a potential detection of sodium in the atmosphere of WASP-12b. *MNRAS*, 446:1071–1082, Jan. 2015. doi: 10.1093/mnras/stu2149.

R. P. Butler, G. W. Marcy, E. Williams, C. McCarthy, P. Dosanjh, and S. S. Vogt. Attaining Doppler Precision of 3 M s-1. *PASP*, 108:500, June 1996a. doi: 10.1086/133755.

R. P. Butler, G. W. Marcy, E. Williams, C. McCarthy, P. Dosanjh, and S. S. Vogt. Attaining Doppler Precision of 3 M s-1. *PASP*, 108:500, June 1996b. doi: 10.1086/133755.

A. C. Cameron. Extrasolar planets: Astrophysical false positives. *Nature*, 492:48–50, Dec. 2012. doi: 10.1038/492048a.

J. M. Carpenter. Color Transformations for the 2MASS Second Incremental Data Release. *AJ*, 121:2851–2871, May 2001. doi: 10.1086/320383.

L. Casagrande, L. Portinari, and C. Flynn. Accurate fundamental parameters for lower main-sequence stars. *MNRAS*, 373:13–44, Nov. 2006. doi: 10.1111/j.1365-2966.2006.10999.x.

L. Casagrande, I. Ramírez, J. Meléndez, M. Bessell, and M. Asplund. An absolutely calibrated $T_{eff}$ scale from the infrared flux method. Dwarfs and subgiants. *A&A*, 512:A54, Mar. 2010. doi: 10.1051/0004-6361/200913204.

F. Castelli and R. L. Kurucz. New Grids of ATLAS9 Model Atmospheres. *ArXiv Astrophysics e-prints*, May 2004.

F. Cavallini, G. Ceppatelli, and A. Righini. Asymmetry and shift of three Fe I photospheric lines in solar active regions. *A&A*, 143:116–121, Feb. 1985.

D. Charbonneau, T. M. Brown, D. W. Latham, and M. Mayor. Detection of Planetary Transits Across a Sun-like Star. *ApJ*, 529:L45–L48, Jan. 2000. doi: 10.1086/312457.

D. R. Ciardi, C. A. Beichman, E. P. Horch, and S. B. Howell. Understanding the Effects of Stellar Multiplicity on the Derived Planet Radii from Transit Surveys: Implications for Kepler, K2, and TESS. *ApJ*, 805:16, May 2015. doi: 10.1088/0004-637X/805/1/16.

A. Claret and P. H. Hauschildt. The limb-darkening for spherically symmetric NextGen model atmospheres: A-G main-sequence and sub-giant stars. *A&A*, 412:241–248, Dec. 2003. doi: 10.1051/0004-6361:20031405.

A. Collier Cameron, D. Pollacco, R. A. Street, T. A. Lister, R. G. West, D. M. Wilson, F. Pont, D. J. Christian, W. I. Clarkson, B. Enoch, A. Evans, A. Fitzsimmons, C. A. Haswell, C. Hellier, S. T. Hodgkin, K. Horne, J. Irwin, S. R. Kane, F. P. Keenan, A. J. Norton, N. R. Parley, J. Osborne, R. Ryans, I. Skillen, and P. J. Wheatley. A fast hybrid algorithm for exoplanetary transit searches. *MNRAS*, 373:799–810, Dec. 2006. doi: 10.1111/j.1365-2966.2006.11074.x.

R. M. Cutri, M. F. Skrutskie, S. van Dyk, C. A. Beichman, J. M. Carpenter, T. Chester, L. Cambresy, T. Evans, J. Fowler, J. Gizis, E. Howard, J. Huchra, T. Jarrett, E. L. Kopan, J. D. Kirkpatrick, R. M. Light, K. A. Marsh, H. McCallon, S. Schneider, R. Stiening, M. Sykes, M. Weinberg, W. A. Wheaton, S. Wheelock, and N. Zacarias. VizieR Online Data Catalog: 2MASS All-Sky Catalog of Point Sources (Cutri+ 2003). *VizieR Online Data Catalog*, 2246, June 2003.

L. da Silva, L. Girardi, L. Pasquini, J. Setiawan, O. von der Lühe, J. R. de Medeiros, A. Hatzes, M. P. Döllinger, and A. Weiss. Basic physical parameters of a selected sample of evolved stars. *A&A*, 458:609–623, Nov. 2006. doi: 10.1051/0004-6361:20065105.

J. R. de Medeiros, J. Setiawan, A. P. Hatzes, L. Pasquini, L. Girardi, S. Udry, M. P. Döllinger, and L. da Silva. A planet around the evolved intermediate-mass star HD 110014. *A&A*, 504: 617–623, Sept. 2009. doi: 10.1051/0004-6361/200911658.

J. R. De Medeiros, S. Alves, S. Udry, J. Andersen, B. Nordström, and M. Mayor. A catalog of rotational and radial velocities for evolved stars. V. Southern stars. *A&A*, 561:A126, Jan. 2014. doi: 10.1051/0004-6361/201220762.

H. Dekker, S. D'Odorico, A. Kaufer, B. Delabre, and H. Kotzlowski. Design, construction, and performance of UVES, the echelle spectrograph for the UT2 Kueyen Telescope at the ESO Paranal Observatory. In M. Iye and A. F. Moorwood, editors, *Optical and IR Telescope Instrumentation and Detectors*, volume 4008 of *Proc. SPIE*, pages 534–545, Aug. 2000.

P. Demarque, J.-H. Woo, Y.-C. Kim, and S. K. Yi. $Y^2$ Isochrones with an Improved Core Overshoot Treatment. *ApJS*, 155:667–674, Dec. 2004. doi: 10.1086/424966.

O. Demircan and G. Kahraman. Stellar mass-luminosity and mass-radius relations. *Ap&SS*, 181: 313–322, July 1991. doi: 10.1007/BF00639097.

B.-O. Demory and S. Seager. Lack of Inflated Radii for Kepler Giant Planet Candidates Receiving Modest Stellar Irradiation. *ApJS*, 197:12, Nov. 2011. doi: 10.1088/0067-0049/197/1/12.

S. Desidera, A. Sozzetti, A. S. Bonomo, R. Gratton, E. Poretti, R. Claudi, D. W. Latham, L. Affer, R. Cosentino, and M. Damasso. The GAPS programme with HARPS-N at TNG. II. No giant planets around the metal-poor star HIP 11952. *A&A*, 554:A29, June 2013. doi: 10.1051/0004-6361/201321155.

M. Desort, A.-M. Lagrange, F. Galland, S. Udry, and M. Mayor. Search for exoplanets with the radial-velocity technique: quantitative diagnostics of stellar activity. *A&A*, 473:983–993, Oct. 2007. doi: 10.1051/0004-6361:20078144.

M. R. Díaz, J. S. Jenkins, M. Tuomi, R. P. Butler, M. G. Soto, J. K. Teske, F. Feng, S. A. Shectman, P. Arriagada, J. D. Crane, I. B. Thompson, and S. S. Vogt. The Test Case of HD 26965: Difficulties Disentangling Weak Doppler Signals from Stellar Activity. *AJ*, 155:126, Mar. 2018. doi: 10.3847/1538-3881/aaa896.

R. F. Díaz, J. M. Almenara, A. Santerne, C. Moutou, A. Lethuillier, and M. Deleuil. PASTIS: Bayesian extrasolar planet validation - I. General framework, models, and performance. *MNRAS*, 441:983–1004, June 2014. doi: 10.1093/mnras/stu601.

L. A. dos Santos, J. Meléndez, J.-D. do Nascimento, M. Bedell, I. Ramírez, J. L. Bean, M. Asplund, L. Spina, S. Dreizler, A. Alves-Brito, and L. Casagrande. The Solar Twin Planet Search. IV. The Sun as a typical rotator and evidence for a new rotational braking law for Sun-like stars. *A&A*, 592:A156, Aug. 2016. doi: 10.1051/0004-6361/201628558.

A. Dotter. MESA Isochrones and Stellar Tracks (MIST) 0: Methods for the Construction of Stellar Isochrones. *ApJS*, 222:8, Jan. 2016. doi: 10.3847/0067-0049/222/1/8.

D. Dravins. Stellar granulation. VI - Four-component models and non-solar-type stars. *A&A*, 228: 218–230, Feb. 1990.

R. Drimmel, A. Cabrera-Lavers, and M. López-Corredoira. A three-dimensional Galactic extinction model. *A&A*, 409:205–215, Oct. 2003. doi: 10.1051/0004-6361:20031070.

J. R. Ducati. VizieR Online Data Catalog: Catalogue of Stellar Photometry in Johnson's 11-color system. *VizieR Online Data Catalog*, 2237, 2002.

X. Dumusque, C. Lovis, D. Ségransan, M. Mayor, S. Udry, W. Benz, F. Bouchy, G. Lo Curto, C. Mordasini, F. Pepe, D. Queloz, N. C. Santos, and D. Naef. The HARPS search for southern extra-solar planets. XXX. Planetary systems around stars with solar-like magnetic cycles and short-term activity variation. *A&A*, 535:A55, Nov. 2011a. doi: 10.1051/0004-6361/201117148.

X. Dumusque, S. Udry, C. Lovis, N. C. Santos, and M. J. P. F. G. Monteiro. Planetary detection limits taking into account stellar noise. I. Observational strategies to reduce stellar oscillation and granulation effects. *A&A*, 525:A140, Jan. 2011b. doi: 10.1051/0004-6361/201014097.

X. Dumusque, F. Pepe, C. Lovis, D. Ségransan, J. Sahlmann, W. Benz, F. Bouchy, M. Mayor, D. Queloz, N. Santos, and S. Udry. An Earth-mass planet orbiting $\alpha$ Centauri B. *Nature*, 491: 207–211, Nov. 2012. doi: 10.1038/nature11572.

X. Dumusque, I. Boisse, and N. C. Santos. SOAP 2.0: A Tool to Estimate the Photometric and Radial Velocity Variations Induced by Stellar Spots and Plages. *ApJ*, 796:132, Dec. 2014. doi: 10.1088/0004-637X/796/2/132.

X. Dumusque, F. Borsa, M. Damasso, R. F. Díaz, P. C. Gregory, N. C. Hara, A. Hatzes, V. Rajpaul, M. Tuomi, S. Aigrain, G. Anglada-Escudé, A. S. Bonomo, G. Boué, F. Dauvergne, G. Frustagli, P. Giacobbe, R. D. Haywood, H. R. A. Jones, J. Laskar, M. Pinamonti, E. Poretti, M. Rainer, D. Ségransan, A. Sozzetti, and S. Udry. Radial-velocity fitting challenge. II. First results of the analysis of the data set. *A&A*, 598:A133, Feb. 2017. doi: 10.1051/0004-6361/201628671.

R. A. Edelson and J. H. Krolik. The discrete correlation function - A new method for analyzing unevenly sampled variability data. *ApJ*, 333:646–659, Oct. 1988. doi: 10.1086/166773.

B. Edvardsson, J. Andersen, B. Gustafsson, D. L. Lambert, P. E. Nissen, and J. Tomkin. The Chemical Evolution of the Galactic Disk - Part One - Analysis and Results. *A&A*, 275:101, Aug. 1993.

N. Espinoza and A. Jordán. Limb darkening and exoplanets: testing stellar model atmospheres and identifying biases in transit parameters. *MNRAS*, 450:1879–1899, June 2015. doi: 10.1093/mnras/stv744.

N. Espinoza and A. Jordán. Limb darkening and exoplanets - II. Choosing the best law for optimal retrieval of transit parameters. *MNRAS*, 457:3573–3581, Apr. 2016. doi: 10.1093/mnras/stw224.

N. Espinoza, R. Brahm, A. Jordán, J. S. Jenkins, F. Rojas, P. Jofré, T. Mädler, M. Rabus, J. Chanamé, B. Pantoja, M. G. Soto, K. M. Morzinski, J. R. Males, K. Ward-Duong, and L. M. Close. Discovery and Validation of a High-Density sub-Neptune from the K2 Mission. *ApJ*, 830: 43, Oct. 2016. doi: 10.3847/0004-637X/830/1/43.

L. J. Esteves, E. J. W. De Mooij, and R. Jayawardhana. Changing Phases of Alien Worlds: Probing Atmospheres of Kepler Planets with High-precision Photometry. *ApJ*, 804:150, May 2015. doi: 10.1088/0004-637X/804/2/150.

S. Feltzing and B. Gustafsson. Abundances in metal-rich stars. Detailed abundance analysis of 47 G and K dwarf stars with [Me/H] ≥ 0.10 dex. *A&As*, 129:237–266, Apr. 1998. doi: 10.1051/aas:1998400.

P. Figueira, N. C. Santos, F. Pepe, C. Lovis, and N. Nardetto. Line-profile variations in radial-velocity measurements. Two alternative indicators for planetary searches. *A&A*, 557:A93, Sept. 2013. doi: 10.1051/0004-6361/201220779.

D. A. Fischer and J. Valenti. The Planet-Metallicity Correlation. *ApJ*, 622:1102–1117, Apr. 2005. doi: 10.1086/428383.

D. A. Fischer, A. W. Howard, G. P. Laughlin, B. Macintosh, S. Mahadevan, J. Sahlmann, and J. C. Yee. Exoplanet Detection Techniques. *Protostars and Planets VI*, pages 715–737, 2014. doi: 10.2458/azu_uapress_9780816531240-ch031.

M. J. Fitzpatrick. The IRAF Radial Velocity Analysis Package. In R. J. Hanisch, R. J. V. Brissenden, and J. Barnes, editors, *Astronomical Data Analysis Software and Systems II*, volume 52 of *Astronomical Society of the Pacific Conference Series*, page 472, Jan. 1993.

J. J. Fortney, M. S. Marley, and J. W. Barnes. Planetary Radii across Five Orders of Magnitude in Mass and Stellar Insolation: Application to Transits. *ApJ*, 659:1661–1672, Apr. 2007. doi: 10.1086/512120.

F. Fressin, G. Torres, D. Charbonneau, S. T. Bryson, J. Christiansen, C. D. Dressing, J. M. Jenkins, L. M. Walkowicz, and N. M. Batalha. The False Positive Rate of Kepler and the Occurrence of Planets. *ApJ*, 766:81, Apr. 2013. doi: 10.1088/0004-637X/766/2/81.

B. J. Fulton, E. A. Petigura, S. Blunt, and E. Sinukoff. RadVel: The Radial Velocity Modeling Toolkit. *PASP*, 130(4):044504, Apr. 2018. doi: 10.1088/1538-3873/aaaaa8.

E. Furlan, D. R. Ciardi, M. E. Everett, M. Saylors, J. K. Teske, E. P. Horch, S. B. Howell, G. T. van Belle, L. A. Hirsch, T. N. Gautier, III, E. R. Adams, D. Barrado, K. M. S. Cartier, C. D. Dressing, A. K. Dupree, R. L. Gilliland, J. Lillo-Box, P. W. Lucas, and J. Wang. The Kepler Follow-up Observation Program. I. A Catalog of Companions to Kepler Stars from High-Resolution Imaging. *AJ*, 153:71, Feb. 2017. doi: 10.3847/1538-3881/153/2/71.

Gaia Collaboration, A. G. A. Brown, A. Vallenari, T. Prusti, J. H. J. de Bruijne, F. Mignard, R. Drimmel, C. Babusiaux, C. A. L. Bailer-Jones, U. Bastian, and et al. Gaia Data Release 1. Summary of the astrometric, photometric, and survey properties. *A&A*, 595:A2, Nov. 2016. doi: 10.1051/0004-6361/201629512.

D. Gavel, R. Kupke, D. Dillon, A. Norton, C. Ratliff, J. Cabak, A. Phillips, C. Rockosi, R. McGurk, S. Srinath, M. Peck, W. Deich, K. Lanclos, J. Gates, M. Saylor, J. Ward, and T. Pfister. ShaneAO: wide science spectrum adaptive optics system for the Lick Observatory. In *Adaptive Optics Systems IV*, volume 9148 of *Proc. SPIE*, page 914805, July 2014. doi: 10.1117/12.2055256.

H. A. C. Giles, D. Bayliss, N. Espinoza, R. Brahm, S. Blanco-Cuaresma, A. Shporer, D. Armstrong, C. Lovis, S. Udry, F. Bouchy, M. Marmier, A. Jordán, J. Bento, A. Collier Cameron, R. Sefako, W. D. Cochran, F. Rojas, M. Rabus, J. S. Jenkins, M. Jones, B. Pantoja, M. Soto, R. Jensen-Clem, D. A. Duev, M. Salama, R. Riddle, C. Baranec, and N. M. Law. EPIC 228735255b - An eccentric 6.57 day transiting hot Jupiter in Virgo. *ArXiv e-prints*, June 2017a.

H. A. C. Giles, A. Collier Cameron, and R. D. Haywood. A Kepler study of starspot lifetimes with respect to light-curve amplitude and spectral type. *MNRAS*, 472:1618–1627, Dec. 2017b. doi: 10.1093/mnras/stx1931.

A. Giménez. Equations for the analysis of the light curves of extra-solar planetary transits. *A&A*, 450:1231–1237, May 2006. doi: 10.1051/0004-6361:20054445.

J. Gomes da Silva, N. C. Santos, X. Bonfils, X. Delfosse, T. Forveille, and S. Udry. Long-term magnetic activity of a sample of M-dwarf stars from the HARPS program. I. Comparison of activity indices. *A&A*, 534:A30, Oct. 2011. doi: 10.1051/0004-6361/201116971.

G. Gonzalez. The stellar metallicity-giant planet connection. *MNRAS*, 285:403–412, Feb. 1997. doi: 10.1093/mnras/285.2.403.

G. Gonzalez and A. D. Vanture. Parent stars of extrasolar planets III: rho^1 CANCRI Revisited. *A&A*, 339:L29–L32, Nov. 1998.

J. I. González Hernández and P. Bonifacio. A new implementation of the infrared flux method using the 2MASS catalogue. *A&A*, 497:497–509, Apr. 2009. doi: 10.1051/0004-6361/200810904.

D. F. Gray. *The Observation and Analysis of Stellar Photospheres*. "Cambridge University Press", Sept. 2005.

G. M. Green, E. F. Schlafly, D. P. Finkbeiner, H.-W. Rix, N. Martin, W. Burgett, P. W. Draper, H. Flewelling, K. Hodapp, N. Kaiser, R. P. Kudritzki, E. Magnier, N. Metcalfe, P. Price, J. Tonry, and R. Wainscoat. A Three-dimensional Map of Milky Way Dust. *ApJ*, 810:25, Sept. 2015. doi: 10.1088/0004-637X/810/1/25.

M. N. Günther, D. Queloz, E. Gillen, J. McCormac, D. Bayliss, F. Bouchy, S. R. Walker, R. G. West, P. Eigmüller, A. M. S. Smith, D. J. Armstrong, M. Burleigh, S. L. Casewell, A. P. Chaushev, M. R. Goad, A. Grange, J. Jackman, J. S. Jenkins, T. Louden, M. Moyano, D. Pollacco, K. Poppenhaeger, H. Rauer, L. Raynard, A. P. G. Thompson, S. Udry, C. A. Watson, and P. J. Wheatley. Centroid vetting of transiting planet candidates from the Next Generation Transit Survey. *MNRAS*, 472:295–307, Nov. 2017. doi: 10.1093/mnras/stx1920.

B. Gustafsson, R. A. Bell, K. Eriksson, and A. Nordlund. A grid of model atmospheres for metal-deficient giant stars. I. *A&A*, 42:407–432, Sept. 1975.

J. D. Hartman, G. Á. Bakos, D. M. Kipping, G. Torres, G. Kovács, R. W. Noyes, D. W. Latham, A. W. Howard, D. A. Fischer, J. A. Johnson, G. W. Marcy, H. Isaacson, S. N. Quinn, L. A. Buchhave, B. Béky, D. D. Sasselov, R. P. Stefanik, G. A. Esquerdo, M. Everett, G. Perumpilly, J. Lázár, I. Papp, and P. Sári. HAT-P-26b: A Low-density Neptune-mass Planet Transiting a K Star. *ApJ*, 728:138, Feb. 2011a. doi: 10.1088/0004-637X/728/2/138.

J. D. Hartman, G. Á. Bakos, G. Torres, D. W. Latham, G. Kovács, B. Béky, S. N. Quinn, T. Mazeh, A. Shporer, G. W. Marcy, A. W. Howard, D. A. Fischer, J. A. Johnson, G. A. Esquerdo, R. W. Noyes, D. D. Sasselov, R. P. Stefanik, J. M. Fernandez, T. Szklenár, J. Lázár, I. Papp, and P. Sári. HAT-P-32b and HAT-P-33b: Two Highly Inflated Hot Jupiters Transiting High-jitter Stars. *ApJ*, 742:59, Nov. 2011b. doi: 10.1088/0004-637X/742/1/59.

A. P. Hatzes. Starspots and exoplanets. *Astronomische Nachrichten*, 323:392–394, July 2002. doi: 10.1002/1521-3994(200208)323:3/4<392::AID-ASNA392>3.0.CO;2-M.

B. Hauck and M. Mermilliod. Uvbybeta photoelectric photometric catalogue. *A&As*, 129:431–433, May 1998. doi: 10.1051/aas:1998195.

R. D. Haywood. *Hide and Seek: Radial-Velocity Searches for Planets around Active Stars*. PhD thesis, University of St Andrews, Nov. 2015.

R. D. Haywood, A. Collier Cameron, D. Queloz, S. C. C. Barros, M. Deleuil, R. Fares, M. Gillon, A. F. Lanza, C. Lovis, C. Moutou, F. Pepe, D. Pollacco, A. Santerne, D. Ségransan, and Y. C. Unruh. Planets and stellar activity: hide and seek in the CoRoT-7 system. *MNRAS*, 443:2517–2531, Sept. 2014. doi: 10.1093/mnras/stu1320.

L. Hebb, A. Collier-Cameron, B. Loeillet, D. Pollacco, G. Hébrard, R. A. Street, F. Bouchy, H. C. Stempels, C. Moutou, E. Simpson, S. Udry, Y. C. Joshi, R. G. West, I. Skillen, D. M. Wilson, I. McDonald, N. P. Gibson, S. Aigrain, D. R. Anderson, C. R. Benn, D. J. Christian, B. Enoch, C. A. Haswell, C. Hellier, K. Horne, J. Irwin, T. A. Lister, P. Maxted, M. Mayor, A. J. Norton, N. Parley, F. Pont, D. Queloz, B. Smalley, and P. J. Wheatley. WASP-12b: The Hottest Transiting Extrasolar Planet Yet Discovered. *ApJ*, 693:1920–1928, Mar. 2009. doi: 10.1088/0004-637X/693/2/1920.

U. Heiter, P. Jofré, B. Gustafsson, A. J. Korn, C. Soubiran, and F. Thévenin. Gaia FGK benchmark stars: Effective temperatures and surface gravities. *A&A*, 582:A49, Oct. 2015. doi: 10.1051/0004-6361/201526319.

K. Heng and B.-O. Demory. Understanding Trends Associated with Clouds in Irradiated Exoplanets. *ApJ*, 777:100, Nov. 2013. doi: 10.1088/0004-637X/777/2/100.

G. W. Henry, F. C. Fekel, and D. S. Hall. An Automated Search for Variability in Chromospherically Active Stars. *AJ*, 110:2926, Dec. 1995. doi: 10.1086/117740.

E. Hog, C. Fabricius, V. V. Makarov, S. Urban, T. Corbin, G. Wycoff, U. Bastian, P. Schwekendiek, and A. Wicenec. The Tycho-2 catalogue of the 2.5 million brightest stars. *A&A*, 355:L27–L30, Mar. 2000.

J. Holmberg, B. Nordström, and J. Andersen. The Geneva-Copenhagen survey of the solar neighbourhood. III. Improved distances, ages, and kinematics. *A&A*, 501:941–947, July 2009. doi: 10.1051/0004-6361/200811191.

J. Horner, R. A. Wittenmyer, T. C. Hinse, and J. P. Marshall. A dynamical investigation of the proposed BD +20 2457 system. *MNRAS*, 439:1176–1181, Mar. 2014. doi: 10.1093/mnras/stu081.

S. B. Howell, J. F. Rowe, S. T. Bryson, S. N. Quinn, G. W. Marcy, H. Isaacson, D. R. Ciardi, W. J. Chaplin, T. S. Metcalfe, M. J. P. F. G. Monteiro, T. Appourchaux, S. Basu, O. L. Creevey, R. L. Gilliland, P.-O. Quirion, D. Stello, H. Kjeldsen, J. Christensen-Dalsgaard, Y. Elsworth, R. A. García, G. Houdek, C. Karoff, J. Molenda-Żakowicz, M. J. Thompson, G. A. Verner, G. Torres, F. Fressin, J. R. Crepp, E. Adams, A. Dupree, D. D. Sasselov, C. D. Dressing, W. J. Borucki, D. G. Koch, J. J. Lissauer, D. W. Latham, L. A. Buchhave, T. N. Gautier, III, M. Everett, E. Horch, N. M. Batalha, E. W. Dunham, P. Szkody, D. R. Silva, K. Mighell, J. Holberg, J. Ballot, T. R. Bedding, H. Bruntt, T. L. Campante, R. Handberg, S. Hekker, D. Huber, S. Mathur, B. Mosser, C. Régulo, T. R. White, J. L. Christiansen, C. K. Middour, M. R. Haas, J. R. Hall, J. M. Jenkins, S. McCaulif, M. N. Fanelli, C. Kulesa, D. McCarthy, and C. E. Henze. Kepler-21b: A 1.6 $R_{Earth}$ Planet Transiting the Bright Oscillating F Subgiant Star HD 179070. *ApJ*, 746:123, Feb. 2012. doi: 10.1088/0004-637X/746/2/123.

S. B. Howell, C. Sobeck, M. Haas, M. Still, T. Barclay, F. Mullally, J. Troeltzsch, S. Aigrain, S. T. Bryson, D. Caldwell, W. J. Chaplin, W. D. Cochran, D. Huber, G. W. Marcy, A. Miglio, J. R. Najita, M. Smith, J. D. Twicken, and J. J. Fortney. The K2 Mission: Characterization and Early Results. *PASP*, 126:398, Apr. 2014. doi: 10.1086/676406.

N. Huélamo, P. Figueira, X. Bonfils, N. C. Santos, F. Pepe, M. Gillon, R. Azevedo, T. Barman, M. Fernández, E. di Folco, E. W. Guenther, C. Lovis, C. H. F. Melo, D. Queloz, and S. Udry. TW Hydrae: evidence of stellar spots instead of a Hot Jupiter. *A&A*, 489:L9–L13, Oct. 2008. doi: 10.1051/0004-6361:200810596.

S. Ida and D. N. C. Lin. Toward a Deterministic Model of Planetary Formation. II. The Formation and Retention of Gas Giant Planets around Stars with a Range of Metallicities. *ApJ*, 616:567–572, Nov. 2004. doi: 10.1086/424830.

S. Ida and D. N. C. Lin. Toward a Deterministic Model of Planetary Formation. III. Mass Distribution of Short-Period Planets around Stars of Various Masses. *ApJ*, 626:1045–1060, June 2005. doi: 10.1086/429953.

O. M. Ivanyuk, J. S. Jenkins, Y. V. Pavlenko, H. R. A. Jones, and D. J. Pinfield. The metal rich abundance pattern - spectroscopic properties and abundances for 107 main-sequence stars. *ArXiv e-prints*, Mar. 2017.

S. V. Jeffers and C. U. Keller. An analytical model to demonstrate the reliability of reconstructed 'active longitudes'. In E. Stempels, editor, *15th Cambridge Workshop on Cool Stars, Stellar Systems, and the Sun*, volume 1094 of *American Institute of Physics Conference Series*, pages 664–667, Feb. 2009. doi: 10.1063/1.3099201.

J. S. Jenkins and M. Tuomi. The Curious Case of HD 41248. A Pair of Static Signals Buried Behind Red Noise. *ApJ*, 794:110, Oct. 2014. doi: 10.1088/0004-637X/794/2/110.

J. S. Jenkins, H. R. A. Jones, C. G. Tinney, R. P. Butler, C. McCarthy, G. W. Marcy, D. J. Pinfield, B. D. Carter, and A. J. Penny. An activity catalogue of southern stars. *MNRAS*, 372:163–173, Oct. 2006. doi: 10.1111/j.1365-2966.2006.10811.x.

J. S. Jenkins, H. R. A. Jones, Y. Pavlenko, D. J. Pinfield, J. R. Barnes, and Y. Lyubchik. Metallicities and activities of southern stars. *A&A*, 485:571–584, July 2008. doi: 10.1051/0004-6361:20078611.

J. S. Jenkins, H. R. A. Jones, K. Goździewski, C. Migaszewski, J. R. Barnes, M. I. Jones, P. Rojo, D. J. Pinfield, A. C. Day-Jones, and S. Hoyer. First results from the Calan-Hertfordshire Extrasolar Planet Search: exoplanets and the discovery of an eccentric brown dwarf in the desert. *MNRAS*, 398:911–917, Sept. 2009. doi: 10.1111/j.1365-2966.2009.15097.x.

J. S. Jenkins, F. Murgas, P. Rojo, H. R. A. Jones, A. C. Day-Jones, M. I. Jones, J. R. A. Clarke, M. T. Ruiz, and D. J. Pinfield. Chromospheric activities and kinematics for solar type dwarfs and subgiants: analysis of the activity distribution and the AVR. *A&A*, 531:A8, July 2011a. doi: 10.1051/0004-6361/201016333.

J. S. Jenkins, F. Murgas, P. Rojo, H. R. A. Jones, A. C. Day-Jones, M. I. Jones, J. R. A. Clarke, M. T. Ruiz, and D. J. Pinfield. Chromospheric activities and kinematics for solar type dwarfs and subgiants: analysis of the activity distribution and the AVR. *A&A*, 531:A8, July 2011b. doi: 10.1051/0004-6361/201016333.

J. S. Jenkins, H. R. A. Jones, M. Tuomi, F. Murgas, S. Hoyer, M. I. Jones, J. R. Barnes, Y. V. Pavlenko, O. Ivanyuk, P. Rojo, A. Jordán, A. C. Day-Jones, M. T. Ruiz, and D. J. Pinfield. A Hot Uranus Orbiting the Super Metal-rich Star HD 77338 and the Metallicity-Mass Connection. *ApJ*, 766:67, Apr. 2013a. doi: 10.1088/0004-637X/766/2/67.

J. S. Jenkins, M. Tuomi, R. Brasser, O. Ivanyuk, and F. Murgas. Two Super-Earths Orbiting the Solar Analog HD 41248 on the Edge of a 7:5 Mean Motion Resonance. *ApJ*, 771:41, July 2013b. doi: 10.1088/0004-637X/771/1/41.

J. S. Jenkins, H. R. A. Jones, M. Tuomi, M. Díaz, J. P. Cordero, A. Aguayo, B. Pantoja, P. Arriagada, R. Mahu, R. Brahm, P. Rojo, M. G. Soto, O. Ivanyuk, N. Becerra Yoma, A. C. Day-Jones, M. T. Ruiz, Y. V. Pavlenko, J. R. Barnes, F. Murgas, D. J. Pinfield, M. I. Jones, M. López-Morales, S. Shectman, R. P. Butler, and D. Minniti. New planetary systems from the Calan-Hertfordshire Extrasolar Planet Search. *MNRAS*, 466:443–473, Apr. 2017. doi: 10.1093/mnras/stw2811.

P. Jofré, U. Heiter, C. Soubiran, S. Blanco-Cuaresma, C. C. Worley, E. Pancino, T. Cantat-Gaudin, L. Magrini, M. Bergemann, J. I. González Hernández, V. Hill, C. Lardo, P. de Laverny, K. Lind, T. Masseron, D. Montes, A. Mucciarelli, T. Nordlander, A. Recio Blanco, J. Sobeck, R. Sordo, S. G. Sousa, H. Tabernero, A. Vallenari, and S. Van Eck. Gaia FGK benchmark stars: Metallicity. *A&A*, 564:A133, Apr. 2014. doi: 10.1051/0004-6361/201322440.

P. Jofré, U. Heiter, C. Soubiran, S. Blanco-Cuaresma, T. Masseron, T. Nordlander, L. Chemin, C. C. Worley, S. Van Eck, A. Hourihane, G. Gilmore, V. Adibekyan, M. Bergemann, T. Cantat-Gaudin, E. Delgado-Mena, J. I. González Hernández, G. Guiglion, C. Lardo, P. de Laverny, K. Lind, L. Magrini, S. Mikolaitis, D. Montes, E. Pancino, A. Recio-Blanco, R. Sordo, S. Sousa, H. M. Tabernero, and A. Vallenari. Gaia FGK benchmark stars: abundances of $\alpha$ and iron-peak elements. *A&A*, 582:A81, Oct. 2015. doi: 10.1051/0004-6361/201526604.

M. I. Jones and J. S. Jenkins. No evidence of the planet orbiting the extremely metal-poor extragalactic star HIP 13044. *A&A*, 562:A129, Feb. 2014. doi: 10.1051/0004-6361/201322132.

M. I. Jones, J. S. Jenkins, P. Rojo, C. H. F. Melo, and P. Bluhm. Study of the impact of the post-MS evolution of the host star on the orbits of close-in planets. II. A giant planet in a close-in orbit around the RGB star HIP 63242. *A&A*, 556:A78, Aug. 2013. doi: 10.1051/0004-6361/201321660.

M. I. Jones, J. S. Jenkins, P. Bluhm, P. Rojo, and C. H. F. Melo. The properties of planets around giant stars. *A&A*, 566:A113, June 2014. doi: 10.1051/0004-6361/201323345.

M. I. Jones, J. S. Jenkins, R. Brahm, R. A. Wittenmyer, F. Olivares E., C. H. F. Melo, P. Rojo, A. Jordán, H. Drass, R. P. Butler, and L. Wang. Four new planets around giant stars and the mass-metallicity correlation of planet-hosting stars. *A&A*, 590:A38, May 2016. doi: 10.1051/0004-6361/201628067.

M. I. Jones, R. Brahm, N. Espinoza, A. Jordan, F. Rojas, M. Rabus, H. Drass, A. Zapata, M. G. Soto, J. S. Jenkins, M. Vuckovic, S. Ciceri, and P. Sarkis. A hot Saturn on an eccentric orbit around the giant star EPIC228754001. *ArXiv e-prints*, July 2017.

S. R. Kane, B. Thirumalachari, G. W. Henry, N. R. Hinkel, E. L. N. Jensen, T. S. Boyajian, D. A. Fischer, A. W. Howard, H. T. Isaacson, and J. T. Wright. Stellar Activity and Exclusion of the Outer Planet in the HD 99492 System. *ApJ*, 820:L5, Mar. 2016. doi: 10.3847/2041-8205/820/1/L5.

A. Kaufer, O. Stahl, S. Tubbesing, P. Norregaard, G. Avila, P. Francois, L. Pasquini, and A. Pizzella. Commissioning FEROS, the new high-resolution spectrograph at La-Silla. *The Messenger*, 95: 8–12, Mar. 1999.

D. M. Kipping. Efficient, uninformative sampling of limb darkening coefficients for two-parameter laws. *MNRAS*, 435:2152–2160, Nov. 2013. doi: 10.1093/mnras/stt1435.

H. Kjeldsen and T. R. Bedding. Amplitudes of stellar oscillations: the implications for asteroseismology. *A&A*, 293:87–106, Jan. 1995.

H. Kjeldsen, T. R. Bedding, R. P. Butler, J. Christensen-Dalsgaard, L. L. Kiss, C. McCarthy, G. W.

Marcy, C. G. Tinney, and J. T. Wright. Solar-like Oscillations in $\alpha$ Centauri B. *ApJ*, 635: 1281–1290, Dec. 2005. doi: 10.1086/497530.

D. A. Klinglesmith and S. Sobieski. Nonlinear Limb Darkening for Early-Type Stars. *AJ*, 75: 175–182, Mar. 1970. doi: 10.1086/110960.

C. Koen, D. Kilkenny, F. van Wyk, and F. Marang. UBV(RI)$_C$ JHK observations of Hipparcos-selected nearby stars. *MNRAS*, 403:1949–1968, Apr. 2010. doi: 10.1111/j.1365-2966.2009.16182.x.

G. Kovács, S. Zucker, and T. Mazeh. A box-fitting algorithm in the search for periodic transits. *A&A*, 391:369–377, Aug. 2002. doi: 10.1051/0004-6361:20020802.

L. Kreidberg. batman: BAsic Transit Model cAlculatioN in Python. *PASP*, 127:1161, Nov. 2015. doi: 10.1086/683602.

G. P. Kuiper. The Empirical Mass-Luminosity Relation. *ApJ*, 88:472, Nov. 1938. doi: 10.1086/143999.

M. Kunitomo, M. Ikoma, B. Sato, Y. Katsuta, and S. Ida. Planet Engulfment by ~1.5-3 M $_{sun}$ Red Giants. *ApJ*, 737:66, Aug. 2011. doi: 10.1088/0004-637X/737/2/66.

F. Kupka, N. Piskunov, T. A. Ryabchikova, H. C. Stempels, and W. W. Weiss. VALD-2: Progress of the Vienna Atomic Line Data Base. *A&As*, 138:119–133, July 1999. doi: 10.1051/aas:1999267.

G. Laughlin, M. Crismani, and F. C. Adams. On the Anomalous Radii of the Transiting Extrasolar Planets. *ApJ*, 729:L7, Mar. 2011. doi: 10.1088/2041-8205/729/1/L7.

D. N. C. Lin, P. Bodenheimer, and D. C. Richardson. Orbital migration of the planetary companion of 51 Pegasi to its present location. *Nature*, 380:606–607, Apr. 1996. doi: 10.1038/380606a0.

L. Lindegren and D. Dravins. The fundamental definition of "radial velocity". *A&A*, 401:1185–1201, Apr. 2003. doi: 10.1051/0004-6361:20030181.

W. Livingston, L. Wallace, O. R. White, and M. S. Giampapa. Sun-as-a-Star Spectrum Variations 1974-2006. *ApJ*, 657:1137–1149, Mar. 2007. doi: 10.1086/511127.

W. C. Livingston. Magnetic fields, convection and solar luminosity variability. *Nature*, 297:208, May 1982. doi: 10.1038/297208a0.

N. R. Lomb. Least-squares frequency analysis of unequally spaced data. *Ap&SS*, 39:447–462, Feb. 1976. doi: 10.1007/BF00648343.

M. López-Morales, R. D. Haywood, J. L. Coughlin, L. Zeng, L. A. Buchhave, H. A. C. Giles, L. Affer, A. S. Bonomo, D. Charbonneau, A. Collier Cameron, R. Consentino, C. D. Dressing, X. Dumusque, P. Figueira, A. F. M. Fiorenzano, A. Harutyunyan, J. A. Johnson, D. W. Latham, E. D. Lopez, C. Lovis, L. Malavolta, M. Mayor, G. Micela, E. Molinari, A. Mortier, F. Motalebi, V. Nascimbeni, F. Pepe, D. F. Phillips, G. Piotto, D. Pollacco, D. Queloz, K. Rice, D. Sasselov, D. Segransan, A. Sozzetti, S. Udry, A. Vanderburg, and C. Watson. Kepler-21b: A Rocky Planet

Around a V = 8.25 Magnitude Star. *AJ*, 152:204, Dec. 2016. doi: 10.3847/0004-6256/152/6/204.

C. Lovis, X. Dumusque, N. C. Santos, F. Bouchy, M. Mayor, F. Pepe, D. Queloz, D. Ségransan, and S. Udry. The HARPS search for southern extra-solar planets. XXXI. Magnetic activity cycles in solar-type stars: statistics and impact on precise radial velocities. *ArXiv e-prints*, July 2011.

R. Luger, E. Kruse, D. Foreman-Mackey, E. Agol, and N. Saunders. An update to the EVEREST K2 pipeline: Short cadence, saturated stars, and Kepler-like photometry down to Kp = 15. *ArXiv e-prints*, Feb. 2017.

P. Magain. A comment on systematic errors in determinations of microturbulent velocities. *A&A*, 134:189–192, May 1984.

E. E. Mamajek and L. A. Hillenbrand. Improved Age Estimation for Solar-Type Dwarfs Using Activity-Rotation Diagnostics. *ApJ*, 687:1264-1293, Nov. 2008. doi: 10.1086/591785.

K. Mandel and E. Agol. Analytic Light Curves for Planetary Transit Searches. *ApJ*, 580:L171–L175, Dec. 2002. doi: 10.1086/345520.

A. W. Mann, G. A. Feiden, E. Gaidos, T. Boyajian, and K. von Braun. How to Constrain Your M Dwarf: Measuring Effective Temperature, Bolometric Luminosity, Mass, and Radius. *ApJ*, 804: 64, May 2015. doi: 10.1088/0004-637X/804/1/64.

G. W. Marcy and R. P. Butler. Precision radial velocities with an iodine absorption cell. *PASP*, 104:270–277, Apr. 1992. doi: 10.1086/132989.

C. Marois, B. Zuckerman, Q. M. Konopacky, B. Macintosh, and T. Barman. Images of a fourth planet orbiting HR 8799. *Nature*, 468:1080–1083, Dec. 2010. doi: 10.1038/nature09684.

D. J. Marshall, A. C. Robin, C. Reylé, M. Schultheis, and S. Picaud. Modelling the Galactic interstellar extinction distribution in three dimensions. *A&A*, 453:635–651, July 2006. doi: 10.1051/0004-6361:20053842.

S. Martell and G. Laughlin. An Improved uvby-Metallicity Calibration for Metal-rich Stars. *ApJ*, 577:L45–L48, Sept. 2002. doi: 10.1086/344165.

M. Mayor and D. Queloz. A Jupiter-mass companion to a solar-type star. *Nature*, 378:355–359, Nov. 1995. doi: 10.1038/378355a0.

M. Mayor, F. Pepe, D. Queloz, F. Bouchy, G. Rupprecht, G. Lo Curto, G. Avila, W. Benz, J.-L. Bertaux, X. Bonfils, T. Dall, H. Dekker, B. Delabre, W. Eckert, M. Fleury, A. Gilliotte, D. Gojak, J. C. Guzman, D. Kohler, J.-L. Lizon, A. Longinotti, C. Lovis, D. Megevand, L. Pasquini, J. Reyes, J.-P. Sivan, D. Sosnowska, R. Soto, S. Udry, A. van Kesteren, L. Weber, and U. Weilenmann. Setting New Standards with HARPS. *The Messenger*, 114:20–24, Dec. 2003.

S. D. McCauliff, J. M. Jenkins, J. Catanzarite, C. J. Burke, J. L. Coughlin, J. D. Twicken, P. Tenenbaum, S. Seader, J. Li, and M. Cote. Automatic Classification of Kepler Planetary Transit Candidates. *ApJ*, 806:6, June 2015. doi: 10.1088/0004-637X/806/1/6.

A. McQuillan, S. Aigrain, and T. Mazeh. Measuring the rotation period distribution of field M dwarfs with Kepler. *MNRAS*, 432:1203–1216, June 2013. doi: 10.1093/mnras/stt536.

S. Meschiari, A. S. Wolf, E. Rivera, G. Laughlin, S. Vogt, and P. Butler. Systemic: A Testbed for Characterizing the Detection of Extrasolar Planets. I. The Systemic Console Package. *PASP*, 121:1016–1027, Sept. 2009. doi: 10.1086/605730.

N. Meunier, M. Desort, and A.-M. Lagrange. Using the Sun to estimate Earth-like planets detection capabilities . II. Impact of plages. *A&A*, 512:A39, Mar. 2010. doi: 10.1051/0004-6361/200913551.

N. Miller and J. J. Fortney. The Heavy-element Masses of Extrasolar Giant Planets, Revealed. *ApJ*, 736:L29, Aug. 2011. doi: 10.1088/2041-8205/736/2/L29.

D. Montes, J. López-Santiago, M. C. Gálvez, M. J. Fernández-Figueroa, E. De Castro, and M. Cornide. Late-type members of young stellar kinematic groups - I. Single stars. *MNRAS*, 328:45–63, Nov. 2001. doi: 10.1046/j.1365-8711.2001.04781.x.

C. Mordasini, Y. Alibert, W. Benz, H. Klahr, and T. Henning. Extrasolar planet population synthesis . IV. Correlations with disk metallicity, mass, and lifetime. *A&A*, 541:A97, May 2012. doi: 10.1051/0004-6361/201117350.

A. Mortier, N. C. Santos, S. G. Sousa, V. Z. Adibekyan, E. Delgado Mena, M. Tsantaki, G. Israelian, and M. Mayor. New and updated stellar parameters for 71 evolved planet hosts. On the metallicity-giant planet connection. *A&A*, 557:A70, Sept. 2013. doi: 10.1051/0004-6361/201321641.

T. D. Morton. isochrones: Stellar model grid package. Astrophysics Source Code Library, Mar. 2015.

T. D. Morton, S. T. Bryson, J. L. Coughlin, J. F. Rowe, G. Ravichandran, E. A. Petigura, M. R. Haas, and N. M. Batalha. False Positive Probabilities for all Kepler Objects of Interest: 1284 Newly Validated Planets and 428 Likely False Positives. *ApJ*, 822:86, May 2016. doi: 10.3847/0004-637X/822/2/86.

C. Moutou, M. Mayor, G. Lo Curto, D. Ségransan, S. Udry, F. Bouchy, W. Benz, C. Lovis, D. Naef, F. Pepe, D. Queloz, N. C. Santos, and S. G. Sousa. The HARPS search for southern extra-solar planets. XXVII. Seven new planetary systems. *A&A*, 527:A63, Mar. 2011. doi: 10.1051/0004-6361/201015371.

A. Müller, V. Roccatagliata, T. Henning, D. Fedele, A. Pasquali, E. Caffau, M. V. Rodríguez-Ledesma, M. Mohler-Fischer, U. Seemann, and R. J. Klement. Reanalysis of the FEROS observations of HIP 11952. *A&A*, 556:A3, Aug. 2013. doi: 10.1051/0004-6361/201321497.

F. Murgas, J. S. Jenkins, P. Rojo, H. R. A. Jones, and D. J. Pinfield. Stellar activity as a tracer of moving groups. *A&A*, 552:A27, Apr. 2013. doi: 10.1051/0004-6361/201219483.

V. Neves, N. C. Santos, S. G. Sousa, A. C. M. Correia, and G. Israelian. Chemical abundances of 451 stars from the HARPS GTO planet search program. Thin disc, thick disc, and planets. *A&A*,

497:563–581, Apr. 2009. doi: 10.1051/0004-6361/200811328.

E. Niemczura, B. Smalley, and W. Pych. *Determination of Atmospheric Parameters of B-, A-, F- and G-Type Stars*. Springer International Publishing (Cham), 2014. doi: 10.1007/978-3-319-06956-2.

R. W. Noyes, L. W. Hartmann, S. L. Baliunas, D. K. Duncan, and A. H. Vaughan. Rotation, convection, and magnetic activity in lower main-sequence stars. *ApJ*, 279:763–777, Apr. 1984. doi: 10.1086/161945.

P. L. Palle, A. Jimenez, F. Perez Hernandez, C. Regulo, T. Roca Cortes, and L. Sanchez. A measurement of the background solar velocity spectrum. *ApJ*, 441:952–959, Mar. 1995. doi: 10.1086/175414.

H. Parviainen and S. Aigrain. LDTK: Limb Darkening Toolkit. *MNRAS*, 453:3821–3826, Nov. 2015. doi: 10.1093/mnras/stv1857.

Y. V. Pavlenko. Determination of abundances in the atmospheres of F-, G-, and K-dwarfs. *Kinematics and Physics of Celestial Bodies*, 33:55–62, Mar. 2017. doi: 10.3103/S0884591317020064.

Y. V. Pavlenko, J. S. Jenkins, H. R. A. Jones, O. Ivanyuk, and D. J. Pinfield. Effective temperatures, rotational velocities, microturbulent velocities and abundances in the atmospheres of the Sun, HD 1835 and HD 10700. *MNRAS*, 422:542–552, May 2012. doi: 10.1111/j.1365-2966.2012.20629.x.

M. J. Pecaut and E. E. Mamajek. Intrinsic Colors, Temperatures, and Bolometric Corrections of Pre-main-sequence Stars. *ApJS*, 208:9, Sept. 2013. doi: 10.1088/0067-0049/208/1/9.

F. Pepe, M. Mayor, F. Galland, D. Naef, D. Queloz, N. C. Santos, S. Udry, and M. Burnet. The CORALIE survey for southern extra-solar planets VII. Two short-period Saturnian companions to <ASTROBJ>HD 108147</ASTROBJ> and <ASTROBJ>HD 168746</ASTROBJ>. *A&A*, 388:632–638, June 2002. doi: 10.1051/0004-6361:20020433.

F. A. Pepe, S. Cristiani, R. Rebolo Lopez, N. C. Santos, A. Amorim, G. Avila, W. Benz, P. Bonifacio, A. Cabral, P. Carvas, R. Cirami, J. Coelho, M. Comari, I. Coretti, V. De Caprio, H. Dekker, B. Delabre, P. Di Marcantonio, V. D'Odorico, M. Fleury, R. García, J. M. Herreros Linares, I. Hughes, O. Iwert, J. Lima, J.-L. Lizon, G. Lo Curto, C. Lovis, A. Manescau, C. Martins, D. Mégevand, A. Moitinho, P. Molaro, M. Monteiro, M. Monteiro, L. Pasquini, C. Mordasini, D. Queloz, J. L. Rasilla, J. M. Rebordão, S. Santana Tschudi, P. Santin, D. Sosnowska, P. Spanò, F. Tenegi, S. Udry, E. Vanzella, M. Viel, M. R. Zapatero Osorio, and F. Zerbi. ESPRESSO: the Echelle spectrograph for rocky exoplanets and stable spectroscopic observations. In *Ground-based and Airborne Instrumentation for Astronomy III*, volume 7735 of *Proc. SPIE*, page 77350F, July 2010. doi: 10.1117/12.857122.

M. A. C. Perryman, L. Lindegren, J. Kovalevsky, E. Hoeg, U. Bastian, P. L. Bernacca, M. Crézé, F. Donati, M. Grenon, and M. Grewing. The HIPPARCOS Catalogue. *A&A*, 323:L49–L52, July 1997.

N. E. Piskunov, F. Kupka, T. A. Ryabchikova, W. W. Weiss, and C. S. Jeffery. VALD: The Vienna

Atomic Line Data Base. *A&As*, 112:525, Sept. 1995.

G. Pojmanski. The All Sky Automated Survey. *Acta Astronomica*, 47:467–481, Oct. 1997.

D. L. Pollacco, I. Skillen, A. Collier Cameron, D. J. Christian, C. Hellier, J. Irwin, T. A. Lister, R. A. Street, R. G. West, D. R. Anderson, W. I. Clarkson, H. Deeg, B. Enoch, A. Evans, A. Fitzsimmons, C. A. Haswell, S. Hodgkin, K. Horne, S. R. Kane, F. P. Keenan, P. F. L. Maxted, A. J. Norton, J. Osborne, N. R. Parley, R. S. I. Ryans, B. Smalley, P. J. Wheatley, and D. M. Wilson. The WASP Project and the SuperWASP Cameras. *PASP*, 118:1407–1418, Oct. 2006. doi: 10.1086/508556.

D. Queloz, M. Mayor, L. Weber, A. Blécha, M. Burnet, B. Confino, D. Naef, F. Pepe, N. Santos, and S. Udry. The CORALIE survey for southern extra-solar planets. I. A planet orbiting the star Gliese 86. *A&A*, 354:99–102, Feb. 2000.

D. Queloz, G. W. Henry, J. P. Sivan, S. L. Baliunas, J. L. Beuzit, R. A. Donahue, M. Mayor, D. Naef, C. Perrier, and S. Udry. No planet for HD 166435. *A&A*, 379:279–287, Nov. 2001. doi: 10.1051/0004-6361:20011308.

A. Quirrenbach, P. J. Amado, J. A. Caballero, R. Mundt, A. Reiners, I. Ribas, W. Seifert, M. Abril, J. Aceituno, F. J. Alonso-Floriano, M. Ammler-von Eiff, R. Antona Jiménez, H. Anwand-Heerwart, M. Azzaro, F. Bauer, D. Barrado, S. Becerril, V. J. S. Béjar, D. Benítez, Z. M. Berdiñas, M. C. Cárdenas, E. Casal, A. Claret, J. Colomé, M. Cortés-Contreras, S. Czesla, M. Doellinger, S. Dreizler, C. Feiz, M. Fernández, D. Galadí, M. C. Gálvez-Ortiz, A. García-Piquer, M. L. García-Vargas, R. Garrido, L. Gesa, V. Gómez Galera, E. González Álvarez, J. I. González Hernández, U. Grözinger, J. Guàrdia, E. W. Guenther, E. de Guindos, J. Gutiérrez-Soto, H.-J. Hagen, A. P. Hatzes, P. H. Hauschildt, J. Helmling, T. Henning, D. Hermann, L. Hernández Castaño, E. Herrero, D. Hidalgo, G. Holgado, A. Huber, K. F. Huber, S. Jeffers, V. Joergens, E. de Juan, M. Kehr, R. Klein, M. Kürster, A. Lamert, S. Lalitha, W. Laun, U. Lemke, R. Lenzen, M. López del Fresno, B. López Martí, J. López-Santiago, U. Mall, H. Mandel, E. L. Martín, S. Martín-Ruiz, H. Martínez-Rodríguez, C. J. Marvin, R. J. Mathar, E. Mirabet, D. Montes, R. Morales Muñoz, A. Moya, V. Naranjo, A. Ofir, R. Oreiro, E. Pallé, J. Panduro, V.-M. Passegger, A. Pérez-Calpena, D. Pérez Medialdea, M. Perger, M. Pluto, A. Ramón, R. Rebolo, P. Redondo, S. Reffert, S. Reinhardt, P. Rhode, H.-W. Rix, F. Rodler, E. Rodríguez, C. Rodríguez-López, E. Rodríguez-Pérez, R.-R. Rohloff, A. Rosich, E. Sánchez-Blanco, M. A. Sánchez Carrasco, J. Sanz-Forcada, L. F. Sarmiento, S. Schäfer, J. Schiller, C. Schmidt, J. H. M. M. Schmitt, E. Solano, O. Stahl, C. Storz, J. Stürmer, J. C. Suárez, R. G. Ulbrich, G. Veredas, K. Wagner, J. Winkler, M. R. Zapatero Osorio, M. Zechmeister, F. J. Abellán de Paco, G. Anglada-Escudé, C. del Burgo, A. Klutsch, J. L. Lizon, M. López-Morales, J. C. Morales, M. A. C. Perryman, S. M. Tulloch, and W. Xu. CARMENES instrument overview. In *Ground-based and Airborne Instrumentation for Astronomy V*, volume 9147 of *Proc. SPIE*, page 91471F, July 2014. doi: 10.1117/12.2056453.

C. E. Rasmussen and C. K. I. Williams. *Gaussian Processes for Machine Learning*. "MIT Press", 2006.

S. Reffert, C. Bergmann, A. Quirrenbach, T. Trifonov, and A. Künstler. Precise radial velocities of giant stars. VII. Occurrence rate of giant extrasolar planets as a function of mass and metallicity.

*A&A*, 574:A116, Feb. 2015. doi: 10.1051/0004-6361/201322360. (R15).

C. Régulo, J. M. Almenara, R. Alonso, H. Deeg, and T. Roca Cortés. TRUFAS, a wavelet-based algorithm for the rapid detection of planetary transits. *A&A*, 467:1345–1352, June 2007. doi: 10.1051/0004-6361:20066827.

G. R. Ricker, J. N. Winn, R. Vanderspek, D. W. Latham, G. Á. Bakos, J. L. Bean, Z. K. Berta-Thompson, T. M. Brown, L. Buchhave, N. R. Butler, R. P. Butler, W. J. Chaplin, D. Charbonneau, J. Christensen-Dalsgaard, M. Clampin, D. Deming, J. Doty, N. De Lee, C. Dressing, E. W. Dunham, M. Endl, F. Fressin, J. Ge, T. Henning, M. J. Holman, A. W. Howard, S. Ida, J. M. Jenkins, G. Jernigan, J. A. Johnson, L. Kaltenegger, N. Kawai, H. Kjeldsen, G. Laughlin, A. M. Levine, D. Lin, J. J. Lissauer, P. MacQueen, G. Marcy, P. R. McCullough, T. D. Morton, N. Narita, M. Paegert, E. Palle, F. Pepe, J. Pepper, A. Quirrenbach, S. A. Rinehart, D. Sasselov, B. Sato, S. Seager, A. Sozzetti, K. G. Stassun, P. Sullivan, A. Szentgyorgyi, G. Torres, S. Udry, and J. Villasenor. Transiting Exoplanet Survey Satellite (TESS). *Journal of Astronomical Telescopes, Instruments, and Systems*, 1(1):014003, Jan. 2015. doi: 10.1117/1.JATIS.1.1.014003.

T. A. Ryabchikova, Y. V. Pakhomov, and N. E. Piskunov. New release of Vienna Atomic Line Database (VALD) and its integration in Virtual Atomic and Molecular Data Centre (VAMDC). *Kazan Izdatel Kazanskogo Universiteta*, 153:61–66, 2011.

S. H. Saar and R. A. Donahue. Activity-Related Radial Velocity Variation in Cool Stars. *ApJ*, 485: 319–327, Aug. 1997. doi: 10.1086/304392.

S. H. Saar and D. Fischer. Correcting Radial Velocities for Long-Term Magnetic Activity Variations. *ApJ*, 534:L105–L108, May 2000. doi: 10.1086/312648.

S. H. Saar, J. Huovelin, R. A. Osten, and A. G. Shcherbakov. HeI D3 absorption and its relation to rotation and activity in G and K dwarfs. *A&A*, 326:741–750, Oct. 1997.

M. Salman Khan, J. S. Jenkins, and N. Becerra Yoma. Discovering new worlds: a review of signal processing methods for detecting exoplanets from astronomical radial velocity data. *ArXiv e-prints*, Nov. 2016.

N. C. Santos, G. Israelian, and M. Mayor. Chemical analysis of 8 recently discovered extra-solar planet host stars. *A&A*, 363:228–238, Nov. 2000.

N. C. Santos, G. Israelian, and M. Mayor. Spectroscopic [Fe/H] for 98 extra-solar planet-host stars. Exploring the probability of planet formation. *A&A*, 415:1153–1166, Mar. 2004. doi: 10.1051/0004-6361:20034469.

N. C. Santos, A. Mortier, J. P. Faria, X. Dumusque, V. Z. Adibekyan, E. Delgado-Mena, P. Figueira, L. Benamati, I. Boisse, D. Cunha, J. Gomes da Silva, G. Lo Curto, C. Lovis, J. H. C. Martins, M. Mayor, C. Melo, M. Oshagh, F. Pepe, D. Queloz, A. Santerne, D. Ségransan, A. Sozzetti, S. G. Sousa, and S. Udry. The HARPS search for southern extra-solar planets. XXXV. The interesting case of HD 41248: stellar activity, no planets? *A&A*, 566:A35, June 2014. doi: 10.1051/0004-6361/201423808.

N. C. Santos, V. Adibekyan, P. Figueira, D. T. Andreasen, S. C. C. Barros, E. Delgado-Mena,

O. Demangeon, J. P. Faria, M. Oshagh, S. G. Sousa, P. T. P. Viana, and A. C. S. Ferreira. Observational evidence for two distinct giant planet populations. *A&A*, 603:A30, July 2017. doi: 10.1051/0004-6361/201730761.

J. D. Scargle. Studies in astronomical time series analysis. II - Statistical aspects of spectral analysis of unevenly spaced data. *ApJ*, 263:835–853, Dec. 1982. doi: 10.1086/160554.

E. F. Schlafly and D. P. Finkbeiner. Measuring Reddening with Sloan Digital Sky Survey Stellar Spectra and Recalibrating SFD. *ApJ*, 737:103, Aug. 2011. doi: 10.1088/0004-637X/737/2/103.

D. J. Schlegel, D. P. Finkbeiner, and M. Davis. Maps of Dust Infrared Emission for Use in Estimation of Reddening and Cosmic Microwave Background Radiation Foregrounds. *ApJ*, 500: 525–553, June 1998. doi: 10.1086/305772.

C. J. Schrijver, J. Cote, C. Zwaan, and S. H. Saar. Relations between the photospheric magnetic field and the emission from the outer atmospheres of cool stars. I - The solar CA II K line core emission. *ApJ*, 337:964–976, Feb. 1989. doi: 10.1086/167168.

G. Schwarz. Estimating the dimension of a model. *Ann. Statist.*, 6(2):461–464, 03 1978. doi: 10.1214/aos/1176344136. URL `https://doi.org/10.1214/aos/1176344136`.

S. Seager and G. Mallén-Ornelas. A Unique Solution of Planet and Star Parameters from an Extrasolar Planet Transit Light Curve. *ApJ*, 585:1038–1055, Mar. 2003. doi: 10.1086/346105.

D. Ségransan, S. Udry, M. Mayor, D. Naef, F. Pepe, D. Queloz, N. C. Santos, B.-O. Demory, P. Figueira, M. Gillon, M. Marmier, D. Mégevand, D. Sosnowska, O. Tamuz, and A. H. M. J. Triaud. The CORALIE survey for southern extrasolar planets. XVI. Discovery of a planetary system around HD 147018 and of two long period and massive planets orbiting HD 171238 and HD 204313. *A&A*, 511:A45, Feb. 2010. doi: 10.1051/0004-6361/200912136.

D. Ségransan, M. Mayor, S. Udry, C. Lovis, W. Benz, F. Bouchy, G. Lo Curto, C. Mordasini, C. Moutou, D. Naef, F. Pepe, D. Queloz, and N. Santos. The HARPS search for southern extra-solar planets. XXIX. Four new planets in orbit around the moderatly active dwarfs <ASTROBJ>HD 63765</ASTROBJ>, <ASTROBJ>HD 104067</ASTROBJ>, <ASTROBJ>HD 125595</ASTROBJ>, and <ASTROBJ>HIP 70849</ASTROBJ>. *A&A*, 535:A54, Nov. 2011. doi: 10.1051/0004-6361/200913580.

M. Sestovic, B.-O. Demory, and D. Queloz. Investigating hot-Jupiter inflated radii with hierarchical Bayesian modelling. *ArXiv e-prints*, Apr. 2018.

J. Setiawan. Planets around evolved stars. In M. Fridlund, T. Henning, and H. Lacoste, editors, *Earths: DARWIN/TPF and the Search for Extrasolar Terrestrial Planets*, volume 539 of *ESA Special Publication*, pages 595–598, Oct. 2003.

J. Setiawan, L. Pasquini, L. da Silva, A. Hatzes, O. von der Luhe, A. Kaufer, L. Girardi, R. R. de La, and J. R. de Medeiros. A study of the activity of G and K giants through their precise radial velocity. Breaking the 10-m/sec accuracy with FEROS. *The Messenger*, 102:13–17, Dec. 2000.

J. Setiawan, A. P. Hatzes, O. von der Lühe, L. Pasquini, D. Naef, L. da Silva, S. Udry, D. Queloz, and L. Girardi. Evidence of a sub-stellar companion around HD 47536. *A&A*, 398:L19–L23, Feb. 2003. doi: 10.1051/0004-6361:20021846.

J. Setiawan, J. Rodmann, L. da Silva, A. P. Hatzes, L. Pasquini, O. von der Lühe, J. R. de Medeiros, M. P. Döllinger, and L. Girardi. A substellar companion around the intermediate-mass giant star HD 11977. *A&A*, 437:L31–L34, July 2005. doi: 10.1051/0004-6361:200500133.

J. Setiawan, P. Weise, T. Henning, R. Launhardt, A. Müller, and J. Rodmann. Evidence for a Planetary Companion around a Nearby Young Star. *ApJL*, 660:L145–L148, May 2007. doi: 10.1086/518213.

J. Setiawan, T. Henning, R. Launhardt, A. Müller, P. Weise, and M. Kürster. A young massive planet in a star-disk system. *Nature*, 451:38–41, Jan. 2008a. doi: 10.1038/nature06426.

J. Setiawan, P. Weise, T. Henning, A. P. Hatzes, L. Pasquini, L. da Silva, L. Girardi, O. von der Lühe, M. P. Döllinger, A. Weiss, and K. Biazzo. Planets Around Active Stars. In N. C. Santos, L. Pasquini, A. C. M. Correia, and M. Romaniello, editors, *Precision Spectroscopy in Astrophysics*, pages 201–204, 2008b. doi: 10.1007/978-3-540-75485-5_43.

R. C. Smith. *Observational Astrophysics*. Cambridge University Press, July 1995.

C. A. Sneden. *Carbon and Nitrogen Abundances in Metal-Poor Stars*. PhD thesis, THE UNIVERSITY OF TEXAS AT AUSTIN., 1973.

M. G. Soto and J. S. Jenkins. SPECIES I: Spectroscopic Parameters and atmosphEric ChemIstriEs of Stars. *ArXiv e-prints*, Jan. 2018.

M. G. Soto, J. S. Jenkins, and M. I. Jones. RAFT - I. Discovery of new planetary candidates and updated orbits from archival FEROS spectra. *MNRAS*, 451:3131–3144, Aug. 2015. doi: 10.1093/mnras/stv1144.

M. G. Soto, M. R. Díaz, J. S. Jenkins, F. Rojas, N. Espinoza, R. Brahm, H. Drass, M. I. Jones, M. Rabus, J. Hartman, P. Sarkis, A. Jordán, R. Lachaume, B. Pantoja, M. Vučković, D. Ciardi, I. Crossfield, C. Dressing, E. Gonzales, and L. Hirsch. EPIC229426032 b and EPIC246067459 b: discovery of a highly inflated and a 'regular' pair of transiting hot Jupiters from K2. *ArXiv e-prints*, Jan. 2018.

S. G. Sousa, N. C. Santos, G. Israelian, M. Mayor, and M. J. P. F. G. Monteiro. A new code for automatic determination of equivalent widths: Automatic Routine for line Equivalent widths in stellar Spectra (ARES). *A&A*, 469:783–791, July 2007. doi: 10.1051/0004-6361:20077288.

S. G. Sousa, N. C. Santos, M. Mayor, S. Udry, L. Casagrande, G. Israelian, F. Pepe, D. Queloz, and M. J. P. F. G. Monteiro. Spectroscopic parameters for 451 stars in the HARPS GTO planet search program. Stellar [Fe/H] and the frequency of exo-Neptunes. *A&A*, 487:373–381, Aug. 2008. doi: 10.1051/0004-6361:200809698.

S. G. Sousa, N. C. Santos, G. Israelian, M. Mayor, and S. Udry. Spectroscopic stellar parameters for 582 FGK stars in the HARPS volume-limited sample. Revising the metallicity-planet correlation. *A&A*, 533:A141, Sept. 2011a. doi: 10.1051/0004-6361/201117699.

S. G. Sousa, N. C. Santos, G. Israelian, M. Mayor, and S. Udry. Spectroscopic stellar parameters for 582 FGK stars in the HARPS volume-limited sample. Revising the metallicity-planet correlation. *A&A*, 533:A141, Sept. 2011b. doi: 10.1051/0004-6361/201117699.

S. G. Sousa, N. C. Santos, V. Adibekyan, E. Delgado-Mena, and G. Israelian. ARES v2: new features and improved performance. *A&A*, 577:A67, May 2015. doi: 10.1051/0004-6361/201425463.

A. Sozzetti, G. Torres, D. Charbonneau, D. W. Latham, M. J. Holman, J. N. Winn, J. B. Laird, and F. T. O'Donovan. Improving Stellar and Planetary Parameters of Transiting Planet Systems: The Case of TrES-2. *ApJ*, 664:1190–1198, Aug. 2007. doi: 10.1086/519214.

B. Strömgren. Spectral Classification Through Photoelectric Narrow-Band Photometry. *ARA&A*, 4:433, 1966. doi: 10.1146/annurev.aa.04.090166.002245.

B. Tingley, A. S. Bonomo, and H. J. Deeg. Using Stellar Densities to Evaluate Transiting Exoplanetary Candidates. *ApJ*, 726:112, Jan. 2011. doi: 10.1088/0004-637X/726/2/112.

C. G. Tinney, R. P. Butler, G. W. Marcy, H. R. A. Jones, A. J. Penny, S. S. Vogt, K. Apps, and G. W. Henry. First Results from the Anglo-Australian Planet Search: A Brown Dwarf Candidate and a 51 Peg-like Planet. *ApJ*, 551:507–511, Apr. 2001. doi: 10.1086/320097.

A. Tokovinin, D. A. Fischer, M. Bonati, M. J. Giguere, P. Moore, C. Schwab, J. F. P. Spronck, and A. Szymkowiak. CHIRON - A Fiber Fed Spectrometer for Precise Radial Velocities. *PASP*, 125:1336–1347, Nov. 2013. doi: 10.1086/674012.

C. G. Toner and D. F. Gray. The starpatch on the G8 dwarf XI Bootis A. *ApJ*, 334:1008–1020, Nov. 1988. doi: 10.1086/166893.

C. G. Toner and B. J. Labonte. Xi-Bootis - Starpatch or Moat Flow. In G. Wallerstein, editor, *Cool Stars, Stellar Systems, and the Sun*, volume 9 of *Astronomical Society of the Pacific Conference Series*, page 161, 1990.

J. Tonry and M. Davis. A survey of galaxy redshifts. I - Data reduction techniques. *AJ*, 84:1511–1525, Oct. 1979. doi: 10.1086/112569.

G. Torres, D. A. Fischer, A. Sozzetti, L. A. Buchhave, J. N. Winn, M. J. Holman, and J. A. Carter. Improved Spectroscopic Parameters for Transiting Planet Hosts. *ApJ*, 757:161, Oct. 2012. doi: 10.1088/0004-637X/757/2/161.

G. Torres, D. M. Kipping, F. Fressin, D. A. Caldwell, J. D. Twicken, S. Ballard, N. M. Batalha, S. T. Bryson, D. R. Ciardi, C. E. Henze, S. B. Howell, H. T. Isaacson, J. M. Jenkins, P. S. Muirhead, E. R. Newton, E. A. Petigura, T. Barclay, W. J. Borucki, J. R. Crepp, M. E. Everett, E. P. Horch, A. W. Howard, R. Kolbl, G. W. Marcy, S. McCauliff, and E. V. Quintana. Validation of 12 Small Kepler Transiting Planets in the Habitable Zone. *ApJ*, 800:99, Feb. 2015. doi: 10.1088/0004-637X/800/2/99.

M. Tuomi, H. R. A. Jones, J. S. Jenkins, C. G. Tinney, R. P. Butler, S. S. Vogt, J. R. Barnes, R. A. Wittenmyer, S. O'Toole, J. Horner, J. Bailey, B. D. Carter, D. J. Wright, G. S. Salter, and D. Pinfield. Signals embedded in the radial velocity noise. Periodic variations in the $\tau$ Ceti velocities. *A&A*, 551:A79, Mar. 2013. doi: 10.1051/0004-6361/201220509.

J. A. Valenti and D. A. Fischer. Spectroscopic Properties of Cool Stars (SPOCS). I. 1040 F, G, and K Dwarfs from Keck, Lick, and AAT Planet Search Programs. *ApJS*, 159:141–166, July 2005. doi: 10.1086/430500.

J. A. Valenti and N. Piskunov. Spectroscopy made easy: A new tool for fitting observations with synthetic spectra. *A&AS*, 118:595–603, Sept. 1996.

J. A. Valenti, R. P. Butler, and G. W. Marcy. Determining Spectrometer Instrumental Profiles Using FTS Reference Spectra. *PASP*, 107:966, Oct. 1995. doi: 10.1086/133645.

F. van Leeuwen. Validation of the new Hipparcos reduction. *A&A*, 474:653–664, Nov. 2007. doi: 10.1051/0004-6361:20078357.

A. Vanderburg, B. T. Montet, J. A. Johnson, L. A. Buchhave, L. Zeng, F. Pepe, A. Collier Cameron, D. W. Latham, E. Molinari, S. Udry, C. Lovis, J. M. Matthews, C. Cameron, N. Law, B. P. Bowler, R. Angus, C. Baranec, A. Bieryla, W. Boschin, D. Charbonneau, R. Cosentino, X. Dumusque, P. Figueira, D. B. Guenther, A. Harutyunyan, C. Hellier, R. Kuschnig, M. Lopez-Morales, M. Mayor, G. Micela, A. F. J. Moffat, M. Pedani, D. F. Phillips, G. Piotto, D. Pollacco, D. Queloz, K. Rice, R. Riddle, J. F. Rowe, S. M. Rucinski, D. Sasselov, D. Ségransan, A. Sozzetti, A. Szentgyorgyi, C. Watson, and W. W. Weiss. Characterizing K2 Planet Discoveries: A Super-Earth Transiting the Bright K Dwarf HIP 116454. *ApJ*, 800:59, Feb. 2015. doi: 10.1088/0004-637X/800/1/59.

A. Vanderburg, P. Plavchan, J. A. Johnson, D. R. Ciardi, J. Swift, and S. R. Kane. Radial velocity planet detection biases at the stellar rotational period. *MNRAS*, 459:3565–3573, July 2016. doi: 10.1093/mnras/stw863.

E. Villaver and M. Livio. The Orbital Evolution of Gas Giant Planets Around Giant Stars. *ApJ*, 705:L81–L85, Nov. 2009. doi: 10.1088/0004-637X/705/1/L81.

S. S. Vogt, G. D. Penrod, and A. P. Hatzes. Doppler images of rotating stars using maximum entropy image reconstruction. *ApJ*, 321:496–515, Oct. 1987. doi: 10.1086/165647.

S. S. Vogt, S. L. Allen, B. C. Bigelow, L. Bresee, B. Brown, T. Cantrall, A. Conrad, M. Couture, C. Delaney, H. W. Epps, D. Hilyard, D. F. Hilyard, E. Horn, N. Jern, D. Kanto, M. J. Keane, R. I. Kibrick, J. W. Lewis, J. Osborne, G. H. Pardeilhan, T. Pfister, T. Ricketts, L. B. Robinson, R. J. Stover, D. Tucker, J. Ward, and M. Z. Wei. HIRES: the high-resolution echelle spectrometer on the Keck 10-m Telescope. In D. L. Crawford and E. R. Craine, editors, *Instrumentation in Astronomy VIII*, volume 2198 of *Proc. SPIE*, page 362, June 1994.

L. M. Walkowicz and S. L. Hawley. Tracers of Chromospheric Structure. I. Observations of Ca II K and H$\alpha$ in M Dwarfs. *AJ*, 137:3297–3313, Feb. 2009. doi: 10.1088/0004-6256/137/2/3297.

L. M. Weiss, G. W. Marcy, J. F. Rowe, A. W. Howard, H. Isaacson, J. J. Fortney, N. Miller, B.-O. Demory, D. A. Fischer, E. R. Adams, A. K. Dupree, S. B. Howell, R. Kolbl, J. A. Johnson, E. P. Horch, M. E. Everett, D. C. Fabrycky, and S. Seager. The Mass of KOI-94d and a Relation for

Planet Radius, Mass, and Incident Flux. *ApJ*, 768:14, May 2013. doi: 10.1088/0004-637X/768/1/14.

R. G. West, C. Hellier, J.-M. Almenara, D. R. Anderson, S. C. C. Barros, F. Bouchy, D. J. A. Brown, A. Collier Cameron, M. Deleuil, L. Delrez, A. P. Doyle, F. Faedi, A. Fumel, M. Gillon, Y. Gómez Maqueo Chew, G. Hébrard, E. Jehin, M. Lendl, P. F. L. Maxted, F. Pepe, D. Pollacco, D. Queloz, D. Ségransan, B. Smalley, A. M. S. Smith, J. Southworth, A. H. M. J. Triaud, and S. Udry. Three irradiated and bloated hot Jupiters:. WASP-76b, WASP-82b, and WASP-90b. *A&A*, 585:A126, Jan. 2016. doi: 10.1051/0004-6361/201527276.

P. J. Wheatley, R. G. West, M. R. Goad, J. S. Jenkins, D. L. Pollacco, D. Queloz, H. Rauer, S. Udry, C. A. Watson, B. Chazelas, P. Eigmüller, G. Lambert, L. Genolet, J. McCormac, S. Walker, D. J. Armstrong, D. Bayliss, J. Bento, F. Bouchy, M. R. Burleigh, J. Cabrera, S. L. Casewell, A. Chaushev, P. Chote, S. Csizmadia, A. Erikson, F. Faedi, E. Foxell, B. T. Gänsicke, E. Gillen, A. Grange, M. N. Günther, S. T. Hodgkin, J. Jackman, A. Jordán, T. Louden, L. Metrailler, M. Moyano, L. D. Nielsen, H. P. Osborn, K. Poppenhaeger, R. Raddi, L. Raynard, A. M. S. Smith, M. Soto, and R. Titz-Weider. The Next Generation Transit Survey (NGTS). *MNRAS*, 475:4476–4493, Apr. 2018. doi: 10.1093/mnras/stx2836.

O. C. Wilson. Flux Measurements at the Centers of Stellar H- and K-Lines. *ApJ*, 153:221, July 1968. doi: 10.1086/149652.

J. T. Wright. *Stellar magnetic activity and the detection of exoplanets*. PhD thesis, University of California, Berkeley, California, USA, 2006.

J. T. Wright and J. D. Eastman. Barycentric Corrections at 1 cm s$^{-1}$ for Precise Doppler Velocities. *PASP*, 126:838, Sept. 2014. doi: 10.1086/678541.

M. Zechmeister and M. Kürster. The generalised Lomb-Scargle periodogram. A new formalism for the floating-mean and Keplerian periodograms. *A&A*, 496:577–584, Mar. 2009. doi: 10.1051/0004-6361:200811296.

# Appendix A

# Appendix for chapter 1

## A.1 RV measurements

Table A.1: RV measurements for HD 11977.

| JD - 2450000 | RV (m/s) | Error (m/s) | JD - 2450000 | RV (m/s) | Error (m/s) | JD - 2450000 | RV (m/s) | Error (m/s) | JD - 2450000 | RV (m/s) | Error (m/s) |
|---|---|---|---|---|---|---|---|---|---|---|---|
| FEROS | | | | | | FEROS | | | | | |
| 3100.480 | -54.5 | 7.5 | 3585.911 | 4.9 | 8.2 | 3582.929 | 8.0 | 9.0 | 4315.791 | -85.3 | 8.7 |
| 3101.488 | -32.4 | 8.6 | 3586.743 | 15.2 | 8.7 | 3583.726 | 24.2 | 9.7 | 4316.850 | -78.8 | 7.7 |
| 3102.481 | -82.6 | 6.9 | 3586.903 | -0.4 | 7.9 | 3583.945 | 23.5 | 9.0 | 4316.927 | -45.1 | 7.2 |
| 3102.486 | -74.4 | 7.1 | 3590.726 | -5.1 | 9.0 | 3584.705 | 25.5 | 8.9 | 4317.857 | -90.2 | 14.9 |
| 3216.910 | -54.8 | 7.5 | 3591.767 | 0.4 | 8.3 | 3585.720 | 11.1 | 9.3 | 4319.871 | -66.3 | 8.1 |
| 3217.842 | -66.7 | 11.1 | 3591.931 | 1.4 | 7.2 | HARPS | | | | | |
| 3218.933 | -59.6 | 8.1 | 3592.733 | 10.0 | 9.9 | 3334.620 | 49.2 | 0.2 | 4787.602 | 120.8 | 0.3 |
| 3331.581 | -12.9 | 5.9 | 3592.933 | 3.6 | 9.5 | 4045.592 | 121.1 | 0.6 | 4891.528 | -10.6 | 0.4 |
| 3332.556 | -2.8 | 5.8 | 3593.725 | -11.4 | 9.9 | 4370.721 | -30.1 | 0.3 | 5083.811 | -1.5 | 0.3 |
| 3334.622 | 11.6 | 6.5 | 3593.929 | -8.4 | 9.0 | 4371.671 | -7.5 | 0.4 | 5084.748 | -2.9 | 0.2 |
| 3335.688 | 6.3 | 5.4 | 3594.715 | -8.0 | 9.0 | 4622.915 | 55.1 | 0.4 | 5085.754 | -8.5 | 0.2 |
| 3336.691 | 16.3 | 5.2 | 3594.926 | -2.6 | 7.9 | 4684.748 | 128.8 | 0.3 | 5086.730 | -2.1 | 0.4 |
| 3338.709 | -12.8 | 6.0 | 3595.853 | 2.5 | 14.2 | 4785.641 | 131.2 | 0.6 | | | |
| 3448.479 | 71.6 | 7.4 | 3932.943 | -20.7 | 7.2 | CHIRON | | | | | |
| 3449.481 | 107.5 | 4.1 | 4041.589 | 44.3 | 6.3 | 6906.820 | -17.7 | 5.4 | 6965.553 | -6.1 | 4.6 |
| 3449.484 | 114.9 | 4.8 | 4112.543 | 115.1 | 5.1 | 6919.634 | -16.1 | 4.0 | 6988.552 | 10.6 | 5.2 |
| 3581.730 | 11.1 | 9.4 | 4113.550 | 116.7 | 3.4 | 6921.717 | -22.6 | 4.7 | 6993.525 | 19.6 | 5.0 |
| 3581.925 | 10.6 | 8.3 | 4115.552 | 105.9 | 2.4 | 6964.740 | -3.5 | 4.6 | 7013.531 | 35.7 | 5.2 |
| 3582.737 | 25.1 | 9.7 | 4313.859 | -65.9 | 16.1 | | | | | | |

Table A.2: RV measurements for HD 47536.

| JD - 2450000 | RV (m/s) | Error (m/s) | JD - 2450000 | RV (m/s) | Error (m/s) | JD - 2450000 | RV (m/s) | Error (m/s) | JD - 2450000 | RV (m/s) | Error (m/s) |
|---|---|---|---|---|---|---|---|---|---|---|---|
| FEROS | | | | | | FEROS | | | | | |
| 3454.506 | -65.8 | 7.7 | 4217.484 | -99.0 | 6.9 | 4157.525 | -23.8 | 9.5 | 5588.777 | -111.3 | 7.2 |
| 3454.509 | -63.9 | 8.7 | 4231.459 | -125.2 | 7.9 | 4162.558 | 65.5 | 8.0 | 5630.650 | -102.9 | 8.6 |
| 3460.566 | -39.0 | 5.5 | 4233.471 | -24.1 | 7.0 | 4216.484 | 31.3 | 6.1 | 5632.546 | -117.8 | 7.7 |
| 3460.569 | -40.2 | 5.3 | 4402.754 | 150.7 | 6.0 | HARPS | | | | | |
| 3685.756 | 27.3 | 8.0 | 4407.858 | 109.3 | 5.6 | 4045.814 | 18.4 | 0.3 | 4622.442 | -93.4 | 0.4 |
| 3687.752 | 52.8 | 7.6 | 4492.534 | 115.9 | 10.0 | 4085.848 | 111.1 | 0.5 | 4623.462 | -25.5 | 0.7 |
| 3688.716 | 51.3 | 7.1 | 4493.533 | 110.1 | 7.5 | 4188.594 | -70.4 | 1.1 | 4684.925 | -18.0 | 0.3 |
| 3689.708 | 75.0 | 7.6 | 4494.540 | 88.4 | 9.9 | 4236.489 | -94.4 | 1.3 | 4685.925 | 7.4 | 0.4 |
| 3689.857 | 70.3 | 7.2 | 4509.602 | 31.7 | 9.1 | 4370.863 | 84.4 | 0.3 | 4786.762 | 49.4 | 0.4 |
| 3690.663 | -1.7 | 7.4 | 4510.579 | 106.2 | 9.5 | 4560.593 | -48.2 | 0.3 | 4788.863 | 39.1 | 0.3 |
| 3809.589 | -142.1 | 6.5 | 4572.613 | -75.1 | 6.2 | 4561.578 | -54.1 | 0.3 | 4877.701 | 135.4 | 0.3 |
| 3813.559 | -133.0 | 6.8 | 4582.500 | -140.6 | 6.5 | 4594.467 | -79.4 | 0.3 | 4891.645 | 66.1 | 0.3 |
| 3869.512 | -108.7 | 8.1 | 4780.881 | 103.1 | 4.9 | 4596.469 | -101.1 | 0.5 | 4893.659 | 98.7 | 0.4 |
| 3873.472 | -114.9 | 8.8 | 5109.833 | -83.5 | 7.5 | CORALIE | | | | | |
| 4040.759 | 147.3 | 6.7 | 5167.827 | -138.1 | 5.1 | 2550.388 | -48.5 | 15.0 | 2719.400 | 240.6 | 10.0 |
| 4042.774 | 139.5 | 6.4 | 5201.738 | 1.5 | 6.4 | 2622.090 | 76.7 | 10.2 | 2999.379 | 10.5 | 10.0 |
| 4112.653 | 5.1 | 7.6 | 5255.591 | 74.9 | 5.0 | 2642.576 | 178.0 | 5.0 | 3001.086 | 29.7 | 10.0 |
| 4113.636 | 4.9 | 6.2 | 5258.694 | 119.2 | 5.7 | 2669.891 | 140.9 | 15.0 | 3047.180 | 113.0 | 10.0 |
| 4114.664 | -12.4 | 6.7 | 5491.768 | 93.1 | 9.3 | 2683.549 | 255.8 | 10.0 | 3052.302 | 130.2 | 10.0 |
| 4115.689 | 22.7 | 7.0 | 5494.891 | 92.6 | 7.1 | 2717.693 | 192.4 | 10.0 | 3782.980 | -118.3 | 10.0 |
| 4120.765 | -2.8 | 8.0 | 5521.825 | -5.6 | 7.7 | CHIRON | | | | | |
| 4121.710 | 25.6 | 7.5 | 5523.764 | -44.3 | 7.4 | 6953.723 | 13.8 | 6.8 | 6979.718 | -18.5 | 6.3 |
| 4122.790 | -28.6 | 7.0 | 5524.789 | 18.9 | 7.4 | 6959.719 | -105.2 | 6.8 | 6987.636 | -36.6 | 5.8 |
| 4123.791 | 43.8 | 6.9 | 5525.881 | -41.4 | 7.5 | 6967.768 | 48.5 | 6.2 | 7012.707 | 60.7 | 6.7 |
| 4124.815 | 18.0 | 7.1 | 5583.808 | -110.4 | 7.2 | 6977.711 | 37.2 | 6.9 | | | |

Table A.3: RV measurements for HD 110014.

| JD - 2450000 | RV (m/s) | Error (m/s) | JD - 2450000 | RV (m/s) | Error (m/s) | JD - 2450000 | RV (m/s) | Error (m/s) | JD - 2450000 | RV (m/s) | Error (m/s) |
|---|---|---|---|---|---|---|---|---|---|---|---|
| FEROS | | | | | | FEROS | | | | | |
| 4112.805 | -166.6 | 10.5 | 4316.480 | 91.8 | 8.2 | 4313.560 | 73.9 | 11.2 | | | |
| 4113.784 | -171.2 | 8.0 | 4492.899 | 120.5 | 9.4 | HARPS | | | | | |
| 4120.857 | -111.7 | 7.4 | 4495.852 | 106.0 | 7.3 | 4235.759 | 38.1 | 0.3 | 4891.766 | -12.2 | 0.2 |
| 4120.861 | -112.5 | 7.9 | 5260.801 | 53.7 | 7.2 | 4560.834 | 364.5 | 0.3 | 4931.641 | 20.2 | 0.2 |
| 4159.903 | -15.0 | 8.3 | 5262.783 | 42.7 | 5.0 | 4594.768 | 289.4 | 0.4 | 5918.873 | -19.2 | 0.2 |
| 4161.809 | -5.6 | 9.5 | 5309.667 | 40.9 | 11.4 | 4595.565 | 284.6 | 0.3 | 5934.864 | -28.9 | 0.2 |
| 4216.540 | -74.1 | 7.2 | 5356.570 | 156.1 | 7.8 | 4596.735 | 287.5 | 0.4 | 5935.844 | -15.5 | 0.2 |
| 4217.765 | -64.0 | 8.9 | 5586.890 | -13.0 | 5.0 | 4622.599 | 189.3 | 0.3 | 5936.861 | -16.4 | 0.2 |
| 4217.770 | -64.7 | 8.8 | 5615.805 | -10.1 | 9.2 | 4623.663 | 204.5 | 0.4 | 5937.861 | -15.6 | 0.2 |
| 4309.474 | 79.8 | 9.4 | 5615.895 | 1.0 | 8.4 | 4684.471 | 272.4 | 0.2 | 5938.860 | -37.8 | 0.2 |
| 4309.479 | 85.6 | 9.3 | 5630.733 | -22.2 | 7.8 | 4685.514 | 247.0 | 0.3 | | | |

| JD - 2450000 | RV (m/s) | Error (m/s) | JD - 2450000 | RV (m/s) | Error (m/s) | JD - 2450000 | RV (m/s) | Error (m/s) | JD - 2450000 | RV (m/s) | Error (m/s) |
|---|---|---|---|---|---|---|---|---|---|---|---|
| 4312.487 | 93.6 | 9.4 | 5672.706 | -134.2 | 7.1 | | | | | | |

Table A.4: RV measurements for HD 122430.

| JD - 2450000 | RV (m/s) | Error (m/s) | JD - 2450000 | RV (m/s) | Error (m/s) | JD - 2450000 | RV (m/s) | Error (m/s) | JD - 2450000 | RV (m/s) | Error (m/s) |
|---|---|---|---|---|---|---|---|---|---|---|---|
| | | FEROS | | | | | | FEROS | | | |
| 3098.776 | 18.8 | 8.5 | 3871.789 | 31.0 | 2.5 | 3449.878 | 18.6 | 7.8 | 4232.597 | 21.8 | 3.9 |
| 3100.692 | -21.3 | 5.9 | 3872.753 | 2.5 | 2.1 | 3449.882 | 17.7 | 8.1 | 4309.610 | -26.9 | 3.6 |
| 3101.783 | 4.8 | 6.1 | 3873.746 | 13.3 | 3.4 | 3449.886 | 14.7 | 7.1 | 4313.621 | 49.6 | 6.5 |
| 3102.783 | -45.6 | 5.8 | 3873.771 | 19.4 | 3.0 | 3463.889 | 33.7 | 5.3 | 4496.892 | -68.4 | 7.4 |
| 3103.692 | -33.0 | 15.8 | 3925.495 | 45.1 | 2.5 | 3570.596 | -14.7 | 4.2 | 5340.713 | 30.2 | 6.0 |
| 3216.473 | -103.9 | 5.1 | 3925.601 | 29.5 | 2.3 | 3807.795 | 18.0 | 7.7 | 5341.695 | 21.9 | 5.1 |
| 3216.479 | -97.1 | 5.5 | 3926.501 | 45.2 | 4.2 | 3807.918 | 50.4 | 7.2 | 5353.529 | 82.9 | 5.6 |
| 3217.537 | -66.8 | 6.8 | 4112.821 | -32.8 | 7.1 | 3869.794 | 0.4 | 5.1 | 5403.589 | -96.4 | 5.9 |
| 3218.561 | -62.1 | 6.9 | 4113.842 | 17.4 | 7.2 | | | HARPS | | | |
| 3447.867 | 38.3 | 6.9 | 4114.843 | 29.5 | 6.9 | 4235.772 | 12.2 | 0.3 | 4622.627 | 9.4 | 0.3 |
| 3448.836 | 2.2 | 6.4 | 4120.864 | 20.9 | 7.0 | 4560.852 | -2.3 | 0.3 | 4684.490 | -20.4 | 0.3 |
| 3448.840 | 4.6 | 6.8 | 4161.812 | 4.9 | 7.4 | 4596.737 | -17.4 | 0.4 | 4891.774 | 18.6 | 0.3 |
| 3448.845 | 1.3 | 6.2 | 4216.545 | -19.5 | 5.6 | | | | | | |

Table A.5: RV measurements for HD 70573.

| JD - 2450000 | RV (m/s) | Error (m/s) | JD - 2450000 | RV (m/s) | Error (m/s) | JD - 2450000 | RV (m/s) | Error (m/s) | JD - 2450000 | RV (m/s) | Error (m/s) |
|---|---|---|---|---|---|---|---|---|---|---|---|
| | | FEROS | | | | | | FEROS | | | |
| 3099.524 | -45.7 | 11.7 | 4114.743 | 17.1 | 11.0 | 3873.511 | -113.9 | 16.1 | 4162.588 | -14.8 | 9.8 |
| 3101.539 | -70.7 | 10.3 | 4114.835 | 39.8 | 9.9 | 4039.874 | 79.8 | 10.1 | 4162.728 | -16.1 | 14.2 |
| 3449.674 | 29.2 | 16.4 | 4115.721 | -30.3 | 49.1 | 4040.875 | -51.3 | 7.2 | 4163.601 | -71.2 | 17.1 |
| 3687.838 | 5.3 | 11.2 | 4121.748 | 90.1 | 8.8 | 4041.799 | 42.6 | 12.5 | 4164.550 | 51.0 | 11.5 |
| 3807.576 | -48.4 | 12.8 | 4121.856 | 106.3 | 12.9 | 4042.873 | -20.1 | 5.1 | 4164.691 | 53.0 | 15.4 |
| 3807.638 | -77.8 | 23.7 | 4122.802 | 82.6 | 11.7 | 4043.863 | 51.1 | 9.4 | 4165.552 | 3.1 | 11.4 |
| 3809.735 | -9.4 | 22.8 | 4122.849 | 77.9 | 8.5 | 4048.838 | 48.3 | 8.4 | 4165.683 | -24.0 | 15.2 |
| 3810.604 | -61.5 | 12.3 | 4123.816 | -19.8 | 10.6 | 4053.864 | -11.7 | 10.2 | 4216.511 | -52.2 | 8.6 |
| 3813.660 | -39.7 | 11.3 | 4123.859 | -11.1 | 13.4 | 4112.688 | 67.7 | 8.7 | 4216.571 | -61.6 | 12.3 |
| 3816.663 | -16.1 | 11.8 | 4124.790 | 19.0 | 10.1 | 4112.783 | 72.0 | 12.2 | 4217.527 | 26.7 | 10.3 |
| 3817.716 | -75.1 | 16.1 | 4124.866 | 26.8 | 10.6 | 4113.652 | -11.0 | 11.8 | 4407.787 | 14.8 | 9.8 |
| 3869.524 | 14.4 | 10.4 | 4159.579 | -10.1 | 16.3 | 4113.734 | -31.6 | 12.9 | 4412.843 | 69.3 | 12.0 |
| 3871.514 | 4.4 | 12.7 | 4159.769 | 13.5 | 21.7 | 4113.839 | -83.8 | 11.6 | 4413.747 | -20.2 | 16.2 |
| 3872.493 | -23.1 | 9.9 | 4160.718 | -26.2 | 15.7 | 4114.645 | 4.2 | 13.2 | 4504.745 | 38.6 | 17.3 |

## A.2 Activity indices

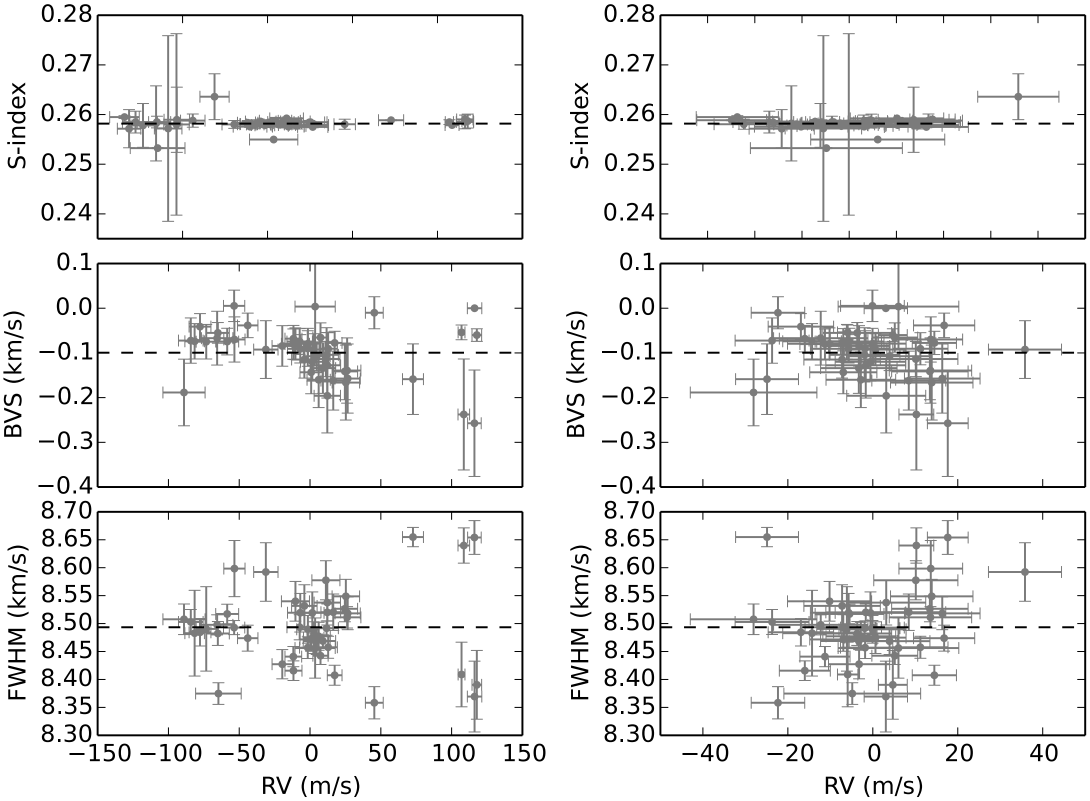

Figure A.1: S-index (upper panel), bisector velocity span (middle panel) and FWHM of the CCF (lower panel) versus the measured RV (left panel) and versus the residual RV for HD 11977, after fitting the 1-planet solution. Only the values for the activity indices laying 2.5$\sigma$ from the mean value of the distribution were considered. The correlation coefficients for the plots in the left panels are $r$= 0.11, -0.29 and 0.05, and for the right panels are $r$ = 0.3, -0.19 and 0.25 for the S-index, BVS and FWHM versus the residual velocity, respectively. Horizontal dashed lines correspond to the mean of the distribution for each plot.

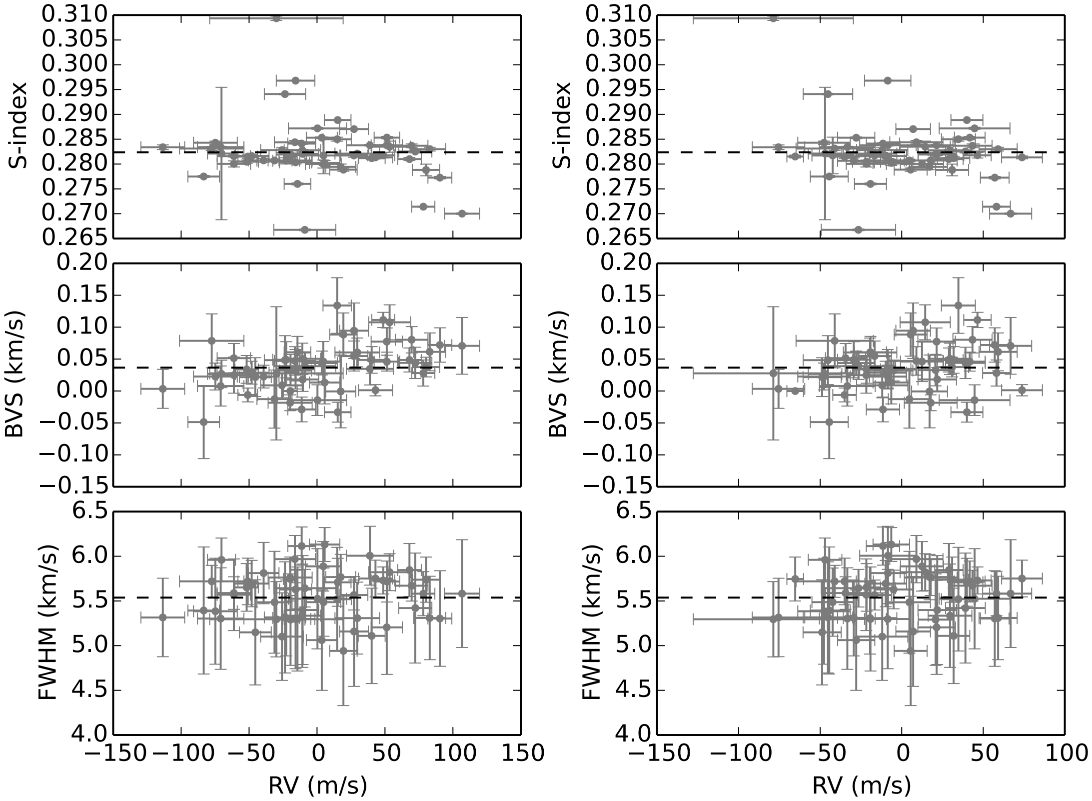

Figure A.2: S-index (upper panel), bisector velocity span (middle panel) and FWHM of the CCF (lower panel) versus the measured RV (left panel) and versus the residual RV for HD 70573, after removing the rotation of the star. Only the values for the activity indices laying 2.5$\sigma$ from the mean value of the distribution were considered. The correlation coefficients for the plots in the left panels are $r$= -0.19, 0.44 and 0.05, and for the right panels are $r = -0.28$, 0.26 and 0.11 for the S-index, BVS and FWHM versus the residual velocity, respectively. Horizontal dashed lines correspond to the mean of the distribution for each plot.

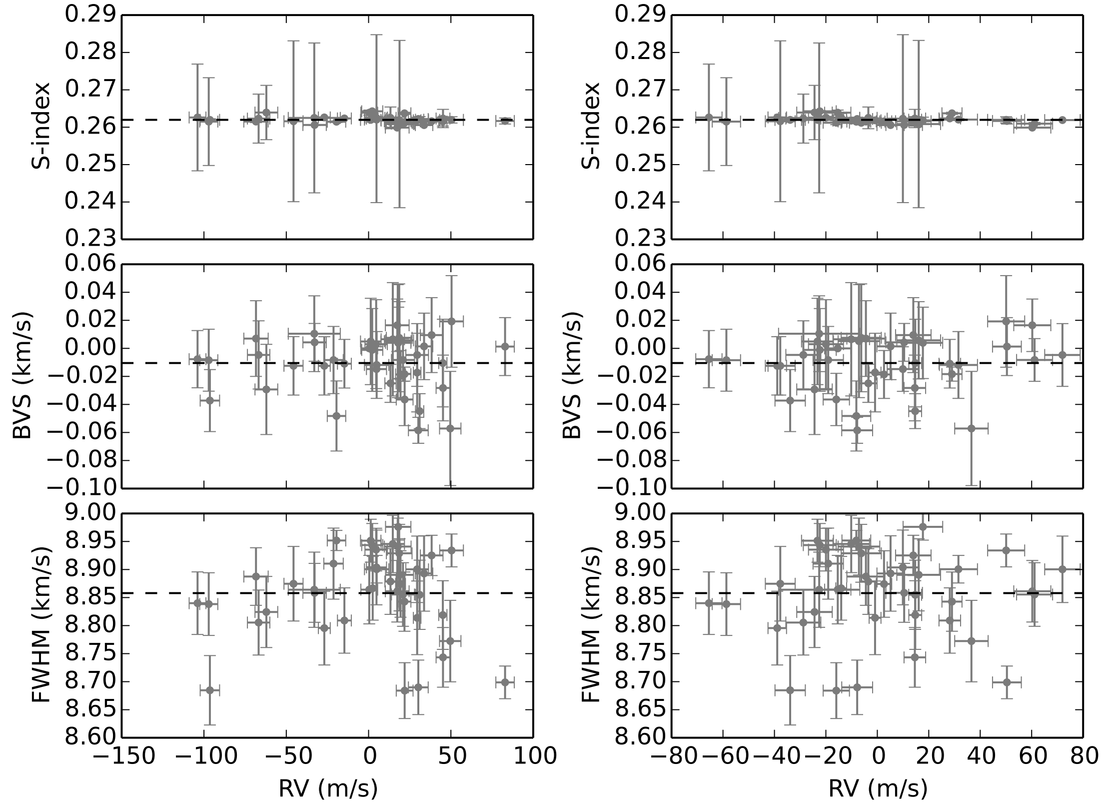

Figure A.3: S-index (upper panel), bisector velocity span (middle panel) and FWHM of the CCF (lower panel) versus the measured RV (left panel) and versus the residual RV for HD 122430, after fitting the best 1-planet solution we were able to obtain. Only the values for the activity indices laying $2.5\sigma$ from the mean value of the distribution were considered. The correlation coefficients for the plots in the left panels are $r$= -0.17, 0.01 and 0.04, and for the right panels are $r = -0.32$, 0.1 and 0.04 for the S-index, BVS and FWHM versus the residual velocity, respectively. Horizontal dashed lines correspond to the mean of the distribution for each plot.

# Appendix B

# Appendix for chapter 2

## B.1 Radial Velocities

Table B.1: CORALIE Radial Velocities of K2-237.

| BJD ( -2450000) | RV ($\mathrm{m\,s^{-1}}$) | $\sigma$ RV ($\mathrm{m\,s^{-1}}$) | BIS ($\mathrm{m\,s^{-1}}$) | S (dex) |
|---|---|---|---|---|
| 7942.60097 | −22339.6 | 38.8 | −78 | 0.2823 |
| 7943.55647 | −21951.7 | 38.2 | −69 | 0.1812 |
| 7943.57794 | −22000.3 | 38.6 | −157 | 0.2420 |
| 7944.56592 | −22378.4 | 38.6 | −37 | 0.1935 |
| 7944.58780 | −22413.6 | 38.6 | −23 | 0.2483 |
| 7945.57852 | −22204.1 | 38.5 | −34 | 0.6665 |
| 7945.60178 | −22196.3 | 38.5 | −55 | 0.2057 |
| 7946.54859 | −22423.8 | 38.5 | −49 | 0.1501 |
| 7946.56573 | −22404.5 | 38.6 | −75 | 0.2128 |

Table B.2: HARPS Radial Velocities of K2-237.

| BJD ( -2450000) | RV ($\mathrm{m\,s^{-1}}$) | $\sigma$ RV ($\mathrm{m\,s^{-1}}$) | BIS ($\mathrm{m\,s^{-1}}$) | S (dex) |
|---|---|---|---|---|
| 8036.55780 | −22434.7 | 26.0 | −11 | 0.2714 |
| 8037.51703 | −22027.7 | 27.9 | 10 | 0.2652 |
| 8038.51742 | −22472.5 | 32.1 | −136 | 0.2711 |
| 8039.53105 | −22085.3 | 24.3 | −20 | 0.2252 |

Table B.3: FEROS Radial Velocities of K2-238.

| BJD ( -2450000) | RV ($\mathrm{m\,s^{-1}}$) | $\sigma$ RV ($\mathrm{m\,s^{-1}}$) | BIS ($\mathrm{m\,s^{-1}}$) |
|---|---|---|---|
| 8062.63804 | 8247.9 | 16.1 | −15.2 |

| BJD<br>( -2450000) | RV<br>($\mathrm{m\,s^{-1}}$) | $\sigma$ RV<br>($\mathrm{m\,s^{-1}}$) | BIS<br>($\mathrm{m\,s^{-1}}$) |
|---|---|---|---|
| 8063.63606 | 8415.9 | 24.1 | 191.2 |
| 8064.55872 | 8193.9 | 15.5 | −102.4 |
| 8065.59564 | 8173.3 | 13.0 | 15.0 |
| 8065.64809 | 8199.5 | 15.9 | −84.7 |
| 8066.51427 | 8366.3 | 14.5 | −144.5 |
| 8109.53786 | 8198.1 | 16.5 | 71.0 |
| 8110.54097 | 8275.7 | 15.5 | 140.0 |
| 8111.54702 | 8352.8 | 14.5 | 81.0 |
| 8113.54191 | 8204.4 | 15.5 | −2.0 |
| 8114.54353 | 8334.6 | 14.8 | 88.0 |

# Appendix C

# Appendix for chapter 3

## C.1 Tables

Table C.1: Line data used in the computation of the atmospheric parameters.

| Wavelength | $\chi_I$ | loggf | Name | Wavelength | $\chi_I$ | loggf | Name | Wavelength | $\chi_I$ | loggf | Name |
|---:|---:|---:|---:|---:|---:|---:|---:|---:|---:|---:|---:|
| 5494.47 | 4.07 | -1.96 | FeI | 5905.68 | 4.65 | -0.78 | FeI | 6393.61 | 2.43 | -1.43 | FeI |
| 5522.45 | 4.21 | -1.47 | FeI | 5927.8 | 4.65 | -1.07 | FeI | 6421.36 | 2.28 | -1.98 | FeI |
| 5524.24 | 4.15 | -2.84 | FeI | 5929.68 | 4.55 | -1.16 | FeI | 6436.41 | 4.19 | -2.4 | FeI |
| 5539.29 | 3.64 | -2.59 | FeI | 5930.19 | 4.65 | -0.34 | FeI | 6481.88 | 2.28 | -2.94 | FeI |
| 5552.69 | 4.95 | -1.78 | FeI | 5933.81 | 4.64 | -2.14 | FeI | 6498.95 | 0.96 | -4.66 | FeI |
| 5560.22 | 4.43 | -1.1 | FeI | 5934.67 | 3.93 | -1.08 | FeI | 6518.37 | 2.83 | -2.56 | FeI |
| 5568.86 | 3.63 | -2.91 | FeI | 5947.53 | 4.61 | -2.04 | FeI | 6533.94 | 4.56 | -1.28 | FeI |
| 5577.03 | 5.03 | -1.49 | FeI | 5956.71 | 0.86 | -4.56 | FeI | 6574.25 | 0.99 | -4.96 | FeI |
| 5586.77 | 3.37 | -0.1 | FeI | 5976.79 | 3.94 | -1.3 | FeI | 6581.22 | 1.48 | -4.68 | FeI |
| 5587.58 | 4.14 | -1.7 | FeI | 5984.83 | 4.73 | -0.29 | FeI | 6591.31 | 4.59 | -2.04 | FeI |
| 5595.05 | 5.06 | -1.78 | FeI | 6003.02 | 3.88 | -1.02 | FeI | 6593.88 | 2.43 | -2.3 | FeI |
| 5608.98 | 4.21 | -2.31 | FeI | 6007.97 | 4.65 | -0.76 | FeI | 6608.04 | 2.28 | -3.96 | FeI |
| 5609.97 | 3.64 | -3.18 | FeI | 6008.57 | 3.88 | -0.92 | FeI | 6609.12 | 2.56 | -2.65 | FeI |
| 5611.36 | 3.63 | -2.93 | FeI | 6015.24 | 2.22 | -4.66 | FeI | 6627.56 | 4.55 | -1.5 | FeI |
| 5618.64 | 4.21 | -1.34 | FeI | 6019.37 | 3.57 | -3.23 | FeI | 6633.76 | 4.56 | -0.81 | FeI |
| 5619.61 | 4.39 | -1.49 | FeI | 6027.06 | 4.07 | -1.2 | FeI | 6667.43 | 2.45 | -4.37 | FeI |
| 5635.83 | 4.26 | -1.59 | FeI | 6056.01 | 4.73 | -0.46 | FeI | 6667.72 | 4.58 | -2.1 | FeI |
| 5636.71 | 3.64 | -2.53 | FeI | 6065.49 | 2.61 | -1.49 | FeI | 6699.14 | 4.59 | -2.11 | FeI |
| 5650.0 | 5.1 | -0.8 | FeI | 6078.5 | 4.79 | -0.38 | FeI | 6703.58 | 2.76 | -3.0 | FeI |
| 5651.48 | 4.47 | -1.79 | FeI | 6079.02 | 4.65 | -0.97 | FeI | 6704.49 | 4.22 | -2.64 | FeI |
| 5652.33 | 4.26 | -1.77 | FeI | 6082.72 | 2.22 | -3.53 | FeI | 6713.75 | 4.79 | -1.41 | FeI |
| 5661.02 | 4.58 | -2.42 | FeI | 6089.57 | 5.02 | -0.87 | FeI | 6725.36 | 4.1 | -2.21 | FeI |
| 5661.35 | 4.28 | -1.83 | FeI | 6093.65 | 4.61 | -1.32 | FeI | 6726.67 | 4.61 | -1.05 | FeI |
| 5677.69 | 4.1 | -2.64 | FeI | 6094.38 | 4.65 | -1.56 | FeI | 6733.15 | 4.64 | -1.44 | FeI |
| 5678.39 | 3.88 | -2.97 | FeI | 6096.67 | 3.98 | -1.76 | FeI | 6739.52 | 1.56 | -4.85 | FeI |
| 5680.24 | 4.19 | -2.29 | FeI | 6098.25 | 4.56 | -1.81 | FeI | 6745.97 | 4.07 | -2.71 | FeI |

| Wavelength | $\chi_I$ | loggf | Name | Wavelength | $\chi_I$ | loggf | Name | Wavelength | $\chi_I$ | loggf | Name |
|---:|---:|---:|---:|---:|---:|---:|---:|---:|---:|---:|---:|
| 5701.56 | 2.56 | -2.16 | FeI | 6120.26 | 0.91 | -5.86 | FeI | 6750.16 | 2.42 | -2.58 | FeI |
| 5717.84 | 4.28 | -0.98 | FeI | 6137.0 | 2.2 | -2.91 | FeI | 6753.47 | 4.56 | -2.35 | FeI |
| 5731.77 | 4.26 | -1.1 | FeI | 6151.62 | 2.18 | -3.26 | FeI | 6756.55 | 4.29 | -2.78 | FeI |
| 5738.24 | 4.22 | -2.24 | FeI | 6157.73 | 4.07 | -1.26 | FeI | 6786.86 | 4.19 | -1.9 | FeI |
| 5741.86 | 4.26 | -1.69 | FeI | 6165.36 | 4.14 | -1.48 | FeI | 6793.26 | 4.07 | -2.43 | FeI |
| 5742.96 | 4.18 | -2.35 | FeI | 6173.34 | 2.22 | -2.84 | FeI | 6796.12 | 4.14 | -2.4 | FeI |
| 5752.04 | 4.55 | -0.92 | FeI | 6187.4 | 2.83 | -4.13 | FeI | 6804.3 | 4.58 | -1.85 | FeI |
| 5754.41 | 3.64 | -2.85 | FeI | 6188.0 | 3.94 | -1.6 | FeI | 6806.86 | 2.73 | -3.14 | FeI |
| 5759.26 | 4.65 | -2.07 | FeI | 6199.51 | 2.56 | -4.35 | FeI | 6810.27 | 4.61 | -1.0 | FeI |
| 5760.36 | 3.64 | -2.46 | FeI | 6200.32 | 2.61 | -2.39 | FeI | 5100.66 | 2.81 | -4.16 | FeII |
| 5775.09 | 4.22 | -1.11 | FeI | 6213.44 | 2.22 | -2.54 | FeI | 5132.67 | 2.81 | -3.95 | FeII |
| 5778.46 | 2.59 | -3.44 | FeI | 6219.29 | 2.2 | -2.39 | FeI | 5136.8 | 2.84 | -4.32 | FeII |
| 5784.67 | 3.4 | -2.53 | FeI | 6220.79 | 3.88 | -2.36 | FeI | 5197.58 | 3.23 | -2.23 | FeII |
| 5793.92 | 4.22 | -1.62 | FeI | 6226.74 | 3.88 | -2.08 | FeI | 5234.63 | 3.22 | -2.22 | FeII |
| 5806.73 | 4.61 | -0.93 | FeI | 6232.65 | 3.65 | -1.21 | FeI | 5264.81 | 3.34 | -3.21 | FeII |
| 5811.91 | 4.14 | -2.36 | FeI | 6240.65 | 2.22 | -3.23 | FeI | 5284.11 | 2.89 | -3.01 | FeII |
| 5814.82 | 4.28 | -1.81 | FeI | 6246.33 | 3.6 | -0.73 | FeI | 5414.08 | 3.22 | -3.61 | FeII |
| 5835.11 | 4.26 | -2.18 | FeI | 6252.57 | 2.4 | -1.64 | FeI | 5425.26 | 3.2 | -3.27 | FeII |
| 5837.7 | 4.29 | -2.3 | FeI | 6265.14 | 2.18 | -2.51 | FeI | 5627.5 | 3.39 | -4.14 | FeII |
| 5849.69 | 3.69 | -2.95 | FeI | 6270.23 | 2.86 | -2.55 | FeI | 5991.38 | 3.15 | -3.55 | FeII |
| 5853.15 | 1.48 | -5.09 | FeI | 6280.62 | 0.86 | -4.34 | FeI | 6084.11 | 3.2 | -3.8 | FeII |
| 5855.09 | 4.61 | -1.56 | FeI | 6297.8 | 2.22 | -2.7 | FeI | 6113.33 | 3.21 | -4.12 | FeII |
| 5856.1 | 4.29 | -1.57 | FeI | 6301.51 | 3.65 | -0.72 | FeI | 6149.25 | 3.89 | -2.72 | FeII |
| 5858.79 | 4.22 | -2.19 | FeI | 6303.47 | 4.32 | -2.62 | FeI | 6239.95 | 3.89 | -3.44 | FeII |
| 5859.6 | 4.55 | -0.63 | FeI | 6311.5 | 2.83 | -3.16 | FeI | 6247.56 | 3.87 | -2.32 | FeII |
| 5861.11 | 4.28 | -2.35 | FeI | 6315.81 | 4.07 | -1.67 | FeI | 6369.46 | 2.89 | -4.21 | FeII |
| 5862.37 | 4.55 | -0.42 | FeI | 6322.69 | 2.59 | -2.38 | FeI | 6416.93 | 3.89 | -2.7 | FeII |
| 5879.49 | 4.61 | -1.99 | FeI | 6330.85 | 4.73 | -1.22 | FeI | 6432.68 | 2.89 | -3.58 | FeII |
| 5880.03 | 4.56 | -1.94 | FeI | 6335.34 | 2.2 | -2.28 | FeI | 6456.39 | 3.9 | -2.1 | FeII |
| 5881.28 | 4.61 | -1.76 | FeI | 6380.75 | 4.19 | -1.34 | FeI | 6516.08 | 2.89 | -3.38 | FeII |
| 5902.48 | 4.59 | -1.86 | FeI | 6392.54 | 2.28 | -3.97 | FeI | | | | |

Table C.2: Line data used in the computation of the chemical abundances.

| Wavelength | $\chi_I$ | loggf | Name | Wavelength | $\chi_I$ | loggf | Name | Wavelength | $\chi_I$ | loggf | Name |
|---:|---:|---:|---:|---:|---:|---:|---:|---:|---:|---:|---:|
| 5148.83 | 2.102 | -2.044 | NaI | 5185.9 | 1.893 | -1.41 | TiI | 5662.93 | 3.695 | -1.975 | FeI |
| 5682.63 | 2.102 | -0.706 | NaI | 5226.53 | 1.566 | -1.26 | TiI | 5667.45 | 5.064 | -1.875 | FeI |
| 5688.19 | 2.104 | -1.406 | NaI | 5206.02 | 0.941 | 0.02 | CrI | 5667.51 | 4.178 | -1.576 | FeI |
| 5688.2 | 2.104 | -0.452 | NaI | 5208.4 | 0.941 | 0.17 | CrI | 5679.02 | 4.652 | -0.92 | FeI |
| 6154.22 | 2.102 | -1.547 | NaI | 5214.13 | 3.369 | -0.74 | CrI | 5679.11 | 5.033 | -2.021 | FeI |
| 6160.74 | 2.104 | -1.246 | NaI | 5272.0 | 3.449 | -0.42 | CrI | 5691.49 | 4.301 | -1.52 | FeI |
| 5528.4 | 4.346 | -0.498 | MgI | 5275.27 | 2.889 | -0.244 | CrI | 5717.83 | 4.284 | -1.13 | FeI |
| 5711.08 | 4.346 | -1.724 | MgI | 5275.31 | 4.106 | -3.342 | CrI | 5731.76 | 4.256 | -1.3 | FeI |
| 5785.31 | 5.108 | -2.11 | MgI | 5275.74 | 2.889 | -0.023 | CrI | 5775.08 | 4.22 | -1.298 | FeI |
| 6318.71 | 5.108 | -2.103 | MgI | 5275.75 | 4.613 | -2.612 | CrI | 6085.25 | 2.759 | -3.095 | FeI |
| 5557.06 | 3.143 | -2.11 | AlI | 5275.77 | 3.556 | -4.56 | CrI | 6271.27 | 3.332 | -2.703 | FeI |
| 6696.02 | 3.143 | -1.347 | AlI | 5287.17 | 3.438 | -0.87 | CrI | 6591.31 | 4.593 | -2.07 | FeI |
| 6698.67 | 3.143 | -1.647 | AlI | 5296.69 | 0.983 | -1.36 | CrI | 6625.02 | 1.011 | -5.35 | FeI |
| 5645.61 | 4.93 | -2.14 | SiI | 5297.37 | 2.9 | 0.167 | CrI | 6625.06 | 5.32 | -6.617 | FeI |
| 5666.67 | 5.616 | -1.797 | SiI | 5298.01 | 2.9 | -0.06 | CrI | 6627.54 | 4.549 | -1.68 | FeI |

| Wavelength | $\chi_I$ | loggf | Name | Wavelength | $\chi_I$ | loggf | Name | Wavelength | $\chi_I$ | loggf | Name |
|---:|---:|---:|---:|---:|---:|---:|---:|---:|---:|---:|---:|
| 5675.41 | 5.619 | -1.234 | SiI | 5298.27 | 0.983 | -1.14 | CrI | 6633.41 | 4.835 | -1.49 | FeI |
| 5690.42 | 4.93 | -1.87 | SiI | 5329.13 | 2.914 | -0.008 | CrI | 6646.91 | 4.435 | -5.242 | FeI |
| 5701.1 | 4.93 | -2.05 | SiI | 5329.78 | 2.914 | -0.795 | CrI | 6646.93 | 2.609 | -3.99 | FeI |
| 5747.66 | 5.614 | -1.544 | SiI | 5329.8 | 3.857 | -4.31 | CrI | 6745.1 | 4.58 | -2.16 | FeI |
| 5772.14 | 5.082 | -1.75 | SiI | 5345.79 | 1.004 | -0.896 | CrI | 6745.95 | 4.076 | -2.77 | FeI |
| 5780.38 | 4.92 | -2.35 | SiI | 5345.85 | 4.618 | -3.048 | CrI | 6746.95 | 2.609 | -4.35 | FeI |
| 6125.02 | 5.614 | -1.465 | SiI | 5348.31 | 1.004 | -1.21 | CrI | 6783.7 | 2.588 | -3.98 | FeI |
| 6131.57 | 5.616 | -1.557 | SiI | 5386.96 | 3.369 | -0.743 | CrI | 6786.85 | 4.191 | -2.07 | FeI |
| 6131.85 | 5.616 | -1.617 | SiI | 5409.78 | 1.03 | -0.67 | CrI | 6793.25 | 4.584 | -4.275 | FeI |
| 6142.48 | 5.619 | -1.296 | SiI | 5442.4 | 3.422 | -1.06 | CrI | 6793.25 | 4.076 | -2.326 | FeI |
| 6145.01 | 5.616 | -1.311 | SiI | 5694.74 | 3.857 | -0.241 | CrI | 6796.04 | 4.186 | -2.563 | FeI |
| 6155.13 | 5.619 | -0.755 | SiI | 5694.78 | 4.535 | -4.146 | CrI | 6796.12 | 4.143 | -2.53 | FeI |
| 6237.31 | 5.614 | -0.975 | SiI | 5694.78 | 4.618 | -1.573 | CrI | 5234.61 | 10.448 | -2.697 | FeI |
| 6243.81 | 5.616 | -1.244 | SiI | 5702.3 | 3.449 | -0.67 | CrI | 5234.62 | 3.221 | -2.23 | FeI |
| 6407.29 | 5.871 | -1.393 | SiI | 5712.73 | 5.522 | -7.605 | CrI | 5264.8 | 3.23 | -3.12 | FeI |
| 6414.97 | 5.871 | -1.036 | SiI | 5712.77 | 3.011 | -1.049 | CrI | 5284.07 | 10.531 | -1.381 | FeI |
| 6526.63 | 5.871 | -1.607 | SiI | 5781.16 | 3.011 | -1.0 | CrI | 5284.1 | 2.891 | -2.99 | FeI |
| 6527.2 | 5.871 | -1.072 | SiI | 5781.17 | 3.322 | -0.854 | CrI | 5325.55 | 3.221 | -3.12 | FeI |
| 6721.84 | 5.863 | -1.527 | SiI | 5781.24 | 4.618 | -2.893 | CrI | 5414.07 | 3.221 | -3.54 | FeI |
| 6741.62 | 5.984 | -1.75 | SiI | 5783.06 | 3.323 | -0.5 | CrI | 5425.24 | 3.199 | -3.16 | FeI |
| 5260.38 | 2.521 | -1.719 | CaI | 5784.96 | 3.321 | -0.38 | CrI | 5534.81 | 11.035 | -3.108 | FeI |
| 5261.7 | 2.521 | -0.579 | CaI | 5787.91 | 3.322 | -0.083 | CrI | 5534.83 | 3.245 | -2.73 | FeI |
| 5349.46 | 2.709 | -0.31 | CaI | 6330.09 | 0.941 | -2.92 | CrI | 5534.89 | 10.545 | -0.44 | FeI |
| 5512.98 | 2.933 | -0.464 | CaI | 6882.51 | 3.438 | -0.375 | CrI | 5991.37 | 3.153 | -3.54 | FeI |
| 5590.11 | 2.521 | -0.571 | CaI | 5004.89 | 2.92 | -1.63 | MnI | 6247.55 | 3.892 | -2.31 | FeI |
| 5867.13 | 5.55 | -4.655 | CaI | 5117.93 | 3.134 | -1.2 | MnI | 6247.57 | 5.956 | -4.827 | FeI |
| 5867.56 | 2.933 | -1.57 | CaI | 5255.33 | 3.133 | -0.851 | MnI | 6456.37 | 3.903 | -2.1 | FeI |
| 6102.09 | 5.229 | -4.839 | CaI | 5255.38 | 5.52 | -8.779 | MnI | 5115.39 | 3.834 | -0.11 | NiI |
| 6156.02 | 2.521 | -2.506 | CaI | 5377.6 | 3.844 | -0.166 | MnI | 5129.37 | 3.679 | -0.63 | NiI |
| 6166.43 | 2.521 | -1.142 | CaI | 5413.66 | 3.859 | -0.647 | MnI | 5155.12 | 3.898 | -0.65 | NiI |
| 6169.04 | 2.523 | -0.797 | CaI | 5505.86 | 2.178 | -2.527 | MnI | 5155.76 | 3.898 | 0.074 | NiI |
| 6169.56 | 2.526 | -0.478 | CaI | 5537.75 | 2.187 | -2.328 | MnI | 5176.56 | 3.898 | -0.44 | NiI |
| 6471.66 | 2.526 | -0.686 | CaI | 5151.88 | 5.033 | -8.85 | FeI | 5220.29 | 3.74 | -1.31 | NiI |
| 6717.68 | 2.709 | -0.524 | CaI | 5151.91 | 1.011 | -3.322 | FeI | 5392.33 | 4.154 | -1.32 | NiI |
| 5173.74 | 0.0 | -1.06 | TiI | 5228.37 | 4.22 | -1.29 | FeI | 5589.35 | 3.898 | -1.14 | NiI |
| 5186.33 | 2.117 | -0.77 | TiI | 5250.64 | 2.198 | -2.181 | FeI | 5593.73 | 3.898 | -0.84 | NiI |
| 5192.96 | 0.021 | -0.95 | TiI | 5307.36 | 1.608 | -2.987 | FeI | 5625.31 | 4.089 | -0.7 | NiI |
| 5194.04 | 2.103 | -0.65 | TiI | 5522.44 | 4.209 | -1.55 | FeI | 5637.11 | 4.089 | -0.82 | NiI |
| 5201.05 | 3.57 | -4.08 | TiI | 5528.89 | 4.473 | -2.02 | FeI | 5682.19 | 4.105 | -0.47 | NiI |
| 5201.08 | 2.092 | -0.66 | TiI | 5529.16 | 3.642 | -2.73 | FeI | 5748.35 | 1.676 | -3.26 | NiI |
| 5210.38 | 0.048 | -0.82 | TiI | 5539.28 | 3.642 | -2.66 | FeI | 5760.83 | 4.105 | -0.8 | NiI |
| 5384.63 | 0.826 | -2.77 | TiI | 5543.93 | 4.218 | -1.14 | FeI | 5805.21 | 4.167 | -0.64 | NiI |
| 5389.98 | 1.873 | -1.1 | TiI | 5543.97 | 4.154 | -6.058 | FeI | 5831.39 | 5.004 | -5.748 | NiI |
| 5449.15 | 1.443 | -1.87 | TiI | 5546.99 | 4.218 | -1.91 | FeI | 6086.28 | 4.266 | -0.53 | NiI |
| 5453.64 | 1.443 | -1.6 | TiI | 5549.94 | 3.695 | -2.91 | FeI | 6111.07 | 4.088 | -0.87 | NiI |
| 5648.56 | 2.495 | -0.26 | TiI | 5633.94 | 4.991 | -0.27 | FeI | 6130.13 | 4.266 | -0.96 | NiI |
| 5662.15 | 2.318 | 0.01 | TiI | 5634.01 | 5.086 | -2.633 | FeI | 6175.36 | 4.089 | -0.53 | NiI |
| 5673.42 | 3.148 | -0.244 | TiI | 5636.69 | 3.64 | -2.61 | FeI | 6186.71 | 4.105 | -0.96 | NiI |
| 5673.43 | 3.112 | -1.533 | TiI | 5638.26 | 4.22 | -0.87 | FeI | 6259.59 | 4.089 | -1.237 | NiI |
| 5679.91 | 2.472 | -0.57 | TiI | 5638.33 | 4.584 | -2.929 | FeI | 6414.58 | 4.154 | -1.18 | NiI |
| 5689.46 | 2.297 | -0.36 | TiI | 5641.43 | 4.256 | -1.18 | FeI | 6424.85 | 4.167 | -1.355 | NiI |

| Wavelength | $\chi_I$ | loggf | Name | Wavelength | $\chi_I$ | loggf | Name | Wavelength | $\chi_I$ | loggf | Name |
|---|---|---|---|---|---|---|---|---|---|---|---|
| 5880.27 | 1.053 | -2.0 | TiI | 5641.48 | 3.642 | -3.079 | FeI | 5105.53 | 1.389 | -1.542 | CuI |
| 6002.63 | 2.16 | -1.49 | TiI | 5649.98 | 5.1 | -0.92 | FeI | 5218.19 | 3.817 | 0.364 | CuI |
| 6303.75 | 1.443 | -1.58 | TiI | 5650.7 | 5.086 | -0.96 | FeI | 5220.06 | 3.817 | -0.59 | CuI |
| 6312.23 | 1.46 | -1.55 | TiI | 5651.46 | 4.473 | -2.0 | FeI | 5700.23 | 1.642 | -2.583 | CuI |
| 6599.1 | 0.9 | -2.085 | TiI | 5652.31 | 4.26 | -1.95 | FeI | 6362.33 | 5.796 | 0.15 | ZnI |
| 5154.06 | 1.566 | -1.75 | TiI | 5662.51 | 4.178 | -0.573 | FeI | | | | |

## C.2 Second method for the uncertainty in microturbulent velocity

As mentioned in section 3.1.5, we include two different estimations for the uncertainty in the microturbulent velocity. The first one was already described (shown in the final catalogue as `err_vt`). Here we described the second method used (`err_vt2`).

We used Equation 12 from Magain (1984),

$$\sigma_{\xi_t} \simeq c(\sigma_\delta^2/\sigma_W^2)\,\frac{\partial \xi_t}{\partial S_{RW}}\bigg|_{S_{RW}=0}, \tag{C.1}$$

where $\xi_t$ is the microturbulent velocity, $c = \partial A/\partial W$ change of abundance with equivalent width, $\sigma_\delta^2$ is the variance of the uncertainty of the equivalent widths (EWs), $\sigma_W^2$ is the variance in the EWs, and $S_{RW}$ is the slope of the linear fit performed to EWs vs Fe I abundance.

We assumed the same approximations than in Magain (1984), with one of them being that $c = c_\mathrm{i} = \partial A_\mathrm{i}/\partial W_\mathrm{i}$, the same for all the lines. In order to compute that value, we plotted $c_\mathrm{i}$ vs $W_\mathrm{i}$ and found the ranges for which $c$ is constant. We adopted $c$ within that range to be the final value.

The dependency of $\xi_t$ with $S_{RW}$ can be adjusted by the cubic spline from Eq. 3.3, with coefficients given by Eq. 3.4. The final value for the microturbulence velocity obtained by SPECIES is reached when $S_{RW} = 0$ (Section 3.1.4), therefore in order to obtain $(\partial\xi_t/\partial S_{RW})|_0$ it is necessary to derive Eq. 3.3, and replace $\xi_t$ by the SPECIES value in Eq. 3.4.

Finally, $\sigma_\delta^2$ and $\sigma_W^2$ are obtained from the ARES files for each star.

## C.3 Second method for the uncertainty in temperature

The method described here is very similar to the one used in Section 3.1.5, meaning that the uncertainty in the temperature is composed by two parts:

$$\sigma_T^2 = \left(\frac{\partial T}{\partial \xi_t}\bigg|_{\xi_t}\right)^2 \sigma_{\xi_t}^2 + \left(\frac{\partial T}{\partial \chi_I}\bigg|_{\chi_I=0}\right)^2 \sigma_{\chi_I}^2, \tag{C.2}$$

Table C.3: Sample of the catalogue produced by SPECIES. Only a few columns and rows are shown. Full table is available online.

| Starname | Instrument | Temperature | $\sigma_T$ | [Fe/H] | $\sigma_{[Fe/H]}$ | log g | $\sigma_{logg}$ | $\xi_t$ | vsini | $\sigma_{vsini}$ | $v_{mac}$ | $\sigma_{vmac}$ | [Na/H] | $\sigma_{[Na/H]}$ | Mass | Radius |
|---|---|---|---|---|---|---|---|---|---|---|---|---|---|---|---|---|
| HD8638 | HARPS | 5654 | 58 | -0.37 | 0.10 | 4.61 | 0.53 | 1.20 | 1.16 | 0.44 | 2.37 | 0.44 | -0.14 | 0.01 | 0.87 | 0.89 |
| HD16714 | HARPS | 5551 | 59 | -0.14 | 0.12 | 4.36 | 0.48 | 0.63 | 1.82 | 0.41 | 2.49 | 0.40 | -0.11 | 0.02 | 0.91 | 0.91 |
| HD23249 | HARPS | 5241 | 300 | -0.89 | 0.91 | 3.81 | 0.11 | 1.20 | 0.00 | 0.00 | 0.00 | 0.00 | -0.34 | 0.68 | 1.04 | 2.07 |
| HD30278 | HARPS | 5395 | 36 | -0.16 | 0.08 | 4.33 | 0.29 | 0.66 | 1.91 | 0.27 | 2.12 | 0.27 | -0.23 | 0.06 | 0.82 | 0.90 |
| HD35854 | HARPS | 4918 | 15 | -0.19 | 0.14 | 4.57 | 0.03 | 1.20 | 1.42 | 0.07 | 0.56 | 0.07 | -0.14 | 0.09 | 0.77 | 0.75 |
| HD37986 | HARPS | 5500 | 39 | 0.29 | 0.09 | 4.30 | 0.33 | 0.80 | 2.08 | 0.31 | 2.50 | 0.31 | 0.34 | 0.02 | 0.98 | 1.03 |
| HD72673 | HARPS | 5250 | 34 | -0.41 | 0.08 | 4.49 | 0.35 | 0.39 | 2.25 | 0.65 | 1.81 | 0.65 | -0.30 | 0.01 | 0.72 | 0.76 |
| HD78429 | HARPS | 5818 | 35 | 0.13 | 0.07 | 4.38 | 0.21 | 0.85 | 1.76 | 0.19 | 3.37 | 0.19 | 0.13 | 0.03 | 1.01 | 1.25 |
| HD92719 | HARPS | 5844 | 27 | -0.08 | 0.05 | 4.48 | 0.19 | 0.77 | 2.31 | 0.19 | 3.31 | 0.19 | -0.06 | 0.06 | 0.99 | 0.96 |
| HD93083 | HARPS | 5030 | 25 | 0.13 | 0.17 | 4.37 | 0.65 | 0.75 | 2.22 | 0.53 | 1.06 | 0.53 | 0.18 | 0.06 | 0.81 | 0.84 |
| HD100508 | HARPS | 5423 | 42 | 0.41 | 0.10 | 4.39 | 0.42 | 0.67 | 2.31 | 0.35 | 2.05 | 0.35 | 0.63 | 0.09 | 0.99 | 1.00 |
| HD119638 | HARPS | 6148 | 29 | -0.10 | 0.05 | 4.43 | 0.22 | 1.11 | 0.66 | 0.25 | 4.63 | 0.25 | -0.04 | 0.05 | 1.07 | 1.17 |
| HD124364 | HARPS | 5608 | 33 | -0.22 | 0.07 | 4.46 | 0.22 | 0.50 | 2.32 | 0.19 | 2.50 | 0.19 | -0.21 | 0.01 | 0.88 | 0.86 |
| HD136894 | HARPS | 5423 | 32 | -0.08 | 0.07 | 4.32 | 0.24 | 0.61 | 1.77 | 0.23 | 2.23 | 0.23 | -0.10 | 0.01 | 0.85 | 0.92 |
| HD151504 | HARPS | 5500 | 38 | 0.12 | 0.09 | 4.35 | 0.32 | 0.61 | 1.77 | 0.27 | 2.34 | 0.27 | 0.12 | 0.07 | 0.98 | 1.00 |
| HD162236 | HARPS | 5398 | 31 | -0.06 | 0.07 | 4.47 | 0.33 | 0.68 | 2.27 | 0.27 | 1.82 | 0.27 | -0.10 | 0.03 | 0.88 | 0.83 |
| HD197210 | HARPS | 5575 | 36 | -0.02 | 0.08 | 4.43 | 0.21 | 0.54 | 1.83 | 0.21 | 2.48 | 0.21 | -0.03 | 0.03 | 0.92 | 0.91 |
| HD210752 | HARPS | 6081 | 28 | -0.56 | 0.09 | 4.39 | 0.03 | 1.19 | 1.38 | 0.17 | 4.33 | 0.17 | -0.21 | 0.48 | 0.88 | 1.00 |
| HD210975 | HARPS | 4650 | 32 | -0.56 | 0.19 | 4.60 | 0.02 | 1.20 | 2.15 | 0.13 | 0.37 | 0.13 | -0.34 | 0.31 | 0.68 | 0.69 |
| HD211415 | HARPS | 5861 | 70 | -0.18 | 0.13 | 4.39 | 0.26 | 0.87 | 2.10 | 0.55 | 3.35 | 0.55 | -0.10 | 0.04 | 0.96 | 1.07 |
| HD213941 | HARPS | 5500 | 45 | -0.49 | 0.09 | 4.30 | 0.25 | 0.50 | 2.16 | 0.34 | 2.53 | 0.34 | -0.33 | 0.01 | 0.75 | 1.00 |
| HD143120 | HARPS | 5750 | 29 | 0.33 | 0.06 | 3.88 | 0.03 | 1.06 | 2.02 | 0.10 | 4.03 | 0.10 | 0.58 | 0.13 | 1.28 | 2.17 |
| HD193995 | HARPS | 5770 | 30 | 0.26 | 0.06 | 4.10 | 0.03 | 1.06 | 1.98 | 0.08 | 3.70 | 0.08 | 0.31 | 0.07 | 1.20 | 1.69 |
| HIP1954 | HARPS | 5750 | 25 | -0.07 | 0.05 | 4.47 | 0.28 | 0.77 | 2.05 | 0.23 | 2.96 | 0.23 | -0.03 | 0.06 | 0.96 | 0.93 |
| HIP3203 | HARPS | 5871 | 28 | -0.06 | 0.05 | 4.51 | 0.26 | 1.00 | 3.84 | 0.22 | 3.33 | 0.22 | -0.06 | 0.06 | 1.01 | 0.95 |
| HIP19911 | HARPS | 5750 | 58 | -0.08 | 0.12 | 4.43 | 0.31 | 0.87 | 4.16 | 0.27 | 3.02 | 0.27 | -0.03 | 0.10 | 0.95 | 0.97 |
| HIP19911 | HARPS | 5750 | 58 | -0.08 | 0.12 | 4.43 | 0.31 | 0.87 | 4.16 | 0.27 | 3.02 | 0.27 | -0.03 | 0.10 | 0.95 | 0.97 |
| HIP118115 | HARPS | 5782 | 30 | -0.03 | 0.06 | 4.25 | 0.23 | 0.78 | 1.81 | 0.20 | 3.47 | 0.20 | -0.02 | 0.06 | 0.99 | 1.26 |
| HIP29442 | HARPS | 5370 | 31 | 0.27 | 0.07 | 4.40 | 0.28 | 0.65 | 2.22 | 0.24 | 1.87 | 0.24 | 0.27 | 0.06 | 0.90 | 0.99 |
| HIP31831 | HARPS | 5893 | 39 | 0.30 | 0.08 | 4.26 | 0.31 | 1.00 | 2.20 | 0.26 | 3.86 | 0.26 | 0.51 | 0.14 | 1.14 | 1.37 |
| HD4307 | FEROS | 5814 | 60 | -0.20 | 0.11 | 3.94 | 0.35 | 1.12 | 0.10 | 0.31 | 4.16 | 0.31 | -0.16 | 0.07 | 1.13 | 1.72 |
| HD14374 | FEROS | 5452 | 37 | -0.02 | 0.08 | 4.45 | 0.36 | 0.75 | 0.10 | 0.30 | 2.02 | 0.30 | 0.09 | 0.05 | 0.90 | 0.83 |
| HD16417 | UVES | 5782 | 46 | 0.12 | 0.09 | 4.05 | 0.18 | 1.05 | 3.17 | 0.23 | 3.78 | 0.23 | 0.06 | 0.07 | 1.18 | 1.67 |
| HD17051 | UVES | 6136 | 150 | 0.13 | 0.12 | 4.30 | 0.75 | 1.14 | 5.35 | 0.67 | 4.77 | 0.67 | 0.19 | 0.01 | 1.18 | 1.15 |
| HD17051 | UVES | 6136 | 150 | 0.13 | 0.12 | 4.30 | 0.75 | 1.14 | 5.35 | 0.67 | 4.77 | 0.67 | 0.19 | 0.01 | 1.18 | 1.15 |
| HD21019 | UVES | 5500 | 60 | -0.45 | 0.10 | 3.86 | 0.80 | 1.20 | 2.02 | 0.66 | 3.24 | 0.66 | -0.35 | 0.04 | 1.68 | 2.28 |
| HD21019 | UVES | 5500 | 60 | -0.45 | 0.10 | 3.86 | 0.80 | 1.20 | 2.02 | 0.66 | 3.24 | 0.66 | -0.35 | 0.04 | 1.68 | 2.28 |
| HD44420 | UVES | 5836 | 35 | 0.30 | 0.07 | 4.34 | 0.15 | 0.90 | 1.19 | 0.14 | 3.50 | 0.14 | 0.58 | 0.00 | 1.11 | 1.16 |

Table C.4: Results from SPECIES for the GBS samples, for the stellar parameters. The spectral types were drawn from Heiter et al. (2015), and denote the temperature classification, plus the luminosity class (V: dwarf, IV: subgiant, III: giant).

| Starname | Sp Type | [Fe/H] | $T$ (K) | log g | $\xi_t$ (km s$^{-1}$) | $v \sin \mathrm{i}$ (km s$^{-1}$) | $M$ ($M_\odot$) |
|---|---|---|---|---|---|---|---|
| 18Sco | G V | 0.11 ± 0.04 | 5872 ± 20 | 4.53 ± 0.15 | 0.87 ± 0.02 | 1.35 ± 0.16 | 1.1 ± 0.0 |
| 61CygB | K V | -0.48 ± 0.37 | 4989 ± 171 | 3.28 ± 2.67 | 0.95 ± 0.18 | 2.61 ± 2.43 | 2.7 ± 1.3 |
| Arcturus | FGK III | -0.20 ± 0.37 | 4752 ± 354 | 2.90 ± 1.90 | 1.73 ± 0.04 | 3.29 ± 1.66 | 3.5 ± 0.2 |
| Gmb1830 | K V | -1.17 ± 0.10 | 5368 ± 61 | 4.66 ± 1.08 | 1.41 ± 0.08 | 0.00 ± 0.00 | 0.1 ± 0.0 |
| HD107328 | FGK III | -0.41 ± 0.09 | 4526 ± 47 | 2.02 ± 0.46 | 1.70 ± 0.03 | 2.30 ± 0.47 | 3.2 ± 0.0 |
| HD220009 | FGK III | -0.86 ± 0.41 | 4120 ± 354 | 1.06 ± 2.78 | 1.34 ± 0.04 | -0.07 ± 3.60 | 3.7 ± 0.1 |
| HD22879 | G V | -0.85 ± 0.13 | 5858 ± 80 | 4.37 ± 0.28 | 0.68 ± 0.06 | 0.00 ± 0.00 | 0.8 ± 0.0 |
| HD49933 | F V | -0.48 ± 0.25 | 6732 ± 137 | 4.33 ± 1.44 | 2.24 ± 0.26 | 4.04 ± 1.90 | 1.3 ± 0.0 |
| Procyon | F V | 0.14 ± 0.26 | 6744 ± 137 | 4.06 ± 1.71 | 1.59 ± 0.18 | 0.00 ± 0.00 | 1.6 ± 0.1 |
| Sun | G V | 0.00 ± 0.05 | 5799 ± 25 | 4.46 ± 0.19 | 0.90 ± 0.02 | 1.56 ± 0.21 | 1.0 ± 0.0 |
| alfCenA | G V | 0.26 ± 0.09 | 5831 ± 42 | 4.34 ± 0.16 | 0.98 ± 0.03 | 1.78 ± 0.34 | 1.1 ± 0.0 |
| betAra | M III | -0.35 ± 0.69 | 4116 ± 500 | 0.59 ± 5.05 | 3.10 ± 0.10 | 6.88 ± 4.08 | 14.3 ± 0.6 |
| betGem | FGK III | 0.18 ± 0.08 | 5010 ± 38 | 3.17 ± 0.24 | 1.30 ± 0.03 | 2.16 ± 0.24 | 3.2 ± 0.2 |
| betHyi | FGK IV | -0.05 ± 0.08 | 5874 ± 38 | 4.04 ± 0.19 | 1.21 ± 0.04 | 3.05 ± 0.28 | 1.2 ± 0.0 |
| betVir | G V | 0.21 ± 0.06 | 6223 ± 28 | 4.21 ± 0.21 | 1.24 ± 0.03 | 1.66 ± 0.34 | 1.4 ± 0.0 |
| delEri | FGK IV | 0.16 ± 0.07 | 5133 ± 35 | 3.87 ± 0.23 | 0.93 ± 0.03 | 1.87 ± 0.24 | 0.9 ± 0.0 |
| epsEri | K V | -0.07 ± 0.13 | 5276 ± 35 | 4.46 ± 1.74 | 1.13 ± 0.04 | 2.53 ± 2.23 | 0.8 ± 0.0 |
| epsFor | FGK IV | -0.39 ± 0.07 | 5370 ± 4 | 4.26 ± 0.42 | 0.69 ± 0.03 | 2.15 ± 0.38 | 1.9 ± 0.1 |
| epsVir | FGK III | -0.06 ± 0.12 | 4830 ± 1 | 2.15 ± 0.24 | 1.48 ± 0.05 | 2.16 ± 0.32 | 4.5 ± 0.1 |
| etaBoo | FGK IV | -0.07 ± 0.26 | 5670 ± 1 | 3.03 ± 0.50 | 1.71 ± 0.13 | 11.96 ± 0.43 | 2.1 ± 0.0 |
| gamSge | M III | 0.14 ± 0.26 | 4481 ± 158 | 2.63 ± 0.92 | 1.98 ± 0.12 | 4.10 ± 0.79 | 4.5 ± 0.0 |
| ksiHya | FGK III | 0.21 ± 0.08 | 5186 ± 36 | 3.16 ± 0.21 | 1.35 ± 0.03 | 4.04 ± 0.21 | 0.1 ± 0.0 |
| muAra | G V | 0.38 ± 0.21 | 5967 ± 106 | 4.62 ± 0.48 | 1.10 ± 0.08 | 1.99 ± 0.44 | 1.3 ± 0.2 |
| muLeo | FGK III | 0.21 ± 0.15 | 4458 ± 1 | 2.23 ± 0.39 | 1.60 ± 0.07 | 1.21 ± 0.37 | 2.3 ± 0.0 |

Table C.5: Results from SPECIES for the GBS samples, for the chemical abundance of the elements in common with Jofré et al. (2015).

| Starname | [Mg/H] | [Si/H] | [Ca/H] | [Ti/H] | [Cr/H] | [Mn/H] | [Ni/H] |
|---|---|---|---|---|---|---|---|
| 18Sco | 0.08 ± 0.07 | 0.08 ± 0.02 | 0.14 ± 0.02 | 0.16 ± 0.10 | 0.10 ± 0.01 | 0.12 ± 0.07 | 0.08 ± 0.03 |
| 61CygB | -0.46 ± 0.14 | -0.87 ± 0.02 | 0.63 ± 0.04 | 0.51 ± 0.11 | -0.02 ± 0.05 | -0.49 ± 0.10 | -0.91 ± 0.18 |
| Arcturus | -0.00 ± 0.08 | -0.13 ± 0.04 | -0.03 ± 0.01 | 0.29 ± 0.10 | -0.23 ± 0.02 | -0.32 ± 0.01 | -0.22 ± 0.02 |
| Gmb1830 | -1.27 ± 0.23 | -0.90 ± 0.20 | -0.82 ± 0.02 | -0.84 ± 0.13 | -1.10 ± 0.05 | nan ± nan | -1.25 ± 0.16 |
| HD107328 | 0.01 ± 0.06 | -0.08 ± 0.04 | -0.21 ± 0.01 | -0.16 ± 0.04 | -0.43 ± 0.04 | -0.61 ± 0.06 | -0.43 ± 0.01 |
| HD220009 | -0.35 ± 0.05 | -0.40 ± 0.03 | -0.56 ± 0.05 | -0.72 ± 0.01 | -0.81 ± 0.02 | -1.05 ± 0.10 | -0.87 ± 0.01 |
| HD22879 | -0.58 ± 0.04 | -0.56 ± 0.05 | -0.55 ± 0.00 | -0.61 ± 0.07 | -0.86 ± 0.01 | 0.04 ± 0.00 | -0.88 ± 0.02 |
| HD49933 | -0.53 ± 0.17 | -0.32 ± 0.03 | -0.33 ± 0.02 | -0.45 ± 0.02 | -0.51 ± 0.03 | nan ± nan | -0.54 ± 0.01 |
| Procyon | 0.08 ± 0.07 | 0.17 ± 0.07 | 0.23 ± 0.01 | 0.04 ± 0.06 | 0.12 ± 0.03 | 0.34 ± 0.42 | 0.08 ± 0.03 |
| Sun | -0.03 ± 0.07 | -0.01 ± 0.02 | 0.02 ± 0.04 | 0.02 ± 0.06 | 0.01 ± 0.01 | 0.01 ± 0.04 | 0.00 ± 0.02 |
| alfCenA | 0.18 ± 0.06 | 0.29 ± 0.02 | 0.29 ± 0.02 | 0.27 ± 0.02 | 0.26 ± 0.01 | 0.42 ± 0.03 | 0.28 ± 0.03 |
| betAra | -0.29 ± 0.23 | 0.17 ± 0.28 | -0.46 ± 0.07 | -0.59 ± 0.06 | -0.41 ± 0.16 | -0.62 ± 0.28 | -0.53 ± 0.06 |
| betGem | 0.15 ± 0.13 | 0.26 ± 0.02 | 0.18 ± 0.01 | 0.19 ± 0.01 | 0.25 ± 0.01 | 0.40 ± 0.29 | 0.08 ± 0.01 |
| betHyi | -0.08 ± 0.07 | -0.04 ± 0.02 | 0.01 ± 0.02 | 0.01 ± 0.04 | -0.06 ± 0.03 | -0.06 ± 0.04 | -0.08 ± 0.01 |
| betVir | 0.11 ± 0.08 | 0.23 ± 0.05 | 0.29 ± 0.01 | 0.27 ± 0.10 | 0.21 ± 0.03 | 0.19 ± 0.08 | 0.20 ± 0.01 |
| delEri | 0.18 ± 0.05 | 0.13 ± 0.01 | 0.21 ± 0.02 | 0.19 ± 0.03 | 0.20 ± 0.01 | 0.40 ± 0.15 | 0.18 ± 0.03 |
| epsEri | -0.06 ± 0.00 | -0.21 ± 0.01 | 0.10 ± 0.07 | 0.06 ± 0.03 | 0.04 ± 0.03 | -0.00 ± 0.09 | -0.12 ± 0.03 |
| epsFor | -0.18 ± 0.07 | -0.27 ± 0.05 | -0.12 ± 0.05 | 0.07 ± 0.03 | -0.42 ± 0.00 | -0.51 ± 0.01 | -0.36 ± 0.00 |
| epsVir | 0.05 ± 0.19 | 0.25 ± 0.01 | -0.02 ± 0.02 | -0.23 ± 0.00 | -0.06 ± 0.03 | 0.09 ± 0.24 | -0.12 ± 0.00 |
| etaBoo | 0.13 ± 0.27 | 0.38 ± 0.08 | 0.19 ± 0.02 | -0.12 ± 0.14 | -0.07 ± 0.09 | 0.38 ± 0.09 | 0.08 ± 0.12 |
| gamSge | 0.15 ± 0.04 | 0.17 ± 0.04 | 1.93 ± 1.85 | 0.51 ± 0.04 | 0.34 ± 0.05 | 0.09 ± 0.04 | -0.06 ± 0.02 |
| ksiHya | 0.12 ± 0.10 | 0.22 ± 0.06 | 0.21 ± 0.01 | 0.23 ± 0.00 | 0.24 ± 0.02 | 0.39 ± 0.38 | 0.10 ± 0.01 |
| muAra | 0.22 ± 0.07 | 0.28 ± 0.02 | 0.30 ± 0.13 | 0.38 ± 0.06 | 0.42 ± 0.04 | 0.58 ± 0.11 | 0.35 ± 0.02 |
| muLeo | 0.38 ± 0.08 | 0.38 ± 0.01 | 0.17 ± 0.03 | 0.20 ± 0.05 | 0.20 ± 0.02 | 0.49 ± 0.36 | 0.13 ± 0.03 |

where the first term corresponds to the contribution from the uncertainty in the microturbulence, and the second term is the contribution from the uncertainty in the slope of the dependence between the individual Fe I abundances and the excitation potential, $\chi_I$. The first term is the same as the one derived in section 3.1.5, but the second term is different and described here.

From equation 16.4 of Gray (2005), we can derive that:

$$\log\left(\frac{w}{\lambda}\right) \propto \log A - \theta_{\mathrm{ex}}\chi_I, \tag{C.3}$$

where $\log(w/\lambda)$ is the reduced equivalent width of the line, $\log A = \log(N_E/N_H)$ the abundance of the element $E$ to hydrogen, $\theta_{\mathrm{ex}} = 5040/T$, and $\chi_I$ is the excitation potential. If we assume that the equivalent width of the line will not change with respect to $\chi_I$, but $\log A$ will, then when we differentiate with respect to $\chi_I$, $\partial/\partial\chi_I$, we obtain

$$\frac{\partial T}{\partial \chi_I} = s_{\chi_I}\frac{T^2}{5040}, \tag{C.4}$$

where $\partial \log A/\partial\chi_I = s_{\chi_I}$ is the slope of the correlation between individual line abundances and excitation potential, and is one of the results obtained from the MOOG output file. The contribution from the uncertainty in the excitation potential will then be the above expression multiplied by the error in the slope.

## C.4 Column description

The columns returned by SPECIES are as follow:

- Col 1: Star name.
- Col 2: Instrument used to obtain the spectra (HARPS, FEROS, HIRES, UVES, CORALIE, AAT).
- Col 3: Velocity in km $s^{-1}$, obtained from the CCF (section 3.1.2), used to correct the spectrum to the restframe.
- Cols 4-11: Atmospheric stellar parameters and their corresponding uncertainty (metallicity, temperature, surface gravity, and microturbulent velocity, respectively)
- Cols 12-13: Number of Fe I and Fe II lines used for the computation of the atmospheric parameters, respectively.
- Col 14: Exception to the atmospheric parameters. A value of one means the parameters were computed correctly. A value of two means that there were problems in the computation (parameters were repeated more than 200 times, or all of them were outside the permitted ranges), or that the code could not converge to a final value after performing over 1 million iterations.
- Cols 15-18: $v \sin \mathrm{i}$ and $v_{mac}$ for each star, with their respective uncertainties.
- Cols 19-54: Abundances for Na, Mg, Al, Si, Ca, Ti I, Ti II, Cr, Mn, Ni, Cu, and Zn, as well as their uncertainties (standard deviation from the mean) and the number of lines used.
- Cols 55-56: Individual abundances for Fe I and Fe II, respectively.
- Cols 57-64: Mass, age, $\log \mathrm{g}_{\mathrm{iso}}$ (explained in Section 3.2.2), and radius obtained, along with their 54% and 16% confidence levels.
- Col 68: Tells whether the temperature computed from the method of Casagrande et al. (2010) was used as the final temperature or not, for the cases when no convergence was reached in the atmospheric parameters (Section 3.1.4).
- Col 69: Tells whether the microturbulent velocity was set to 1.2 km $s^{-1}$, for the cases when no convergence was reached in the atmospheric parameters (section 3.1.4).
- Col 70: Tells whether the surface gravity was set to be equal to $\log \mathrm{g}_{\mathrm{iso}}$ (section 3.1.6).
- Cols 71-72: Error in the microturbulence and temperature, computed using the methods described in Sections C.2 and C.3.
- Cols 73-75: Value, uncertainty, and relation used to obtain the temperature from photometry (section 3.1.3).